Dielectric and Magnetic Studies of Wide-bandgap Mott Insulators and their Composites

A Thesis Submitted to
Indian Institute of Technology Guwahati
for the degree of

Doctor of Philosophy

By

Deep Chandra Joshi

Department of Physics
Indian Institute of Technology Guwahati
Guwahati-781039, Assam (India)

Dedicated to my beloved Parents: Sri. Chandra Sekhar Joshi, Smt. Munni Joshi, and, Dr. Bhanu Prakash Joshi, Mrs. Sushma Joshi and Jr. Tejashwa Joshi

INDIAN INSTITUTE OF TECHNOLOGY GUWAHATI

Department of Physics

Guwahati – 781039

Declaration

"*Dielectric and Magnetic Studies of Wide-bandgap Mott Insulators and their Composites*" is the result of my own doctoral research work. This work was carried out under the supervision of Dr. Subhash Thota at the Department of Physics, Indian Institute of Technology Guwahati. To the best of my knowledge, the work presented in this thesis has not been submitted to any other Institute/University for the award of any degree.

Deep Chandra Joshi
Research Scholar (Roll No: 136121010)
Department of Physics
Indian Institute of Technology Guwahati
Guwahati-781039, India

INDIAN INSTITUTE OF TECHNOLOGY GUWAHATI

Department of Physics

Guwahati – 781039

Certificate

It is certified that the work described in this thesis, entitled "*Dielectric and Magnetic Studies of Wide-bandgap Mott Insulators and their Composites*", done by Mr. Deep Chandra Joshi, a Ph.D. student of Department of Physics, Indian Institute of Technology Guwahati, for the award of degree of Doctor of Philosophy has been carried out under my supervision. This work has not been submitted elsewhere for the award of any degree.

Dr. Subhash Thota
Associate Professor
Department of Physics
Indian Institute of Technology Guwahati
Guwahati-781039, India

Acknowledgements

With the divine grace of Almighty Lord Shiva

Foremost, I would like to express my sincere gratitude to my beloved thesis supervisor Dr. Subhash Thota for providing me the once in a lifetime opportunity to work under his supervision. Without his motivation, enthusiasm, encouragement and continuous support this work would have not been completed. I must acknowledge him for keeping an exceptional trust and confidence on me. I am deeply beholden for his constructive criticism, patience, immense knowledge and concern to bring out my hidden ideas and focused them to perform my best. I would also like to express my special thanks of gratitude to Mrs. Revathi Thota, Veda Samhitha Thota and Prativa Pramanik for always supporting me during all stages of my work and for sharing such a wonderful relationship.

I owe my deepest gratitude to my doctoral committee members, Prof. P. K. Giri (Chairman), Dr. D. Pamu, Dr. Pankaj Tiwari and Dr. N. Peela for their continual supervision and examine my progress work and seminars during my research work. Their advices and valuable suggestions have significantly improved the quality of my thesis work. I would like to express my sincere gratitude to Prof. P. Poulose, Head of the Department of the Physics for giving me the opportunity to work in the department and to avail all the departmental facilities. I am also grateful to all the faculty members of the Physics department. I would also like to thank Dr. Sidananda Sarma for his technical help and friendly discussion. I express my sincere thanks to all the collaborators Prof. M. S. Seehra, Dr. T. Sarkar, Dr. R. J. Choudhary, Dr. S. Pittala, Dr. A. Mohanta, Dr. R. N. Chauhan, Dr. K. Dasari, for providing me the experimental facilities. From the bottom of my heart I wish to thank IIT Guwahati for providing me the financial support. I also acknowledge the funding agencies DAE-BRNS, DST-FIST and the Central Instruments Facility (CIF-IITG) for supporting my research work.

It is my pleasure to thank the fellow lab mates, D. Harish, S. Nayak, P. Pramanik, R. George, Dr. T. A. Dar, S. Ghosh, T. Nagendrababu, A. Thakur, A. Mehr and R. K. Yadav for their suggestions and providing a working environment throughout my study. I would like to thank my juniors R. Soni, T. S. Santhosh, P. Kampelly, S. Vikas, S. Biswas, A. Naughai, R. Sinha, N. Brigwan, K. Monica, T. Harish, U. Pandey, Dr. D. Pandey, A. Chandel, and J. Joshi for their valuable help. Words are not enough to express my gratitude to my seniors Dr. T. S. Kumar, Dr. P. Rajender, Dr. P. Mahesh, Dr. R. G. Rao, and G. Rajender for their help and inspiration. I am indebted to my friends V. Belwal, G. Kaira, S. K. Singh, A. Giri, G. Bhandari, R. Bhatt, A. Balodhi, A. Mathew, P. Talukdar, R. Modak, P. Negi, K. Patra, P. Kunwar, B. Pant, L.S. Mehra for supporting me during all the phases of my life.

Finally, it is an honor for me to express my heartfelt gratitude to my family members; my sweet parents Smt. Munni Joshi and Sri. Chandra Sekhar Joshi, my brother Dr. B. P. Joshi, my sister-in-law Mrs. Sushma Joshi and my nephew Jr. Tejaswa, without whom this thesis would not have been possible.

Deep Chandra Joshi

Research Scholar (Roll No: 136121010)

Synopsis Report

High-permittivity magneto-dielectric materials and their composites have drawn a tremendous attraction in recent past due to their versatile applications such as in piezoelectric transducers, low-power CMOS devices, sensors and spintronics [1-11]. Apart from the Perovskite systems (Pb[Zr,Ti]O_3, $CaCu_3Ti_4O_3$, $KNaNbO_3$, etc.), lead-free 3*d* transition metal oxide based magnetic ceramics with static dielectric constant (ε_r) more than 1000 are very limited in the literature [12-17]. Compounds such as $La_{1-x}Ca_xMnO_3$, $BaTiO_3$, $YBa_2Cu_3O_6$, and $FeTiTaO_6$ are considered as important systems because of their negligible temperature variation of ε_r and relaxor-like ferroelectric behavior [18-25]. There has not been enough attention paid to the high-frequency dielectric behavior of alkali metal (Na or Li) doped nonperovskite wide-bandgap oxides such as ZnO and NiO, and their composites. Among various lead-free 3*d* transition metal oxide systems Li and Ti doped wide-bandgap Mott insulators are the best known examples because of their colossal dielectric permittivity and temperature independent behavior of ε_r [12, 26]. Internal grain-boundary layer mechanism and thermally excited relaxation process are the key sources for such enhanced ε_r and non-zero dipole moment [26]. Dielectric relaxation in Fe, Mg, Al, Co, Zr and V doped wide-bandgap oxides are also widely investigated aiming to understand the ac-conductivity, space-charge polarization (Maxwell–Wagner type) at low frequencies and defect-dipole induced polarization mechanism at high frequency regions [27-30]. The present research work has primarily motived to develop the two-phase composite systems of $Zn_{1-x}Ni_xO$/NiO and $Ni_{1-x}Na_xO$ whose physical properties are comparable to those of Li, Ti doped NiO. When we initiated this problem no report was available focusing on the structural, dielectric and magnetic properties of above composites either in the form of both bulk or nanostructures. Hence, an attempt was made to understand the growth mechanism and other physical properties of the above mentioned composites. The detailed layout of the thesis is as follows:

Chapter 1 provides a brief introduction to the High-κ dielectrics and their significance in microelectronics. This chapter also presents an important up-to-date research on the dielectric properties of alkali metal doped ZnO and NiO. This chapter reviews few important concepts like: Mott-Insulators, Lyddane-Sachs-Teller relation $\left[\frac{\epsilon_0 - S'}{\epsilon_\infty} = \left(\frac{\omega_l}{\omega_t}\right)^2\right]$, Debye relaxation, various dielectric polarization mechanisms including Maxwell–Wagner–Sillars and defect-dipole polarization with special emphasis on the influence of domain-wall displacement, microstructure, depletion and depolarization effects. In addition, a brief introduction to molecular field theory of antiferromagnetism in transition metal oxides which crystalizes in rock salt type crystal structure was presented. Finally, a detailed description of the research problem and its approach is illustrated in this chapter.

Chapter 2 describes a detailed overview of various experimental techniques employed in this research work including the synthesis procedure of $Zn_{1-x}Ni_xO$/NiO and $Ni_{1-x}Na_xO$ based on low-temperature sol-gel processing and standard solid-state reaction method. This chapter also demonstrates various characterization techniques including structural characterization using X-ray and electron diffraction techniques and thermal properties using

thermogravimetric-analysis (TGA) and differential scanning calorimetry (DSC). For a detailed crystal structure analysis, we performed the Rietveld refinement of diffraction data using Fullprof and Powder-cell softwares. Particulars of elemental analysis performed by the X-ray photoelectron spectroscopy (XPS) was described thereafter. Morphological characterization techniques such as transmission electron microscopy (TEM) has also been discussed. In the subsequent sections we presented the details of various characterization tools employed in this work such as: (*i*) frequency and temperature dependence of dielectric measurements, (*ii*) Raman spectroscopy to understand the vibrational excitation, (*iii*) electron-spin resonance technique to probe the local atomic environment, and (*iv*) magnetic measurements using superconducting quantum interference device (SQUID) based magnetometer and vibrating sample magnetometer.

Chapter 3 presents a detailed structural and dielectric properties of polycrystalline wurtzite h.c.p $Zn_{1-x}Ni_xO$ and cubic NiO two-phase composites. In this chapter we demonstrated that these composites exhibit a dielectric anomaly across the transition temperature (T^*) ~ 541 K associated with the changeover from antiferro to paramagnetic ordering of NiO. Such transition is accompanied by the change in crystal structure from rhombohedral to cubic phase. For $T > T^*$, a giant dielectric cusp was observed across 683 K (410˚C) for $x = 1$ together with the above mentioned anomaly at T^* close to the antiferromagnetic Néel temperature T_N of NiO. For $T > T^*$ the dielectric permittivity cusp obeys the empirical scaling law based on the equation $(\varepsilon_A/\varepsilon_r = 1+0.5(T-T_A)^2/\delta^2)$ with the shape parameter value 'δ' ~ 88 and 39.73 ˚C for the compositions $x = 0.30$ and 0.163, respectively. Dynamic variation of the dispersion in ε_r at temperatures close to T^* follows the Vogel–Fulcher law with Debye frequency $\nu_0 \sim 1.33 \times 10^9$ Hz and 1.33×10^6 Hz, freezing temperature $T_g \sim 181$˚C and 240˚C, and activation energy $E_A = 0.11$eV and 0.023 eV for $x \sim 0.30$ and 0.16, respectively. Diffuseness exponent 'γ' = 1.91 and 1.77 estimated from the experimental data for the compositions $x = 0.30$ and 0.163, respectively are close to 'γ' = 2 usually exhibited by an ideal relaxor ferroelectric system. These results are further supported by the butterfly loop characteristics of C-V curves. The relaxor behavior (mixed phase ferroelectric–glass) for heavily doped $Zn_{1-x}Ni_xO$/NiO system is mainly driven by the compositional heterogeneity. The temperature dependence of ac-resistivity $\rho_{ac}(T)$ provide strong evidence of variable-range-hopping of charge carriers between the localized states through a mechanism involving spin-dependent activation energies. The temperature variation of carrier hopping energy $\varepsilon_h(T)$ and nearest-neighbor exchange-coupling parameters $J_{ij}(T)$ are evaluated for all the compositions using small-Polaron model. For all the composite systems, $J_{ij\text{-Average}}$ nearly equals to 70 meV which is slightly greater than the exciton binding energy 60 meV of pure zinc-oxide. A systematic comparative analysis of the above results with the Na doped NiO system is presented.

Chapter 4 focuses on the nature of magnetic exchange interactions in $Zn_{1-x}Ni_xO$-NiO composites. The magnetic exchange constants $|J_1|$ and $|J_2|$ for the two-sublattices have been evaluated using both molecular-field approximation ($J_1 \sim 0.15$ meV and $J_2 \sim 1.15$ meV for $x = 1$) and Green's-function theory ($J_1 \sim 0.78$ meV and $J_2 \sim 1.77$ meV for $x = 1$). Magnitudes of these exchange constants determined from the Green's-function analysis are

compared systematically with the values obtained from the spin-wave dispersion curves ($J_1 \sim 0.137$ meV and $J_2 \sim 1.90$ meV for $x = 1$) and Raman scattering ($J_2 \sim 1.98$ meV). Additionally, the carrier activation energies 'ε_h' and nearest-neighbour exchange coupling parameters 'J_{ij}' (~1.61 meV) calculated from the temperature dependence of ac-resistivity $\rho_{ac}(T)$ across T_N of NiO. Such analysis is based on the small-polaron model involving spin dependent activation energies. These results are compared with the theoretical estimations performed by the Green's-function theory. Furthermore, the role of oxygen stoichiometry on the temperature variation of J_{ij}, ε_r, ρ_{ac}, and unit-cell volume 'V_C' have been discussed for both $Zn_{1-x}Ni_xO$/NiO and $Ni_{1-x}Na_xO$.

Chapter 5 is devoted to the growth and characterization of low-dimensional nanostructures of $Zn_{1-x}Ni_xO$/NiO. First two sections of this chapter are dedicated to the formation mechanism, crystal structure and morphology. These preliminary studies are followed by a detailed investigation of the electron-spin-resonance (ESR) and Raman spectroscopic studies. The temperature variation of X-band ESR parameters viz. resonance field $H_R(T)$ and line-width $\Delta H_{PP}(T)$ was analyzed using the power-law variation ($\delta H_R = (\Delta H_{PP})^n$) of Nagata and Ishihara model. This model was used to understand the orientation of statistical ensemble of particles with respect to a given direction of the anisotropy axis. This analysis yields the exponent 'n' $\simeq$ 2.13 and 2.85 for the nanocomposite system $Zn_{1-x}Ni_xO$/NiO and pure NiO suggesting the presence of partial and randomly oriented ellipsoidal nanocrystallites, respectively. Further, the Raikher and Stepanov model has been employed to probe the role of amorphous Ni^{3+} clusters on the observed ESR spectra. The vibrational excitations obtained from the Raman spectroscopy reveals that after Ni substitution in wurtzite ZnO, a new zone-boundary phonon mode was emerged at 129 cm^{-1} for all the compositions. Such phonon mode is usually forbidden in the first-order Raman scattering of ZnO. In addition to the 2M Magnon mode, two extra modes appear at 558 and 900 cm^{-1} due to the increased volume fraction of NiO within the $Zn_{1-x}Ni_xO$ matrix. A systematic correlation of all the above results with the magnetic anisotropy of the nanocomposites is discussed.

Chapter 6 presents a brief summary of important findings of our experimental results. In this chapter we also identify some open issues which are potentially interesting for the future studies.

List of Publications:

Peer Reviewed Journals:

[1] *"Dielectric behavior of $Zn_{1-x}Ni_xO$/NiO two-phase composite",*
***D. C. Joshi**, S. Thota, S. Nayak, D. D. Harish, P. Mahesh, A. Kumar, D. Pamu, Md. Qureshi*
Journal of Physics D: Applied Physics ***47**, 435305 (2014).*

[2] *"The X-ray photoelectron spectroscopy and high-temperature structural studies of $Zn_{1-x}Ni_xO$/NiO two-phase composites",*
***D. C. Joshi**, S. Nayak, P. Suresh, K. S. Suresh, B. V. Kumar, and S. Thota*
Physica Status Solidi (B) **252**, 2323 (2015).

[3] *"Peculiarities of the temperature dependence of electron spin resonance and Raman studies of $Zn_{1-x}Ni_xO$/NiO two-phase nanocomposites",*
***D. C. Joshi**, S. Nayak, A. Kumar, A. Mohanta, D. Pamu and S. Thota*
Journal of Applied Physics ***119**, 074303 (2016).*

[4] *"Localized Charge Carrier Transport Properties of $Zn_{1-x}Ni_xO$/NiO Two-Phase Composites",*
***D. C. Joshi**, K. Dasari, S. Nayak, R. Palai, P. Suresh and S. Thota*
Journal of Electronic Materials ***45**, 2059 (2016).*

[5] *"Magnetic exchange interactions and dielectric studies of $Zn_{1-x}Ni_xO$-NiO composites",*
***D. C. Joshi**, P. Pramanik, S. Nayak, K. Dasari, R. J. Choudhary and S. Thota,*
Journal of Physics D: Applied Physics ***50**, 325002 (2017).*

[6] *"Growth mechanism and electron spin resonance studies of $Zn_{1-x}Ni_xO$/NiO two-phase nanocomposite",*
***D. C. Joshi**, D. D. Harish, S. Nayak, D. Roy, Md. Qureshi, R.L.N. Saiprasad, T. Shiyani, D. Pamu, S. Thota*
IEEE Xplore Emerging Electronics (ICEE), 2014 IEEE 2nd International Conference.

[7] *"Nature of Magnetic Ordering in Nanocomposites of $Zn_{1-p}Ni_pO$ and NiO",*
***D. C. Joshi**, P. Pramanik, R. George, T. Sarkar and S. Thota, Physica E (2018), (Manuscript under review, 2018).*

[8] *"Dielectric Relaxation and Magnetic studies of Na doped NiO",*
***D. C. Joshi**, P. Pramanik, T. Sarkar and S. Thota. (Under Preparation).*

Research work presented in international/national conferences and workshops:

[1] *"Growth mechanism and Electron-Spin-Resonance studies of $Zn_{1-x}Ni_xO$/NiO two-phase Nanocomposite"*
***D. C. Joshi**, D.D. Harish, D. Roy, S. Nayak, Md. Qureshi, R.L.N. Sai prasad, T. Shiyani, D. Pamu, S. Thota*
2nd IEEE International Conference on Emerging Electronics, 3-6 Dec 2014, IISc Bangalore, Karnataka, India.

[2] *"The localized charge carrier transport properties of $Zn_{1-x}Ni_xO$/NiO ($0.3 \leq x \leq 1$) two-phase composites"*
***D. C. Joshi**, K. Dasari, S. Pittala, S. Nayak and S. Thota*
57th Electronic Materials Conference, The Ohio State University, Columbus, Ohio, 24-25 June 2015, USA.

[3] *"Effect of 'Na' Doping on the Structural, Dielectric and Electronic Characteristics of Wide Band-Gap NiO".*
***D. C. Joshi**, K. Dasari, S. Nayak, P. Pramanik, P. Suresh, S. Pittala, and S. Thota*
9th Workshop on frontiers in Electronics & 2nd Workshop on multifunctional nanomaterials, 15-18 Dec 2015, San Juan, PR, USA.

[4] *"Compositional dependence of structural and X-ray photoelectron spectroscopic studies of $Zn_{1-x}Ni_xO$/NiO Two-Phase Composites"*
***D. C. Joshi**, S. Nayak, P. Pramanik, K. Dasari, R. Palai, Md. Qureshi and S. Thota*
2nd International Conference On Material Science and Technology, 5-8 June 2016 St. Thomas College Pala Arunapuram, India.

[5] *"Magnetic Properties of $Zn_{1-x}Ni_xO$/NiO two-phase Nanocomposites"*
***D. C. Joshi**, T. Sarkar, S. Nayak, P. Pramanik, S. Das, and S. Thota*
5th International Conference on Magnetic Materials and Application, 1-3 Feb 2017, Hyderabad, India.

[6] *"X-ray Photoelectron Spectroscopic Studies of Na Doped NiO"*
***D. C. Joshi**, S. Nayak, P. Pramanik, R. George, R. Soni, K. Dasari and S. Thota*
National Seminar on Advances In Material Science, 24-25 March 2017, Gauhati University, Assam, India.

[7] *"The role of Na doping on the Electronic, Structural and Dielectric Properties of NiO"*
***D. C. Joshi**, T. Nagendrababu, P. Pramanik and S. Thota*
National Conference on Nanomaterials and its Applications, 20-21 Sept 2017; Golaghat; Assam, India.

[8] *"The role of Na doping on the Antiferromagnetic ordering of NiO"*
***D. C. Joshi**, P. Pramanik and S. Thota,* International Conference on Advanced Functional Materials,18-20 Dec, 2017, Basar, Telangana State, India.

[9] *"Indo-US Symposium On Recent Advances In Magnetism and Spintronics",* 5-6 Feb 2018, Victor Menezes Convention Centre (VMCC), IIT Bombay, Powai, Mumbai, India.

Contents

List of Figures

List of Tables

List of Abbreviations and Symbols

XRD — X-ray diffraction
XPS — X-ray Photoelectron spectroscopy
B.E — Binding Energy
T_N — Néel temperature
h — hours
ZFC — Zero-Field Cooled
FC — Field Cooled
FWHM — Full width at half maxima
Å — Angstrom
ε_r — Relative dielectric permitivitty
pm — Picometer
nm — Nanometer
mm — Millimeter
cm — Centimeter
μm — Micro-meter
K — Kelvin
μ_B — Bohr magnetron
HRS — high resistive state
LRS — low resistive state
RS — Resistive switching
MIM — metal-insulator-metal
Resistive Random Access Memories — RRAM
non-volatile memory devices — NVMD
Havriliak-Negami — HN

Chapter-I

Introduction to High- κ Dielectrics and Wide-bandgap Mott-Insulators

1.1 Background and Motivation:

This chapter deals with the High-κ dielectrics and wide-bandgap Mott-insulators in a single picture by reviewing some basic concepts like dielectric relaxation mechanism and antiferromagnetic properties of Mott-insulators with special emphasis on technological applications along with the fundamental physics. Compounds with high relative-dielectric-permittivity (often refers to High-κ systems) are in extensive use since many decades in electronic industry as gate-oxide layer in Metal-Oxide-Semiconductor Field Effect Transistors (MOSFET) [1–3]. Among such High-κ materials, silicon-dioxide (SiO_2) is an excellent candidate for the gate-oxide material in MOSFET devices which has been used extensively in complementary metal–oxide–semiconductor CMOS technology [4]. However, these High-κ oxides finds limitations as integration of number of transistors increases, the SiO_2 layer thickness scales down to few atomic layers thick (~15-20 Å) leading to high leakage-current density J_{Leak} (surpasses 1 A/cm^2), high power consumption and reduced device reliability. Such effects are mainly driven by the tunneling effects at very low-dimensions [5]. To overcome this problem SiO_2 has been supplanted by few other High-κ materials such as, Aluminum-oxide (Alumina Al_2O_3), Zirconium-dioxide (Zirconia ZrO_2), and Hafnium-oxide (HfO_2). All these oxides are expected to increase gate capacitance (40 mF/m^2) without any leakage current (2-3 orders of reduction in the magnitude) [5,6].

On the other hand, insulating properties of these dielectrics can be tuned by applying specific electrical and magnetic fields to achieve unusual property, called resistive switching (RS) [5,6]. The switching effect between a high resistive state (HRS or "0") to a low resistive state (LRS or "1") makes one single memory entity (One Bit). The technology based on the concept of resistance change (i.e. RS) is revolutionizing the field of non-volatile memory devices (NVMD) by improving the performance of Resistive Random Access Memories (RRAM) [7,8]. In the case of conventional solid-state non-volatile computer storage devices (popularly known as Flash Memory), the negative-AND logic gate (NAND) plays an important role which stores information in the form of a tiny cloud of electrons in a quantum well [8]. On the contrary, RRAM stores the information using the concept of change in resistance of the memory cell, which minimizes the power consumption of the entire device by reducing the leakage currents. Two-terminal nonlinear devices based on the metal-insulator-metal (MIM) diodes are typical components of RRAM devices. Such MIM devices are very similar to conventional semiconductor diodes but MIMs are capable of very fast operation as compared to the semiconductor diodes. Key advantage of MIM based memories are: (*a*) high switching speeds (~1 ns), (*b*) low power-dissipation (few μW and10^{-10} J/bit), (*c*) long cycling endurance (> 10^6 cycles), (*d*) easy fabrication procedure, and (*e*) excellent scalability.

Figure 1.1 shows the schematic diagram of RS mechanism involved in a MIM-structured memory cell [6,9]. A typical RRAM memory element contains two metal electrodes analogous to a capacitor like geometry in which an insulating metal oxide is sandwiched. The Resistive switching action at room temperature is accompanied by applying pulsed voltages of ±5 V. These pulses lead to a giant change (>1000%) in the resistance with super-fast switching speed of the order of nanoseconds, which can be tuned to a desired value by applying the appropriate potential [6,9].

Figure 1.2 shows the schematic diagram of MIM tunnel junction with stacked tri-layer structure of Ni-NiO-Cr for the Millimeter wave detection [10]. Generally, to obtain high efficiency for the MIM tunnel junction dissimilar materials are selected which results in non-linear current-voltage (I-V) characteristics and high sensitivity [10]. The cut-off frequency (f_c) of the diode is inversely proportional to the junction area (A) of the diode which can be determined by using the following equations:

$$f_c = \frac{1}{2\pi R_a C_d} \qquad (1.1)$$

$$C_d = \frac{\varepsilon_0 \varepsilon_r A}{d} \qquad (1.2)$$

In the above equations, R_a is the antenna resistance and C_d is the capacitance of the diode, and d is the separation between two electrodes. By varying the overlapping positioning of the contact area and reducing the junction area to micro/nano scale, the operating frequencies of MIM diode can be increased significantly [11]. In order to detect the millimeter waves (operating frequency 94 GHz) the contact area of Ni-NiO-Cr based MIM tunnel junction should be of 1 μm^2 [10].

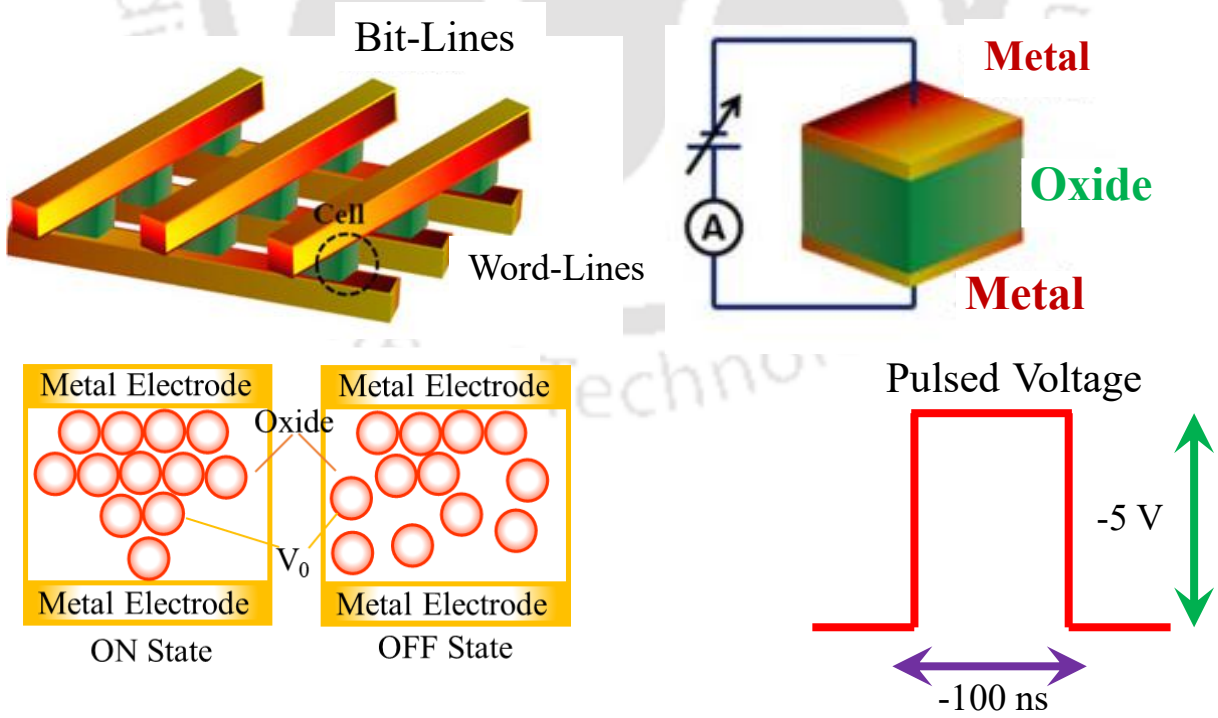

Figure 1.1: A schematic diagram representing the resistive switching mechanism in a metal/oxide/metal-structured memory cell [6,9].

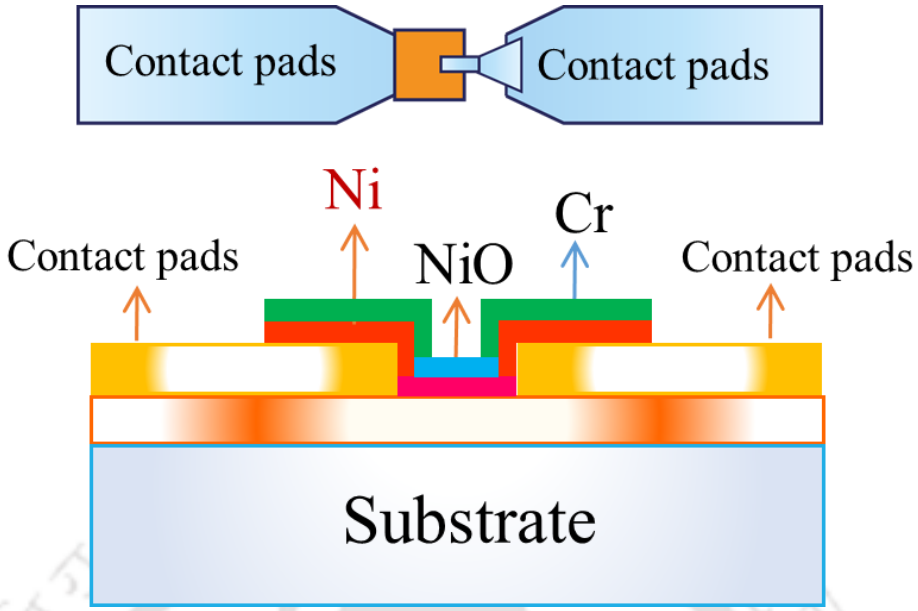

Figure 1.2: Schematic illustration of the cross-sectional view and top-view of MIM tunnel junction [10].

It is well known that the charge transport across the MIM occurs due to quantum-mechanical tunneling of electrons [12,13]. Figure 1.3 shows a typical schematic diagram of the MIM band and Fowler-Nordheim tunneling method (the process whereby electrons tunnel through a barrier in the presence of a high electric field). When the electron reaches the energy-barrier, some part of energy will be absorbed by the insulator in-between the metal electrodes, and electron passes through the barrier reaching to the second electrode. However, the other part reflects back due to barrier inhomogeneity of the insulator (Figure 1.3). The amount of energy absorbed and/or

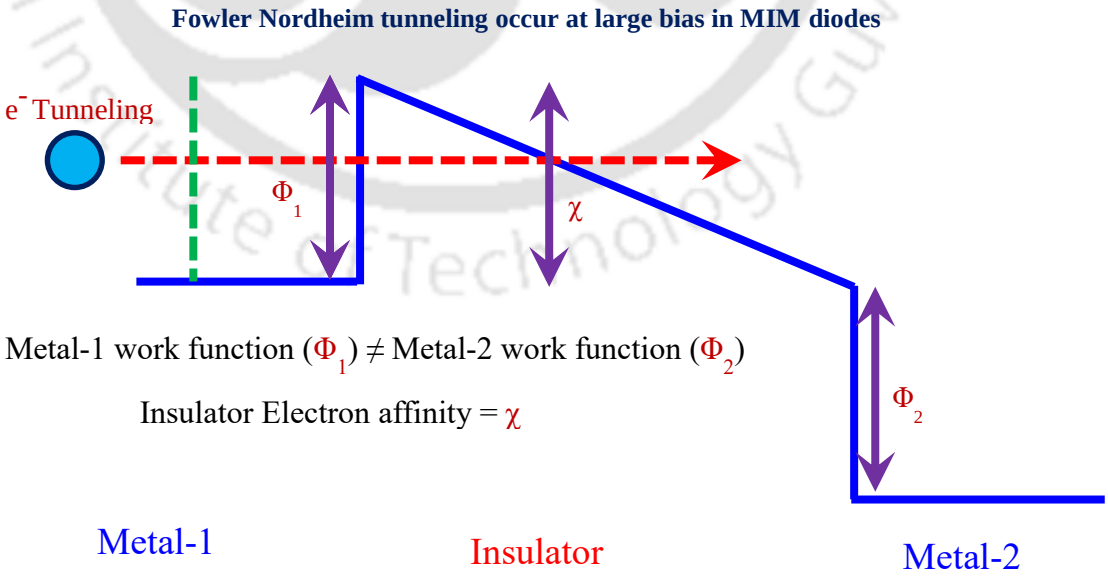

Figure 1.3: A typical schematic of MIM band diagram with FN tunneling [12].

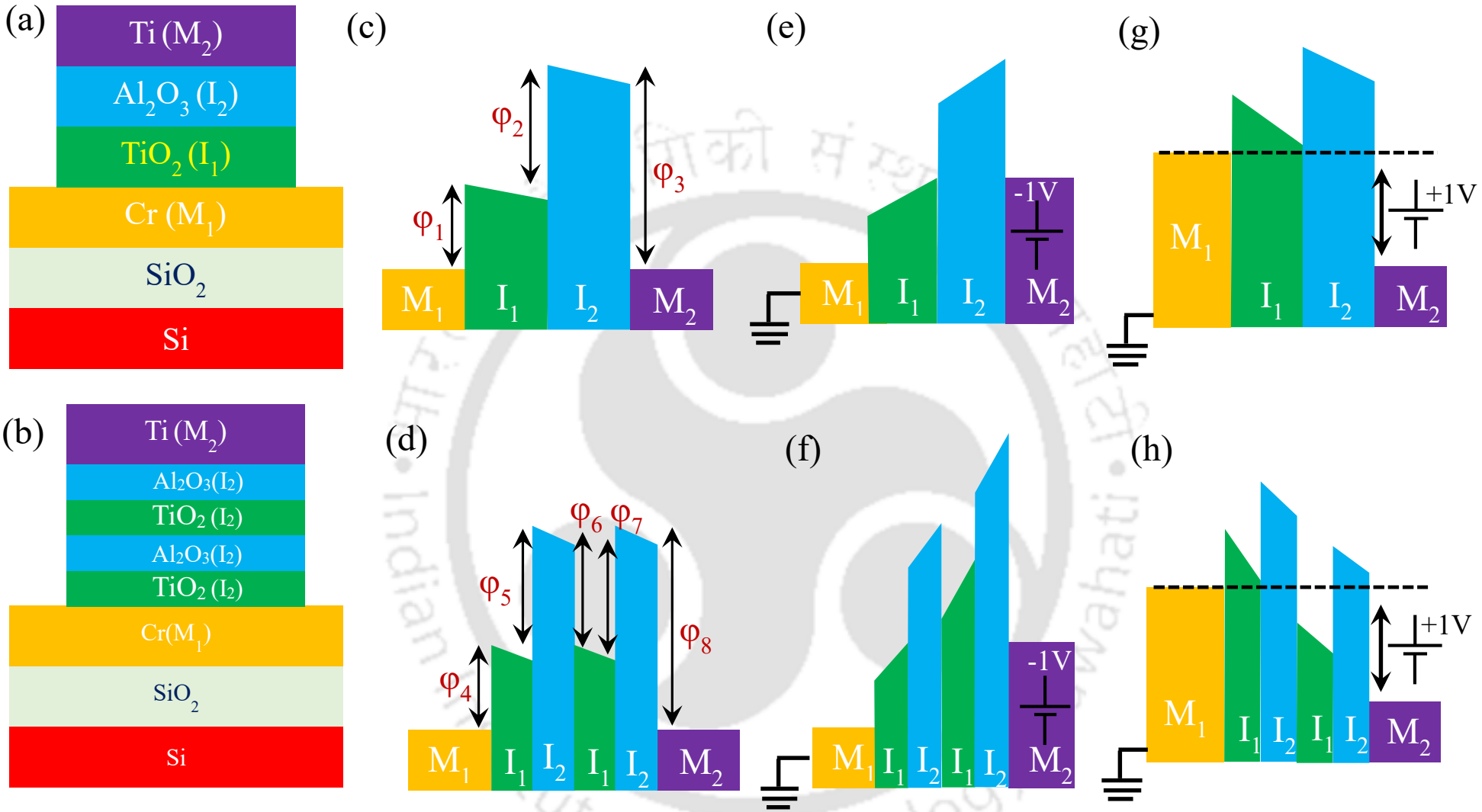

Figure 1.4:(a) A schematic cross-sectional view of the MI^2M diode. Energy band diagram of the MI^2M diode: (c) no bias applied; (e) negative bias applied to Ti; (g) positive bias applied to Ti; (b) A schematic diagrams of the cross-sectional view of the MI^4M diode. Energy band diagrams of the MI^4M diode; (d) no bias applied; (f) negative bias applied to Ti; (h) positive bias applied to Ti [13].

reflected completely depends upon the different characteristics of compound. For example, material parameters such as (*i*) work-function difference of metal electrodes ($\Phi \sim 4.5$ eV), (*ii*) electron affinity of the insulator material ($\chi \sim 3.9$ eV), (*iii*) thickness of the barrier ($\varphi \sim 0.6$ eV), (*iv*) externally applied potential energy, etc. Owing to the tunneling phenomena involved, the absorbed energy beam makes it travel at ultra-high speeds. Since quantum-tunneling is a highly nonlinear phenomenon, and hence these diodes are exploited for the rectification, mixing, and detection of THz (3×10^{13}Hz) AC signals.

Another important parameter to determine the performance and efficiency of MIM diode is I-V characteristics. The high non-linearity and asymmetry (defined as the ratio of forward current to reverse current *i.e.* I_F/I_R) in I-V curves are essential characteristic to obtain high efficiency and performance in MIM diode [12]. The non-linearity of a diode is defined as dI/dV= V/I, here dV, dI, V and I are the change in voltage, change in current, voltage and current, respectively [12]. For a single layer MIM diode, the different potential barrier (φ) between two metals separated by an insulating layer leads to asymmetric behavior in I-V characteristics. However, the non-linearity and asymmetry in I-V curves for a single layer MIM is not sufficient to achieve the required performance and efficiency [12]. In order to overcome this problem more than one insulating layer is required in these MIM diodes [12]. Figure 1.4a, b shows the schematic diagrams of the cross-sectional view of double insulating layer metal-insulator-insulator-metal (MI^2M) and four insulating-layers MI^4M architectures, respectively. The bottom and top layer of metals were comprised of Chromium 'Cr' and Titanium 'Ti', respectively. The insulating layers of TiO_2 and Al_2O_3 were sandwiched between the bottom and top layer of metals M_1 and M_2. There are three different interfaces between two metals in the MI^2M diode and five different interfaces in MI^4M diode. All these interfaces have different values of 'φ', which depends upon the barrier height at each interface, which plays a crucial role in deciding its tunneling efficiency, asymmetry and non-linearity in MIM diodes [12]. Figure 1.4c, d shows the energy band diagram of the MI^2M and MI^4M diode, respectively. Usually, the work function of the metal (Φ) and electron affinity (χ) of the insulator across metal-insulator boundaries decide the shape of energy band diagram [12]. The barrier heights (φ) depend upon the difference between Φ and χ *i.e.* $\varphi = \Phi - \chi$. For 15 mm thick insulating layers of TiO_2 and Al_2O_3 MIM diode, the barrier heights were obtained φ_1=0.6 eV, φ_2=1.1 eV φ_3=1.53 eV, φ_4=0.2 eV, φ_5=0.8 eV, and φ_6=0.83 eV [12]. Also, the shape of energy band diagram can be changed by applying a bias to one of the metals M_1 or M_2. Application of negative bias to the 'Ti' layer increases the probability of tunneling of an electron from 'Ti' to 'Cr' as compared to 'Cr' to 'Ti' (figure 1.4e, f). On the other hand, the tunneling probability from 'Cr' to 'Ti' increases when a positive bias is applied to 'Ti' (figure 1.4g, h).

1.2 Polarization in Dielectrics:

In this section, we discuss the polarization process in dielectric materials and dispersion of dielectric polarization. This section also reviews the dielectric relaxation in few wide-bandgap transition metal oxides. It is well known that the dielectric material is a special class of materials which are poor conductors of electricity but support efficient electric field within them. Within dielectric compound all the charges are bound to the atoms or

molecules, contrary to the moving charges in conducting materials [14]. In other words, a dielectric is an electrical insulator which contains dipoles that can be polarized by applying an external electric field (**E**). Dielectric materials can be used for energy storage in capacitors, charge storage in the photosensitive materials used in laser printers and copying machines [15]. Also, the dielectric materials are considered as potential candidates for mechanical actuation and sound generation devices [14,16–18]. There are two important mechanisms by which electric fields can distort the charge distribution of a dielectric, the first process is "stretching" and the second process is "rotating" [19]. When a dielectric is placed in an electric field, the positively charged core nucleus is pushed in the direction of the **E**, and the electrons are displaced in the opposite direction leading to the localized dipole-moment ($p = qd$) and finite dielectric polarization ($\boldsymbol{P_e} = p/V$, where V is the volume) [14,19]. Such polarization process creates an internal electric field ($\mathbf{E_{in}}$) that reduces the overall field within the dielectric. If a dielectric is composed of weakly bonded molecules, those molecules not only become polarized but also reorient so that their symmetry axis aligns in the direction of **E**. The formation of dipole moments and their orientation relative to the electric field are the two important factors that contribute to the polarization of molecules/atoms in the neutral dielectric.

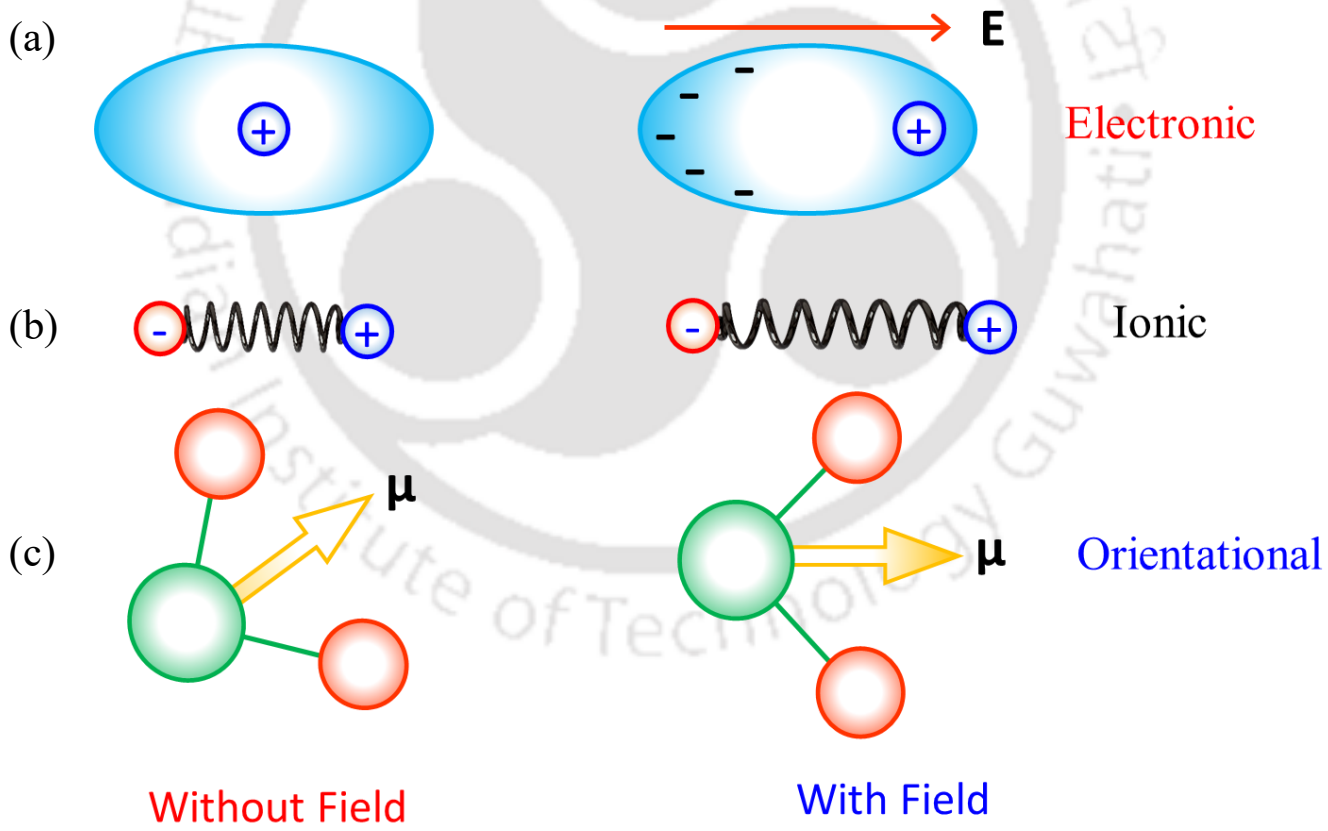

Figure 1.5: Schematic diagram for various polarization processes: (a) Electronic polarization, (b) Ionic polarization, and (c) Orientational polarization [14].

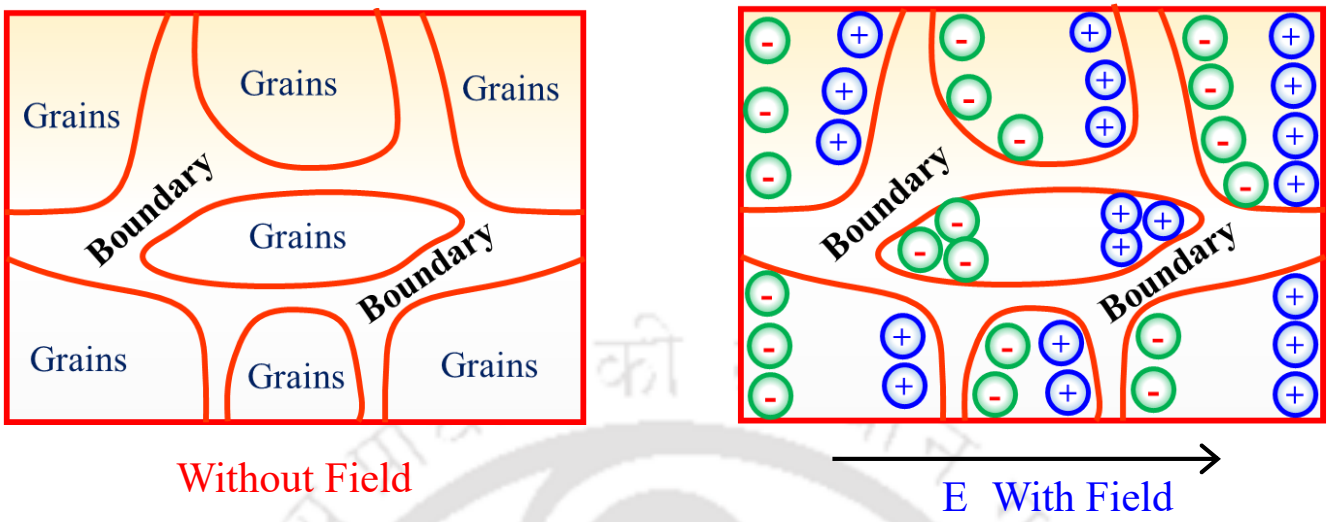

Figure 1.6: Schematic diagram for interfacial (space-charge) polarization process [14].

Figure 1.5a shows a schematic view of localized dipoles formed due to the displacement of core-nucleus and electron-cloud by the application of external electric field, finally leading to the induced dipole moment (*p*) [14]. The electronic polarization ($\boldsymbol{P_e}$) is directly proportional to the field-strength and remains temperature independent. On the other hand, if the dielectric consists of polar-atoms (having permanent dipole moment) then the application of external electric field leads to the rotation of permanent dipole moment along the direction of **E** and thus contribute to polarization. Such polarization is popularly known as orientation-polarization ($\boldsymbol{P_o}$) as shown in Figure 1.5c [14]. It is interesting to note that $\boldsymbol{P_o}$ is essentially a temperature dependent quantity, with increasing the temperature all the permanent dipoles randomize inside the dielectric. Apart from these two polarization mechanism ($\boldsymbol{P_e}$ and $\boldsymbol{P_o}$), two more important polarization mechanism possible in dielectric material are: (*i*) space charge polarization $\boldsymbol{P_S}$ (Figure 1.6) and (*ii*) Ionic polarization $\boldsymbol{P_i}$ (Figure 1.5b). The overall dielectric behavior of the system is governed by the total polarization $\boldsymbol{P_{Tot}}$ which can be expressed as follows [14,20].

$$\boldsymbol{P_{Tot} = P_e + P_i + P_o + P_s} \qquad (1.3)$$

1.2.1 Dispersion (or Relaxation) of Dielectric Polarization:

The polarization response of a material is a complex function of ac-electric field frequency ($f=1/t$) and temperature (T), which can be expressed as [14,20,21]:

$$\boldsymbol{P}(t) = \boldsymbol{P}\left[1 - exp\left(-\frac{t}{\tau}\right)\right] \qquad (1.4)$$

where **P** is the maximum-polarization achieved after the application of the **E** and τ is the relaxation time for an individual polarization process [14,20,21]. The relaxation time 'τ' is defined as the time taken for a polarization process to reach 63% of the maximum value of **P** [14]. Depending upon the relaxation processes the relaxation time varies accordingly, for example, the relaxation time for a water molecule is ~10^{-11} s. Figure 1.7 shows a dependence of polarizability on frequency over a wide range (10 Hz ≤ f ≤ 10^{16} Hz), extending from the static to ultraviolet region [20]. From the figure 1.7 one can clearly observe that there are number of polarization mechanisms activated at certain frequency range [4,20]. The most common polarization mechanisms, starting from high frequencies is the "Electronic Polarization" which occurs because of the relative shift of electron cloud and nucleus due to the application of **E**. Since the electrons have very small mass (m_e ~ 9.109 × 10^{-31} kg), electronic polarization can follow the high-frequency region and drops-off quickly at very high frequencies (f ≥10^{15} Hz) [14,20]. The electronic polarization process is a very rapid and develops instantaneously after applying the electric field. Moreover, this polarization process does not involve hopping of ions/atoms between the localized sites hence becomes temperature independent. As all the solids are comprised of a nucleus surrounded by electrons, electronic polarization occurs in all solids, liquids, and gases [14]. The second mechanism is "Ionic Polarization" which occurs due to the ionic charges in a dielectric medium. Ionic polarization is an important process associated with the relative displacement of positive and negative ions in an electric field. Ions can respond equally well to the external electric field and significantly contribute to the dielectric relaxation [14]. Since the electric field has to displace heavier ions instead of electron cloud, the response of ionic polarization is slower

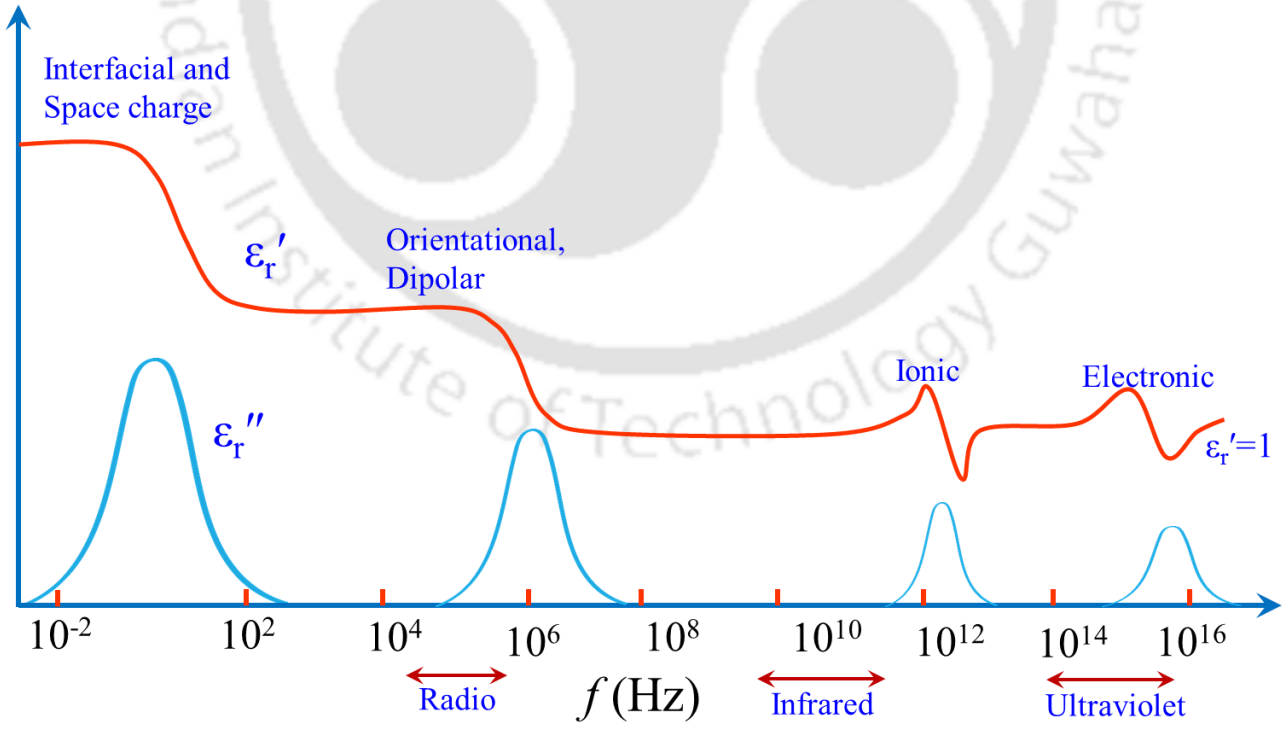

Figure 1.7: Frequency dependence of polarization dispersion [14].

than the electronic polarization, thus resonance occurs in the infrared frequency ranging between $f = 10^{12}$ Hz and 10^{13} Hz, which is of the same order of lattice vibrational frequency [14]. Above this cut-off frequency ($f_c > 10^{13}$ Hz), ions do not follow the electric field (due to the large time lag (~100 times higher) between the time period of ionic vibration and applied field) and hence, ionic polarization does not occur at optical frequencies. The third kind of relaxation process is the "Orientational polarization" also known as "Dipolar Polarization" which arises from the rotation of permanent dipoles along the direction of field. In contrast to the ionic polarization, the built in dipole moments are independent of each other, which can rotate freely [14,19,22]. These rotations are strongly counterbalanced by the thermal energy and hence the polarization becomes strongly temperature as well as frequency dependent. As compared to solids, it is easier for the polar molecules to reorient themselves in a liquid medium. Orientation polarization occurs when the frequency of the applied voltage is in the audio frequency range (f ~10^6 Hz) [14]. The final dielectric relaxation mechanism is the "Space-charge Polarization". When two dissimilar phases are in contact with each other an interfacial electric field will develop at the junction [14,23,24]. This interface (double layer) acts as a pseudo capacitor whose frequency response is completely different as compared to the frequency characteristics of bulk material. The accumulation of charge across the interface due to the external electric field **E** produces a net dipole moment and space/surface charge polarization $\boldsymbol{P}_s$, which contributes to the total polarization of the dielectric. Similar to the orientational polarization, this polarization process is also a function of temperature and usually increases with increasing the temperature. Since this process involves the diffusion of charges over several interatomic distances, this is the slowest process (≤kHz range) among all the polarization mechanisms. In general, the successful hopping of charge carriers decides the relaxation time for the space charge polarization.

1.2.2 Lorentz Field in a Dielectric Material:

When a dielectric is subjected to an external field, the atom/molecule inside the dielectric experiences a driving force from both external as well as internally generated electric field $\boldsymbol{E_{Local}}$ (induced by the dipoles). The local internal field produced by the dipoles can significantly deviate from the value of macroscopic electric field, since the macroscopic field is averaged over large number of dipoles. In order to estimate this local field $\boldsymbol{E_{Local}}$ one has to calculate the total field acting on a dipole, which is the combination of external field and dipolar field [14,20]. A systematic study related to the evaluation of $\boldsymbol{E_{Local}}$ was first reported by Lorentz. He first considered an artificial spherical cavity having radius **R** across a dipole in the dielectric. This artificial sphere is very small as compared to the scale of dielectric but large on atomic scale and hence it can be treated as a continuous medium as far as the dipole is concerned (as shown in the Figure 1.8 a). Now, the local field acting on the central dipole inside the shell is given by the sum [14,20]:

$$\boldsymbol{E_{Local} = E_0 + E_1 + E_2 + E_3} \qquad (1.5)$$

where $\boldsymbol{E_0}$ is the external applied field and $\boldsymbol{E_1}$ is the depolarization field (field due to the polarization charges residing at the external surfaces of the dielectric) [14,20]. The $\boldsymbol{E_2}$ is the field due to the polarization charges pre-

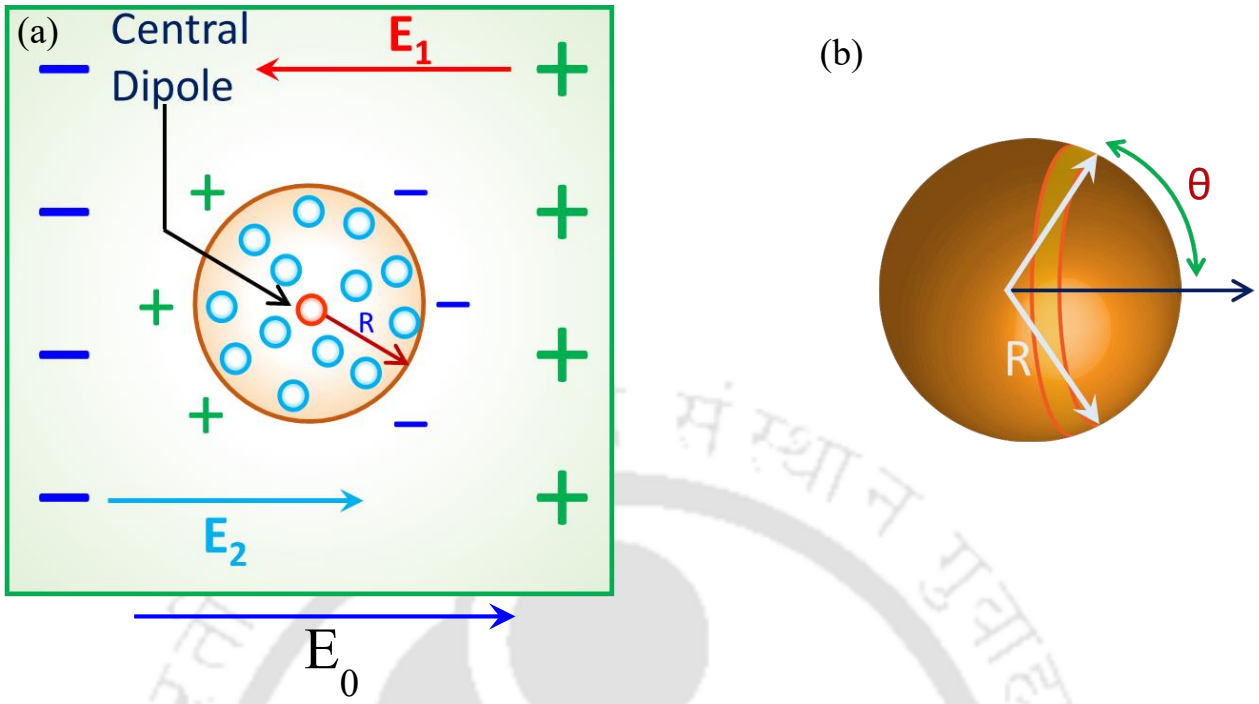

Figure 1.8: (a) The procedure for computing the local field. (b) The procedure for calculating $\mathbf{E}_2$, the field due to the polarization charge on the surface of the Lorentz sphere [14, 20].

-sent on the surface of Lorentz sphere (Figure 1.8 b), which is also known as Lorentz field, and $\boldsymbol{E_3}$ is the field due to other dipoles lying within the artificial sphere. To evaluate $\boldsymbol{E_2}$ we may consider the polarization charges on the surface of the Lorentz cavity as a continuous distribution. According to the Coulomb's law, field due to the charge at a point located at the center of the sphere is given by:

$$\boldsymbol{E_2} = \frac{4\pi}{3}\boldsymbol{P} \qquad (1.6)$$

The field $\boldsymbol{E}_3$ is the only term that depends on crystal structure of a dielectric medium. For a reference site with cubic surroundings in a sphere, $E_3 = 0$ if all the atoms are replaced by point dipoles parallel to each other. The total local field at a cubic site is then given by:

$$\boldsymbol{E_{Local}} = \boldsymbol{E_0} + \boldsymbol{E_1} + \frac{4\pi}{3}\boldsymbol{P} = \boldsymbol{E} + \frac{4\pi}{3}\boldsymbol{P} \qquad (1.7)$$

This is known as the Lorentz relation: the field acting on an atom in a cubic site is the macroscopic field $\boldsymbol{E}$ and $4\pi\boldsymbol{P}/3$ from the polarization of the other atoms in the specimen. The concept of $\boldsymbol{E_{Local}}$ can be understood by using the molecular theory of dielectrics. According to this theory all physical properties may be expressed in terms of molecular characteristics and molecular interactions. The polarizability 'α' of an atom can be expressed in terms of elementary dipole moment of the atom $\boldsymbol{p}$ and local electric field $\boldsymbol{E_{Local}}$ at the atom using the relation:

$$\boldsymbol{p} = \alpha\boldsymbol{E_{Local}} \qquad (1.8)$$

The polarizability 'α' for a non-spherical atom will be a tensor. For a homogeneous medium *i.e.* crystals with N atoms in a volume V, the polarization is given by the product of polarizabilities of the atoms times the local

electric field:

$$\boldsymbol{P} = \sum_i N_i \boldsymbol{p_i} = \sum_i N_i \alpha_i \boldsymbol{E_{Local}} \quad (1.9)$$

Our aim is to relate the dielectric constant to the polarizabilities; the result will depend on the relation that holds between the macroscopic electric field and the local electric field. Substituting E_{Local} from the Lorentz relation (equation 1.7), for a net polarization:

$$\boldsymbol{P} = \sum_i N_i p_i \left(\boldsymbol{E} + \frac{4\pi}{3}\boldsymbol{P}\right) \quad (1.10)$$

The polarization is induced by electric field, and therefore is a function of electric field. The relationship is written in the following way:

$$\boldsymbol{P} = \chi \boldsymbol{E} \quad (1.11)$$

where χ is called the dielectric susceptibility. Normally, χ is a tensor and depends on the direction of applied electric field. The relative dielectric permittivity (ε) of an isotropic or a cubic medium relative to vacuum is defined in terms of macroscopic field **E**:

$$\epsilon = \frac{\boldsymbol{E}+4\pi\boldsymbol{P}}{\boldsymbol{E}} = 1 + 4\pi\chi \quad (1.12)$$

One can solve for **P** to find the dielectric susceptibility

$$\chi = \frac{\boldsymbol{P}}{\boldsymbol{E}} = \frac{\sum_i N_i \alpha_i}{1 - \frac{4\pi}{3}\sum_i N_i \alpha_i} \quad (1.13)$$

Using the relation (equation 1.12), we can write the expression in terms of dielectric constant:

$$\frac{\epsilon - 1}{\epsilon - 2} = \frac{4\pi}{3}\sum_i N_i \alpha_i \quad (1.14)$$

The above equation is popularly known as "Clausius-Mossotti" relation [25–28]. This relates dielectric constant to the electronic polarizability but only for crystal structures for which the Lorentz local field (equation 1.7) holds. Since $\varepsilon \propto n^2$, we can rewrite equation (1.14) in terms of refractive index (n)

$$\frac{n^2 - 1}{n^2 - 2} = \frac{4\pi}{3}\sum_i N_i \alpha_i \quad (1.15)$$

This is known as Lorentz–Lorenz equation which links the index of refraction with polarizability [25–28].

1.2.3 Dielectric Losses:

The term "Dielectric-Loss" quantifies the inherent dissipation of the energy in a dielectric material, which transforms the electromagnetic energy into heat [14,29]. A highly efficient dielectric supports large quantity of charge with negligible dissipation. Generally, two types of loss mechanisms exist which can dissipate energy within a non-ideal dielectric (*i*) conduction loss (dissipation due to the flow of charge within the material), and (*ii*) dielectric loss (dissipation of energy through the movement of charges in an alternating electromagnetic field caused by the lag between polarization and field direction). It is well known from the Joule-Lenz law that the power-loss 'P_{wr}' in a conducting material is directly proportional to the square of electrical voltage 'V' applied to the material, and is governed by the relation $P_{wr} = V^2/R$, where 'R' is the resistance of the conductor [14,19]. In contrast, the power loss in a dielectric is determined by more intricate irregularities, and meaningful only under

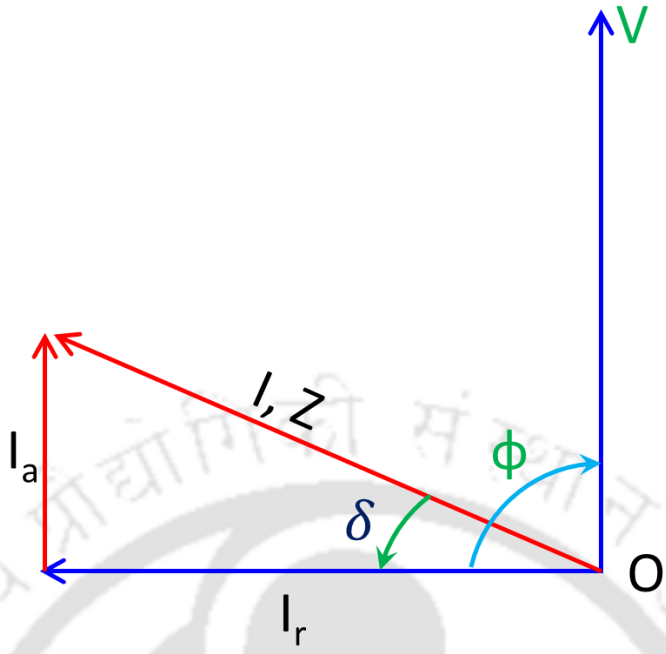

Figure 1.9: Phase diagram of current and voltage in a capacitor with a dielectric material.

the application of alternating voltage. Figure 1.9 shows the vectorial representation of voltage, charging-loss and currents in a capacitor after applying the alternating voltage. For an ideal dielectric (no power dissipation), the charges are in phase with voltage and the resulting current 'I_r' will be out of phase by 90° [30]. However in reality, the charges are never in phase with voltage and phase angle φ, the angle between 'I' and 'V' in phasor diagram is slightly less than $\pi/2$. Hence, the total current through the capacitor can be resolved into two components; (*i*) active current I_a, and (*ii*) reactive current I_r. In a capacitor, the angle δ ($\delta = 90° - \varphi$) is more meaningful parameter which is named as dielectric loss-angle. The tangent of δ is equal to the ratio of active currents to the reactive currents or in other words ratio of active power P (power loss) to the reactive power P_r:

$$Tan\ \delta = \frac{I_a}{I_r} = \frac{P}{P_r} \qquad (1.16)$$

The dielectric loss angle is an important parameter for the dielectric materials which is typically described by the Loss-Tangent (Tan δ). Often the quality factor Q of an insulation portion is determined as the reciprocal of Loss-Tangent:

$$Q = \frac{1}{Tan\ \delta} = Tan\ \phi \qquad (1.17)$$

The magnitude of dielectric losses P in an insulating material having a capacitance C, which is described from the relation $P_{wr} = V^2/R$ and $I_r = V \times \omega \times C$ as:

$$P = VI_a = VI_r Tan\ \delta = V^2 \omega\ C\ Tan\ \delta \qquad (1.18)$$

$$P = 2\pi f V^2 C\ Tan\ \delta = (2\pi f V^2 \varepsilon_0 Tan\ \delta)A/d \qquad (1.19)$$

Inserting the effective length $\Lambda = A/d$ in equation (1.19) and substituting the numerical value of ε_0 the expression

of dielectric losses can be expressed as:

$$P = 5.56 \times 10^{-11} V^2 f \, \Lambda \, \epsilon \, Tan \, \delta \qquad (1.20)$$

Equations 1.19 and 1.20 are shape independent and used extensively for dielectrics.

1.2.4 Frequency Response:

The dynamic response of dipolar polarization to the change of electric field is not instantaneous and always retarded; this process is known as "Dielectric-Relaxation" [14]. Dielectric relaxation give rise to a decay time to reach the equilibrium value, such phenomenon is called the "Debye-Relaxation" and the delay time to reach the new equilibrium state is known as the relaxation time constant 'τ' [14,21,31]. The relaxation time 'τ' is associated with the viscosity of material and depends strongly on the temperature. Depending upon the nature of dielectrics the relaxation time 'τ' varies. For crystals, the value of 'τ' at room temperature lies in between 10^{-11} and 10^{-9} s. On the other hand, for amorphous solids and polymers 'τ' ranges from few seconds to hours depending upon the temperature of the system. In order to understand such complicated dynamic response, Debye proposed the following assumptions for non-interacting dipoles:

1. At high frequencies, ($\omega >> 1/\tau$), the relative dielectric permittivity (or dielectric constant $\varepsilon'(\infty)$) comprises of only the ionic and electronic contributions.
2. As $\omega \rightarrow 0$, the relative dielectric constant $\varepsilon'(0)$ is given by the sum of high-frequency dielectric constant $\varepsilon'(\infty)$ and dipolar permittivity $\varepsilon'_{dipolar}$.
3. The polarization decays exponentially *i.e.* $P(t) = P_0 \left[exp\left(-\frac{t}{\tau_r}\right)\right]$.

From the above assumptions, one can derive the following expression [14]:

$$\epsilon(\omega) = \epsilon(\infty) + \frac{\epsilon(0)-\epsilon(\infty)}{1+i\omega\tau} \qquad (1.21)$$

After separating the above equation into the real and imaginary components:

$$\epsilon'(\omega) = \epsilon'(\infty) + \frac{\epsilon'(0)-\epsilon'(\infty)}{1+\omega^2\tau^2} \qquad (1.22)$$

$$\epsilon''(\omega) = (\epsilon'(0) - \epsilon'(\infty)) \frac{\omega\tau}{1+\omega^2\tau^2} \qquad (1.23)$$

$$Tan\, \phi = \frac{\epsilon''(\omega)}{\epsilon'(\omega)} = \frac{\left(\epsilon'(0)-\epsilon'(\infty)\right)\omega\tau}{\epsilon'(0)+\epsilon'(\infty)\omega^2\tau^2} \qquad (1.24)$$

These three equations (1.22-1.24) are collectively known as the Debye equations, which describe the behavior of an assembly of non-interacting ideal dipoles that have the same time constant [14]. However, many dielectric materials don't follow the Debye relaxations [32]. In 1941, K. S. Cole and R. H. Cole modified the Debye equations by introducing a correction term in the distribution of relaxation times [31]:

$$\epsilon(\omega) = \epsilon(\infty) + \frac{\epsilon(0)-\epsilon(\infty)}{1+(i\omega\tau)^{\alpha}} \qquad (1.25)$$

In the above equation, 'α' represents the deformation of the semicircle-arc in the Cole-Cole plot, *i.e.* it is the angle from the ε′ axis to the center of the semicircle arc. Later in 1966, a generalized relaxation equation was proposed by Havriliak and Negami for polar dielectrics, which is given by [33]:

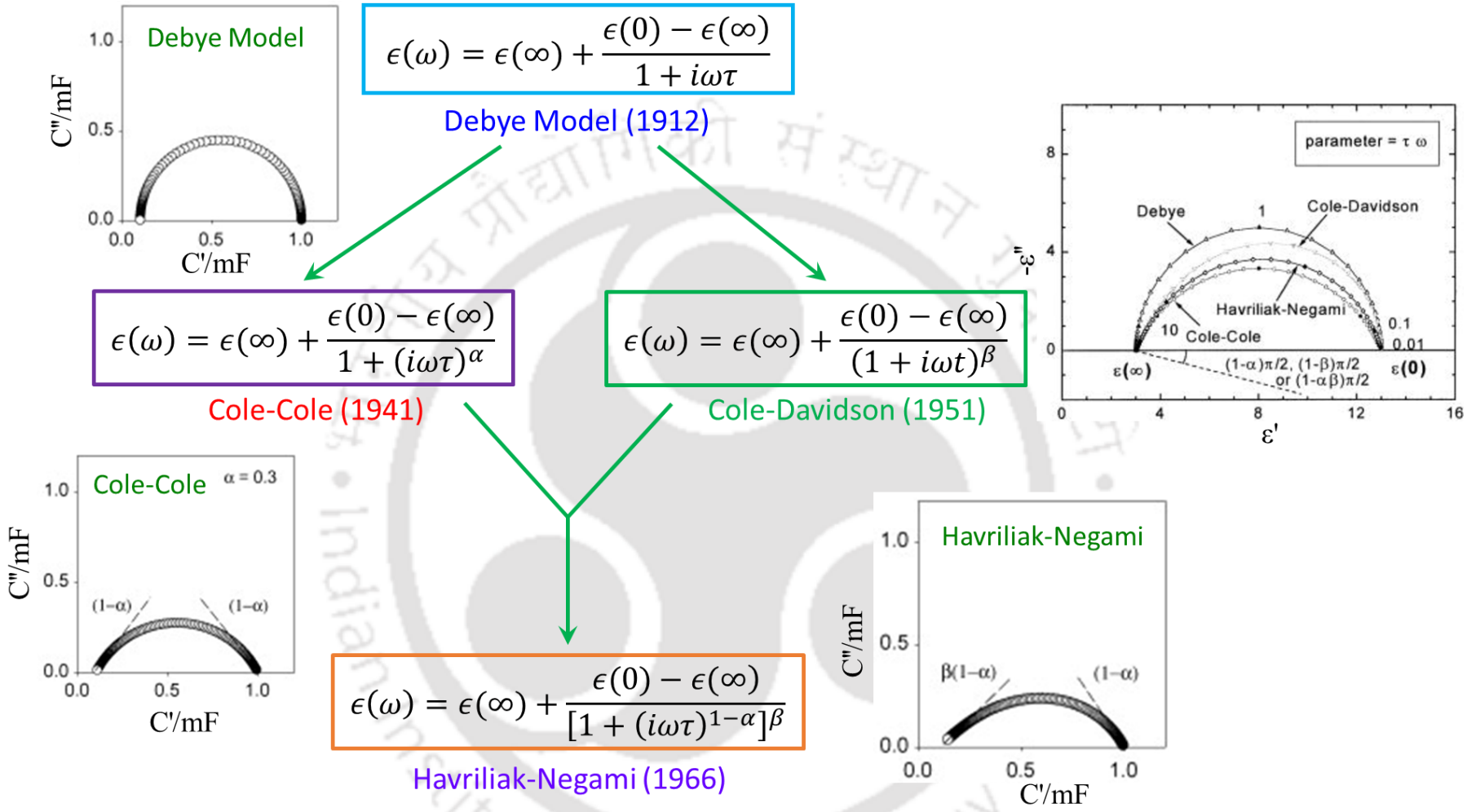

Figure 1.10: Evolution map for Debye, Cole-Cole, Cole-Davidson and Havriliak-Negami model [33].

$$\epsilon(\omega) = \epsilon(\infty) + \frac{\epsilon(0)-\epsilon(\infty)}{[1+(i\omega\tau)^{1-\alpha}]^{\beta}} \quad (1.26)$$

The above equation is popularly known as Havriliak-Negami (HN) formula. The symmetric and asymmetric broadening of the Loss-Tangent peaks is deliberated by the shape parameters α and β, respectively. Typically, for Debye like relaxations, α = 0 and β = 1. Usually, the Debye relaxation is limited to the non-polar or weakly polar materials. The Cole-Cole and Cole-Davidson relaxation mechanism are few special case of HN equation with shape parameter β = 1 and α = 0, respectively [33,34]. Figure 1.10 shows the evaluation map for the HN equation. The relaxation time constant 'τ' is temperature dependent and generally follows the Arrhenius law [14,35]:

$$\tau = \tau_0 \, exp\left(\frac{E_a}{k_B T}\right) \quad (1.27)$$

In the above equation 'E_a' represents the energy barrier for reorientation motion, and the pre-exponential factor τ_0 is an inverse attempt frequency. For ZnO single crystals, the pre-exponential factor τ_0 lies in the range between 10^{-13} and 10^{-11} s. However, for systems like polymers, disordered materials, glasses and relaxor ferroelectrics, the Arrhenius analysis leads to unphysical values for τ_0 (~ 10^{-40} s) and E_a (~7 eV). Therefore, Vogel, Fulcher and Tammann independently proposed a temperature dependent relaxation mechanism characterized by the following expression [36]:

$$\tau = \tau_0 \, exp\left(\frac{E_a}{T-T_F}\right) \quad (1.28)$$

The above equation is popularly known as Vogel-Fulcher equation. In this equation T_F is the Vogel-Temperature and is related to the dynamic glass-transition temperature. This formula provides a very reasonable values of τ_0 (~10^{-10} s) and E_a (0.019 eV) for disordered and relaxor-ferroelectrics [37].

1.3 Dielectric Behavior of few Transition Metal Oxides:

High-κ dielectrics play an important role for the development of advanced energy-storage devices such as pseudo-capacitors, electrochemical batteries and barrier layered super-capacitors [4,5]. As discussed in previous section, many transition metal oxides exhibit giant dielectric permittivity and found potential application as gate dielectrics in metal-oxide-semiconductor field-effect transistor (MOSFET) [38]. The colossal magnitude of ε'(∞) allows very high storage capacity (terabit/inch^2) together with reduced-scale dimensionality for static/dynamic random access memory devices [9]. The origin of colossal dielectric permittivity and physical mechanisms of dielectric relaxation in transition metal oxides is still under debate and has been paid a detailed attention in recent years. Ferroelectricity, transport of charges via hopping mechanism, metal-to-insulator transition, charge-density wave formation and interface effects are the core mechanisms responsible for the giant dielectric permittivity in the transition metal oxides [39–41]. Among all the transition metal oxides exhibiting colossal value of relative dielectric permittivity (ϵ_r), Nickel oxide (NiO) is an archetypal example. This wide band-gap Mott insulator exhibits very high dielectric constant (ε ≥ 10^5) after the substitution of alkali metals and other transition metals such as Ti at the Ni^{2+}octahedral sites or at the O^{2-}/Ni^{2+}vacancies [42–46]. Wu *et al.* reported a giant dielectric permittivity (ε ≥ 10^5) across 300 K in 'Li' and 'Ti' co-doped NiO ceramics [46]. The observed dielectric constant

is temperature independent above 200 K which shows an abnormal hundred-fold drop at low temperature (< 300 K), as shown in figure 1.11 [46]. Such peculiar dielectric behavior is generally observed in non-perovskites, and non-ferroelectric Mott-Insulators and hence received enormous scientific interest in recent years. Formation of microstructural heterogeneities like co-existence of semiconducting grains and insulating grain boundaries contribute to such colossal value of ϵ_r [46–50]. The application of external electric field creates accumulation of free charge carriers across the interface between the grain boundaries, leading to a strong interfacial/Space-Charge polarization (Maxwell-Wagner), as discussed in the previous section [46]. Another important relaxation phenomena associated with colossal dielectric behavior in transition metal oxides is the clustering and dissociating processes of oxygen vacancies [51–53]. In ceramic oxides, the localization and dissociation of oxygen vacancies contribute to the 'Polaron-Hopping' conduction [53]. In this mechanism the concentration of small-Polarons, caused by the formation and dissociation of oxygen vacancies finally results in a giant increase in dielectric permittivity thereby decreasing the hopping activation energy and hopping length [53]. Liu *et al.* studied the contribution of oxygen vacancies to the dielectric response of $Sm_{1.5}Sr_{0.5}NiO_{4-\delta}$ ceramics and reported that giant dielectric permittivity ($\varepsilon_r \sim 10^4$ at 20 kHz) is largely associated with the formation of 'small-Polaron' and 'interfacial polarization' [53].

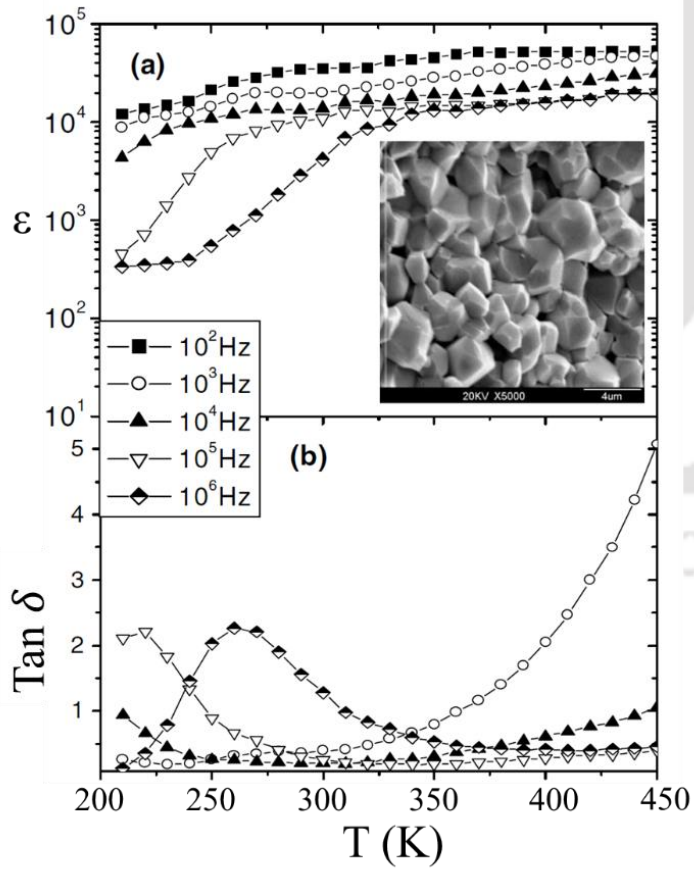

Figure 1.11: The temperature dependence of (a) the dielectric constant ε and (b) the loss tangent Tanδ for the $Li_{0.05}Ti_{0.02}Ni_{0.93}O$ sample at various frequencies between 100 Hz and 1 MHz. The inset shows a typical scanning electron micrograph of the samples [53].

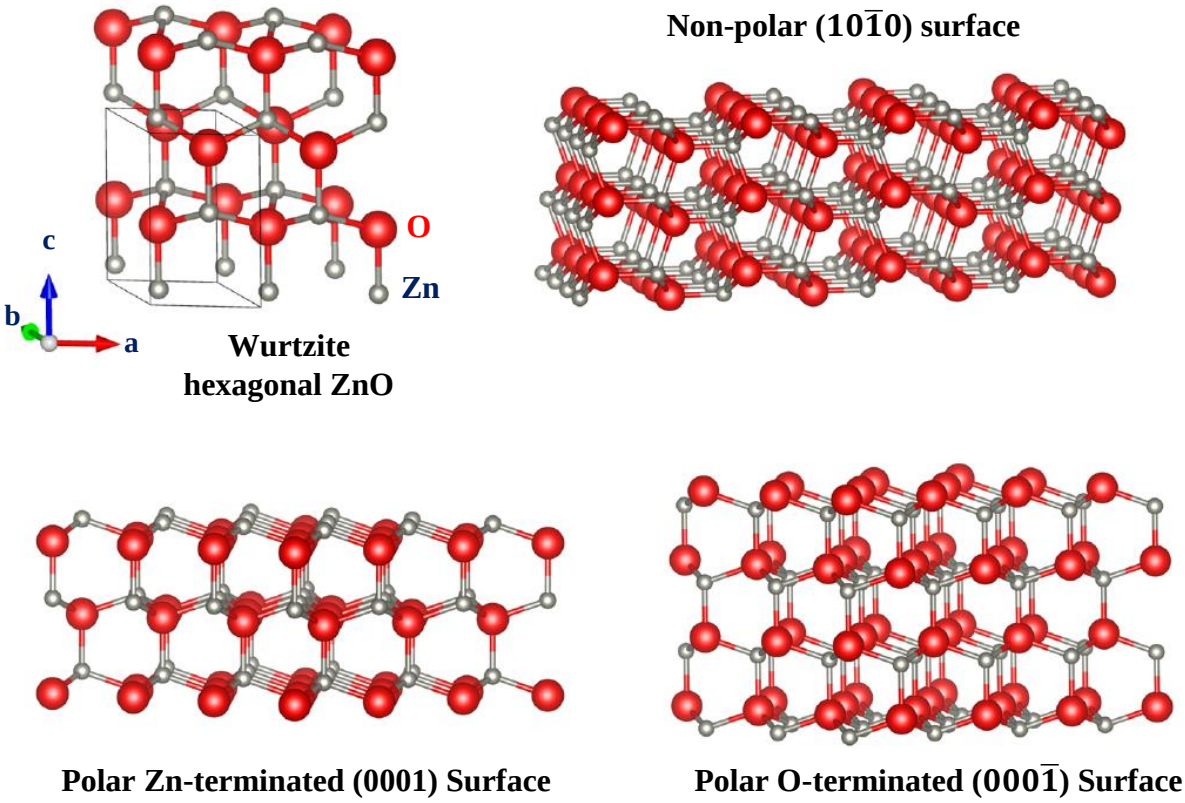

Figure 1.12: Stick-and-ball representations of the hexagonal wurtzite h.c.p ZnO structure with Non-polar (10$\bar{1}$0) Surface, Polar Zn-terminated (0001) Surface and Polar O-terminated (000$\bar{1}$) Surface [54–57].

Another important family member of the transition metal oxides is ZnO, which gained enormous attraction due to its potential application in solar-cells, surface acoustic waves, gas sensors, pressure sensor, anti-reflecting coating, heat mirrors and artificial neuronal computing [58–60]. The hexagonal wurtzite ZnO exhibits non-centrosymmetric crystal structure with a finite dipole moment in the repeated unit-cell perpendicular to the surface of *c*-axis, known as polar-*c* axis (shown in figure 1.12), which results in piezoelectricity and pyroelectricity in the system [54–56]. Generally at low temperatures ($100 \leq T \leq 333$ K), ZnO exhibits four different dielectric relaxations with activation energies ranging between 0.21 eV and 0.35 eV [61]. Figure 1.13 shows the temperature dependence of real $\varepsilon'(T)$ and imaginary $\varepsilon''(T)$ component of dielectric constant of a [0001] orientated single crystal of ZnO [61]. The main characteristic features observed from figure 1.13 are: (*i*) Colossal dielectric constant ($\varepsilon_r \sim 10^3$), (*ii*) Debye relaxations across 200 K, and (*iii*) Shifting of peak position towards higher temperature in $\varepsilon''(T)$ with increasing frequency *f*, corresponding to the thermally activated relaxation [61]. Such thermally activated relaxation follows Arrhenius relation given by equation 1.27 with parameters; $E_a = 0.35$ eV and $\tau = 1.348 \times 10^{-12}$ sec, obtained from the slope and intercept of logarithmic variation of frequency with respect to 1000/T plots, respectively (shown in inset of Figure 1.13 a) [61]. Also, the replacement of the parent cation 'Zn^{2+}' in the host ZnO matrix could lead to the structure distortions and dynamic changes in the bond strengths [62]. For example, pure ZnO is polar in nature but does not undergo any structural phase transition at ambient condition. However,

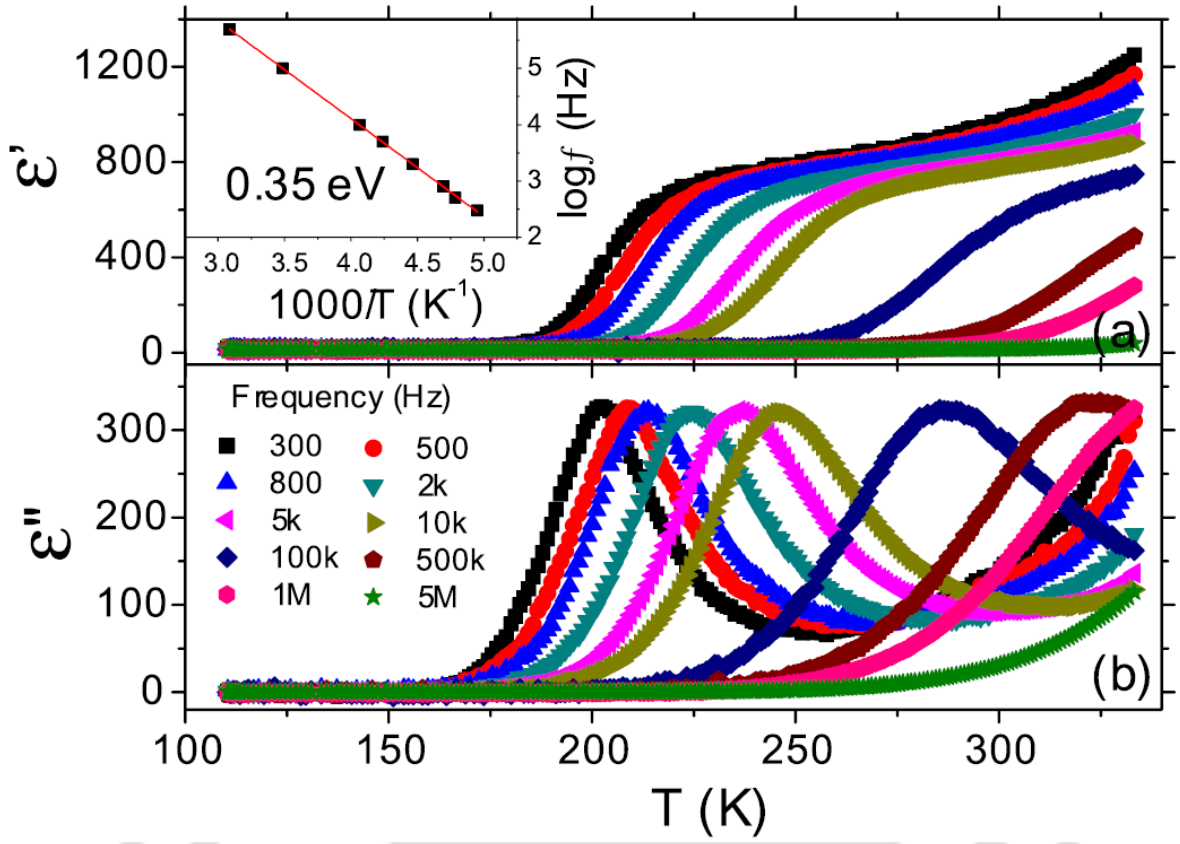

Figure 1.13: Temperature dependence of (a) ε′ and (b) ε″ for a [0001]-orientated ZnO single crystal measured at various frequencies [61].

the incorporation of 'Li^{+}' and 'Mg^{2+}' dopants in polycrystalline ZnO induces a ferroelectric phase transition across 330 K. The ionic/atomic size mismatched between dopants and host generates off-centered site occupation leading to the appearance of such spontaneous polarization [62]. On the other hand, the substitution of superparamagnetic cobalt nanoparticles inside ZnO induces local-lattice distortion and structural inhomogeneity, leading to the weakly coupled relaxor-ferroelectricity and magneto-electric coupling in ZnO-Co thin-films [63].

1.4 Insulating Properties of Antiferromagnetic Transition Metal Oxides (Mott Insulators):

The Mott insulators such as NiO, CoO, CuO, MnO, Fe_3O_4, Ti_2O_3 and VO_2 are periodic materials whose properties radically contradict the elementary band picture. According to the conventional band theory these compounds should show good electrical conductivity, however, these compounds exhibit insulating (or semiconductor) behavior due to strong electron–electron interactions, which are not considered in conventional band theory. Before the discovery of antiferromagnetism, it was pointed out that (according to the Wilson theory of metals and insulators) NiO, CoO and MnO should exhibit metallic behavior whereas these compounds are transparent insulators with wide-energy bandgap ($E_G \geq 4.3$ eV). The Ni ions should have eight *d*-electrons, and the only splitting of the *d*-band to be expected into the e_g and t_{2g} bands, with four and six electrons per atom.

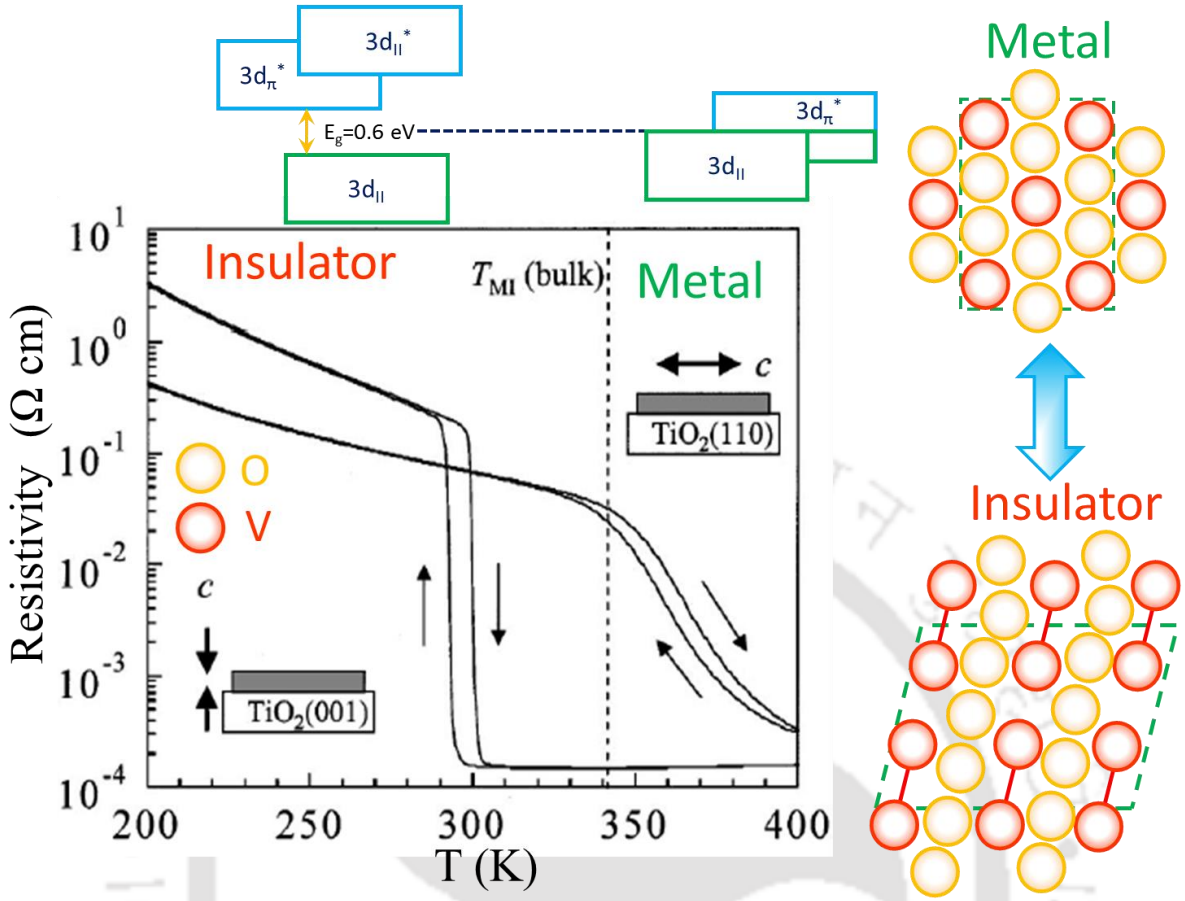

Figure 1.14: Temperature dependence of resistivity for the VO_2 films formed on TiO_2 (001) and TiO_2 (110) substrates. The dash line represents the Metal-Insulator transition (~ 341 K) in a VO_2 single crystal [72].

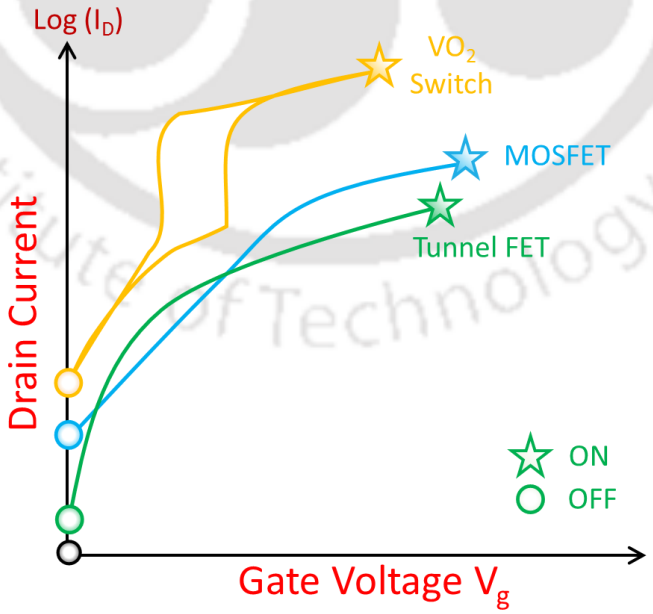

Figure 1.15: Drain current I_D versus Gate voltage V_g characteristics of VO_2 switch, MOSFET and Tunnel FET [73, 74].

The e_g band with room for four electrons can split into two sub-bands by the antiferromagnetic lattice, the energies of these two bands are separated by the term U; one is occupied and other is empty [64,65]. From the literature, no significant increase in the conductivity was observed in pure NiO above its Néel temperature [65]. From the temperature dependence of conductivity analysis, Honig *et al.* observed that in single crystal of NiO the carrier activation energy $E_A \sim 0.74$ eV and thermo-power $E_S \sim 0.30$ eV imply the Polaron hopping process with very high hopping activation energies $W_H \sim 0.44$ eV [66,67].

The physics of Mott insulators in two and higher dimensions has been studied extensively in the past decade, in particular, much attention was paid to Cu-based transition metal oxides because of the discovery of superconductivity in these compounds [68–71]. While a quantitative analysis of the experimental data using a well-developed theory in these Cu-based systems remains elusive, nevertheless, much progress has been made in describing a number of antiferromagnetic Mott insulators [68–71]. Defined in a general sense, electron-electron interactions also drive a quantum phase transition from a metallic to an insulating ground state in these systems [68–71]. For example, VO_2 is a classic example of an oxide with one-electron center (V^{4+}), which forms pairs at low-temperatures, however, such pairing disappears at 340 K, leading to high conductivity (Figure 1.14). A typical Mott metal-to-insulating transition in temperature dependence of resistivity ρ(T) of VO_2 2D structures grown on (001) and (110) oriented TiO_2 single crystal substrates using pulsed laser ablation technique is shown in Figure 1.14 [72]. One can clearly notice hysteresis in the ρ(T) data across 300 K which can be tuned for the resistive switching applications in memory devices. The vertical dashed line represents the location of transition in single crystal bulk VO_2. Such resistive switching has been observed in Verwey-type transitions in Fe_3O_4 as well [73,74]. These metal-insulator-transitions are extremely fast which can deliver deep-subthermal switching behavior (<10 mV/decade at 300 K). The switch ON and OFF currents in these Mott transitions are very fast and better than silicon MOSFET (Figure 1.15). Most of these Mott insulators found in nature also have conventional order parameters, describing, for example, the charge-density-wave (CDW) or the spin-density-wave (SDW) orders. However, Mott insulators with exotic ground states, such as the current carrying ground states have also been proposed theoretically [68–71]. Due to all the above reasons in the present thesis, we have chosen NiO as primary compound.

1.4.1 Antiferromagnetism in Transition-Metal Oxides: Molecular field Theory:

In any cubic crystal-field, or in the case of octahedral coordination by eight anions, the 3*d*-state of a transition-metal cations splits into six states of t_{2g} symmetry with orbital wave functions of the form:

$$xy\, f(r),\ \ yz\, f(r),\ \ zx\, f(r),$$

and four states with e_g symmetry and wave functions.

$$(x^2-y^2)\, f(r),\ \ (z^2-x^2)\, f(r)$$

The energy difference between these states split by fields of other symmetries is called the “crystal-field splitting”. While considering the spins of the transition-metal ions, one should often have to ask whether the crystal-field splitting or Hund’s-rule coupling is the larger. If the crystal-field splitting is larger, then the ion may be forced

into a "Low-spin" state. For example, an Fe^{2+} ion in the $3d^6$ state may be forced into a state with zero-spin only in the e_g band. In case of FeS_2, the Fe is in d^6 state and the t_{2g} band has no spin, so this system is a non-magnetic non-metal. On the other hand, if the Hund's-rule term is larger, for example in the case of Co^{2+} the spin moment is equal to $3\mu_B$. It is interesting to note that the transitions from high to low-spin can occur in the presence of external pressure. For example, a transition from high to low occurs between 40 *k*bar and 130 *k*bar pressure when Fe ions replace Mn in MnS_2 [75]. In simple cubic compounds like NiO, MnO and CoO the metal ions lie on a face-centered-cubic. As pointed out by Ziman (1952), for this structure and for spherical orbitals, antiferromagnetism with a finite Néel temperature must be due to interactions between next-nearest neighbors. Because in any antiferromagnetic structure each moment will have an as many parallel as antiparallel neighbors. In NiO and CoO the orbitals are not spherical, but in MnO the $3d^5$ ion is spherical. In this compound the antiferromagnetic Néel temperature is anomalously low, and there remains abnormally strong short-range order above the T_N (=116 K). Such kind of antiferromagnetic insulators are often called as Mott-Insulators. Usually, a magnetic ion in a crystal experiences exchange interactions with other nearest neighboring magnetic ions. According to the concept of molecular field theory, these magnetic interactions are usually replaced by an effective-field called Molecular-field [76]. Let the two-sub-lattices consist of "a" and "b" atoms which are ordered antiferromagnetically, then the Heisenberg's exchange Hamiltonian can be written as:

$$H_{ex} = -2 \sum_{a \neq b} J_{ab} S_a \cdot S_b \qquad (1.29)$$

where J_{ab} is the exchange constant and S_a and S_b are the spins on atoms a and b, respectively. The total fields acting on "a" and "b" atoms are

$$H_a = H_0 + H_{eff} = H_0 + \gamma M_b \qquad (1.30)$$

$$H_b = H_0 + H_{eff} = H_0 + \gamma M_a \qquad (1.31)$$

In the above equation, γ is the molecular field coefficient and H_{ex} is external applied field. Let J_{ab} be non-zero only for the nearest-neighbors (*z*). Then we can write the expectation values of H_{ex} as:

$$\langle H_{ex} \rangle = -2 J_{ab} \langle S_a \rangle \cdot \sum \langle S_b \rangle \qquad (1.32)$$

$$\langle H_{ex} \rangle = -g \mu_B H_{eff} \cdot \langle S_a \rangle \qquad (1.33)$$

Substituting the equation (1.32) into (1.33), we will get the following relation

$$H_{eff} = 2z J_{ab} \langle S_b \rangle / g \mu_B = \gamma M = \gamma g \mu_B N_a \langle S_b \rangle \qquad (1.34)$$

In the above equation N_a is the number of atoms in "a" sublattice, μ_B is the Bohr magneton, and g is the Landé g-factor.

$$\gamma = 2 J_{ab} z / N_a g^2 \mu_B^2 \qquad (1.35)$$

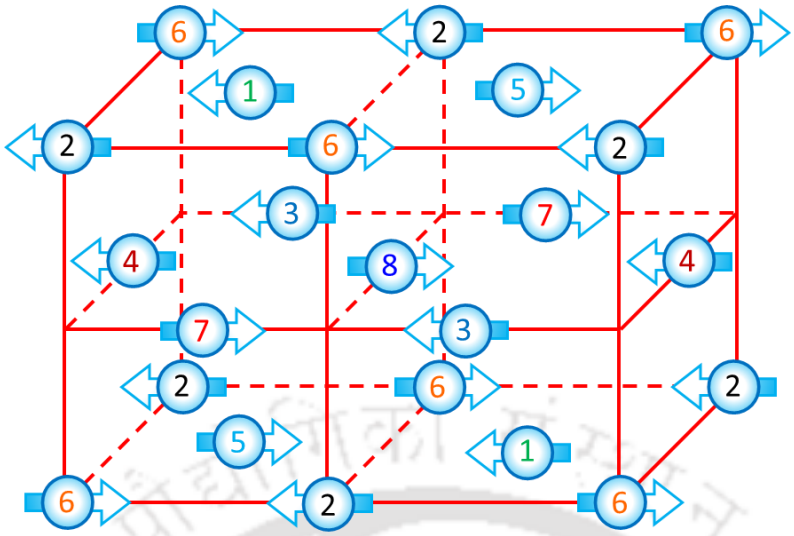

Figure 1.16: The face-centered cubic lattice divided into Eight Sub-Lattices [75, 76].

Thus from the above equation 'γ' is proportional to the exchange constant J_{ab}. Antiferromagnetic Mott-insulators (MnO, NiO, CoO, and FeO) crystallize in the NaCl-type (FCC) structure. Since there are four magnetic ions (e.g. Ni^{2+}) per unit cell, the two-sublattice model is inadequate. In comparison, the simple cubic (SC) lattice has only one atom/cell and BCC lattice has two atoms per unit cell. When a material orders antiferromagnetically below its T_N, the size of the magnetic unit cell becomes double that of the chemical unit-cell because of antiferromagnetic ordering. Therefore, the magnetic unit cell of the corresponding SC, BCC, and FCC chemical unit cells have two, four, and eight magnetic ions, respectively. Thus, in describing ordering in SC, BCC, and FCC cells, we need to consider 2, 4, and 8 sublattices, respectively. For discussing ordering in NiO, the Ni^{2+} ions are divided into eight sublattices as shown in figure 1.16. An elaborated discussion pertaining to the evaluation of exchange constants, role of finite-size and surface effects will be presented in Chapter-IV with a systematic correlation with the dielectric relaxation, ac-electrical conductivity and vibrational excitations.

1.5 Description of the Problem and its Approach:

Although enormous literature is available on the electrical, magnetic and optical properties of wide-bandgap oxides, but still there remains some open issues and challenges concerning to their dielectric and structural relaxation. Particularly, the topic related to the two-phase composites comprising of Mott-Insulators and wide-bandgap nonmagnetic-oxides is virtually unexplored. Thus, in the present research work we mainly focus on the structural, dielectric and magnetic behavior of two different wide-bandgap transition metal oxide composite systems namely $Zn_{1-x}Ni_xO$/NiO and $Ni_{1-x}Na_xO$/NiO. The main motivation in choosing such systems is that they are expected to show colossal dielectric permittivity with low-loss at temperatures just above the room temperature so that they can be useful for technological applications like ferroelectric-tunneling resistive-memory devices, and low-power and high-speed non-volatile memory cells [9,46,59,77,78]. Very recently, Li *et al.* reported magneto-

electric coupling and relaxor-ferroelectricity in the nano-composite of ZnO-Co thin-films synthesized by pulsed laser ablation and ion implantation techniques [63]. These authors reported that the relaxor behavior was driven by local lattice distortion induced by ion implantation of superparamagnetic cobalt nanoparticles [63]. Motivated by such study, we have chosen the $Zn_{1-x}Ni_xO$/NiO and $Ni_{1-x}Na_xO$/NiO two-phase composites aiming to understand the global dielectric and magnetic behavior for various doping levels. Our approach in investigating these composites is two-fold: First we attempt to study the role of thermally driven structural phase transition of NiO clusters on the global dielectric response and ac-conductivity behavior over a wide range of frequencies (100Hz $\leq f \leq$ 30MHz) and temperatures ($50^oC \leq T \leq 550^oC$). Secondly, we aim to understand the magnetic exchange interactions in these composites with special emphasis on the role of finite-size and surface effects on the magnetic and dielectric behavior. We have also made attempts to understand the local atomic environment and vibrational excitations in these composites and correlate these results with the temperature variation of structural, magnetic and dielectric properties which is the main goal of this thesis. Among many wide-bandgap oxides, zinc oxide gained a substantial interest in research community and remains a very interesting compound because of its wide energy bandgap (E_g ~ 3.3 eV) and large exciton binding energy (60 meV) [79,80]. Even though pure ZnO is a polar crystal, it does not undergo any phase transition at atmospheric pressure. It is not possible to reverse its polarization by an external applied field. However recent studies reported that the replacement of Zn atoms by Li, Be, and Mg can induce a ferroelectric phase transition across 330 K [62]. Furthermore, transition metal doped ZnO fulfils all the criteria of a dilute magnetic semiconductor (DMS) [81]. Recently, ferroelectric and multiferroic properties were also observed in various transition metal doped ZnO thin films. Such unique functionalities motivated us to choose ZnO as base compound with Ni as the doping element. Since at heavy doping levels NiO emerges as secondary phase inside the ZnO core which undergoes thermally driven structural phase transition across 523 K. Moreover, NiO is very interesting material for its various applications in super-capacitor, exchange bias controlled spin valve and electro-chromic devices [82,83]. This compound has become much more attractive due to its giant dielectric permittivity (with $\varepsilon_r \sim 10^5$) at room temperature and hundred fold drop of permittivity values at low temperatures [46]. Similar results ($\varepsilon_r \sim 10^5$-10^6) were reported in Li and La co-doped NiO ceramics.

Chapter-II

Experimental Details

This chapter describes all the experiments carried out during the doctoral research work. First section of this chapter deals with the synthesis procedure of bulk and nanostructured samples in detail. In the later sections, we discuss various characterization techniques employed to study the crystal structure, dielectric properties, magnetic and optical behavior of $Zn_{1-x}Ni_xO$/NiO and $Ni_{1-x}Na_xO$ polycrystalline samples. All the precursors were procured from Alfa-Aesar GmbH and Sigma-Aldrich Chemicals.

2.1 Synthesis of the Transition Metal Oxides:

2.1.1 Sol-gel Processing:

For the synthesis of bulk and nanostructures of $Zn_{1-x}Ni_xO$/NiO composites, we employed soft-chemistry based sol-gel technique because of its inherent advantages, such as, it requires low temperature for processing, allows higher degree of solubility, provides homogeneous dispersion of dopants and has the advantage of controlling the composition accurately. Sol-gel processing is a simple and versatile method for preparing materials of excellent functionalities with sophisticated nanostructures [84–86]. This technique allows selecting a wide range of precursors as starting materials to prepare magnetic and non-magnetic ceramic oxides [84–86]. Metal alkoxides ($M(OR)_n$), derivative of ethanol, are the most important precursors employed in sol-gel processing [87–89]. In this process, the metal alkoxides undergo hydrolysis and poly-condensation, resulting in the formation of metalloxane bonds to form a colloid solution (called sol). Sol is defined as a suspension of very small size (~1 nm -1µm) particles in which only short-range forces like Van-der Waals and surface-charge dominate significantly. The sol then forms an inorganic continuous network or gel with metal-oxo or metal-hydroxo connections in solution. Hence, in the sol-gel process the suspension undergoes a sol to gel transition, irrespective of the precursors. Subsequently, the drying process removes the liquid phase from gel and causes porosity in the material. Finally, thermal treatment is performed for further poly-condensation leading to the stable oxide in the form of fine powder.

Figure 2.1 depicts various steps involved in the sol-gel processing. Initially, the starting materials were dissolved in the solvent (distilled water, acid or ethanol) and then mixed together thoroughly. For the synthesis of $Zn_{1-x}Ni_xO$/NiO ($0.001 \leq x \leq 1$) nanoparticles, the metal-acetates of $C_4H_{10}O_6Zn$ and $C_4H_{14}O_8Ni$ were taken as precursors with oxalic acid ($C_2H_2O_4$) and ethanol (C_2H_6O) as solvents to dissolve the acetates [90,91]. Stoichiometric amounts of the above mentioned precursors were first dissolved in ethanolic solution under constant stirring at 70–80 °C for 3 hours in air using a spiral-cooled-condenser (Figure 2.2 a) to obtain a green color sol. A solution containing 6 grams of oxalic acid was dissolved in 200 ml of ethanol and added drop- wise to the above prepared warm-transparent sol to obtain a light green color gel. This gel product

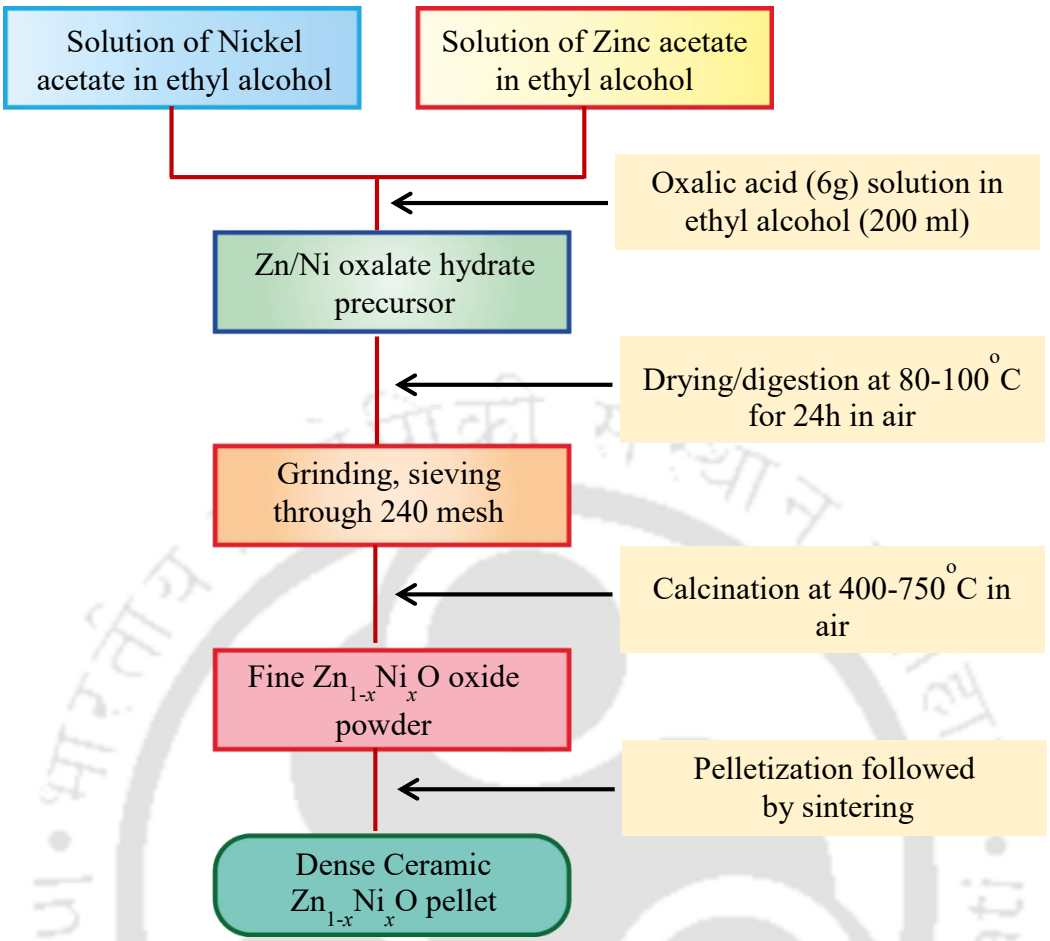

Figure 2.1: Flow Chart showing the different steps involved in sol-gel Processing.

was allowed to grow for 6 hours in air and then dried at 80–110°C for 24 hours to obtain a dehydrated xerogel network. This dried mixed-oxalate product was crushed in an agate mortar and sieved through 240 Mesh to obtain fine uniform distribution of the particles. Similar procedure is implemented for the synthesis of various compositions of Ni doped Zn-oxalate hydrate. This xerogel was calcined at temperatures between 500-800°C to remove the volatile substances such as crystallizing water, CO and CO_2 to form the final product. Consequently, all the synthesized samples are calcined at 500°C for 2–8 hours in air for proper decomposition and yield the desired compound $Zn_{1-x}Ni_xO$/NiO in the form of fine ash-color powder. For lower nickel compositions, the color of sample looks like ash-dust (figure 2.2 b), and jet-black for higher nickel compositions (figure 2.2 c) [90,91]. For large grain-sized samples, the calcined product was heated at 600°C for 8 hours and then pressed into thin pellets using a hydraulic press followed by sintering between 1200°C and 1350°C for 8-12 hours in air. Similar procedure was employed for the synthesis of un-doped NiO bulk grain size samples.

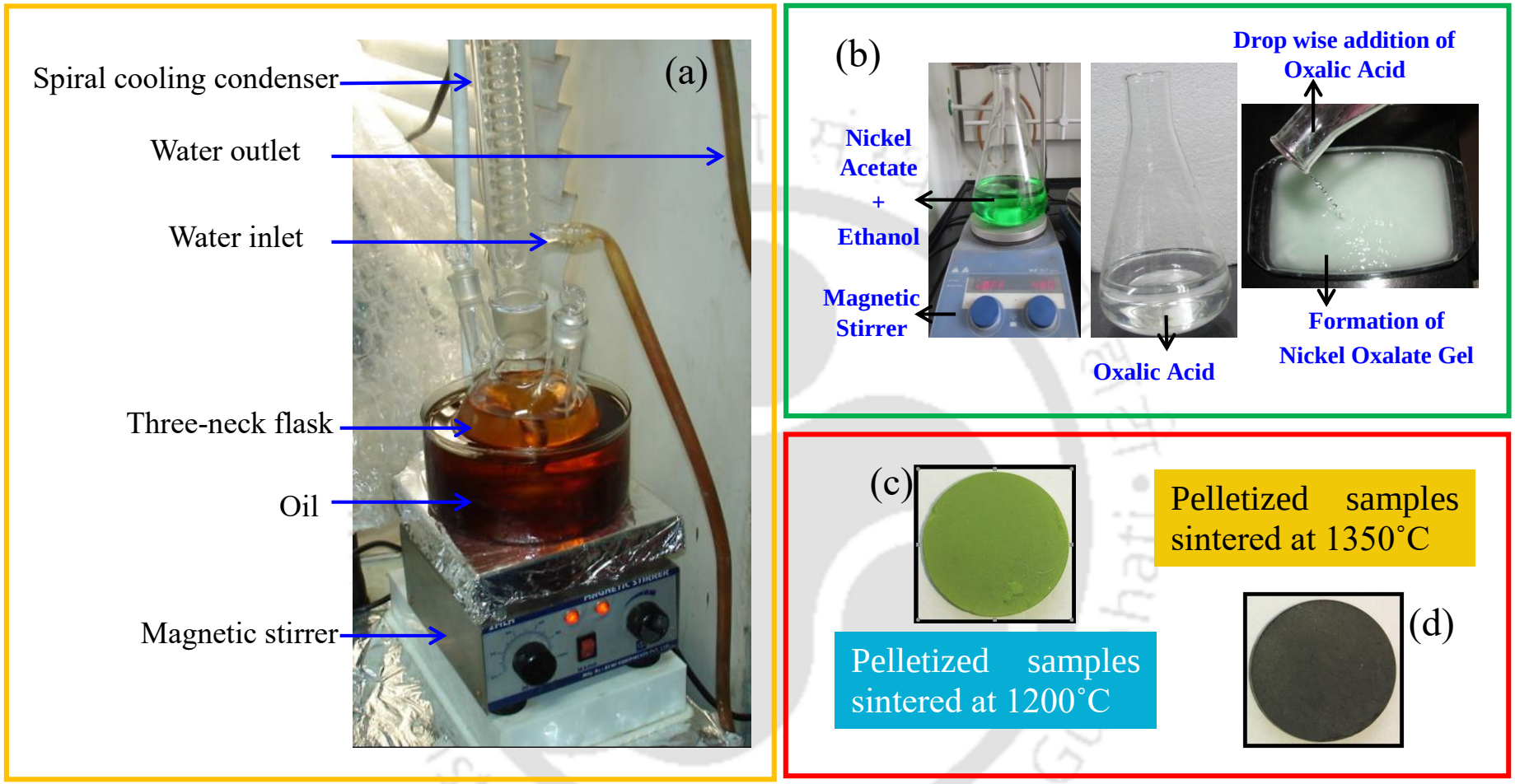

Figure 2.2: (a) Spiral cooled condensation mechanism; (b) pictorial representation of the formation of Nickel Oxalate gel, (c) The pelletized pale apple green colored oxygen rich NiO sintered at 1200°C and (d) jet black colored oxygen deficient NiO system sintered at 1350°C.

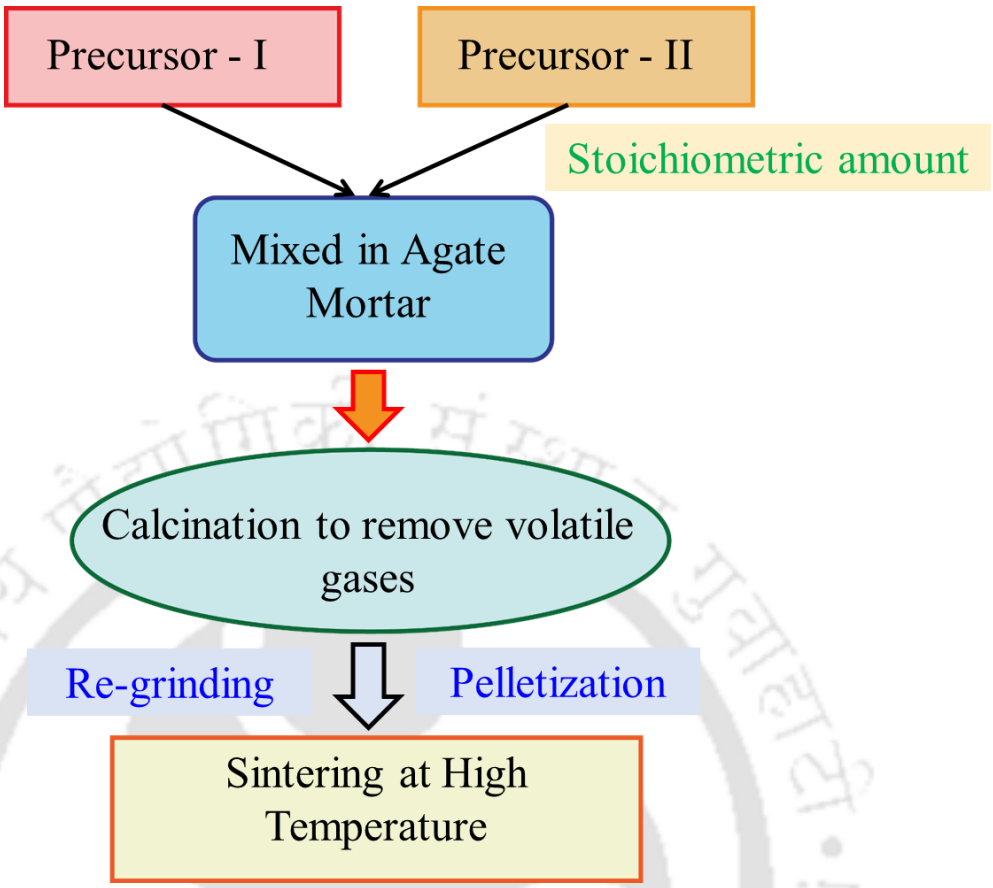

Figure 2.3: Flow Chart for Solid State reaction technique.

2.1.2 Solid State Reaction Method:

Besides high-temperature sintering of the sol-gel product for the bulk grain sized sample preparation, we also employed standard-solid state reaction method. Two batches of samples ($Ni_{1-x}Na_xO$ and $Zn_{1-x}Ni_xO$/NiO) were prepared using solid-state-reaction method. Main advantage of the solid-state reaction is that it has high thermodynamic stability. Figure 2.3 shows the various steps involved in a typical solid-state reaction technique. In the present case, stoichiometric amounts of ZnO, NiO, and Na_2CO_3 were chosen as starting compounds. To attain the high degree of homogeneity and to avail higher surface area for reactants, these stoichiometric amounts of precursors were mixed and ground together in an agate mortar for 4 hours. Such mixture was first calcined in air for 4 hours between 500°C and 600°C to remove the volatile substances. This mixture was pelletized using a 13 mm diameter KBr die and hydraulic-press to form compact cylindrical pellets. These pellets were finally sintered in the temperature range 1200-1350°C for 8 - 12 hours in air with heating rate 4°C/minute which leads to chemical decomposition and results in the formation of dense ceramic compound. The final sintering temperature and pre-sintering conditions are varied depending on the nature of the sample for required properties.

2.2 Characterization Techniques:

2.2.1 Crystal Structure and Morphology:

In the present thesis, the crystal structure and phase purity of the synthesized samples were determined by using the X-ray diffraction (XRD) analysis. The XRD is an important non-destructive technique primarily used for the phase identification of a crystalline material and provides detailed information on the unit cell dimensions and interaxial angles. This technique also provides useful information of various structural properties of crystalline compound such as micro-strain, grain-size, phase composition, and defect structure. The XRD analysis is based on constructive interference of monochromatic X-rays after being reflected from the crystalline sample. When an X-ray beam, generated by a cathode ray tube, is radiated/incident upon a crystal, the beam undergoes diffraction from the set of planes (Miller indices (*hkl*)), once the geometrical condition satisfies the Bragg's law given below (Figure 2.4) [29]:

$$2d_{hkl}\, sin\theta = n\lambda \qquad (2.1)$$

In the above equation 'd_{hkl}' is the inter-planer spacing between set of (*hkl*) planes, θ is the Bragg's angle/or Diffraction angle, *n* is an integer and λ is the wavelength of X-ray radiation. Figure 2.4 shows the geometry of the Bragg's law for the X-ray diffraction from a set of crystallographic planes. The locus of the diffracted beams taken together from the different sets of planes is collectively known as the diffraction pattern of the crystal. In the present work two different powder X-ray diffractometers were used to study the crystal structure and phase purity; (*i*) Panalytical-XPert Pro diffractometer and (*ii*) Rigaku (TTRAX-III) diffractometer (18 kW rotating anode X-ray source) with Cu K_α as the radiation (λ = 0.15406 nm) source. The temperature dependent X-ray diffraction

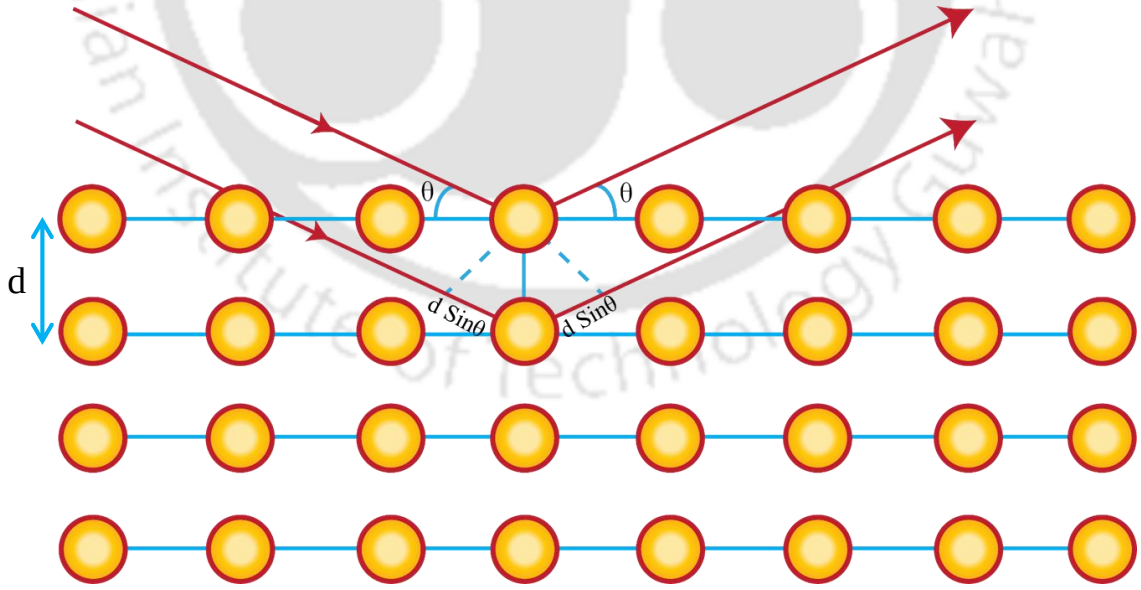

Figure 2.4: Schematic diagram for Bragg's law of diffraction.

Patterns were taken with a Rigaku RINT2000 diffractometer using Cu K_α radiation operating at 40 kV and 200 mA from 100ºC to 600ºC. All these X-ray diffractometers work under the Bragg-Brentano reflection geometry with a specific arrangement where the sample stage is fixed at the center of the circle, and both the X-ray source and detector rotates using a goniometer assembly. In order to extract the detailed crystallographic information from the obtained diffraction pattern we have also performed the Rietveld refinement using the open source programs FullProf-Suite and Powder-cell [92,93]. On the other hand, to probe the surface morphology and microstructure of the samples investigated in the present work we employed a scanning electron microscope (SEM, M/s LEO, 1430vp) working under secondary-electron (SE) mode. This instrument is also equipped with energy dispersive X-ray spectrometer (EDS/EDAX) which is used to trace the elements present in the samples.

2.2.2 Elemental Analysis using the X-ray Photoelectron Spectroscopy:

In the present thesis, X-ray photoelectron spectroscopy (XPS) was employed to probe the composition and chemical states of the investigated samples. This technique is one of the most powerful non-destructive surface sensitive technique to study the chemical and physical phenomenon occurring at surfaces of various materials such as metals, oxides, semiconductors, glasses, polymers etc. The XPS was first developed by Prof. Kai Siegbahn and co-workers at Uppsala University, Sweden between 1940 and 1950 and later awarded Nobel Prize in 1981. This spectroscopy technique has gained attention by the scientific community due to the following important reasons: (*i*) It can provide the quantifications of elemental composition from the solid surface up to a thickness of ≤ 10 nm). (*ii*) It can also provide an insight to the chemical and atomic environment of the elements present in the compound. (*iii*) Using XPS one can obtain the above information with relative ease and minimal sample preparation. (*iv*) The ability to explore first few atomic layers and assign chemical states to the detected atoms. (*v*) Since the mean free path of the electrons in any solid is very small, the detected electrons originated from the top few atomic layers provide important information which makes XPS a unique surface-sensitive technique for chemical analysis. In XPS, a monochromatic beam of soft X-rays (Mg K_α (1253.6 eV) and Al K_α (1486.6 eV)) are exposed to sample which interact with the core-level electron and transfer its energy to the electron leading to the emission of core-level electrons (photoelectric effect). The XPS spectrum is recorded between the variations of the number of detected core-level photoelectrons per energy interval versus their kinetic energy or Binding energy. Each element has a unique XPS characteristic spectrum. For the system containing different set of elements, the spectrum is comprised of intermixture of the individual peaks of the constituent elements.

The basic principle behind the XPS is Photoelectric effect in which electrically charged particles are released from or within (core) a material when it absorbs electromagnetic radiation as shown in figure 2.5. In the case of XPS, the interaction of soft X-rays with specimen leads to the photoemission process and its energy is analyzed by the spectrometer. Generally, the X-ray radiation (usually, Mg K_α (1253.6 eV) and Al K_α (1486.6 eV)) is capable to induce electrons not only from outer shells but also from the core levels. The emission of an electron from the *1s* shell of an atom is schematically represented in figure 2.6. The kinetic energy of an incident

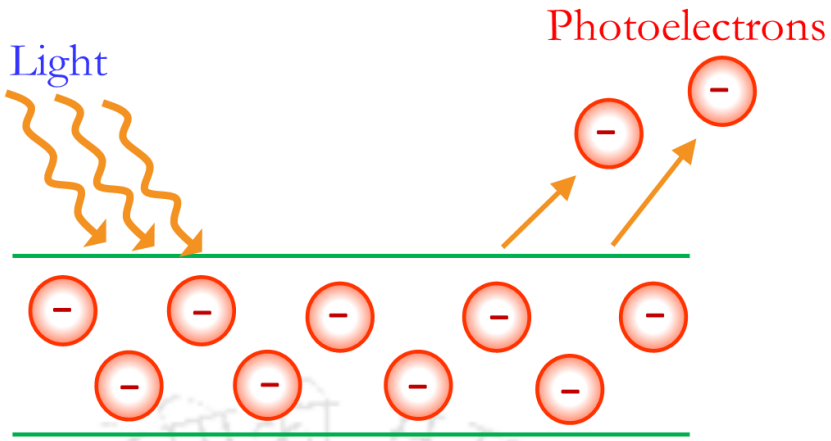

Figure 2.5: Schematic diagram for Photoelectric Effect.

photoelectron (E_K) is equivalent to the difference between X-ray photon energy ($h\nu$) and the binding energy of the core-level electron (E_b). Relation between these parameters and the work function of the instrument (Φ_s) is given by the expression below [94–96]:

$$E_b = h\nu - E_K - \Phi_s \qquad (2.2)$$

In addition, the work function of the instrument (Φ_s) is defined as the difference between the energy of the Fermi level (E_F) and the energy of the vacuum level (E_V). E_V is the zero point of the electron energy scale:

$$\Phi_s = E_F - E_V \qquad (2.3)$$

Usually, Φ_s will be determined from a detailed calibration for the spectrometer used. From equation 2.3 it is clear that only binding energies lower than the excitation radiation (in the present case 1486.6 eV for Al-K_α and 1253.6 eV for Mg-K_α) are probed. In addition to the photoelectric process, relaxation of the excited ion may occur by the emission of Auger electrons (figure 2.7). The Auger emission is dominated for elements having low atomic numbers (Z < 30). When an electron is emitted from a core level, another electron from a higher level falls to occupy the core level vacancy [94–96]. In order to conserve the total energy of the system, a third electron is emitted during this process, which is known as Auger electron (figure 2.7) [94–96]. Auger emission is independent of the photon energy and therefore the X-ray source. Another important relaxation process, which can significantly contribute to the XPS spectrum, is the "Shake-up"/"Shake-down" process in which electrons from the valence levels are excited to the bound/unbound states (figure 2.8). Moreover, 'Multiplet' splitting of the XPS peaks can also occur when atoms having unpaired electron couple with other unpaired electrons in the atoms giving rise to several possible final state configurations, consequently peaks shift to higher binding energy from the principle peak [94–96]. Some less intense Plasmon peaks also appear at higher binding energies from the principle peak at equal spacing due to specific amounts of energy losses when the photoelectron excites free electrons in a material.

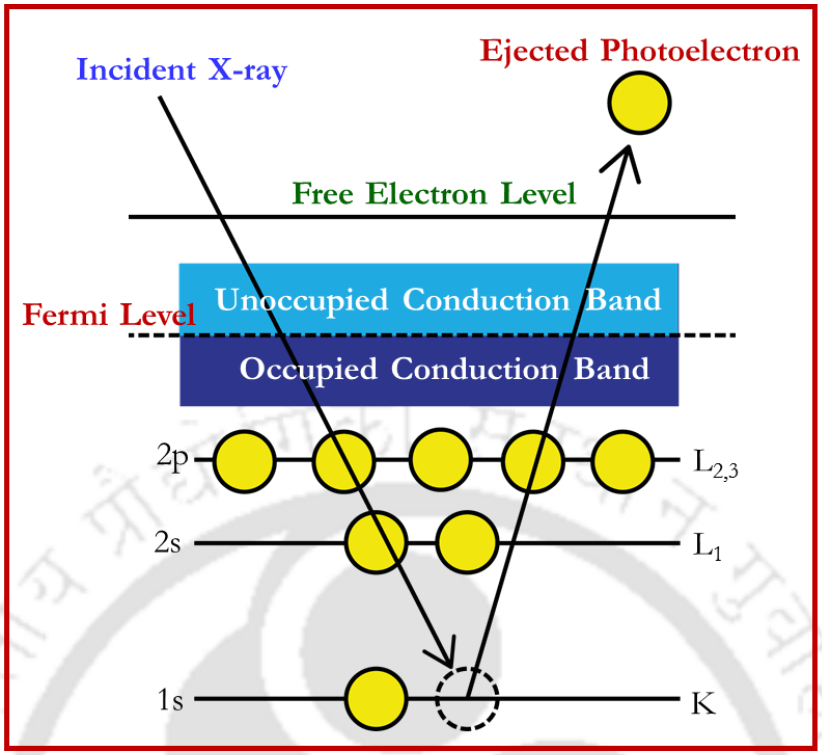

Figure 2.6: Energy level diagram for the Emission of Core-level photoelectron

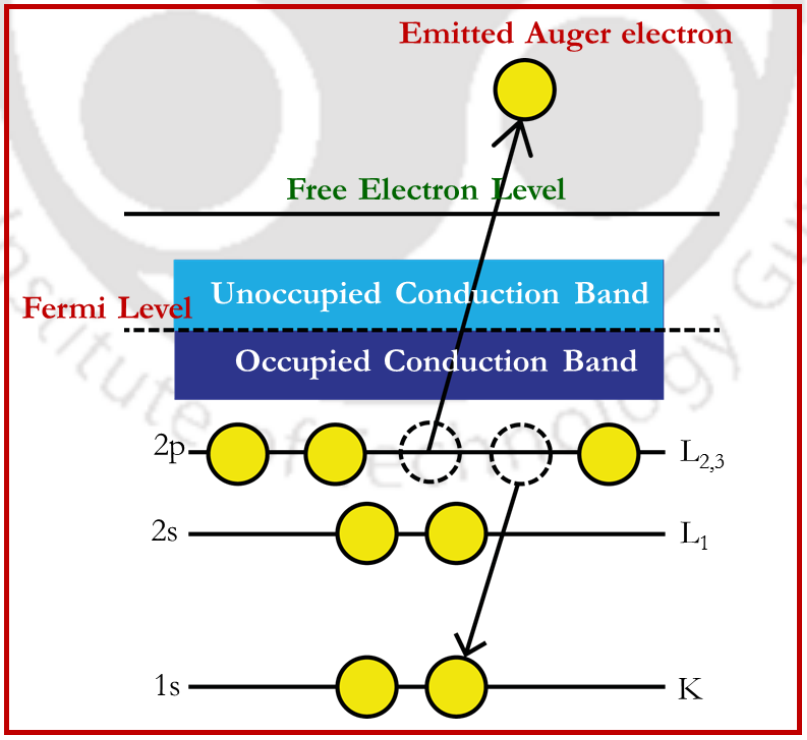

Figure 2.7: Energy level diagram for the Emission of Auger electron

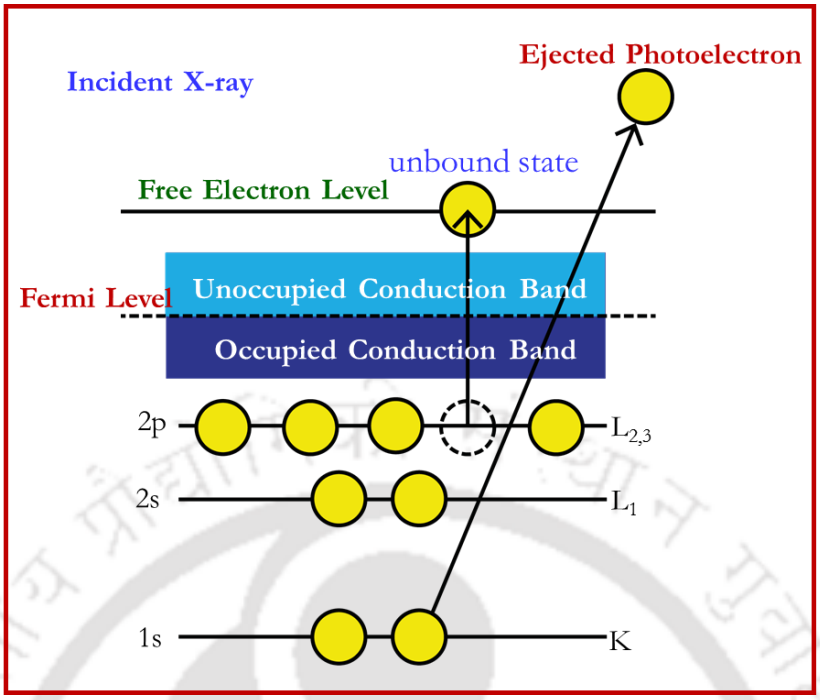

Figure 2.8: Energy level diagram to understand the Shake-up/Shake-off process.

2.2.3.1 XPS Instrumentation:

Typically, an XPS spectrometer comprises of a source of primary radiation (Al-K_α or Mg-K_α), an electron energy analyzer, extraction optics with energy filter, and sample holder mounted under an ultra-high vacuum chamber (< 10^{-9} millibar) (Figure 2.9). The following constraints are applicable when operating under normal conditions: (*a*) The photoelectron and Auger electron emissions are not affected by any external electrostatic or magnetic fields. Thus, the system should be calibrated to compensate the earth's magnetic field. (*b*) The photoelectron and Auger electron emissions are able to travel the region between the sample and the detector (around 1 m in distance). (*c*) Sample from which the emission arises must not be modified in any form during the course of analysis. (*d*) Investigated samples must be stable within the ultra-high vacuum chamber of the spectrometer. Since XPS is associated with the core-level electrons emitting from a solid surface, the sources used in XPS for X-ray generation must be able to produce photons of sufficient energy to interact with suitable number of core electrons [94–96]. X-rays are produced by bombarding an anode material with high-energy electrons. Normally, electrically heated tungsten filament is used as a thermal source for the emission electrons, however, for some focused X-ray monochromators, a lanthanum hexaboride emitter is used due to its higher current density. The X-ray emission efficiency of an anode is determined by the electron energy, relative to the X-ray photon energy. For example, the Al K_α (1486.6 eV) photon flux from an aluminum anode increases by a factor of more than five, if the electron energy is increased from 4 keV to l0 keV [94–96]. At a given energy, the photon flux from an X-ray anode is proportional to the electron current striking the anode. The maximum anode current is determined by the efficiency with which the heat, generated at the anode, can be dissipated. For this reason,

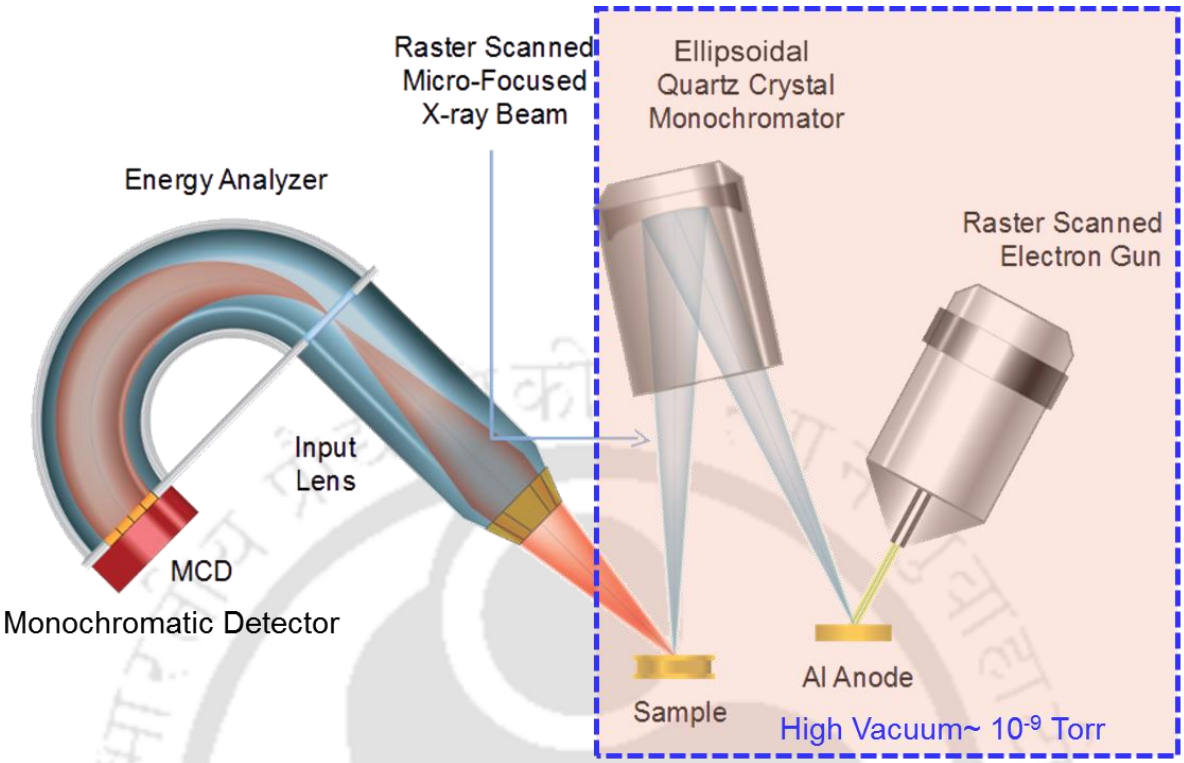

Figure 2.9: Schematic representation of an XPS system [94].

X-ray anodes are usually connected with water-cooled attachments [94–96].

Apart from the production of X-rays, it is also important to detect the emitted core level electrons with the best sensitivity. For this, energy analyzers with very high detection limit (0.1 to 1 atomic %) and good resolution must be used. In general, the two types of electron analyzers are used: (*i*) Cylindrical mirror analyzer (CMA) and (*ii*) Hemispherical sector analyzer (HSA) [94–96]. CMA analyzer were used when the resolution (0.4 to 0.6 % of the energy) is not the priority and sample dimension is smaller than 1mm (diameter < 1 mm). On the other hand, for better resolution HAS were used which can achieve better resolution than CMA by a factor of ten. For HAS, the energy of the ejected electron must satisfy the below condition to reach the detector [94–96]:

$$E = e\Delta V \frac{R_1 R_2}{R_2^2 - R_1^2} \qquad (2.4)$$

In the above expression, both R_1 and R_2 are the inner and outer radius of the hemisphere respectively, and ΔV is the applied potential difference between the inner and outer surface of hemisphere. Finally, to count the individual electrons arriving at the detectors electron multipliers were used. These electron multipliers consist of spiral-shaped glass tube with conical collector at one end and a metal anode at other end. In the present thesis, all the spectra were recorded by a dual source X-ray photoelectron spectroscope (Al-K_α @ 1486.8 eV, Mg-K_α @ 1253.6 eV) from VG-Microtech equipped with an ultrahigh vacuum (8×10^{-8} Torr) chamber with pass energy of 100 eV.

2.2.3 Impedance Spectroscopy:

In order to investigate the dielectric properties and ac-electrical conductivity of the investigated samples we employed high precision RF Impedance analyzer. This instrument is an important characterization tool used in the field of ferroelectrics and high-κ dielectrics using which one can probe the different relaxation mechanism and transition temperatures [97–99]. The frequency and temperature dependence of ac-resistivity and dielectric permittivity of the $Zn_{1-x}Ni_xO$/NiO and $Ni_{1-x}Na_xO$ polycrystalline samples were measured using two different high precision RF Impedance analyzers; one from Solartron (SI-1260) and other from Wayne-Kerr Electronics Pvt. Ltd. (WK-3030B). Both these instruments are equipped with temperature controller (Eurotherm-2204 e) and heater capable of reaching 600°C. For these measurements, two sides of the sintered pellet were fashioned like parallel-plate electrode geometry using silver coating. Constant ac-peak-to-peak sinusoidal driving potential of 100 mV with varying frequencies between 100 Hz and 20 MHz has been used as input signal. In order to match the input/output impedances of the instrument and investigating sample under high frequency limits, a 50 Ω feedthrough terminator cable was connected at the input and simultaneously a 50 Ω power splitter was used at output terminal as shown in figure 2.10. The most common and standard technique to measure impedance is by applying a single-frequency voltage (V) or current (I) to the interface and measuring the phase shift and amplitude (or real and imaginary parts) of the resulting current at that frequency using either analog circuit or fast Fourier transform (FFT) analysis of the response [100,101]. Generally, three different types of electrical stimulations can be used: (*i*) For the transient measurements, a step function of voltage [$V(t) = V_0$ for $t > 0$, $V(t) = 0$ for $t < 0$] may be applied at $t = 0$ to the system and the resulting time-varying current *I(t)* measured. The ratio $V_0/I(t)$, often called the indicial impedance or the time varying resistance, measures the impedance resulting from the step function voltage perturbation at the electrochemical interface. (*ii*) The second technique is to apply a signal $V(t)$ composed of random noise to the interface and measure the resulting current. Fourier- transformation of the results is required to pass into the frequency domain and obtain definite value of the impedance. This approach offers the advantage of fast data collection because only one signal is applied to the interface for a short time. The technique has the disadvantages of requiring true random noise. (*iii*) The third approach, the most common and standard one, is to measure impedance by applying a single-frequency voltage or current to the interface and measuring the phase shift and amplitude, or real and imaginary parts, of the resulting current. Figure 2.11 shows the general architecture of any commercial Impedance-Gain-Phase Analyzer. Figure 2.12 shows the simplest way of connecting the capacitance (C) and resistance (R) network of the measurement. The following are the four specific components that we extracted to study the dielectric behavior of $Zn_{1-x}Ni_xO$/NiO and $Ni_{1-x}Na_xO$: Capacitance (C), Dissipation factor (D) Impedance (Z), and Phase Angle (Φ).

2.2.5 Vibrational Excitations and Raman Spectroscopy:

Raman spectroscopy is an important spectroscopic characterization technique, which provides an insight in to the chemical structures to recognize substances from the characteristic spectral patterns and to determine quantitatively or semi-quantitatively molecular structure of a substance. This technique is based on the inelastic

scattering of monochromatic light, usually emitted from a laser source. The interaction of photons and matter essentially leads to three different process (*i*) Absorption of photons, (*ii*) Scattering of photons and (*iii*) Un-interacted photons, which may pass directly through matter [102,103]. If the energy of an incident photon corresponds to the energy gap between the ground state of a molecule and an excited state, then the photon may be absorbed and the molecule promoted to the higher energy excited state [102,103]. Another possible interaction is scattering of photon from a molecule within the matter, which can be detect by collecting these photons at an angle to the incident light beam. These scattering process are mainly classified into two type: (*i*) Rayleigh scattering (elastic scattering) and (*ii*) Raman scattering (inelastic scattering). In Rayleigh scattering, the light interacts with very small particles ($\lambda_{particle} << \lambda_{photon}$) with scattered photons having the same wavelength as the incident laser light and intensity (I) is inversely proportional to the fourth power of the incident wavelength $\left(I \propto \frac{1}{\lambda_{photon}^4}\right)$ [102,103]. However, the main scattering technique used for the molecular identification is Raman scattering, where the light interacts with the molecule and polarizes the cloud of electrons around the nuclei. Such distortion generates short-lived states (often called as Virtual states) which is unstable in nature and quickly re-radiates the photon. As compared to Rayleigh scattering process, in Raman scattering a small percentage of excited molecules relax down to a vibrationallly-excited state, hence the wavelengths of emitted photons are smaller than the excited photons (Raman shift, Stokes lines). Since only a very small number of molecules use this relaxation process, Raman scattering always gives very low intensity. Figure 2.13 shows the difference between Rayleigh scattering and Raman (Stokes and Anti-stokes) scattering process. The Raman scattering process from the vibrational ground-state '*m*' leads to absorption of energy by the molecule and its promotion to a higher energy excited vibrational state (*n*). This is called Stokes scattering. Nevertheless, due to thermal energy, some molecules may be present in an excited state such as '*n'* in Figure 2.13. Scattering from these states to the ground state '*m'* is called anti-Stokes scattering and involves transfer of energy to the scattered photon. The relative intensities of the two processes depend on the population of the various states of the molecule. Usually, Raman scattering is recorded only on the low-energy side to give Stokes scattering but occasionally anti-Stokes scattering is preferred. In order to detect such low intensity photon a high quality Raman spectrometer is required. The following are four major components of any high quality Raman spectrometer: (*a*) Excitation source (usually a continuous-wave (CW) laser), (*a*) Sample illumination and collection system, (*c*) Wavelength selector, (*d*) Detection and computer control/processing systems. A schematic arrangement of these components are shown in figure 2.14. In the present study, Raman spectrometer from LABRAM HR800 with an excitation wavelength λ = 488 nm of an Ar-ion laser was used to probe the vibrational and molecular bond structure of $Zn_{1-x}Ni_xO$/NiO and $Ni_{1-x}Na_xO$ samples.

2.2.6 Local Atomic Environment using Electron Spin Resonance:

In order to probe the local atomic environment of 'Ni' inside the $Zn_{1-x}Ni_xO$/NiO two-phase composites, we used the Electron Spin Resonance (ESR) spectroscopy technique at different temperature between 120 and 310 K

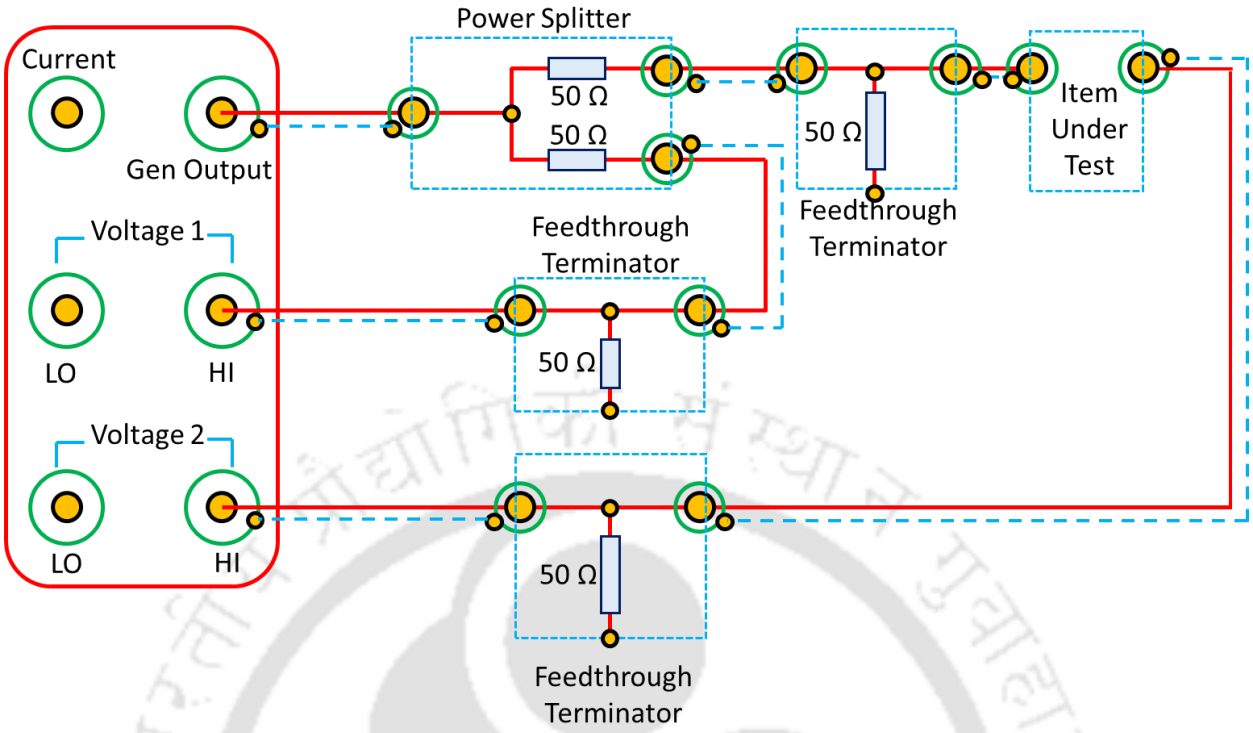

Figure 2.10: Typical connections for high frequency voltage measurements.

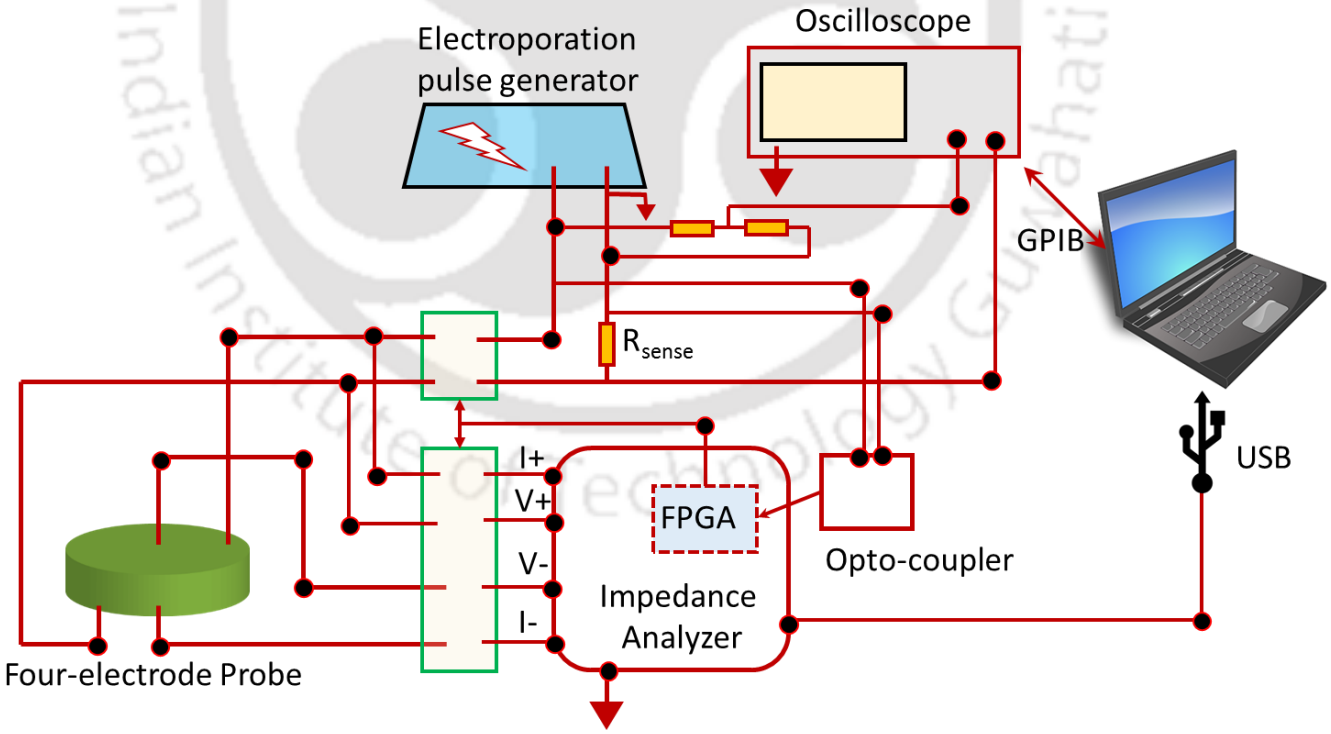

Figure 2.11: Schematic representation of an Impedance Analyzer [100].

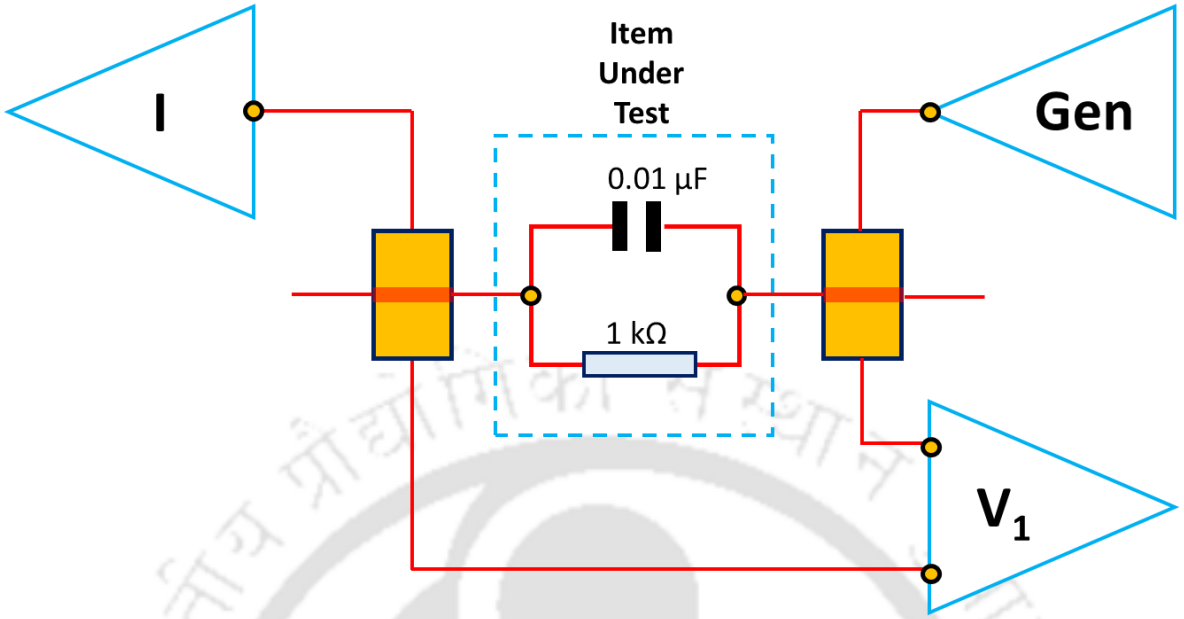

Figure 2.12: Connection for a simple impedance measurement [100].

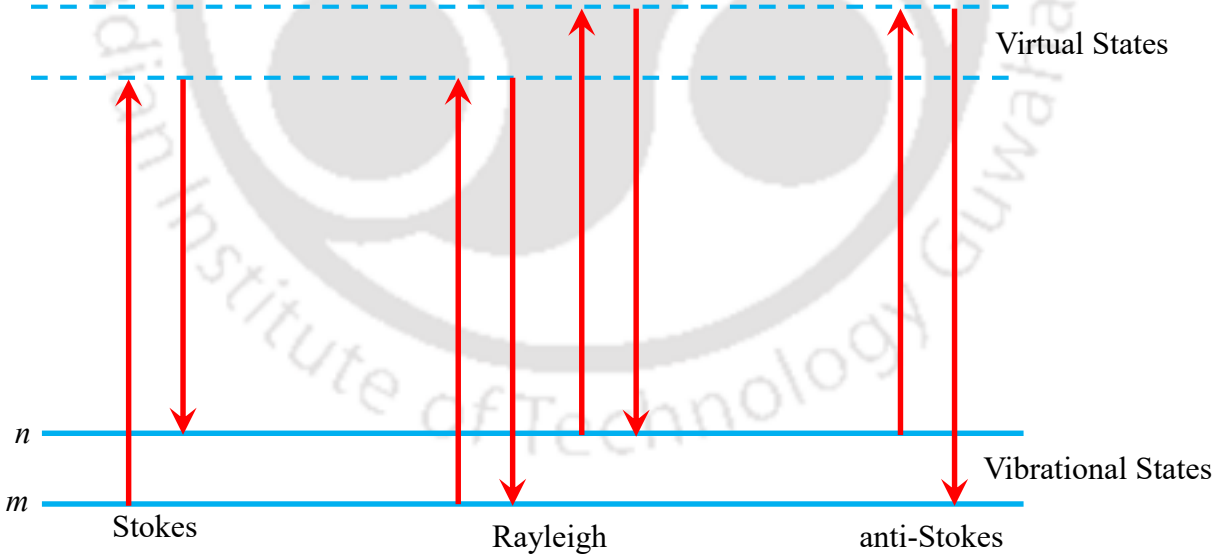

Figure 2.13: Diagram of the Rayleigh and Raman scattering processes. The lowest energy vibrational state '*m*' is shown at the foot with states of increasing energy above it. Both the low energy (upward arrows) and the scattered energy (downward arrows) have much larger energies than the energy of a vibration [102, 103].

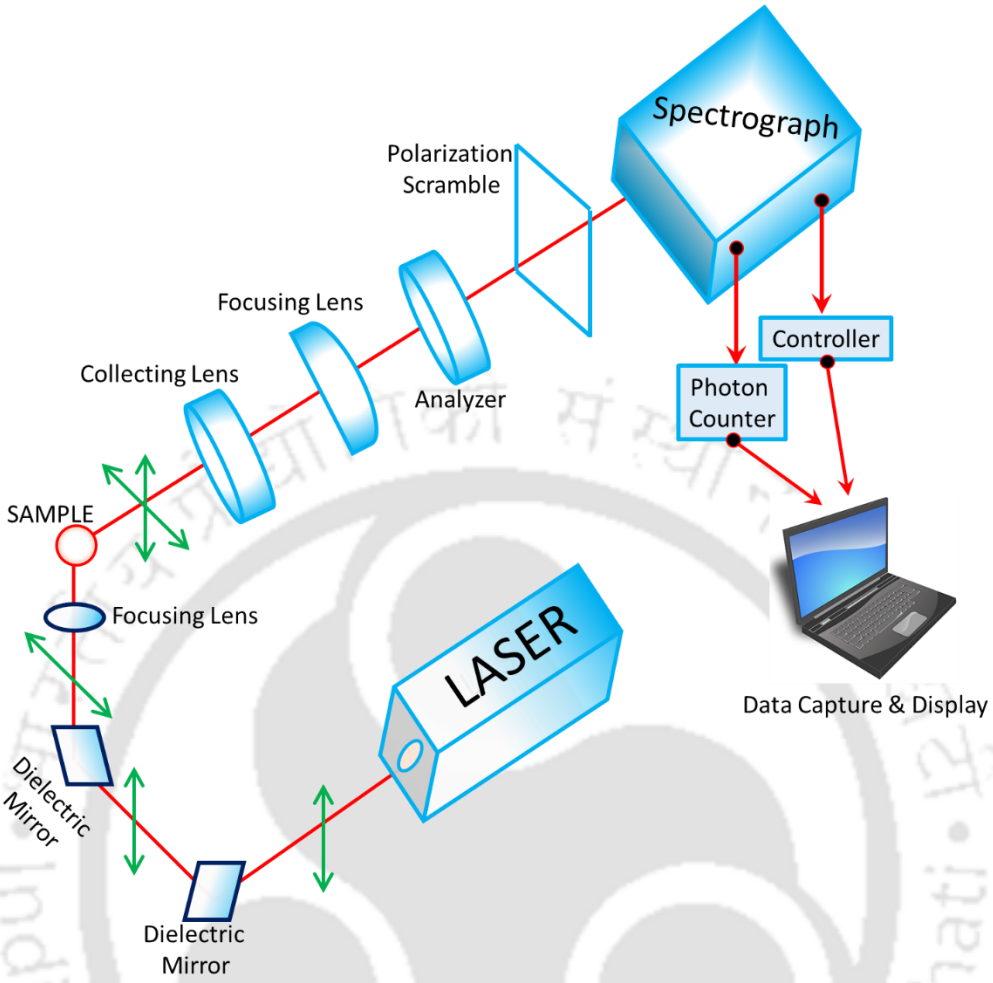

Figure 2.14: Schematic diagram of major component in a Raman Spectrometer [102].

When an electron is placed inside an external magnetic field, the electron spin degeneracy splits down which is governed by the spin Hamiltonian $\hat{H}_s = g\,\mu_B B\,\hat{S}_z$, here g is called the Landé g factor, μ_B is the Bohr magneton and B is the magnetic field strength. The ESR spectrum is obtained in continuous wave by sweeping the magnetic field to obtain the resonance when $h\nu = g\mu_B B$ [104,105]. Using a simple electromagnet, magnetic field up to 15 kOe are easily obtained, hence, one can use the microwave radiation with frequency (ν < 42 GHz). Within this microwave region, the most common choice is X-band (ν ~ 9-10 GHz) frequency in which the free electron resonance can be found at 3.39 kOe. Figure 2.15 shows the simplified block diagram of typical ESR spectrometer. In general, klystron tube is used for the generation of plane-polarized microwaves and power levels are adjusted by using the attenuator. The microwaves entering from the klystron tube are directed towards the Magnet Cavity by using circulator. These waves are again reflected back from cavity (with reduced power) to Circulator, which are then directed to Diode detector. If any power is reflected back by the detector that will be completely absorbed

Table 2.1: List of common frequencies used for electron spin resonance (ESR) spectroscopy

Designation	ν (GHz)	λ (cm)	B (electron) G
L	1.1	27	390
S	3.0	10	1070
X	9.5	3.2	3400
K	24	1.2	8600
Q	35	0.85	12500
W	95	0.31	34000
-	360	0.083	128000

by the load. The detector converts the plane-polarized microwaves into electrical signal, which is proportional to the microwave power reflected from the cavity. Thus, the absorption of microwaves by the sample could be detected by noting a decrease in current in the micro-ammeter. Under ideal conditions, a commercial X-band spectrometer can detect about 10^{12} spins at room temperature. Table 2.1 shows some common frequencies used in ESR spectrometer. In the present work, a Bruker EMX EPR spectrometer (Model 1444) working in the X-band frequency (9.451 GHz) was employed with maximum sensitivity of 2000:1. This setup was assembled with low-temperature liquid nitrogen cryostat capable of reaching 120 K.

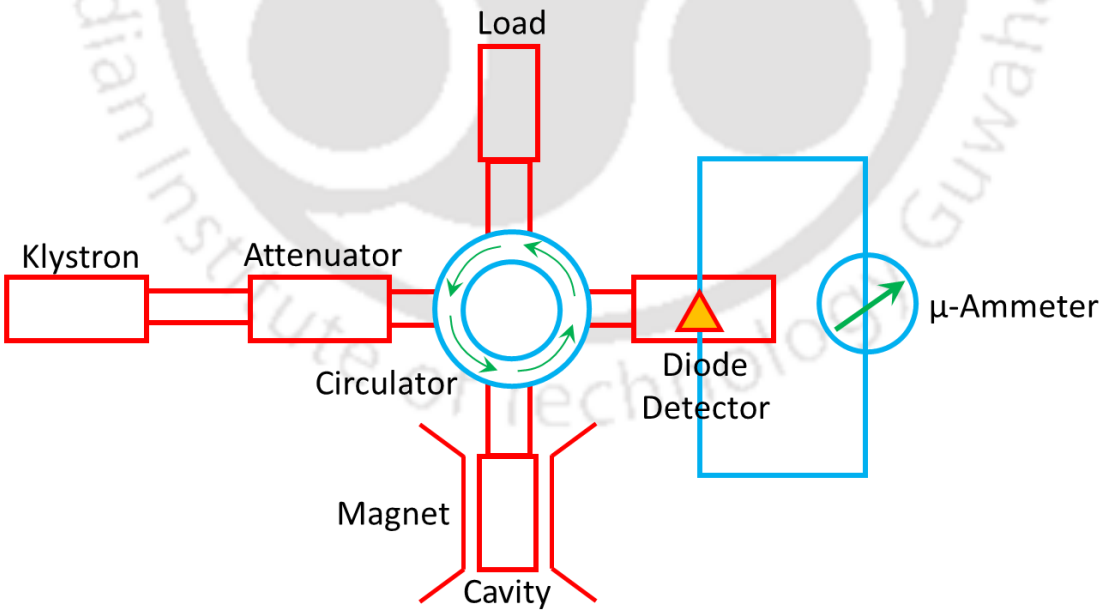

Figure 2.15: Block diagram of electron spin resonance (ESR) spectrometer [104].

2.2.7 Magnetization Measurements:

In order to probe the magnetic structure of these composites we used two different magnetic characterization units. For high temperature magnetic measurements ($27^{\circ}C \leq T \leq 500^{\circ}C$) a vibrating sample magnetometer from Quantum Design Technology capable of reaching 70 kOe magnetic field was used. Whereas for low temperature magnetization measurements (between 10 K and 320 K) we used a superconducting quantum interference device (SQUID) based magnetometer from Quantum design (Magnetic property Measurement system (MPMS) (7XL SQUID) [106]. The device may be configured as a magnetometer to detect extremely small magnetic fields small enough to measure the magnetic fields in living organisms using the Josephson junctions. The basic phenomena governing the operation of SQUID devices are flux quantization in superconducting loops and the Josephson-effect [106]. In 1962, B. D. Josephson showed that the electrical current density through a weak electric contact between two superconductors depends on the phase difference $\Delta\varphi$ of the two superconducting wave functions [106,107]. Moreover, the voltage across the weak contact is interrelated with the time derivative of $\Delta\varphi$. In a typical superconducting ring with one (known as RF-SQUID) or two (DC-SQUID figure 2.16) weak contacts, $\Delta\varphi$ is additionally influenced by the magnetic flux Φ through this ring. Hence, such a structure can be used to convert magnetic flux into an electrical voltage which is the basic working principle of a SQUID magnetometer. When a sample moves up and down it produces an alternating magnetic flux in the pick-up coils. These coils together with a SQUID antenna transfer the magnetic flux from the sample to an RF-SQUID with high degree of accuracy of measuring the magnetic moment of the order 10^{-8} emu. The RF-SQUID act as a magnetic-flux to voltage converter. The variation in the voltage is proportional to the change in magnetic flux of the sample. The voltage is then magnified and read out by the magnetometer's electronics (figure 2.16). The principal components of this measurement system comprise of the following aspects:

(i) Temperature control system: Precision control of the temperature in the range 2 K to 400 K.

(ii) Magnet control system: Current from a power supply is set to provide magnetic fields from zero to ±7 Tesla.

(iii) Superconducting SQUID amplifier system: The RF-SQUID detector is the heart of the magnetic moment detection system. It provides reset circuitry, auto-ranging capability, a highly balanced second-derivative sample coil array.

(iv) Sample handling system: The ability to step and rotate the sample through the detection coils without transmitting undue mechanical vibration to the SQUID is of primary importance.

(v) *Computer operating system:* All operating features of the MPMS are automated, computer controlled. The user interface at the PC console provides the option of working under standard sequence control, or diagnostic control, which will invoke individual functions.

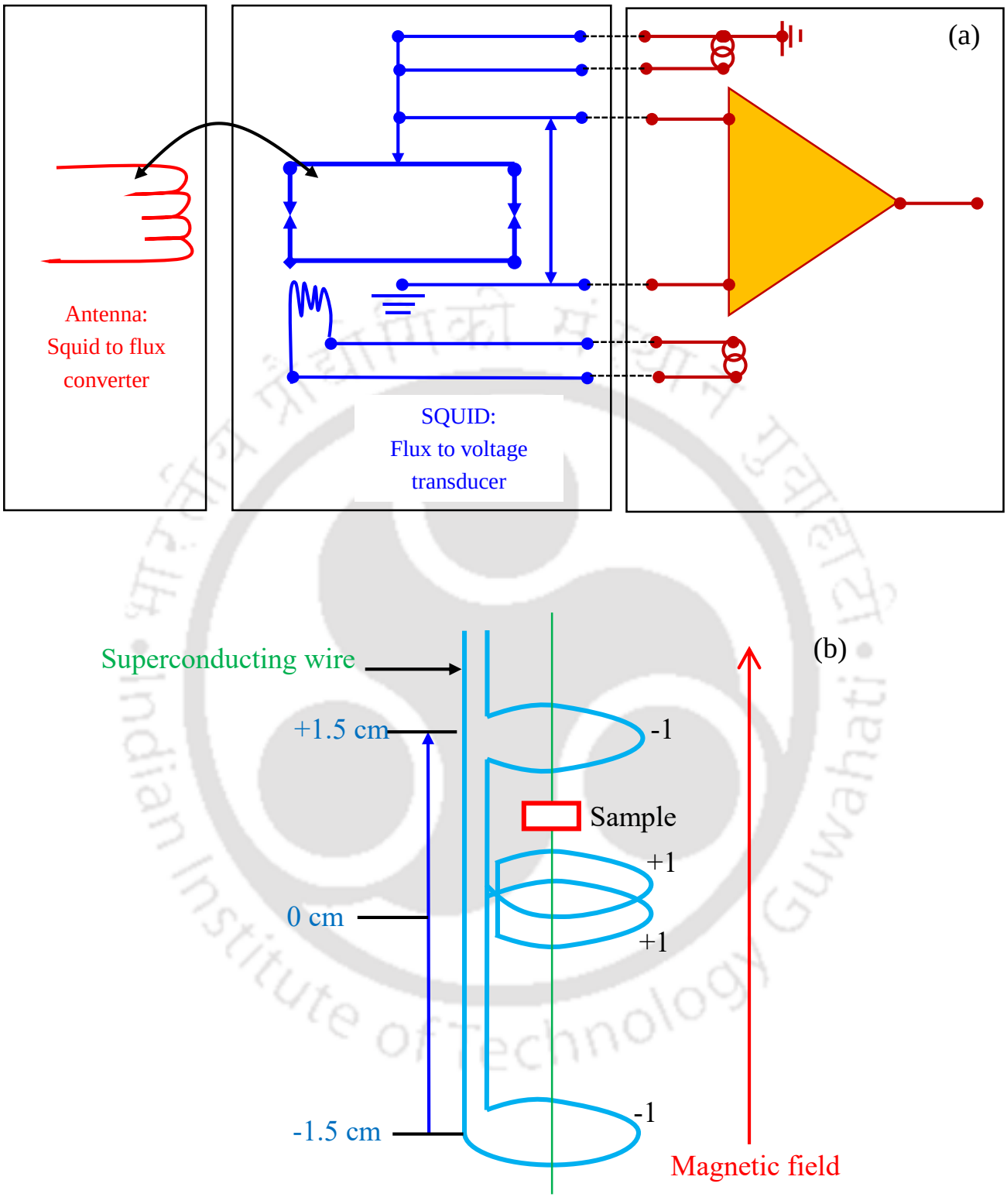

Figure 2.16: (a) Schematic diagram of the superconducting quantum interference device (SQUID) flux to voltage converter and (b) pick-up coil [106, 107].

Chapter-III

Electronic Structure and Dielectric Relaxation in $Zn_{1-x}Ni_xO$/NiO and $Ni_{1-x}Na_xO$

This chapter deals with the synthesis and characterization of $Zn_{1-x}Ni_xO$/NiO two-phase composites and $Ni_{1-x}Na_xO$ with special emphasis on their high temperature crystal structure, dielectric, and magnetic properties. In the introductory section, we elucidate the importance of oxide semiconductors and their composites. The gaps in literature related to their electronic structure and high temperature dielectric and structural properties of $Zn_{1-x}Ni_xO$/NiO composites and $Ni_{1-x}Na_xO$ are also discussed. Later sections deal with brief experimental details, results and discussion followed by summary of important findings.

3.1 Introduction and Situation of the problem:

Oxide semiconductors with wide band-gap ($E_G \geq 3$ eV) are playing a vital role in the evolution of transparent electronic devices and in renewable energy [108–111]. Latest developments in this field with base compounds ZnO and NiO is providing a fertile new ground for creating devices like Varistors, Spin-Valves, Transparent TFTs, Solar-cells, Lithium-ion Batteries, Light emitting diodes, electrochemical supercapacitors etc. [112–122]. Although the physical properties of both the oxides ZnO and NiO are well-known, their characteristics under low-dimensional nano-structures and doping with various elements in the periodic table are still under investigation with vigor to explore their scientific applications [112,122]. For instance, in the case of NiO, the crystallite size dependence of magnetic properties (Néel temperature T_N variation), optical energy bandgap studies and dielectric properties were recently reported [112,113,122]. ZnO nanorods and nanoparticles are also capable of generating high output voltage (~3 V) from thermopower waves (i.e. the energy conversion from chemical energy to thermal energy which in turn converts to electrical energy) [114]. One-dimensional hierarchical composite materials based on ZnO nanowires and electrospun blend nanofibers can act as highly effective photocatalysts [115]. On the other hand, the nanocomposite systems based on both ZnO and NiO have attracted immense scientific interest recently because of their potential applications in gas-sensing devices, electrode material for efficient dye solar cells, and bactericidal agent [116,118,120]. Recently, studies on the electrochemical characteristics of porous ZnO-NiO nanocomposite reported large specific capacitance (~ 649.0 F g^{-1}) values so that this system can act as outstanding electroactive material for supercapacitors [121]. A few authors reported the possibility of tuning the optical band-gap in Ni doped ZnO samples by varying the doping concentration and oxygen vacancies for optoelectronic applications [123,124]. Wang et al. reported the X-ray photoelectron spectroscopy (XPS), high-resolution transmission electron microscopy and Raman scattering studies of dilutely doped $Zn_{1-x}Ni_xO$ ($x \leq 0.01$) nanocrystals [124]. Magneto-electric coupling and relaxor-ferroelectric properties are reported in the case of ZnO-Co thin-film nano-composite synthesized through combination of pulsed laser ablation and ion implantation [63]. In such thin films relaxor behavior was driven by local lattice distortion induced by ion

implantation of superparamagnetic nanoparticles [63]. In this direction, we studied the dielectric behavior of $Zn_{1-x}Ni_xO$ system with various doping levels of nickel, where nickel oxide emerged as a secondary phase in the zinc oxide matrix. Our primary aim is to exploit the rhombohedral to cubic structural phase transition of NiO across the Néel temperature $T_N \sim 523$ K to realize a giant dielectric anomaly and relaxor behavior in the bulk two-phase composite of ZnO-NiO, which may lead to the system comparable to those proposed by Li et al. [19]. Nonetheless, little literature is available on the broadband dielectric spectroscopic studies of either $Zn_{1-x}Ni_xO$ (dilute doping $x < 0.05$) or bulk solid solutions of ZnO-NiO [125–129]. The first report on such systems appeared in 1997, in which a positive temperature coefficient of electrical resistivity with a maximum across $T \sim 400^{\circ}C$ was observed together with a sharp decrease in the resistivity due to the Ohmic network formation [125–127]. Later, Ghosh et al. studied the effect of low nickel doping and ac-driving frequency on dielectric response of ZnO ceramics at room temperature, without reporting any temperature variation of dielectric properties [130]. Nevertheless, a giant relative dielectric permittivity $\varepsilon_r > 10^5$ near room temperature was observed by Wu et al. in $Li_{0.05}Ti_{0.02}Ni_{0.93}O$, which was enhanced by the grain-boundary layer mechanism found in boundary layer capacitors [46]. These authors also reported a hundred-fold drop in 'ε_r' value at low temperatures, which was associated with thermally excited relaxation process rather than thermally driven phase transition [46]. On the other hand, several authors previously reported weak ferroelectric behavior in ZnO by substituting Li^+ (ionic radius 0.60 Å) or Be^{2+} (ionic radius 0.3 Å) due to the size-mismatch between the host and doped ions [131–133]. Nevertheless, a detailed study related to the high temperature structural and dielectric properties of $Zn_{1-x}Ni_xO$-NiO system was lacking in the literature when we initiated this work. On the other hand, no report is available till now on the $Ni_{1-x}Na_xO$ system which is completely new. Thus, our main focus in the present chapter is to explore the effect of rhombohedral to cubic structural phase transition of NiO (at $T_N \sim 523$ K) on the physical properties of $Zn_{1-x}Ni_xO$/NiO composites and $Ni_{1-x}Na_xO$. A systematic correlation of such physical properties with results obtained from the XPS and temperature dependent structural data is also presented in this chapter.

3.2 Experimental Details:

In this section, we provide a detailed synthesis procedure and discuss various characterization techniques employed to study the properties of $Zn_{1-x}Ni_xO$/NiO and $Ni_{1-x}Na_xO$. Various compositions ($0 \leq x \leq 1$) of the polycrystalline samples of $Zn_{1-x}Ni_xO$/NiO with bulk-grain sizes were synthesized by two different methods: (*i*) standard solid-state-reaction method (SSRM), and (*ii*) sol-gel processing (SGP) followed by sintering at high temperatures. For the SSRM we used the ZnO and NiO as raw materials which were thoroughly grounded and pressed to pellets using hydraulic press. These pellets are sintered at two different sintering temperatures, 1200°C and 1450°C for 8 hours in air to check the variation in the oxygen stoichiometry. We employed SSRM for the synthesis of $Ni_{1-x}Na_xO$ ($0.002 \leq x \leq 0.20$) using Na_2CO_3 and NiO as precursors at a sintering temperature at 950°C for 4 hours in air. Whereas in the case of SGP, we used hydrated acetates of zinc ($C_4H_{10}O_6Zn$) and nickel ($C_4H_{14}NiO_8$) as precursors, and oxalic acid ($C_2H_2O_4$) and ethanol (C_2H_6O) as solvents [122]. The synthesis

process involved mixing of the ethanolic solutions of precursors in appropriate amounts under constant stirring at 80°C for 3 hours in air using a spiral-cooled-condenser to obtain a transparent sol. The oxalic acid solution was added drop wise to the warm transparent sol to obtain a gel-like suspension which was allowed to grow for 24 hours at room temperature. Drying/digesting of the above product at 80-90˚C in air for 24 hours yielded a Xerogel network, consisting of mixed oxalate dihydrate of $Zn_{1-x}Ni_xC_2O_4 \cdot nH_2O$ as initial product. For dilute nickel compositions ($x \leq 0.05$), the crystal structure of this compound is similar to that of α-$ZnC_2O_4 \cdot 2H_2O$, however, for higher compositions, the structure closely resembles the orthorhombic structure of $NiC_2O_4 \cdot 2H_2O$ with lattice parameters a ~11.84 Å, b ~ 5.345 Å, c ~15.716 Å, Z = 8, and space group *Cccm* [122,134]. This powder was sieved through 240 Mesh and grinded in an agate mortar before decomposition. Calcination of the oxalate product at 500˚C for 2 hours in air gave $Zn_{1-x}Ni_xO$ as major phase for low compositions. Nevertheless, for moderate compositions, NiO was presented as secondary phase. For high concentrations, NiO phase dominated. These sample are in nanometer size after calcination. In order to fabricate large grain sized samples, the thermally decomposed powder was pressed into pellets by using a hydraulic-press, and then sintered at 1450˚C for 4-8 hours in air. Phase compositions of the pellets were studied using a Panalytical-XPert Pro diffractometer with Cu $K_{\alpha 1}$ radiation (λ = 0.15406 nm). The temperature-dependent X-ray diffraction (XRD) patterns were taken with the instrument Rigaku RINT2000 diffractometer using Cu K_α radiation operating at 40 kV and 200mA from 100 to 600ºC. For dielectric measurements, the two circular sides of the sintered pellet were painted with silver, and hence, fashioned like the conventional parallel-plate electrode geometry. Dielectric measurements are performed using two different Impedance–analyzers: the first instrument is from Wayne-Kerr Electronics Pvt. Ltd., (Model 1J43100) with frequency capabilities (100-20 MHz) and the second instrument is from Solartron (Model SI1260) with operating frequency from 0.5µHz-32 MHz. All these measurements were performed with V_{ac} = 100 mV ac peak-to-peak amplitude with no dc-voltage contribution. Both these instruments are assembled with a heater and temperature controller so that the measurements can be performed from room temperature to high-temperatures (600ºC).

3.3 Results and Discussion

3.3.1 Structural Characterization (Temperature Dependence):

Figure 3.1 shows XRD patterns of the $Zn_{1-x}Ni_xO$ sintered pellets for dilute (x = 0.01, 0.025), moderate (x = 0.163) and higher compositions (x = 0.35, 0.45 and 0.55). These patterns confirmed that beyond a certain critical composition x_c ~ 0.163, NiO emerges out as a major secondary phase. All the XRD patterns for higher compositions $x > x_c$ confirmed the presence of two phase composition, *i.e.* wurtzite h.c.p structured ZnO and rhombohedrally distorted cubic NiO. In order to understand the effect of secondary phase (NiO) on the lattice parameters and structural distortion of heavily doped $Zn_{1-x}Ni_xO$ samples at high temperatures we have performed the x-ray diffraction measurements at various temperatures above and below the Néel temperature (T_N) of NiO. Figure 3.2 shows the XRD pattern of $Zn_{0.45}Ni_{0.55}O$ pellet recorded between the temperatures 100ºC to 600ºC. We

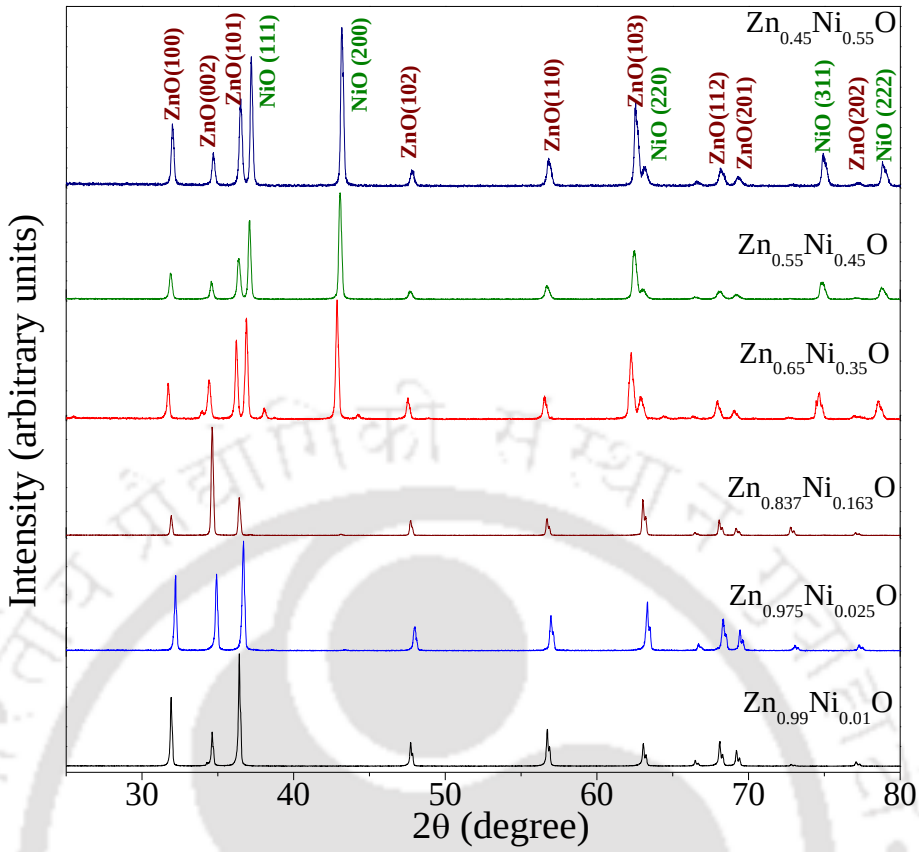

Figure 3.1: The X-ray diffraction patterns of the two-phase composite system $Zn_{1-x}Ni_xO$/NiO in the form of pellets for various concentrations of nickel ranging from dilute (x ~ 0.01, 0.025), moderate (x ~ 0.16), and higher compositions (x ~0.35, 0.45 and 0.55).

observed that all the diffraction peaks shift towards lower Bragg angle side with increasing the temperature. In order to probe such small changes, all the diffraction patterns were plotted on a common scale for both the systems $Zn_{0.45}Ni_{0.55}O$ and NiO. For the simplicity of analysis, only few selected diffracting planes are chosen for both the systems. Figures 3.3 and 3.4 depict the diffraction peak intensity versus Bragg angle of these planes and their temperature variation [Miller Indices of Planes for (111), (200), (220) and (222) planes of $Zn_{0.45}Ni_{0.55}O$ and (111), (200), (220), (311) and (222) reflections from NiO]. The corresponding unit-cell volumes V_C for both the phases are shown in the figure 3.5. A clear dip across the Néel temperature of NiO (T_N ~ 523 K) was observed for hexagonal lattice parameters '*a*' and '*c*' of wurtzite phase of $Zn_{0.45}Ni_{0.55}O$. While, a slight change in the slope of linear behavior of nickel oxide was noticed across T_N. It is well known that pale apple green color stoichiometric nickel oxide exhibits rhombohedral (space group: R-3m) to cubic (space group: Fm3m) structural phase transition associated with the long-range antiferromagnetic to spin-disorder paramagnetic state across 523 K [122,135,136]. At normal temperature and pressures NiO exhibits a slightly distorted face-centered-cubic structure (NaCl-type) that gains stability by squeezing inward along the <111> crystallographic direction [137]. As the temperature of the specimen was raised above T_N the rhombohedral distortion became smaller and approaches to perfect cubic

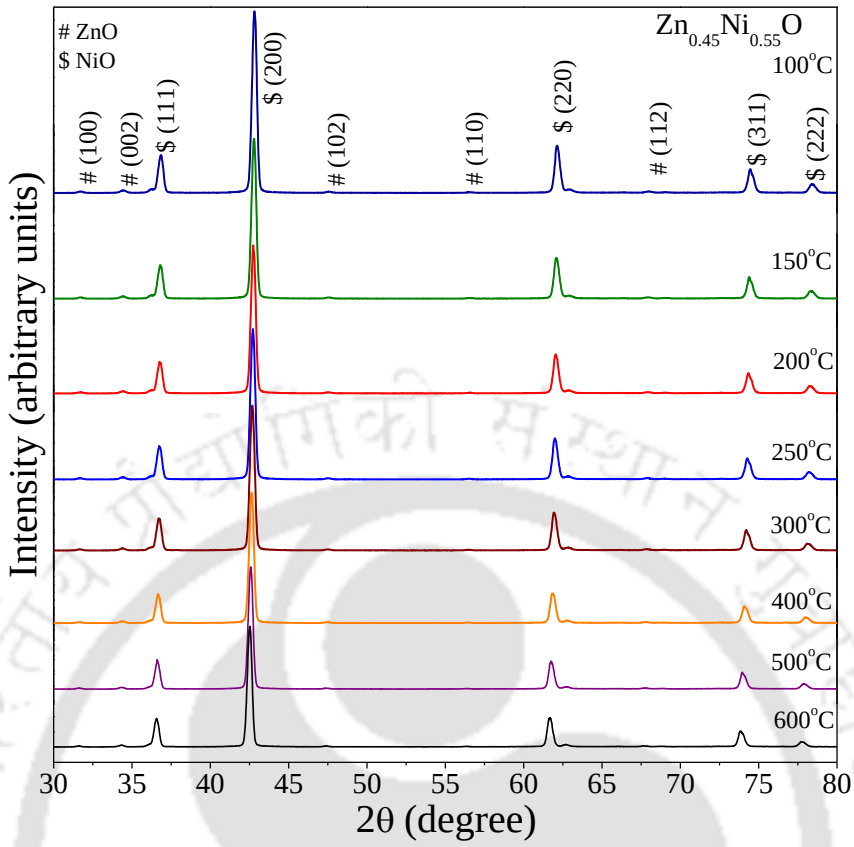

Figure 3.2: The X-ray diffraction pattern of the sintered pellets of two-phase composite $Zn_{0.45}Ni_{0.55}O$/NiO recorded at various temperatures between 100˚C and 600˚C.

structure. Above T_N, NiO exhibits f.c.c structure in which Ni and O ions are arranged alternatively in [111] crystallographic direction. Whereas, for $T< T_N$ the size ratio of the nickel and oxygen ions becomes unfavorable and leads to deviation from the cubic symmetry to rhombohedral distortion [137]. While such structural change belongs to NiO but the effect was significant on both hexagonal lattice parameters '*a*' and 'c' of $Zn_{0.45}Ni_{0.55}O$.

Using the XRD pattern and the reduced cell-parameters and the rhombohedral angle 'α′' were evaluated for pure NiO pellet sintered at 1450º C. The inset of figure 3.5 depicts the temperature dependence of rhombohedral angle 'α′(T)'. Generally, as a conventional notion the rhombohedral angle (slightly distorted cube) is characterized by 'α' which corresponds to the four-NiO molecules within the rhombohedral unit cell. This angle 'α' is different from that of monomolecular unit cell rhombohedral angle 'α'' (slightly greater than 60º) and both are connected by the following relation [47]:

$$(\alpha - 90°) = \frac{\sqrt{3}(\alpha' - 60°)}{2} \qquad (3.1)$$

In practice all the transition-metal oxides exhibits the close-packed arrangement of oxygen ions forms the main framework of the crystal structure, whereas the smaller metal cations occupy the interstitial sites. The distribution

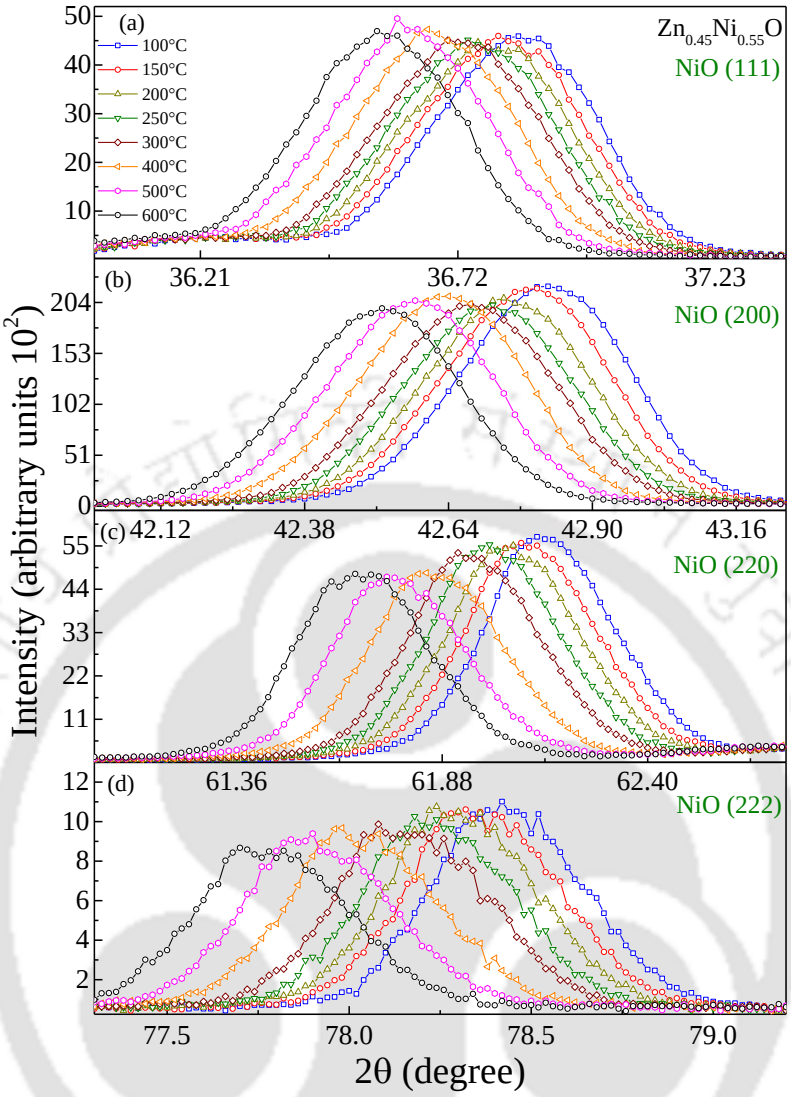

Figure 3.3: The shift of various the diffraction peaks of NiO bulk grains present as a secondary phase in $Zn_{0.45}Ni_{0.55}O$ matrix recorded at various temperatures in the range 100˚C-600˚C.

of cations will be either in the octahedral voids (six-fold co-ordination in typical haematite or rocksalt types of crystal structures) or in tetrahedral holes (four-fold co-ordination in wurtzite-type structure) [47,137,138]. The crystallographic phase transformations in such type of metal-oxides will takes place if the arrangement of oxygen ions changes from hexagonal to cubic close-packing or vice-versa [138]. Sometimes the relocation of cations between octahedral and tetrahedral sites may also cause substantial change in the volume of unit-cell even though the original oxygen ion framework remains unaltered. Earlier studies by Rooksby reveal that the maximum rhombohedral distortion in NiO occurs at low temperature close to -183˚C (liquid air-temperature ~ 90 K) and the distortion eliminates smoothly with rise of temperature. The magnitude of the lattice constant '*a*' and axial-rhombohedral angle 'α'' reported by Rooksby at three different temperatures are as follows:

For T = -183˚C, 18˚C and 275 ˚C are '*a*' = 2.946 Å, α' = 60º 12', '*a*' = 2.951 Å, α' = 60º 4.2', and '*a*' = 2.966Å

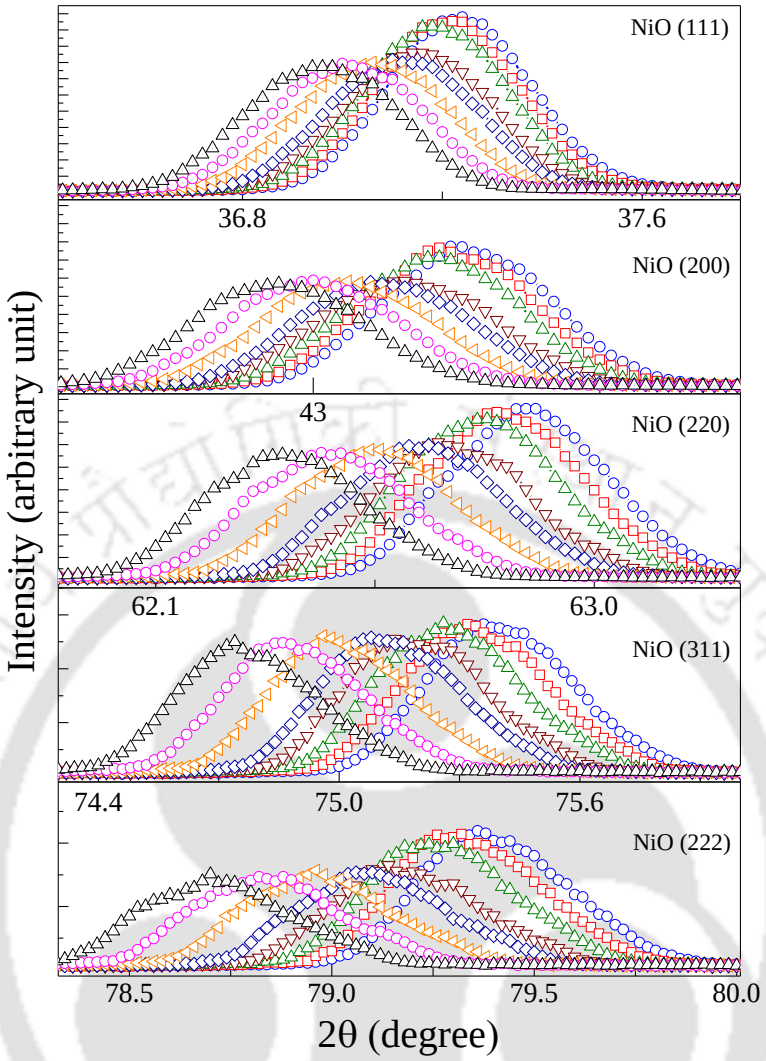

Figure 3.4: The change in the diffraction peak positions for different planes recorded between the temperatures 100˚C and 600˚C for bulk grain sized NiO pellet sintered at 1350˚C for 12 hours in air.

α' = 60º, respectively [137]. These values of 'α'' are slightly higher as compared to previously reported values by several authors [47,137,138].

For pure NiO case, we have evaluated the magnitudes of both 'α' and 'α'' using temperature dependent XRD data. Accordingly, the variation of α'as a function of temperature for NiO is shown in the inset of figure 3.5. We observed that the variation of $\alpha'$is quite high (~ 60º 8′, 'α' ~ 90º 7′) at temperature close to 150ºC as compared to the data reported by Rooksby. From the figure 3.5 we noticed that the magnitude of α'suddenly drops to 60º indicating that the distortion is completely vanishes across ~ 300ºC. In contrast, no distortion was noticed in the NiO secondary phase present in the $Zn_{0.45}Ni_{0.55}O$ matrix, yet, we observed an anomalous decrease in the unit-cell volume between 150ºC and 300ºC. For T > 300ºC the unit-cell volume increases continuously with increasing the temperature. These results are consistent with the previously reported data of Rooksby in which no significant

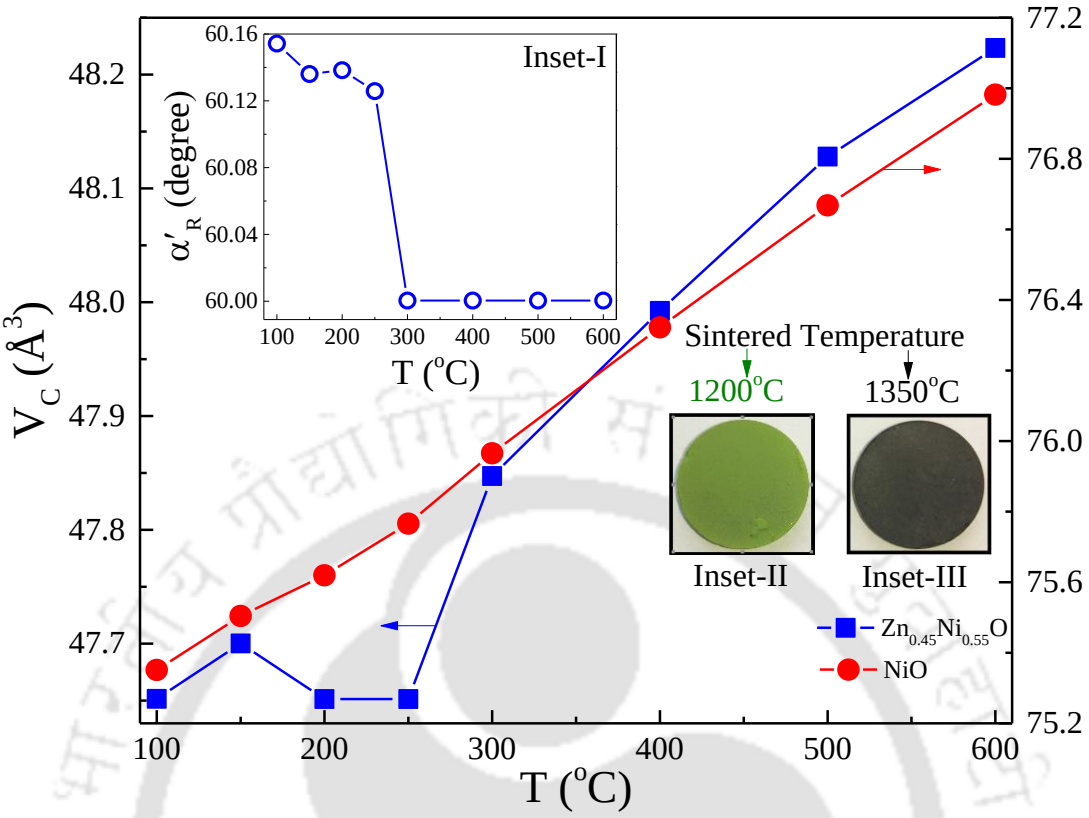

Figure 3.5: The temperature variation of the unit-cell volume V_C of h.c.p. structured $Zn_{0.45}Ni_{0.55}O$ (L.H.S. scale) and f.c.c. structured NiO secondary phase (R.H.S. scale) present together with $Zn_{0.45}Ni_{0.55}O$ system. The inset-I shows the temperature dependence of axial-rhombohedral angle α' estimated for the oxygen rich pure NiO system (*i.e.* x =1). The insets II and III shows the pale apple-green colored oxygen rich NiO and jet-black colored oxygen deficient NiO system without any ZnO, synthesized at sintering temperature 1200˚C and 1350˚C for 12 hours in air, respectively.

distortion was observed in $NiFe_{0.01}O$ and NiO + Co_3O_4 powders. Our results confirm that the cubic-symmetry can be sustainable till 300ºC for the ZnO + NiO solid solutions. For example, Shimomura *et. al.* reported 'α' ~ 90° 3.8' at 20ºC of sample containing excess oxygen content i.e. $NiO_{1.20}$ synthesized by oxidizing the nickel foil of thickness 0.06 mm [138]. These authors reported some interesting change in the magnetic ordering as well. At sufficiently higher oxygen contents the rhombohedrally distorted lattice exhibits ferromagnetic like character as revealed from the cooling and heating cycles of the dc-magnetic susceptibility measurements recorded in the presence of external magnetic field of 1000 Oe [47,137,138]. Such unexpected magnetic behavior may originate from the excess oxygen present in the specimen and/or nickel vacancies (absolute excess of anions).

Few authors reported 'α' ~ 90°4.2' at 20ºC for NiO single crystals of perfect stoichiometry [47,137,138]. Schron et al. explained the origin of crystallographic distortion in 3*d* transition metal oxides such as NiO, MnO, FeO and CoO using spin-polarized density function theory (DFT) approach [139]. According to their results the spin-orbit interaction drives the magnetic anisotropy in CoO and FeO due to the partially filled t_{2g} subshell while transverse electron interaction plays an important role for the magnetic anisotropy in MnO and NiO due to the

completely empty or filled t_{2g} subshell [139]. These authors calculated the strain tensor $\hat{\epsilon}$ due to antiferromagnetic ordering and the orbital occupancy. They discussed the rhombohedral lattice distortion (including monoclinic) by applying the condition $Tr(\hat{\epsilon}) = 0$ to the volume-conserving monoclinic strain tensor. In the case of MnO and NiO, the stress components '*t*' and '*e*' of the calculated strain-tensor completely vanishes causing purely rhombohedral distortion along the [111] direction [139]. These authors reported a detailed study on the role of occupation of the t_{2g} minority-states for the rhombohedral and monoclinic distortion which decreases significantly with the filling of minority spin channel states of t_{2g} orbitals [139]. It is well known that depending upon the stoichiometry the color of NiO can change from pale apple green to jet black. To probe this issue, we have prepared two batches of NiO samples: the first batch was sintered at 1200˚C for 12 hours in air and the second batch was sintered at relatively higher temperatures approximately 1450˚C for 12 hours in air (depicted in the inset of Figure 3.5). We observed that the samples sintered at low temperatures appear pale apple green color (Inset-II of figure 3.5) corresponds to the near-stoichiometric or excess oxygen content in NiO, whereas, the pellets sintered at higher

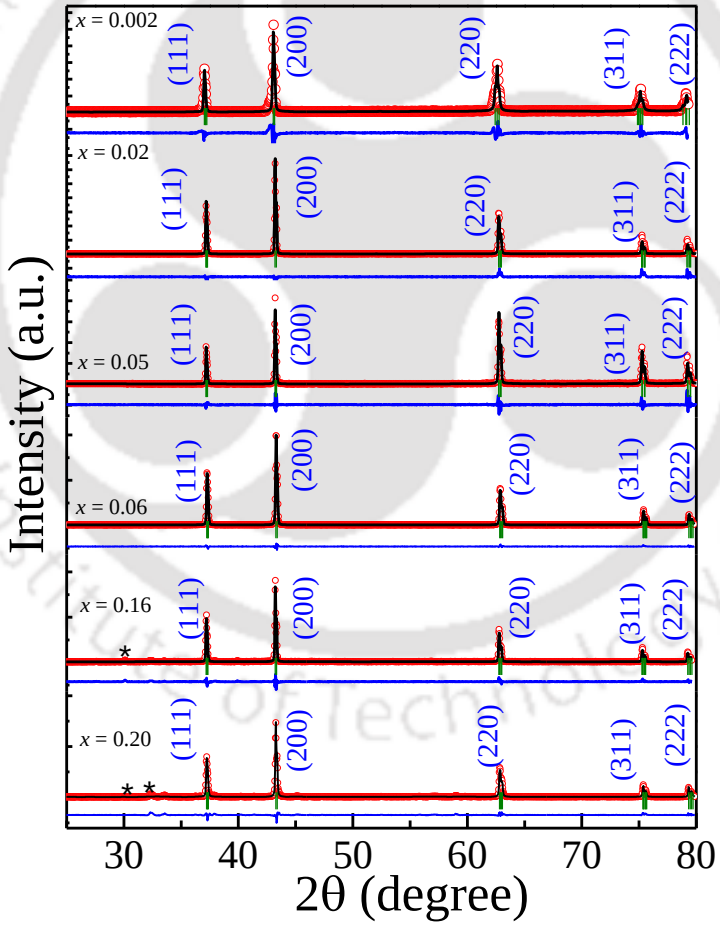

Figure 3.6: The X-ray diffraction patterns of $Ni_{1-x}Na_xO$ polycrystalline sample for compositions *x* lie between 0.002 and 0.20 together with the Rietveld refinement data.

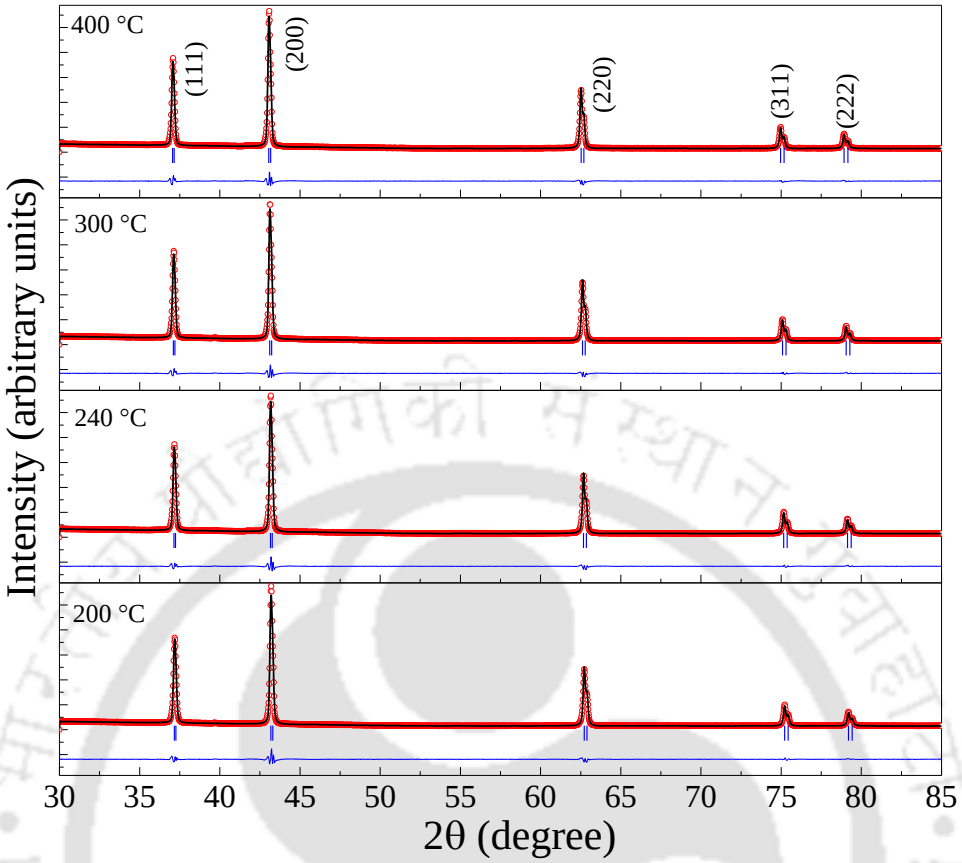

Figure 3.7: The X-ray diffraction pattern of the $Ni_{0.95}Ni_{0.05}O$ sample recorded at various temperatures between 200˚C and 400˚C together with the Rietveld refinement data.

temperatures exhibits jet black color (Inset-III of figure 3.5) due to limited availability of oxygen at higher temperatures. It is well known that green colored system exhibits insulating properties, while, the black color NiO samples show deficiency of Ni^{2+} ions often represented as $Ni_{0.98}O_{1.00}$ and behaves like a p-type semiconductor [122,139]. Based on the results obtained from the present investigations and existing literature results we speculate that all the investigated samples including pure NiO system contains excess oxygen content, which leads to a higher lattice distortion of 60º 8′ at 150˚C. These results are reproducible for the bulk grain size samples prepared using SSRM and SGP. Figure 3.6 shows the XRD pattern of various compositions of $Ni_{1-x}Na_xO$ which shows no significant alteration in the cubic symmetry of parent NiO (‘*a*’= 4.18 Å). However, for $x > 0.16$, an additional phase of NaO_2 (Space group: *Pa-3*) emerges out as secondary phase inside the $Ni_{1-x}Na_xO$ matrix. A slight shift of the peak positions towards lower Bragg’s angle was noticed with increase in the ‘Na’ doping concentration signifying the fact that lattice parameter decreases after the incorporation of Na at Ni sites. Figure 3.7 shows the temperature dependent XRD pattern together with Rietveld refinement of $Ni_{0.95}Na_{0.05}O$ measured across the Néel temperature of NiO to probe the structural distortion (if any present in the system). The corresponding lattice parameter ‘*a*’ and unit-cell volume ‘V_C’ are shown in the figure 3.8. Both the parameters ‘*a*’

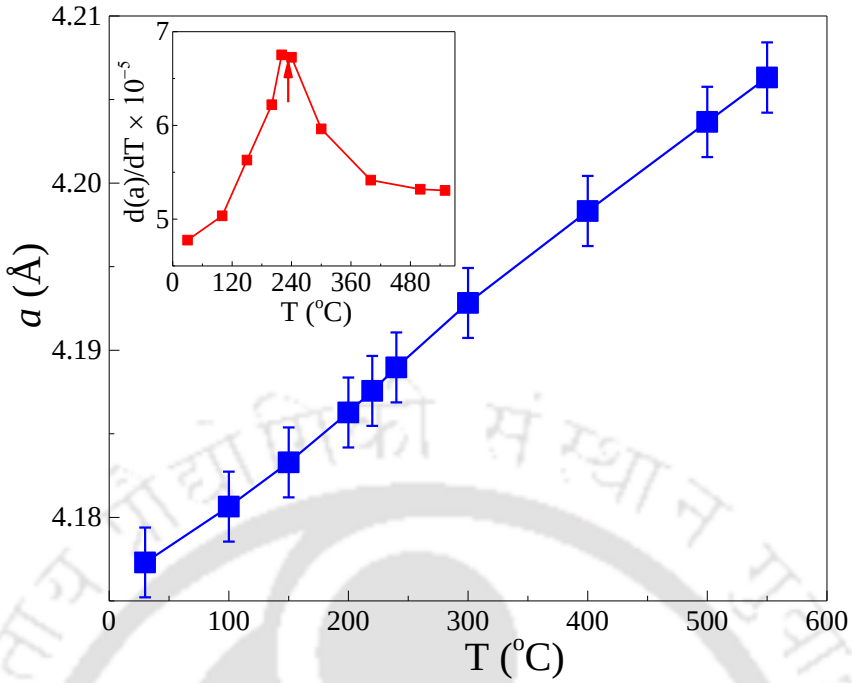

Figure 3.8: The temperature dependence of lattice parameter *a*(T) for $Ni_{0.95}Ni_{0.05}O$. The inset shows the temperature dependence of d(*a*)/dT.

and 'V_C' increases progressively with increase in temperature with a slight change in the slope of linear behavior of '*a*(T)' and 'V_C(T)'. To clearly probe such minute change, we have plotted the temperature derivative (d*a*/dT) (as shown in the inset of Figure 3.8). A kink was clearly notice across the T_N suggesting the changes occurring in the f.c.c. lattice of $Ni_{0.95}Na_{0.05}O$.

3.3.2 Local Atomic Environment using X-ray Photoelectron Spectroscopy:

The composition and chemical states of the investigated two-phase composites were analyzed by means of X-ray photoelectron spectroscopy (XPS). Figures 3.9 and 3.10 shows the XPS spectra of pure NiO and $Zn_{0.45}Ni_{0.55}O$/NiO composites sintered at 1200˚C, respectively. XPS spectra corresponding to O-1s, Ni-2p, and Zn-2p core levels of both NiO and $Zn_{0.45}Ni_{0.55}O$/NiO composites are calibrated by the binding energy of carbon C-1s orbitals located at 283.9 eV. These spectra are considered as the internal reference spectrum shown in figures 3.9a and 3.10a [140–142]. The presence of asymmetric behavior in two unresolved overlapping peaks of oxygen 1*s* spectrum indicates that oxygen exist in two chemical states in both the compounds which are associated with the surface and chemical bonds (indicated by arrows in both figure 3.9b and 3.10b). The Ni 2p spectrum shown in figure 3.9c for pure NiO contains a doublet whose binding energies are centered at 857.75 eV and 876.5 eV (shown by arrow marks) associated with the Ni $2p_{3/2}$ and Ni $2p_{1/2}$ states, respectively [140–144]. The binding energy difference between these two doublets is Δ ~ 18.75 eV with prominent two satellite peaks designated as S_1(~ 864.5 eV) and S_2(~ 883.25 eV) which suggest that the nickel present in the composites is not in the metallic form but as compound NiO [140]. If nickel exists in the form of individual metallic species, the binding energy

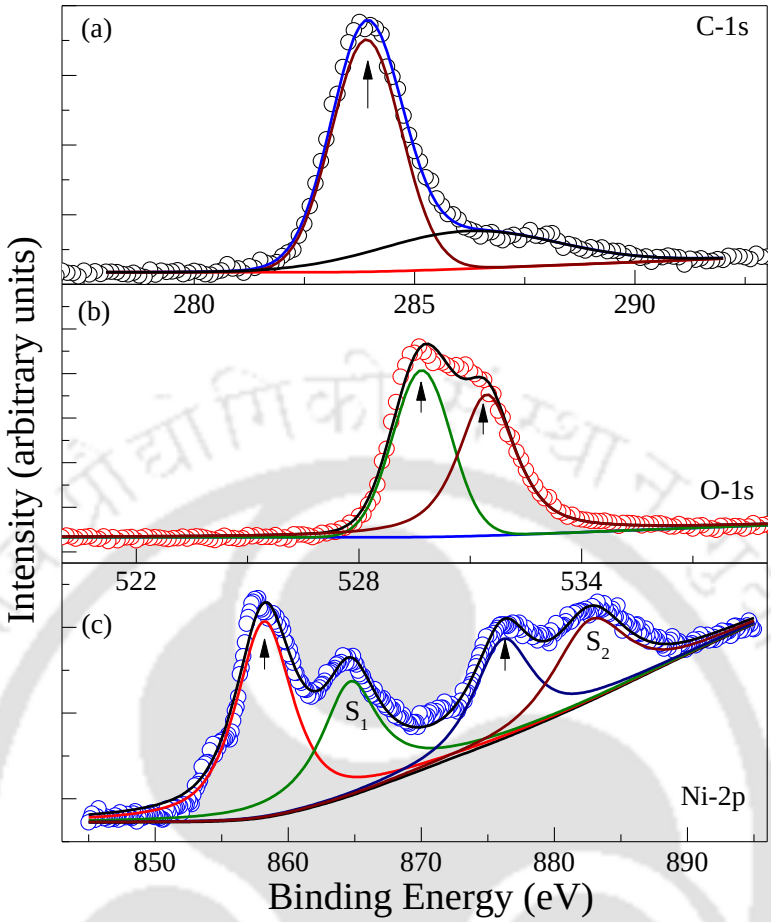

Figure 3.9: The X-ray photoelectron spectroscopic (XPS) graphs depicting the intensity of core level x-rays (counts per seconds) versus binding-energy(eV) of oxygen rich bulk grain-sized NiO sample. (b), (c) and (a) shows the core level X-ray intensity spectra of O-1s, and Ni-2p together with C-1s core level spectrum as standard calibrated spectrum. The peaks designated as S_1 and S_2 represents the satellite peaks of Ni-2p levels. The arrow marks show the center position of the peaks.

separation should be ~ 17.4 eV [140]. The Zn 2p spectra contains sharp and high symmetric peaks with binding energies centered at 1022.25 eV and 1045.50 eV as shown in figure 3.10c. This doublet is associated with the Zn $2p_{3/2}$ and Zn $2p_{1/2}$ core levels [140]. The difference between these two lines often characterized as the spin-orbit splitting parameter $\Delta \sim 23.2$ eV which confirms the +2 oxidation state of Zn. This value of 'Δ' matches well with the previously reported values of standard ZnO [143,144]. On the other hand, the core level XPS spectrum of Ni 2*p* for $Zn_{0.45}Ni_{0.55}O$ is shown in figure 3.10d. Two peaks are observed at 855.38 eV and 873.32 eV associated with the Ni $2p_{3/2}$ and Ni $2p_{1/2}$ lines, respectively. The binding energy separation between Ni $2p_{3/2}$ and Ni $2p_{1/2}$ lines is ~ 17.95 eV which is slightly less as compared to the 18 eV of stoichiometric NiO [140]. As described earlier if the nickel exists in pure metallic form the binding energy separation should be equivalent to 17.4 eV. From the above values, we conclude that nickel exists in divalent oxidation state within the core of $Zn_{0.45}Ni_{0.55}O$ system. These results are consistent with the previously observed binding energy separation ~ 18.75 eV for Ni 2*p* states in dilutely

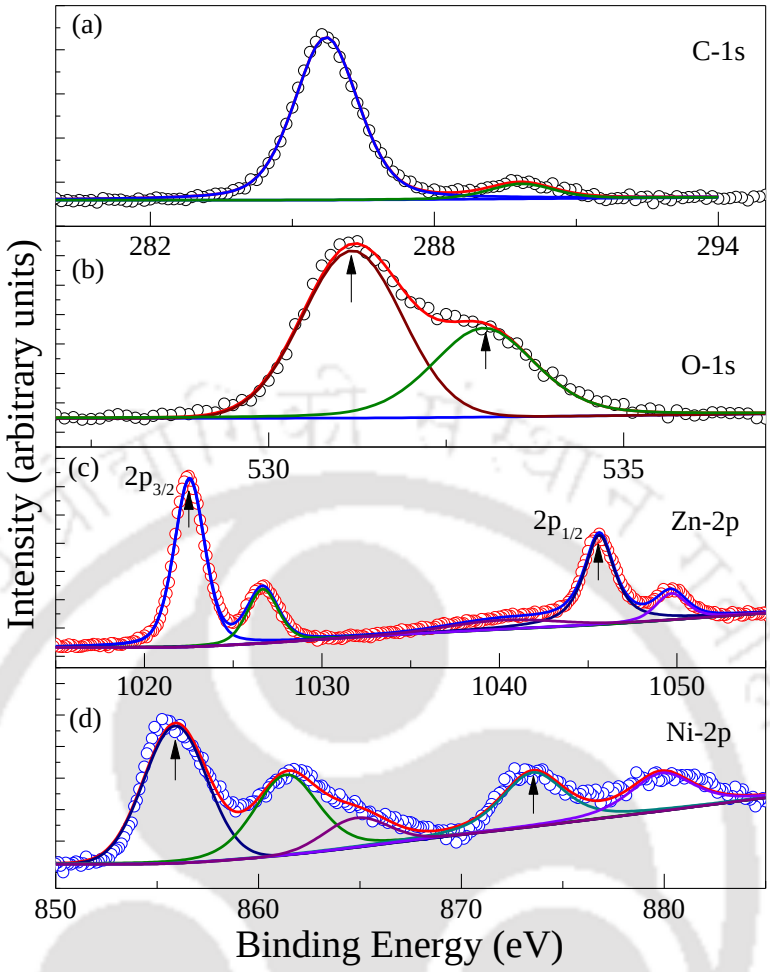

Figure 3.10: The X-ray photoelectron spectra of $Zn_{0.45}Ni_{0.55}O$ sample synthesized at sintering temperature 1200˚C for 12 hours in air. (a), (b), (c) and (d) shows the core level intensity of X-ray spectra of Zn-2p, O-1s, and Ni-2p together with C-1s core level spectrum as standard calibrated spectrum, respectively. The arrow marks show the peak center positions.

doping levels ($0 \geq x \geq 0.1$) [145,146]. Also, a slight shift in the peak positions of Ni 2*p* spectrum of $Zn_{0.45}Ni_{0.55}O$ is noticed as compared to pure NiO system discussed earlier (Figure 3.9c). The difference corresponding to the Ni $2p_{3/2}$ peak positions in NiO and $Zn_{0.45}Ni_{0.55}O$ is ~ 2.37 eV, whereas for Ni-$2p_{1/2}$ state the binding energy difference is ~ 3.18 eV. Such shift in the peak positions of the Ni-2*p* XPS spectrum between $Zn_{0.45}Ni_{0.55}O$ and pure NiO case is due to the different atomic environment faced by the Ni^{2+} ions when incorporated inside the ZnO matrix. Also, the shift in the satellite peaks of Ni-2*p* with increasing the 'Ni' composition within the ZnO matrix signifies the attenuation of nonlocal screening because of reduced site occupancy of two adjacent 'Zn' ions. Earlier studies by Matthea et al. [146] suggests that even the finite-size/or surface effects cannot lead to significant change in the characteristic peak positions of Ni 2*p* XPS spectra in nano-size crystal of NiO. Nevertheless, from the literature we noticed that a detailed study of the Ni-2*p* and O-1*s* spectra of hydroxyl ion contaminated NiO

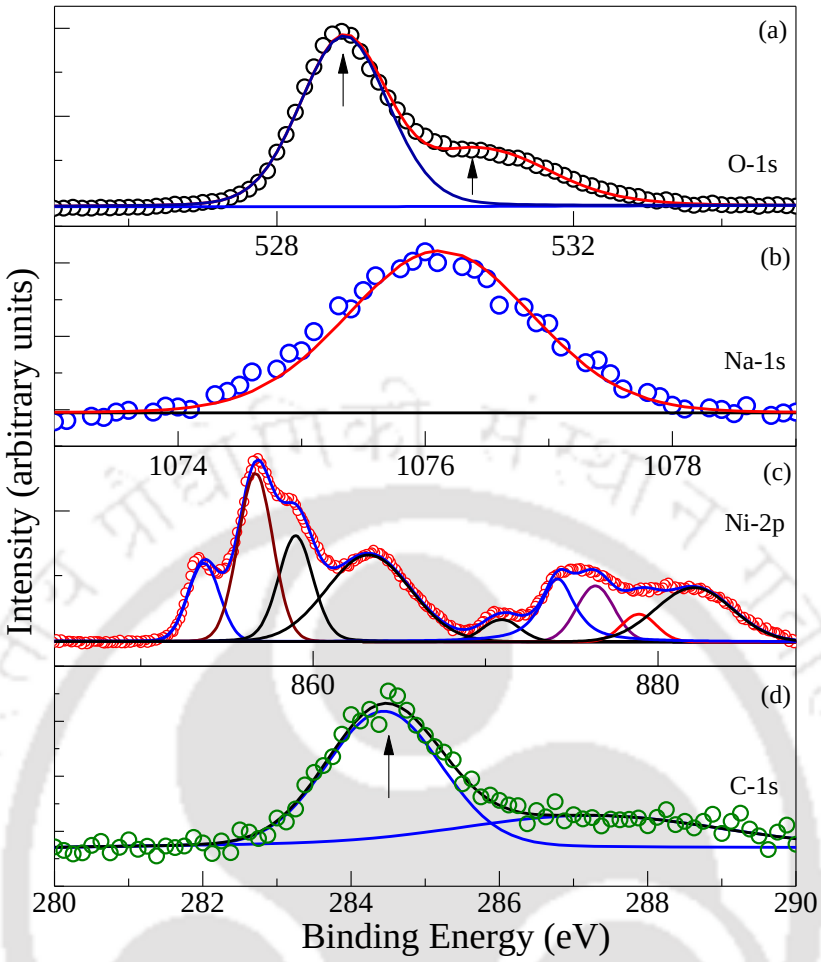

Figure 3.11: The X-ray photoelectron spectra of $Ni_{0.95}Na_{0.05}O$ sample. (a), (b), (c) and (d) shows the core level intensity of X-ray spectra of O-1s, Na-1s and Ni-2p together with C-1s core level spectrum as standard calibrated spectrum, respectively.

samples can cause some change in Ni-2*p* peak shape and position [146]. Gaskell *et. al*. performed the surface studies for $Ni_{1-x}Zn_xO$ solid solutions over a wide composition range using Auger and XPS measurements and noticed a measurable change in Ni-2*p* photoemission spectra with increasing the zinc content inside the NiO matrix [145].

Figure 3.11 shows the XPS spectra of $Ni_{0.95}Na_{0.05}O$ bulk sample. The O-1*s* spectra (figure 3.11a) resolved into three Gaussian-Lorentzian peaks centered at 528.9 eV and 530.76 eV signifying the presence of surface oxygen and chemically bonded oxygen. Whereas, the Na-1*s* core level photoelectron spectra exhibit single major peak at ~1076.12 eV signifying the presence of monovalent oxidation state of sodium (Na^+). On the other hand, the Ni-2*p* core level spectrum for $Ni_{0.95}Na_{0.05}O$ system (figure 3.11 c) exhibits a complex behavior as compared to pure NiO (figure 3.9 c). For $Ni_{0.95}Na_{0.05}O$, the Ni-2*p* XPS spectra were deconvoluted into nine peaks centered at 853.6 eV, 856.66 eV, 858.9 eV, 863.2 eV, 870.91 eV, 874.1 eV, 876.37 eV, 878.9 eV and 882.09 eV. These transitions as associated with the multiplet splitting effects and non-local screening of 'Ni^{2+}' by oxygen and sodium ions. The

binding energy separation between the doublets of Ni (Δ ~17.3 eV) signify the divalent oxidation state of Ni inside the core of $Ni_{0.95}Na_{0.05}O$ matrix. The different atomic environment faced by 'Ni' inside the core of $Ni_{1-x}Na_xO$ matrix also causes a significant shift of binding-energy towards the higher energy side of all the satellite peaks.

3.3.3 Dielectric Relaxation (Temperature and Frequency Dependent Studies):

Figure 3.12 shows temperature dependence of relative dielectric permittivity $\varepsilon_r(T)$ of the $Zn_{1-x}Ni_xO/NiO$ with various doping concentrations (x), measured at constant ac-driving frequency of 1 kHz. Very large values of ε_r ($\sim 10^3$) are observed in these composites, with an anomaly across the critical temperature $T^* \sim 257^\circ C$, though the anomaly at T^* strongly depends on the '*x*'. For samples with $x \geq 0.163$, the anomaly takes a broad cusp shape and gradually becomes a sharp peak centered at $T^* \sim 246^\circ C$ for $x = 0.025$. This behavior noticed in both $\varepsilon_r(T)$, and loss-tangent Tan (δ) versus T is similar to the typical ordered ferroelectric to disordered para-electric phase transition occurring at the ferroelectric Curie temperature $T_C \sim T^*$. Such a transition is highly susceptible to the frequency of the electric field, nickel doping concentration and sintering temperature. The possible origin of such transition could be due to the shrinkage of the lattice volume when the smaller ionic radius Ni^{2+}(0.69Å) ions occupy the tetrahedral sites of Zn^{2+} (which has larger ionic radius of ~ 0.74 Å), leading to permanent local electric dipoles [122]. Such difference in the ionic radii may disturb the hexagonal regularity of the unit-cell and causes off-centered symmetry, thereby resulting in ferroelectric behavior. Although pure zinc oxide is a polar crystal, it does not undergo any phase transition at atmospheric pressure. Reversing its polarization by applying an external electric field is difficult until it melts at 2248 K. The substitution of host Zn^{2+} by other ions may plays an important role in the appearance of ferroelectric ordering, although the driving mechanism of this phase transition is not well understood. The ferroelectricity in ZnO based systems is a well-established phenomenon, in which Zn^{2+} is substituted with either slightly lower or higher ionic radii elements. For example, systems like ZnO-Cr (0.73 Å), ZnO-Be (0.45 Å), and ZnO-Li (0.76 Å) exhibit weak ferroelectric behavior [131–133,147]. On the other hand, the Mg^{2+} ion ($ls^2 2s^2 2p^6$) substitution in ZnO play a different role as compared to the isoelectronic Li^+ and Be^{2+} ions ($1s^2$). Thus, the changes in electronic configuration play a more important role than the difference in the ionic radius. Nevertheless, this situation can be reversed at higher doping levels where the secondary phase of NiO becomes major product, surrounded by the grains of ZnO as a minor phase. In such heavily doped samples, we observed significant contribution of the crystallographic phase transition of NiO to the global dielectric behavior of $Zn_{1-x}Ni_xO/NiO$ composites. It is well known that nickel oxide exhibits rhombohedral (R3m) to cubic (Fm3m) structural phase transition, which is associated with the antiferro to paramagnetic Néel temperature T_N at 523 K [112]. The inset of figure 3.12 shows the variation of T^* as a function of composition together with the standard data of NiO. For dilute doping concentrations ($x < 0.05$), the critical transition T^*occurs ~ 25°C below the standard transition of defect-free NiO. Nevertheless, it is clearly evident from figure 3.12 that for higher compositions ($x >$ 0.16), where NiO exists as major phase, the ferroelectric Curie temperature approaches the antiferromagnetic Néel temperature, $T^*(T_C) \rightarrow T_N$. Across any such structural transition, the breakdown of translational symmetry causes

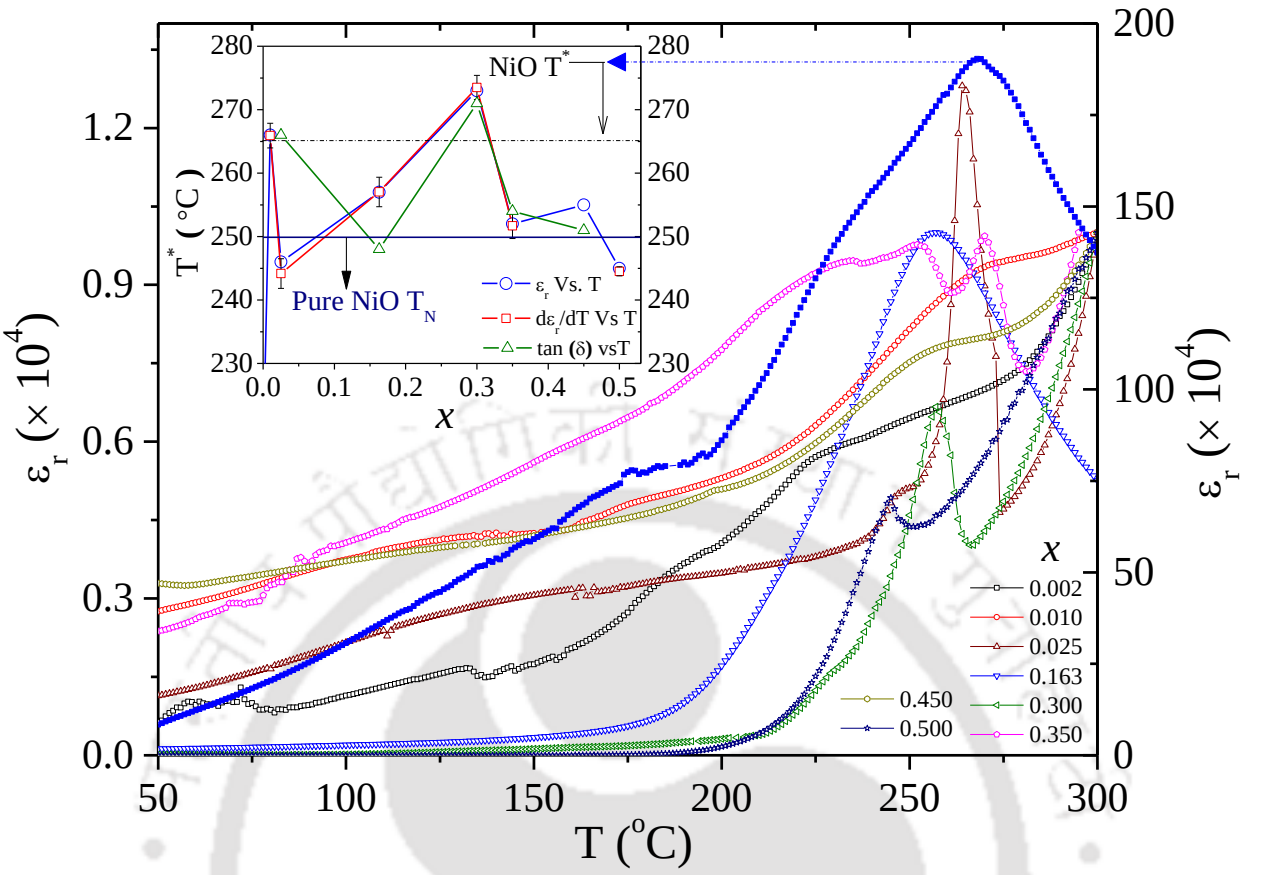

Figure 3.12: Temperature variation of relative dielectric permittivity $\varepsilon_r(T)$ of two-phase composite $Zn_{1-x}Ni_xO/NiO$ for various composition (x) in the range $0.002 \leq x \leq 0.5$ measured at 1 kHz. The inset shows the variation of critical temperature 'T^{*}' as a function of 'x' together with the data of pure NiO on the right-hand-side scale.

disordering in the system. At the same temperature the transverse optical lattice vibration ($\omega_t \neq 0$) becomes finite and the atoms are displaced along a specific crystallographic axis [148]. Under such unstable conditions (where the longitudinal optical phonon frequency ω_l approaches zero) in the non-cubic phase, the high frequency dielectric permittivity (ε_∞) reaches its maximum value, following the Lyddane-Sachs-Teller relation $\{(\varepsilon[0]\text{-}S')/\varepsilon[\infty]\} = (\omega_l / \omega_t)^2$, where S′ is the permanent dipole polarization, with $\varepsilon[0]$ and $\varepsilon[\infty]$ being static and high frequency dielectric permittivity, respectively [148,149]. A detailed descript of Lyddane-Sachs-Teller concept is given below.

In 1941, Lyddane, Sachs and Teller derive a relationship between the dielectric constants ($\varepsilon(0)$ and $\varepsilon(\infty)$) of a crystal and the long-wavelength (longitudinal ω_l and transverse ω_t) lattice frequencies which is given by the following relation [148–150]:

$$\frac{\epsilon(0)}{\epsilon(\infty)} = \frac{\omega_l^2}{\omega_t^2} \qquad (3.2)$$

This equation is popularly known as Lyddane-Sachs-Teller (LST) relation. It is interesting that the above relation is free from all the microscopic parameters such as effective charge and force constant. The LST relation has been

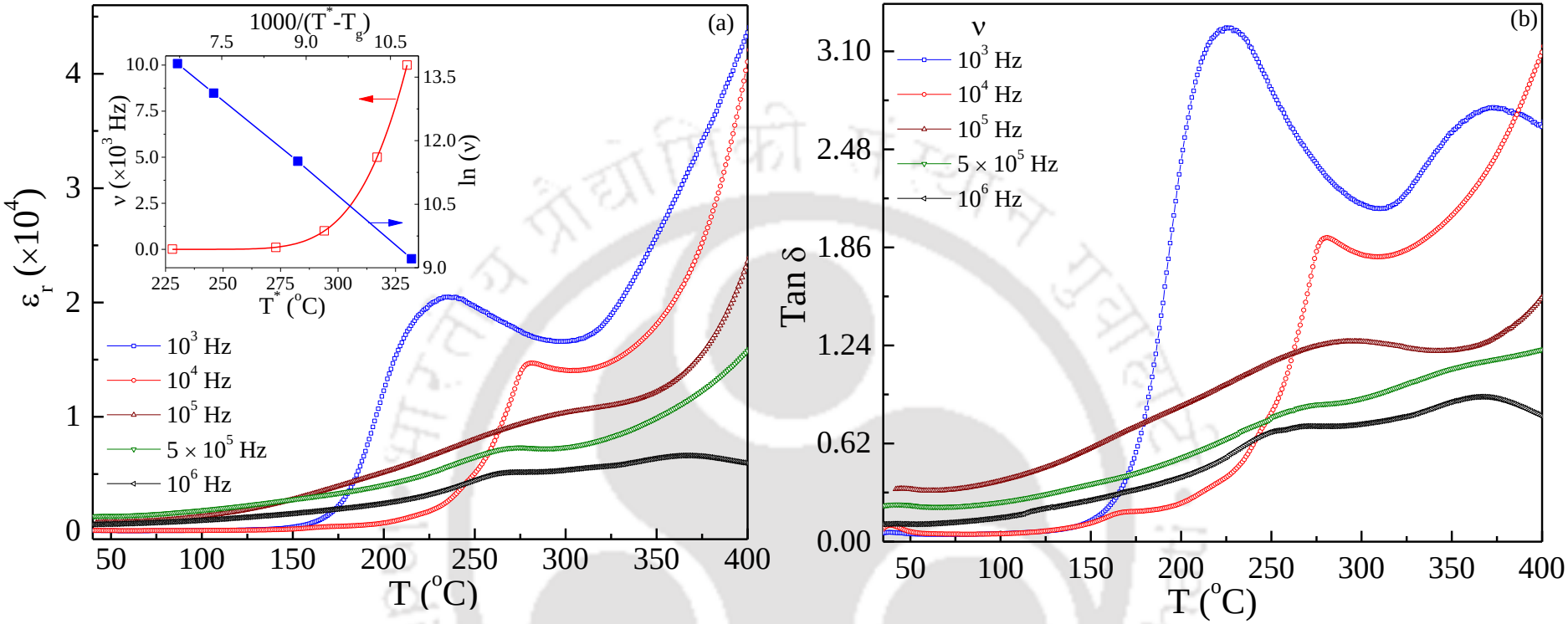

Figure 3.13: (a) Temperature dependence of the relative dielectric permittivity $\varepsilon_r(T)$ of the $Zn_{0.7}Ni_{0.3}O$/NiO pellets measured at various frequencies in the range 10^3-10^6 Hz. The open square symbols on the right hand side scale of the inset represents the frequency variation of transition temperature T^* and corresponding solid red line is the least-square fit to the Vogel–Fulcher law. The graph shown on the left hand side scale in the inset illustrates the linear dependence of ln(υ) on $1/(T^*- T_g)$. (b) Temperature dependence of the dissipation factor Tan(δ) for various frequencies of $Zn_{0.7}Ni_{0.3}O$/NiO.

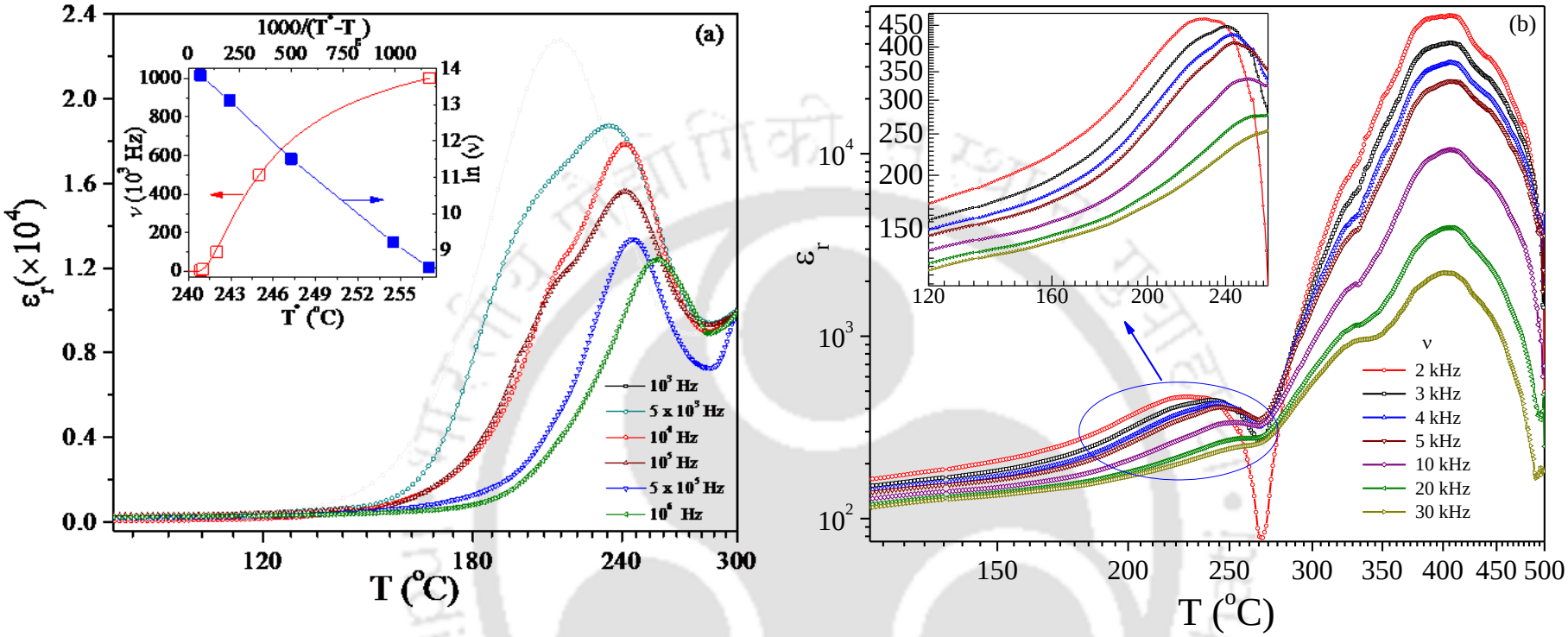

Figure 3.14: (a) The relative dielectric permittivity 'ε_r' versus temperature 'T' recorded at various frequencies between 10^3 Hz -10^6 Hz for the critical composition $x_C \sim 0.163$. The RHS scale of the inset shows the frequency variation of T^* and fit to the Vogel–Fulcher law. The LHS scale of the inset demonstrates the linear dependence of ln(υ) on $1/(T^*- T_g)$. (b) Temperature variation of 'ε_r' versus 'T' measured at various frequency between 2×10^3 Hz and 3×10^4 Hz of pure NiO pellet sintered at 1450˚C for 8 hrs in air.

widely used to explain the anomalous dielectric behavior of any ferroelectric system across the structural phase transition. During 1960, Cochran proposed the concept of mode-softening to elucidate the mechanism of ferroelectric structural phase transitions [148,151]. According to Cochran's model, whenever a crystal undergoes a structural phase transition, the crystal becomes unstable against a particular normal mode of lattice vibrational (Phonon) whose frequencies tend to zero. This phenomenon is termed as mode-softening [148,151]. The high temperature symmetrical-phase sustains some unstable-Phonons (often called as soft-mode) whose frequency tends towards to zero (softening of Phonon modes) as the temperature approaches the critical temperature T_C. Such softening of Phonon modes freezes the corresponding lattice vibrations and leads to a structural transition (from high- to low-symmetry crustal structure) with a finite dipole moment [148,151,152]. For order-disorder phase transition the crystal can be modeled by two sub-lattices: First sub-lattice consists of normal oscillators and the second sub-lattice comprises the random motion of particles. The random motion of particles in a sub-lattice can undergoes dielectric-relaxation process likely to be Debye-relaxation (discussed in Chapter 1, Section 1.3.4). Hence, it is important to consider such Debye relaxation modes in the LST relation. The contribution of total Polarization **P** of the crystal is now the sum of two sub-lattices: (*i*) $\mathbf{P_1}$ due to the electrons and atoms and (*ii*) $\mathbf{P_2}$ is due to the Brownian/random motion of the particles. Collectively, one can write the total Displacement vector as:

$$\boldsymbol{D} = \boldsymbol{E} + 4\pi\boldsymbol{P} = \boldsymbol{E} + 4\pi\boldsymbol{P_1} + 4\pi\boldsymbol{P_2} \tag{3.3}$$

and the corresponding dielectric permittivity can be written as:

$$\epsilon = \frac{\boldsymbol{D}}{\boldsymbol{E}} = \frac{4\pi\boldsymbol{P_1}}{\boldsymbol{E}} + \frac{4\pi\boldsymbol{P_2}}{\boldsymbol{E}} + 1 = \epsilon_d + \epsilon' \tag{3.4}$$

So, our total dielectric constant has two terms associated with the two sub-lattices *i.e.* First one associated with the normal oscillator and other with the Debye relaxation. Using the equations 1.12 and 1.13 the magnitude of ϵ_d can be written as:

$$\epsilon_d = \frac{4\pi\alpha N}{1-i\omega\tau} = \frac{1+2\beta}{1-\beta},\ \beta = \frac{4\pi}{3}\sum_i N_i\alpha_i \tag{3.5}$$

and the expression for ϵ' is:

$$\epsilon'(0) = \frac{1+2(\beta_{el}+\beta_{ion})}{1-(\beta_{el}+\beta_{ion})} \tag{3.6}$$

For high frequency, the ionic polarizability does not contribute:

$$\epsilon'(\infty) = \frac{1+2\beta_{el}}{1-\beta_{el}} \tag{3.7}$$

Substituting the values of $\epsilon'(0)$ and $\epsilon'(\infty)$ in LST relation:

$$\frac{\epsilon(0)}{\epsilon'(\infty)} = \frac{4\pi\alpha N}{\epsilon'(\infty)} + \frac{\omega_l^2}{\omega_t^2} \tag{3.8}$$

Alternatively, the above equation can be written in a more general way as given below:

$$\frac{\epsilon(0)-S'}{\epsilon'(\infty)} = \frac{\omega_l^2}{\omega_t^2} \qquad (3.9)$$

In this equation S' is the strength of the permanent dipole moments [148,149,151,153]. Across the ferroelectric transition, the suppression of long-range harmonic modes occurs and short-range anharmonic ordering takes place leading to the softening of optical phonon frequencies ($\omega_l \rightarrow 0$) [149]. Under these circumstances, the high frequency dielectric permittivity (ε_∞) attains its maximum value.

For dilute compositions, the transition looks like a weak anomaly, however, as '*x*' increases beyond 0.163, T^* increases rapidly. Such dielectric phase transition in Li or Cr doped ZnO with non-relaxor ferroelectric properties is well reported in the literature, which was associated with the relative translational shifts of Zn and O sub-lattices [154–158]. Both theoretical and experimental reports revealed that the extent of indirect interaction of dipoles, formed by off-center impurities (Li or Cr), via free charge carriers increases with increasing doping concentration. This interaction may cause significant increase in the transition temperature (320-500 K) with increasing doping concentration (5-15 mol %) in ZnO [154,155]. At room temperature, the static and high frequency relative dielectric permittivities of ZnO and NiO are $\varepsilon_r \sim 8.49$, $\varepsilon_\infty \sim 3.72$ and $\varepsilon_r \sim 11.75$, $\varepsilon_\infty \sim 5.7$, respectively [158]. Higher values of dielectric permittivity observed in the present case as compared with the above values can be ascribed to the fact that ferroelectric regions of Ni doped ZnO sites are surrounded by non-ferroelectric grains of NiO regions, similar to relaxor ferroelectrics. Another possibility is that an internal barrier layer capacitor (IBLC) mechanism associated with the Schottky barrier formation across the grain boundaries of the ceramic microstructure can also be responsible for the unusually high permittivities [159].

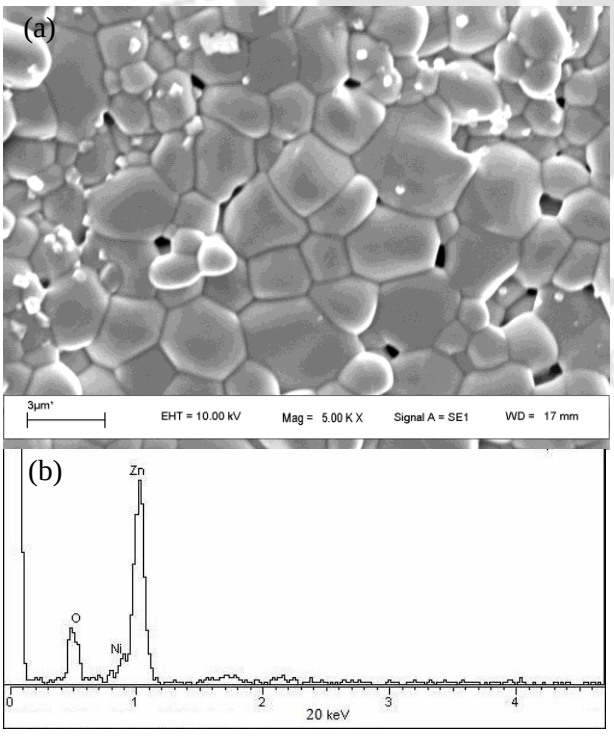

Figure 3.15: (a) The scanning electron micrograph of $Zn_{0.837}Ni_{0.163}O$/NiO pellet recorded under secondary electron mode, and (b) the corresponding energy dispersive X-ray analysis EDXA spectrum.

Figures 3.13 and 3.14 depict frequency dependent behavior of $\varepsilon_r(T)$ and Tan δ of the $Zn_{1-x}Ni_xO/NiO$ solid solutions for the samples with $x = 0.30$ and $x = 0.163$. These two compositions are chosen because the contribution of NiO to the overall dielectric behavior of the composite is expected to be significant. The figures 3.13 and 3.14 exhibit typical characteristics of a relaxor ferroelectric in which the temperature corresponding to the maximum value of $\varepsilon_r(T)$ shifts towards higher temperature side. For the sample with $x = 0.30$, the transition temperature T^* shifts from 228˚C to 330˚C, as the measuring frequency is increased from 10^3 Hz to 10^6 Hz. For the sample with $x = 0.163$, T^* shifts from 211˚C to 257˚C from $f = 10^3$ Hz to 10^6 Hz. For T < 150˚C, no significant changes in the $\varepsilon_r(T)$ has been noticed, however, beyond 175˚C, $\varepsilon_r(T)$ increases very sharply and becomes more diffusive at higher frequencies. It is well known that typical relaxor systems are incapable of carrying macroscopic polarization at temperatures significantly below the ordering temperature, but a local (rms) polarization has been identified to exist at much higher temperatures $T > T_C$ [160]. Numerous theoretical models have been proposed in the literature to elucidate the relaxor behavior [161], such as, super-paraelectric model (similar to super-paramagnetism), "dipolar-glass" model (like spin-glasses), and random field model [152,160–164]. The basic idea behind all these models is that the collapse of long-range dipolar interactions (due to compositional heterogeneity) results in the formation of ultrafine polar clusters [165]. The surface morphology obtained from the scanning electron microscope (SEM) (recorded under secondary electron mode) and its corresponding energy dispersive X-ray (EDX) spectrum for the $x_c \sim 0.163$ are shown in figure 3.15. This micrograph clearly reveals the formation of tiny polar clusters (as discussed above). The main impetus for compositional heterogeneity is believed to arise from a positional disorder due to occupancy of tetrahedral sites by Ni^{2+} ions, resulting in a locally varying ferroelectric transition temperature for various frequencies. As the nickel composition increases from 0.002 (dilute) to 0.163 (moderate), one can expect domination of long-range dipolar interactions in the solid solutions of $Zn_{1-x}Ni_xO_{Major}/NiO_{Minor}$ and yield typical ferroelectric behavior. However, for heavier doping levels ($x > 0.163$), the irregularities in the long-range dipolar interactions results in the formation of polar clusters.

The density of such polar clusters grows with the compositional disorder; as a consequence, relaxor behavior may appear. We analyzed the dynamic variation of the $\varepsilon_r(T)$ and the dispersion of the permittivity at temperatures close to T^* using the Vogel–Fulcher law given below:

$$\nu = \nu_0 \exp\left(-\frac{E_A}{k_B(T^* - T_g)}\right) \qquad (3.10)$$

In the above equation E_A is the activation energy, T^* is the critical temperature, T_g is the freezing temperature of the polarization function, k_B is the Boltzmann constant, and the pre-exponential factor 'ν_0' is known as the attempt frequency (it corresponds to the Debye relaxation frequency) [38]. The temperature dependence of the dynamic behavior of dipole reorientation in most relaxor ferroelectrics obeys Vogel–Fulcher law and this law is widely used to characterize the relaxor ferroelectrics [36,63]. The scattered open square symbols on the left-hand-side scale of the inset of figures 3.13a and 3.14a depicts the frequency variation of T^*. The connecting line is the

least-square fit of the Vogel–Fulcher equation, which is in good agreement with the experimental data. This analysis results in the following parameters, $\nu_0 = 1.33 \times 10^9$ Hz, $T_g = 181^{\circ}C$, $E_A = 0.11$ eV for $x \sim 0.30$, and $\nu_0 = 1.33 \times 10^6$Hz, $T_g = 240^{\circ}C$, $E_A = 0.023$ eV for $x \sim 0.16$. The linear behavior of ln(ν) versus $1000/(T^*-T_g)$ as shown in the right-hand side scale of inset of figures 3.13a and 3.14a further confirms the validity of the Vogel–Fulcher relation. Nonetheless, the attempt frequencies obtained in the present case are smaller as compared to the standard relaxor ferroelectrics like $K_{1-x}Li_xTaO_3$, $BaTiO_3$-$BaAlO_3$ or $(K_{1-x}Na_x)NbO_3$ [166–168]. Such standard relaxors exhibit ν_0 values as high as 10^9-10^{12} Hz. Lower values of ν_0 signify that the investigated composite system is a weakly coupled relaxor since none of the parent oxides are standard ferroelectrics. Such kind of systems does not exhibit the attempt frequencies as high as standard relaxor ferroelectrics as mentioned above. Very recently, Li et. al. reported low values of ν_0 (= 46×10^3 Hz) in ZnO-Co based dilute magnetic system [63]. Thus, one cannot expect attempt frequencies of the order 10^9-10^{12} Hz in such weakly coupled relaxor systems. Usually, the relaxor ferroelectrics are characterized by frequency dispersion of the complex susceptibility, where the temperature corresponding to the susceptibility maximum shifts to higher temperatures with increasing frequency. Vogel-Fulcher law is not the only criteria to judge relaxor behavior. The empirical scaling of dielectric permittivity peak in relaxor ferroelectrics can also be characterized by the scaling line deviation using the Uchino-Nomura's criteria as discussed below [169].

In the present case, temperature dependence of reciprocal dielectric permittivity $\varepsilon_r^{-1}(T)$ shows a straight line behavior indicating that the data is following the Curie–Weiss law for all temperatures $T > T_C$.

$$\frac{1}{\varepsilon_r} = \frac{T - T_C}{C} (T > T_C) \qquad (3.11)$$

Using this equation, we have calculated the Curie constant $C = 7.4\times10^5$ °C and 1.6×10^6 °C for $x = 0.163$ and 0.30, respectively for $f \sim 10^6$ Hz. Nevertheless, significant deviation from the Curie–Weiss behavior has been observed across 384°C, 282°C for $x = 0.30$ and 0.163, respectively. These values are close to the temperature at which local polarization sets in, and is often called Burns temperature (T_d). Usually, T_d increase progressively with increasing the measuring frequency [169,170]. Such deviation from the Curie-Weiss law is treated as a common signature of the relaxor ferroelectric behavior [36,171]. The difference between Burns and Curie temperatures $\Delta T_d = T_d - T_C$ is often treated as a characteristic parameter which represents the degree of deviation from high-temperature linearity. Usually, higher values of ΔT_d represent prompt development of randomly oriented local polarization clusters, resulting in enhanced relaxor behavior. In the present case $\Delta T_d = 105$, 103, 109 and 20°C for $\upsilon = 10^3$, 10^4, 5×10^5 and 10^6 Hz, respectively, for $x = 0.30$ and $\Delta T_d = 41$, 40, 37 and 25°C for $\upsilon = 10^4$, 10^5, 5×10^6 and 10^6Hz, respectively for $x = 0.163$. In general, the high-temperature slope of dielectric cusp is described by an empirical Lorenz-type relation [172], where the degree of diffuseness of peak is quantified by the parameter 'δ' (widely known as shape parameter):

$$\frac{\varepsilon_A}{\varepsilon_r} - 1 = \frac{(T - T_A)^2}{2\delta^2} \qquad (3.12)$$

In the above equation, the fitting parameters T_A and ε_A signify critical temperature and magnitude of relative permittivity across the Lorenz peak. For x = 0.163 and 0.30 the high-temperature slope of dielectric cusp fits well with the above-mentioned Lorenz-type relation. The calculated values of 'δ' from the fitting parameters are 23, 80, 29.92, and 39.73°C for $\upsilon = 10^4$, 10^5, 5×10^5 and 10^6Hz, respectively for x = 0.163 and δ =192, 33, 178, 88°C for $\upsilon = 10^3$, 10^4, 5×10^5 and 10^6 Hz, respectively for x = 0.30. In order to cross check the relaxor behavior alternatively, we have used Uchino and Nomura's criteria (or modified Curie-Weiss law) for the relaxor ferroelectrics, which is given by following equation [169]:

$$\frac{1}{\varepsilon} - \frac{1}{\varepsilon^*} = \frac{(T - T^*)^\gamma}{C} \qquad (3.13)$$

where 'C' is the Curie constant, 'γ' is a diffusion coefficient and 'ε^*' represents the maximum dielectric constant at T^*. For typical ferroelectrics, 'γ' should be approximately equal to unity. However, for relaxor systems 'γ' should range from 1-2. Figure 3.16 shows the log-log plot ($\log(1/\varepsilon - 1/\varepsilon^*)$ versus $\log(T-T^*)$) associated with equation-(3.13). The 'γ' values obtained from the slope of above plots are 1.77 and 1.91 for x = 0.16 and 0.30, respectively. These values lie within the range of typical relaxor systems. We did the same analysis for pure NiO system as well. Figure 3.14b shows ε_r versus T plot of NiO (for ν = 1 kHz-30 kHz) sintered at 1450˚C in air for 8 hrs. A giant and broad dielectric peak across 410±10˚C and an anomaly across 268˚C (designated as T_{NiO}^*) can be clearly noticed. Although the origin of dielectric peak across 410˚C is not fully understood, the anomaly across 268˚C is undoubtedly originating due to the symmetry-breaking structural disorderness, which in turn is associated with the magnetic ordering of the system T_N. Nevertheless, the difference between T_N values reported in pure NiO and the current experimental result is approximately +15 K and -40 K for $f \sim 10^6$ Hz and 10^4 Hz, respectively. Such difference may be ascribed to the presence of random fields, including local electric fields and elastic fields which hinder the long-range dipole arrangement [169].

Furthermore, we have studied the role of extrinsic origins like (*a*) sample-electrode contact impedance and (*b*) instrument related parasitic-series inductance/resistance effects on the observed relaxor-like behavior and giant dielectric permittivity of the current system. All the dielectric measurements in the present investigation have not shown any negative-capacitance effect at high temperatures. Normally, such negative-capacitance and sample-electrode contact impedance may cause an underestimation of the global dielectric behavior of the system. Therefore, the observed dielectric anomaly across T_N of NiO, together with the weakly coupled relaxor-like behavior in the ZnO/NiO two-phase composite system is not an artifact. Further evidence to the weak ferroelectric like behavior was obtained from the capacitance (C) versus voltage (V) measurements where an external dc-voltage (±5 V) superimposed with a small ac-signal of amplitude 0.1 V was applied across the capacitor geometry of the sample. The dc-voltage was swept from positive to negative bias and reached back to the initial value sim-

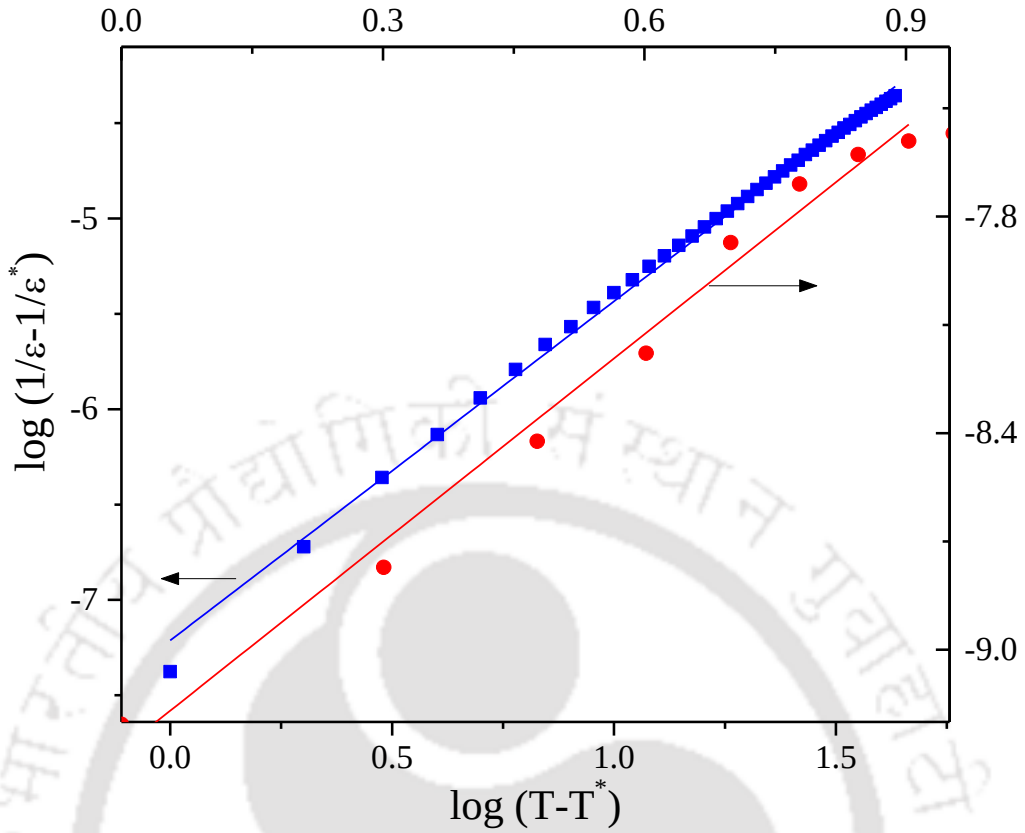

Figure 3.16: Logarithmic variation of the difference in reciprocal value of relative dielectric permittivity, log(1/ε-1/ε*) as a function of log(T-T*) for two composition x ~ 0.163 (red) and x ~ 0.30 (blue) of $Zn_{1-x}Ni_xO$/NiO. The solid line represents the modified Curie-Weiss law fitting to the experimental data.

-ilar to a complete hysteresis cycle. Figure 3.17 shows the C-V characteristics of $Zn_{0.65}Ni_{0.35}O$/NiO measured at different frequencies of the ac-signal at room temperature. These curves resemble the butterfly-shape hysteresis loops, which clearly indicate the presence of ferroelectric nature with domain switching behavior of the investigated system. Also, one can clearly notice the voltage shift in the maxima of the capacitance value due to polarization. On the other hand, incorporation of Na inside NiO matrix did not show any relaxor behavior, instead the magnitude and location of the dielectric transitions are different as that of undoped NiO. Figure 3.18 (a-c) shows ε_r(T) for the three different 'Na' doping concentration x = 0.02, 0.16 and 0.20, respectively, measured using Impedance-Analyzer from Solatron with Model No SI1260 between the frequencies 100 Hz and 20 MHz. All these samples show very large value of ε_r (~ 10^2 for moderate doping concentrations $x \leq 0.16$) at f ~ 1-10 *k*Hz at 300K. It is interesting to observe that ε_r(T) exhibit two major transitions at 258°C and 310°C. The first transition is due to antiferromagnetic to paramagnetic transition accompanied by the structural distortion from rhombohedral to cubic. Interestingly, this hump smears-out with increase in 'Na' concentration in NiO. The second transition is due to the diffusion of Na inside the NiO.

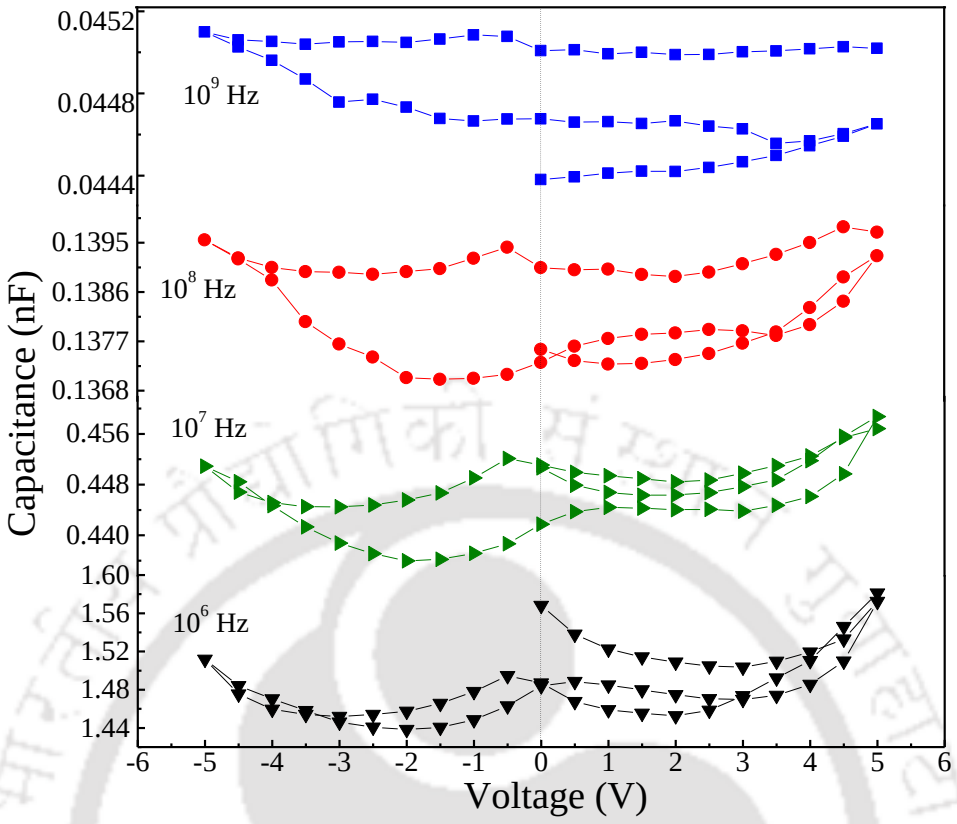

Figure 3.17: Capacitance-voltage (C-V) characteristics of $Zn_{0.65}Ni_{0.35}O$/NiO pellet measured at various frequencies between 10^6 and 10^9 Hz at room temperature.

3.3.4 Temperature Dependence of ac-Resistivity:

Figure 3.19 shows the temperature dependence of ac-resistivity of various compositions of $Zn_{1-x}Ni_xO$ including pure NiO measured at constant ac-frequency $f = 10^6$ Hz. All the plots depict a gradual decrease in the resistivity value as the temperature is increases from 20ºC to 400ºC with weak anomaly across 255ºC close to orthorhombic to cubic structure phase transition of NiO which exits as secondary phase in the $Zn_{1-x}Ni_xO$ matrix (the vertical dotted line shows the position of transition). The formation of localized energy states due to the distorted bond angles, defect-centers and impurities contributes significantly to such changes of resistivity [173,174]. Figure 3.20 shows the logarithmic variation of ρ_{ac} as a function of $1/T^{1/4}$ corresponding to the data shown in figure 3.19. Nearly linear behavior has been observed in all the graphs providing the signature of variable-range-hopping of the charge carriers following the equation $\rho = \rho_o \exp\left(\frac{T_o}{T}\right)^{1/4}$ where the parameter 'ρ_o' is known as pre-exponent factor and 'T_o' is the characteristic temperature coefficient [175]. Both the parameters ρ_o and T_o were extracted from the slopes and intercepts of figure 3.20 for different compositions. Generally, the variation of exponential factor in the above equation decides the nature of hopping process [173,176,177]. For the variable-range-hopping of charge carriers the exponential value should be equivalent to 1/4. In order to confirm this behavior, we plotted the double logarithmic graphs of $[\rho/\rho_o]$ as a function of ln(T), as shown in the

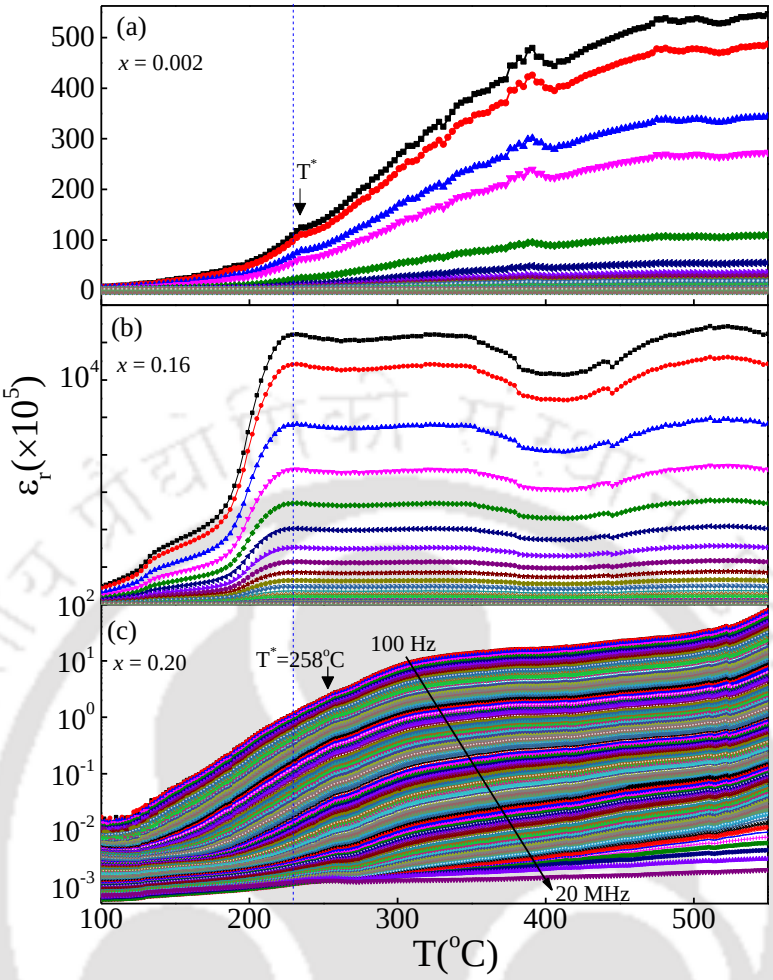

Figure 3.18: Temperature dependent relative dielectric permittivity $\varepsilon_r(T)$ of $Ni_{1-x}Na_xO$ system for (a) x=0.002, *(b)* x=0.16 and *(c)* x=0.2 measured at various frequencies between 100 Hz and 20 MHz.

figure 3.21 for three different compositions of $Zn_{1-x}Ni_xO/NiO$ ($0.163 \leq x \leq 1$) system. The slope values obtained from $\ln(\ln[\rho/\rho_o])$ versus $\ln[T]$ plots lies between -0.250 and -0.249 for all the three compositions. These values are close to -1/4 confirming that the localized charge transport is through the variable-range-hopping (VRH) of the charge carriers in all the samples. Figure 3.22 shows the $\ln(\ln[\rho/\rho_o])$ as a function of $\ln(T)$ for pure NiO sample sintered at 1450ºC. Three different temperature regimes was identified where a straight-line behavior was obtained with slopes -0.250, -0.246 and -0.253 for low temperature regime (100 ºC <T < 250ºC), intermediate temperature (250ºC< T <270ºC), and high temperature regimes (T > 300ºC), respectively. Thus, it is clear from these slope values that as the temperature increases the charge transport mechanism shows slight deviation from the VRH behavior. At exceedingly higher Ni substitution, the composite system (ZnO_{Minor}/NiO_{Major}) is expected to carry nearly stoichiometric nickel oxide $Ni_{1-\Delta}O$, ($\Delta \rightarrow 0$). This dominates the conventional conduction mechanism instead of the defects driven conductivity that usually appears in the cation deficient system $Ni_{1-\Delta}O$, ($\Delta \neq 0$) [178,179]. We expect that such cation deficient system $Ni_{1-\Delta}O$ may form at either low '*x*' values or at high

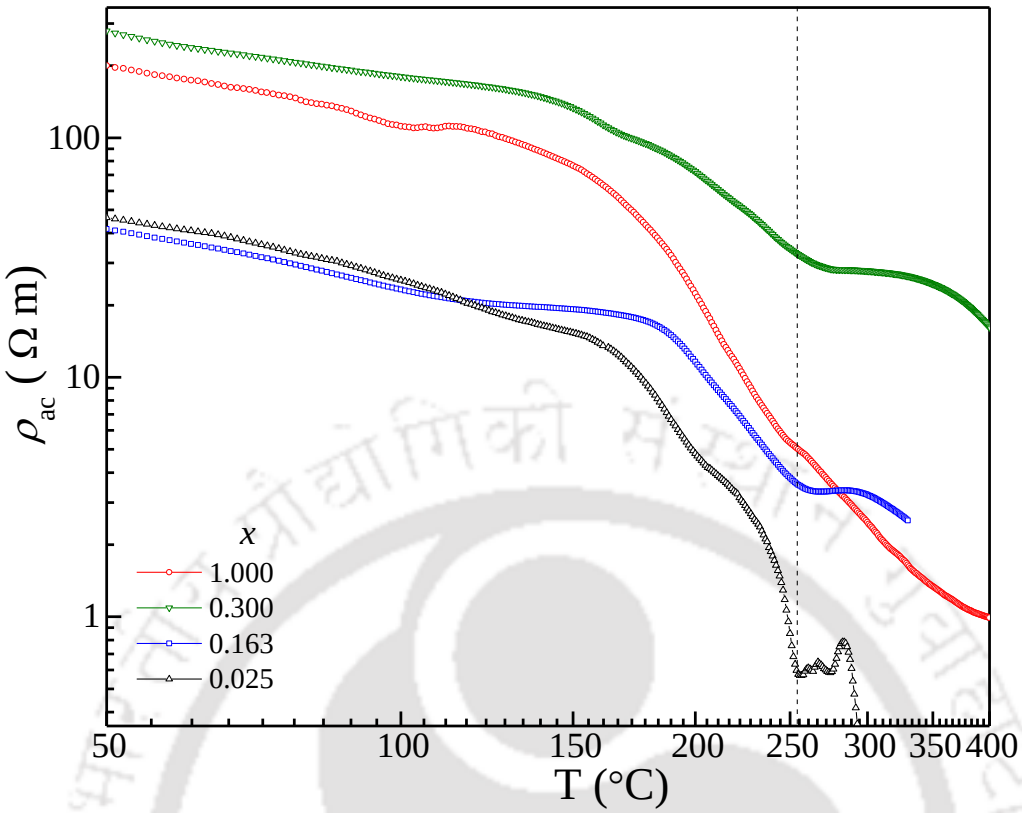

Figure 3.19: The temperature dependence of ac-resistivity $\rho_{ac}(T)$ of $Zn_{1-x}Ni_xO$ ($0.025 \leq x \leq 0.300$) and pure NiO sintered pellets measured at 1 MHz constant ac-frequency.

sintering temperatures. Typically, perfect stoichiometric NiO crystal exhibits higher order of resistivity values ($\rho \sim 10^{13}$ Ω cm) at room temperature [180]. However, in the present case we observed nearly nine-fold drop in the resistivity as compared to the above values in pure NiO system measured at room temperature [180]. Such decrease in the resistivity value could be attributed to the formation of oxygen vacancies at higher sintering temperatures (~ 1450 ºC for 24 hours) leading to the deviation from stoichiometry [181,182]. Therefore, the samples grown by the low-temperature processes exhibits fewer vacancies then those sintered at higher temperatures [180–182]. It is well known that NiO can be pale apple green or jet black depending up on the stoichiometry (Δ). The green color compound corresponds to the 1:1 composition of NiO and act as perfect insulator, while the black material has deficiency of Ni^{2+} ions often represented as $Ni_{0.98}O_{1.00}$, which behaves like a p-type semiconductor [183,184].

3.3.4.1 Concept of Polarons:

Landau first proposed the concept of 'polaron' in 1933 to describe the conduction of electrons/holes in polar compounds [185]. In a polar/ionic system, the Coulombic interaction between conduction electron/hole and lattice ions leads to a strong electron-phonon coupling. This interaction results a cloud of virtual phonon around the electron/hole and is known as polaron [51,185,186]. Figure 3.24 shows the schematic representation of a

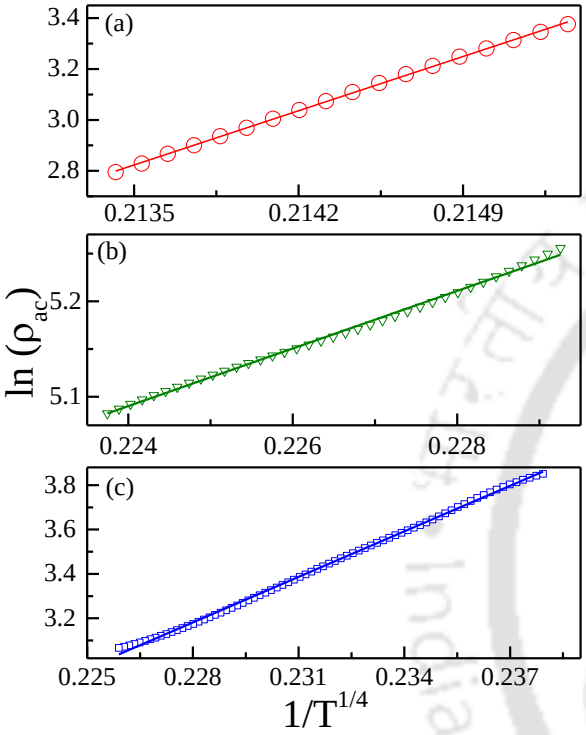

Figure 3.20: The logarithmic dependence of ac-resistivity ($\ln(\rho_{ac})$ versus $T^{-1/4}$) of $Zn_{1-x}Ni_xO$ for the compositions (a) x =1.00, (b) x = 0.300 and (c) x=0.163.

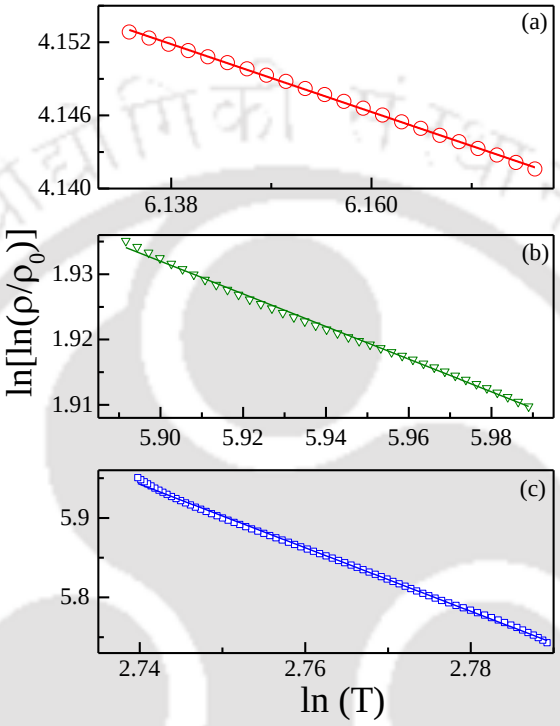

Figure 3.21: The double logarithmic variation of ρ/ρ_o (*i.e.* $\ln[\ln(\rho/\rho_o)]$) versus ln(T) of $Zn_{1-x}Ni_xO$ pellets for (a) x = 1.00, (b) x = 0.300 and (c) x=0.163.

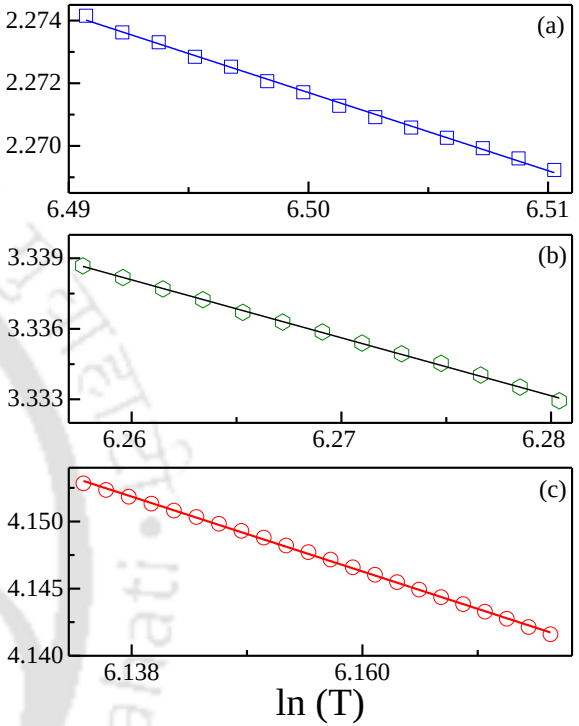

Figure 3.22: The $\ln[\ln(\rho/\rho_o)]$ versus ln(T) plots at three different temperature regimes: (a) high temperature regimes (T>300°C), (b) intermediate temperature regime (250°C<T<270°C) and (c) low temperature regime (100°C<T<250°C) of a pure NiO sample sintered at 1450°C.

polaron (electron polaron), where electron attracts the nearby positive ions and repels the negative ions, which generates a self-induced polarization ($\boldsymbol{P_e}$). Conventional polarons (electron or hole polarons) result from the interaction of electrons with longitudinal-optical (LO) phonons. Apart from the conventional polarons there are number of other quasiparticle polarons such as spin-polaron, which originates due to the electron and atomic magnetic moment interaction, and piezo-polaron due to the electron and acoustic phonons interactions [51,185,186]. Depending upon the radius of a polaron we can further classify the polarons into two types: (*a*) *Large polarons* and (*b*) *Small polarons*. If the radius of a polaron is significantly larger than the lattice parameter of the material then such polaron is known as large-polaron, also called as Fröhlich polaron [51,185,186]. Generally, the strength of the electron-phonon interaction is expressed by a dimensionless coupling constant 'α' which is introduced by Fröhlich as follow [51,185–187]:

$$\alpha = \frac{e^2}{\hbar c}\sqrt{\frac{m_b c^2}{2\hbar\omega_{LO}}}\left(\frac{1}{\epsilon(\infty)} - \frac{1}{\epsilon(0)}\right) \qquad (3.14)$$

In the above equation the parameter ε(0) represents the static dielectric constant, ε(∞) is high-frequency dielectric constant, m_b is the effective band mass of the charge carrier, and ω_{LO} is the LO phonon angular frequency. The polaronic effects are significant when $\alpha \geq 1$, because, the value of α is generally about double that of total number of phonons in the phonon cloud of a given electron. For semiconducting materials, the value of α lies in the range 0.3-0.5. With increase in the ionic and dipolar nature of the system, the α value increases significantly. For example, alkali halides exhibit the value of α between 2 and 4, and the famous high-κ system Strontium-Titanate $SrTiO_3$ shows α value as high as 4.5. The wave functions for large polarons are widely distributed over the lattices. According to the Feynman reduced mass approximation for the polaron, the α value is related to the effective mass of the polaron which is given by the following equation:

$$m^* \approx m_b\left(1 + \frac{\alpha}{6}\right) \quad for\ \alpha \ll 1 \qquad (3.15)$$

$$m^* \approx m_b(0.02\,\alpha^4) \quad for\ \alpha \gg 1 \qquad (3.16)$$

Hence the effective mass of a polaron m^* is higher than the band mass of the electron. Such large m^* leads to a large inertia as electrons drag the lattice distortion, and they collectively move inside the crystal. On the other hand, if the radius of a polaron is comparable to the lattice parameter of the material then such polaron is known as small-polaron. In small polarons (or discrete-polarons), the confinement of an electron is within one unit-cell dimension because of the shape and strength of the effective potential-well of the crystal lattice. In this case, the polaron binding energy E_p is higher than the half-band-width (D) of the electron band and leads to a strong-coupling regime, $\lambda = (E_p/D) > 1$. Thus, in general the small polaron band in a crystal is exceptionally narrow. The transport of a small polaron in an ideal crystal from site to site mainly occurs via two different processes; (*i*) Tunneling of a small-polaron between neighboring sites with no change in the phonon-population, and (*ii*) Tunneling of a small-polaron between the adjacent sites with change in the phonon-population [188,189]. Small-polarons generally follow the thermally activated hopping process, which is related to the drift-mobility and Hall-

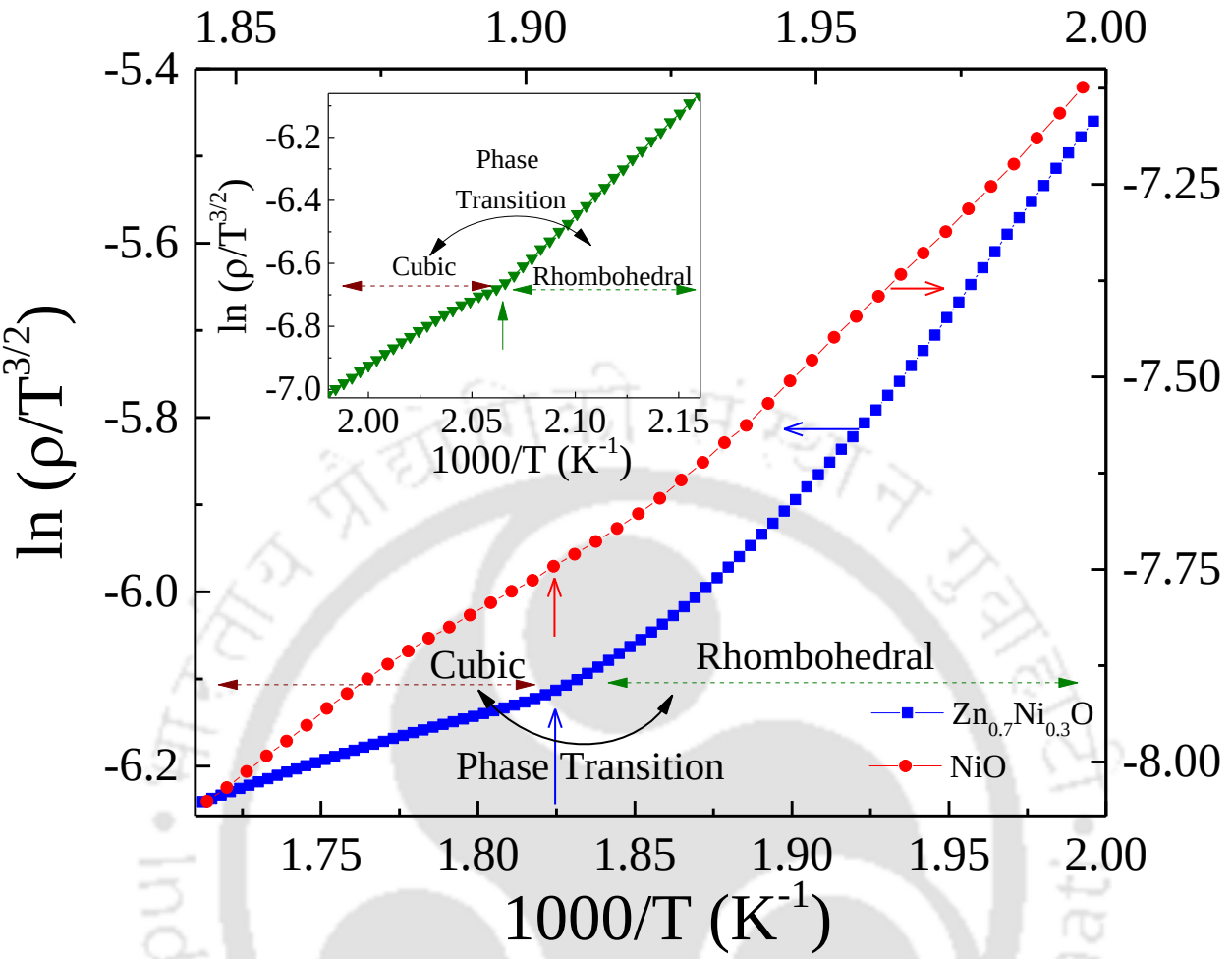

Figure 3.23: ln ($\rho/T^{3/2}$) versus 1000/T plots of $Zn_{0.7}Ni_{0.3}O$ and pure NiO sintered pellets measured at 1 MHz constant ac-frequency. The inset shows ln ($\rho/T^{3/2}$) versus 1000/T plot for $Zn_{83.7}Ni_{16.3}O$. The vertical arrow marks indicate Rhombohedral to Cubic phase transition across T_N (= 523 K) of pure NiO.

-mobility, under some approximations, which is expressed by the Arrhenius law, as given below:

$$\mu_{drift} \propto T^{-1} exp\left(-\frac{E_a}{k_B T}\right) \quad (3.17)$$

$$\mu_{Hall} \propto T^{-\frac{1}{2}} exp\left(-\frac{E_a}{3\,k_B T}\right) \quad (3.18)$$

In the above equations the activation energy $E_a = E_P/2$. According to the theory of small-polaron transport, a distinction is made between adiabatic hopping and anti-adiabatic hopping. In adiabatic hopping, an electron relaxes at all times (takes transition) within the potential-well created by its own lattice-distortion. In anti-adiabatic hopping, electron jumps out of the potential-well, and then the lattice moves to equilibrate with the electron's new position. However, in reality the behavior is always somewhere between these two extremes.

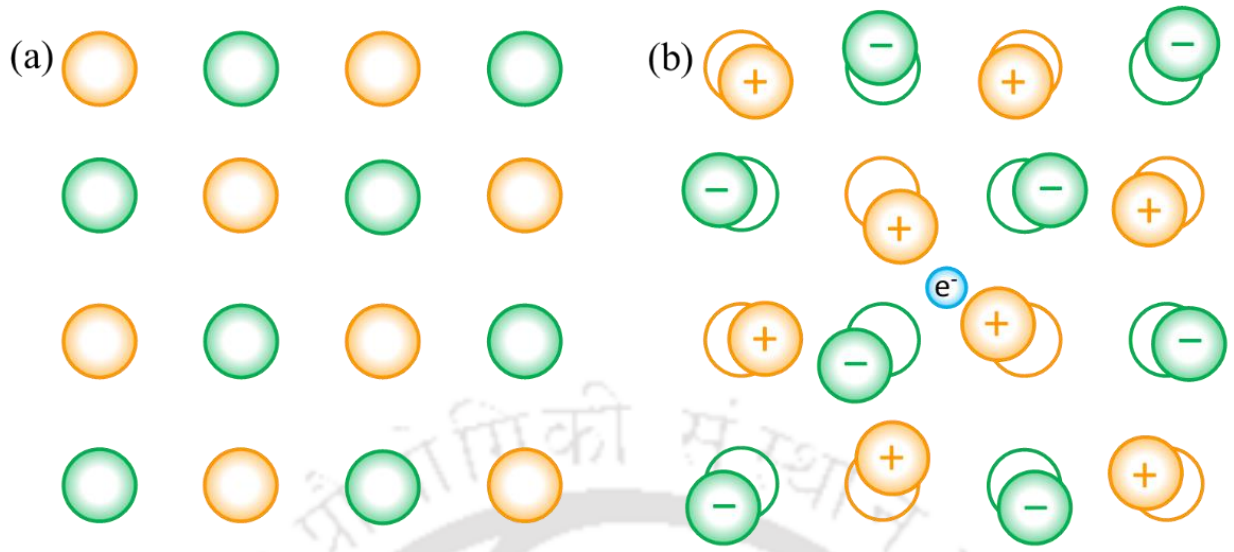

Figure 3.24: Schematic diagram of polaron (electron) formation [51, 185].

3.3.4.2 Activation energy and Exchange Constant:

For higher compositions major quantity of NiO phase formation is expected along with $Zn_{1-x}Ni_xO$ as minor phase, therefore one can expect that the conduction mechanism may get dominated by the naturally formed p-type nickel oxide [179,190–192]. Also, at very high sintering temperatures the cation deficiency generally causes the formation of holes [180,193–195]. These holes are freed on the expenditure of dissociation energy 'ε_d' and possibly will drift to a more distant cation, there by converting the latter to Ni^{3+} [185,196–198]. Such charge carrier transfer rate from one site to the next is determined by immediate surroundings of the localized carriers and phonon excitations [185,196,199]. On the basis of the earlier work by Holstein [200], Emin [201,202], Austin [186], Mott and Keem [176,199], we have estimated the average hopping activation energy 'ε_h' using the slope and intercepts of $\ln(\rho/T^{3/2})$ versus $1000/T$ (K^{-1}) fitting the experimental data to the following expression (as shown in figure 3.24):

$$\rho(T) = \frac{\hbar k T}{\Delta N_C e^2 a^2 \sqrt{\pi}} \left\{ \frac{(4\varepsilon_b k_B T)^{\frac{1}{2}}}{\varphi^2} \right\} \exp\left[\frac{\varepsilon_d + \varepsilon_h(T)}{k_B T} \right], \qquad (3.19)$$

where 'ε_b' is the small polaron binding energy which takes care of the contribution from lattice and electronic energies and is equivalent to ~ $A^2/2M\,\omega^2(T)$. Here 'A' is the electron-lattice coupling constant, 'M' being the effective ionic mass, and '$\omega(T)$' is lattice vibrational frequency. All the other parameters being (*i*) 'a' is the jump distance, (*ii*) 'ΔN_C' is vacancy concentration of Ni^{++} ions corrected for compensating centers, (*iii*) 'φ' is the transfer integral corresponding to Ni^{2+}-O-Ni^{3+}, and (*iv*) 'k_B' is the Boltzmann constant. Using the temperature variation of Seebeck coefficient 'α' in units 2.303 k_B/e we have estimated the value of dissociation energy $\varepsilon_d \sim 0.2$ eV. By substituting the ε_d value in equation (3.19) one can roughly estimate the behavior of '$\varepsilon_h(T)$' [181].

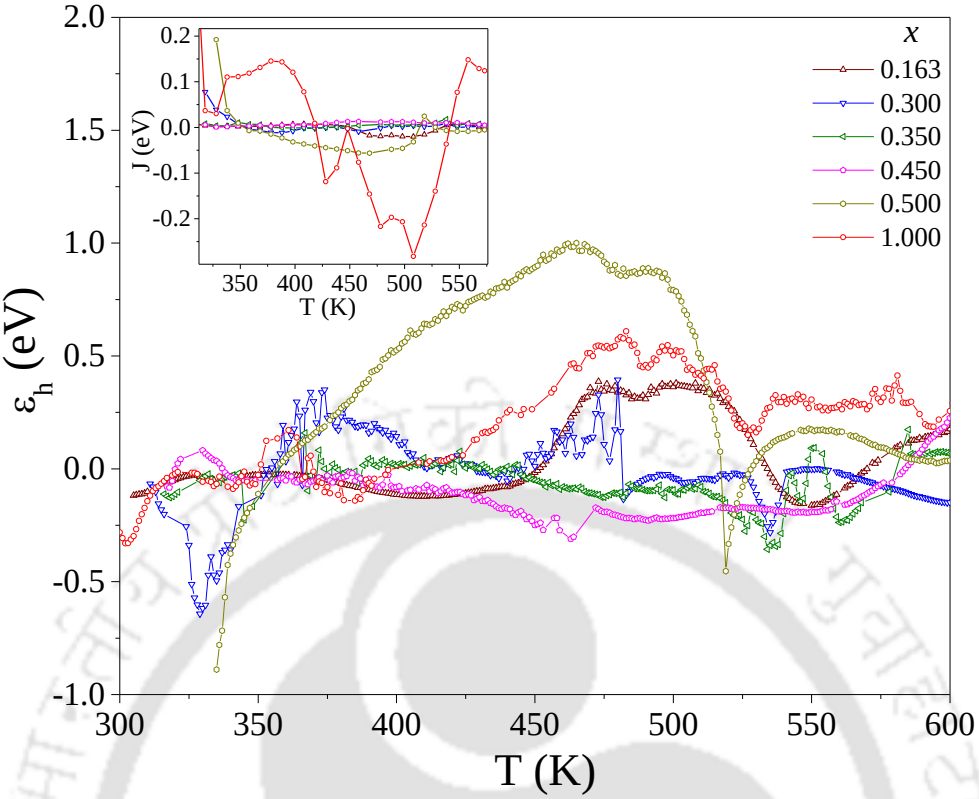

Figure 3.25: Temperature dependence of hole activation energy $\varepsilon_h(T)$ of $Zn_{1-x}Ni_xO$/NiO for various composition between x = 0.163 and 0.50, and pure NiO system. The inset depicts temperature variation of nearest-neighbor exchange coupling parameter $J(T)$.

Figure 3.25 shows the temperature variation of the hole activation energy '$\varepsilon_h(T)$' for various compositions of $Zn_{1-x}Ni_xO$/NiO systems. Clear anomalies are observed across the antiferromagnetic to paramagnetic transition temperature T_N in both the plots $\ln(\rho/T^{3/2})$ versus $1000/T$ (K^{-1}) and 'ε_h' versus 'T' for both $Zn_{1-x}Ni_xO$/NiO two phase composite as well as NiO system. It is well known that pure NiO exhibits a crystallographic phase transition from rhombohedral (R-3m) to cubic (Fm-3m) phase associated with the antiferromagnetic to paramagnetic transition across 523 K (Néel temperature T_N) [203]. The temperature variation of ε_h shown in figure 3.25 also suggests that the activation energy for polaron hoping around Ni centers in ZnO ($x < 0.10$) is almost comparable for the case of cation deficient $Ni_{1-\Delta}O$ ($\Delta \neq 0$) system. But, for larger values of 'x' the magnitude of 'ε_h' across 'T_N' are more than two orders higher than the values reported by Adler, and Austin for the case of stoichiometric nickel oxide ($Ni_{1-\Delta}O$, $\Delta \rightarrow 0$) [72,71]. Following the analysis of Keem et al. [199,204] the localized charge carrier hopping energy at a particular site can be determined by considering the energies of both lattice (ε_L) and magnetic (ε_m) contributions separately at a given temperature using the equation:

$$\varepsilon_h(T) = \frac{\varepsilon_b}{2} + \varepsilon_m(0) - \varepsilon_m(T) = \frac{\varepsilon_b}{2} + \sum_j{}' J_{ij}\left\{\langle S_i.S_j\rangle_0 - \langle S_i.S_j\rangle_T\right\} = \frac{\varepsilon_b}{2} - 6J_{12}\langle S\rangle_0^2\{1-\xi(T)\}, \qquad (3.20)$$

where $\varepsilon_m(T)$ is the magnetic energy of the trivalent nickel ion at temperature 'T', 'S_i' is the Spin moment on i^{th} site, 'J_{ij}' is the exchange coupling parameter summed over nearest neighbors, and '$\xi(T)$' is the fraction specifying

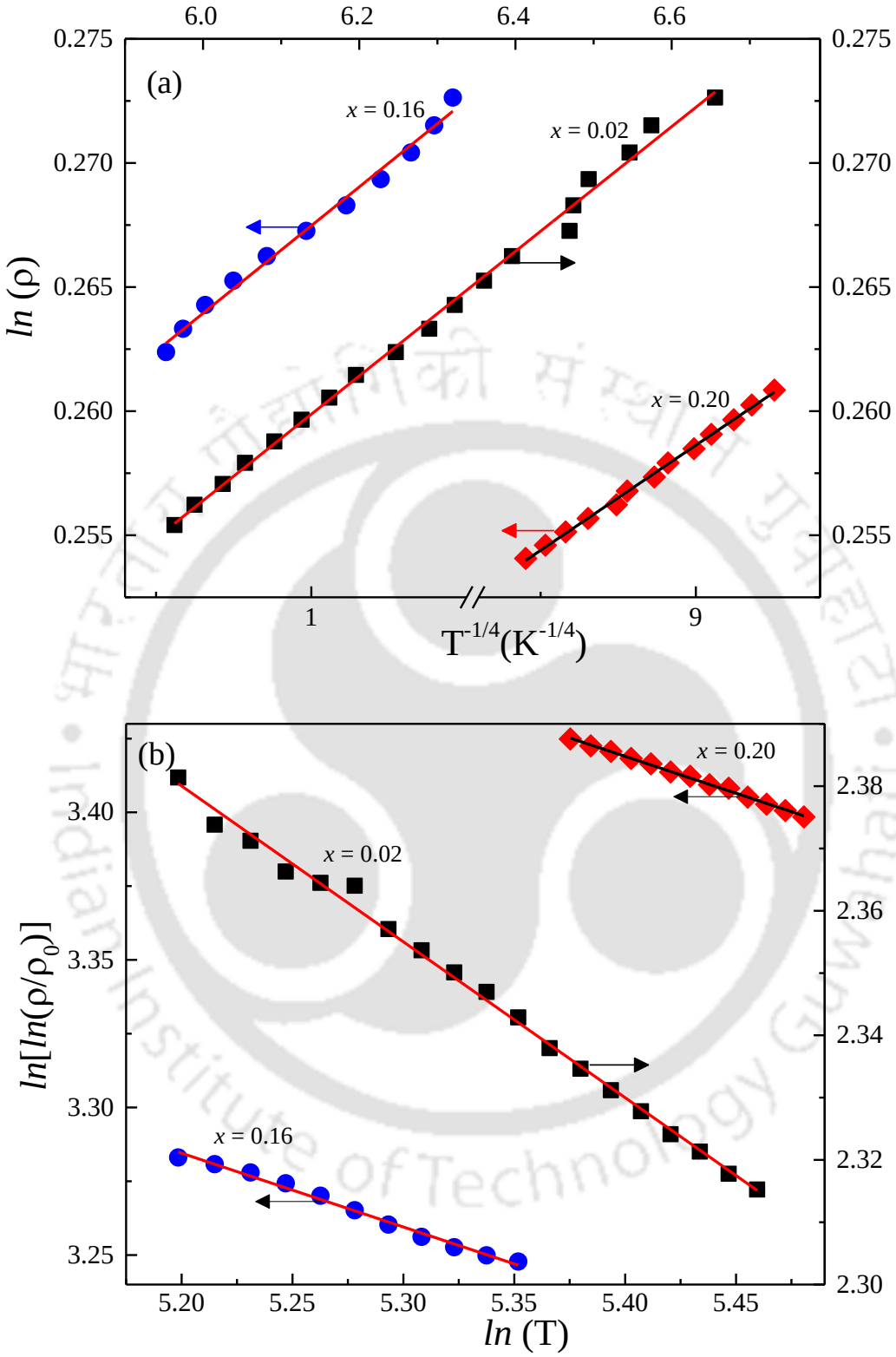

Figure 3.26: (a) The ln(ρ)) versus $T^{-1/4}$ and (b) ln[ln(ρ/ρ₀)]) versus ln(T) plots of $Ni_{1-x}Na_xO$ for x =0.02, 0.16 and 0.20.

the ratio of sublattice magnetization. Considering, the spin $S = [S(S+1)]^{0.5}\hbar$, for divalent nickel ion, the hole activation energy estimated as $\varepsilon_h(T) = \varepsilon_b/2 - 12J[1-\xi(T)]$. Consequently, we have evaluated the temperature variation of 'J' (as shown in the inset of figure 3.25 J vs. T) by utilizing the data of average hopping energy obtained from equation (3.20) and considering the value of 'ε_b' to be approximately 0.01 eV (from Ref [181]). Further, the magnitude of 'ξ(T)' was obtained from high-temperature dc-magnetic susceptibility data [112]. The calculated values of 'J(T)' is shown in the inset of figure 3.25 which is consistent with the experimental results of Srinivasan and Seehra [205], and theoretical estimation of Hutchings and Samuelsen [206] based on Green's function analysis. Similar results were observed in the case of $Ni_{1-x}Na_xO$ (figures 3.26-3.27) with 'ε_h'~0.08 eV and J~5meV for x=0.02. Nevertheless, detailed high resolution magnetic susceptibility measurements in the temperature range 300 K - 550 K are warranted for the $Zn_{1-x}Ni_xO/NiO$ system to determine the exact nature of the exchange interaction across 'T_N'. Such results are discussed in chapters IV and V with a systematic correlation of the nearest-neighbor exchange interaction (J) obtained from the resistivity data and magnetization measurements (J_{ex}) are presented. Such analysis is extremely important considering the fact that as the thermal energy surpasses the mean interaction between dipoles (either magnetic $\boldsymbol{\mu}_e$ or electric dipoles $\boldsymbol{p}_e$) seizes away and the long-range order disappears making the system paramagnetic/para-electric. The following section summarizes the important findings of the above results.

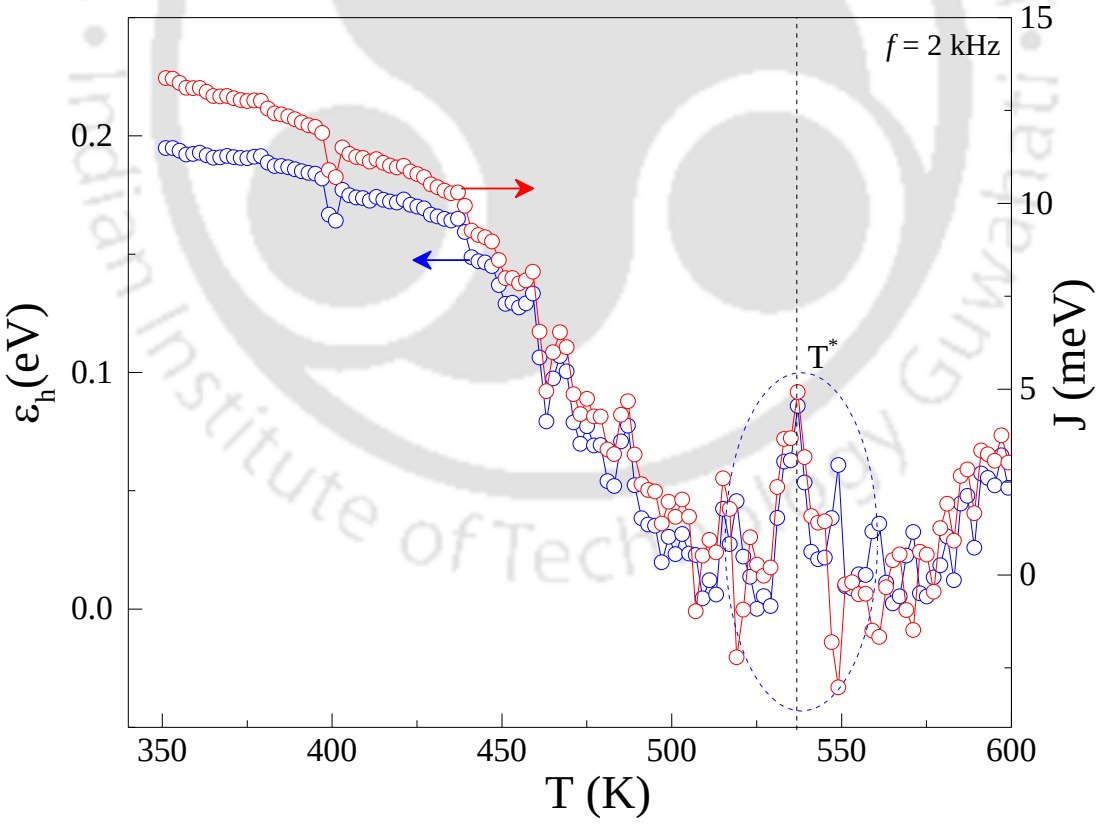

Figure 3.27: Temperature dependence of hole activation energy ε_h(T) (L.H.S) and nearest-neighbor exchange coupling parameter J(T) (R.H.S) for $Ni_{0.98}Na_{0.02}O$ measured at constant frequency f=2 kHz.

3.4 Conclusions:

We have successfully synthesized various compositions of the two-phase composites comprising Wurtzite h.c.p. structured ZnO and rhombohedrally distorted NiO together with $Ni_{1-x}Na_xO$. Interpretation of the experimental results from XPS, and temperature dependence of crystal structure and dielectric properties have led to the following important conclusions: (*i*) Ni-2p and Zn-2p both exhibit doublet corresponding to $2p_{3/2}$ and $2p_{1/2}$ with spin-orbit splitting $\Delta \sim 17.9$ eV and 23.2 eV, respectively, confirming the divalent oxidation state of Zn and Ni. However, in the case of pure NiO the difference in the binding energy of Ni $2p_{3/2}$ and Ni $2p_{1/2}$ is ~ 18.75 eV (> 18 eV) signifying the excess oxygen in the system. (*ii*) The slight change in the Ni-2p satellite peaks with increasing the composition '*x*' is associated with the attenuation in non-local screening because of reduced site occupancy of two adjacent Zn ions. (*iii*) In the case of $Ni_{1-x}Na_xO$, the O-1*s* spectra exhibits three Gaussian-Lorentzian peaks centered at 528.9 eV and 530.76 eV signifying the presence of surface oxygen and chemically bonded oxygen. Whereas, the Na-1*s* core level photoelectron spectra exhibits single major peak at ~1076.12 eV signifying the presence of monovalent oxidation state of sodium. (*iv*) The temperature variation of the axial-rhombohedral angle 'α(T)' of oxygen-rich NiO system exhibits an abrupt drop from 60º8′ to 60º at 300ºC associated with T_N. Conversely, no significant distortion was noticed in the NiO present as secondary-phase in the $Zn_{1-x}Ni_xO$ core, yet, we observed an anomalous decrease in the unit-cell volume (V_C) between 150ºC and 300ºC for both the h.c.p. $Zn_{1-x}Ni_xO$ system and f.c.c. NiO. (*v*) The high-temperature dielectric properties presented in this chapter has established the presence of two transitions at T^* ($T_{N\text{-}NiO}$) = 541 K (268ºC) and T_2 = 683 K (410ºC), associated with the structural phase transition from rhombohedral to cubic phase of NiO, while the T_2 is linked with the T_C of Ni. (*vi*) Formation of tiny polar clusters due to the compositional heterogeneity for the samples with $x \geq 0.16$ drove the system to exhibit weakly coupled relaxor-like behavior with locally varying temperature maximum T^* (~ 530 K at 10^6 Hz), obeying the Vogel–Fulcher law and Uchino-Nomura criteria. (*vii*) Temperature dependence of ac-resistivity ρ_{ac}(T) analysis provides strong evidence for the variable-range-hopping of charge carriers between the localized states. Using this ρ_{ac}(T) data and applying the small-polaron model the carrier hopping energy ε_h and nearest-neighbor exchange-coupling parameter J_{ij} is evaluated which exhibits a well-defined anomaly across T_N.

Chapter-IV

Magnetic Exchange Interactions in $Zn_{1-x}Ni_xO$/NiO and $Ni_{1-x}Na_xO$

In this chapter, we focus on the high-temperature magnetic properties of $Zn_{1-x}Ni_xO$/NiO two-phase composites and $Ni_{1-x}Na_xO$ and made a comparison between the dielectric properties and crystal structure. This chapter also highlights the changes occurring in the nearest-neighbor exchange interaction strength estimated from the molecular-field approximation and Green's-function theory. A systematic comparison of these magnitudes was carried out against various values obtained from experimental methods. The role of oxygen-rich and oxygen-deficient conditions on the magnetic ordering of NiO system is discussed in detail. The introductory section presents detailed literature survey on magnetic behavior of $Zn_{1-x}Ni_xO$ and NiO, together with their scientific and industrial applications. In the later sections, we present details of various characterization techniques employed, experimental results and their discussion followed by summary of results.

4.1 Literature Review:

Antiferromagnetic compounds such as NiO, MnO, CoO, CuMnAs, and IrMn play a more practical role in spintronic devices as compared to conventional ferromagnetic systems because of the some added functionalities inherent to antiferromagnets, such as the exchange bias [110, 111, 207–215]. Antiferromagnetic systems are also considered as key elements for commercial magnetic field sensors and magnetic-random-access memories [110,111,207–210]. Also, the promising spin-transport characteristics of insulating antiferromagnets, together with their exceptional magnetic-field hardness, play a major role in the lossless spin transmission and spin interconnects [214]. Such features make antiferromagnetic insulators attractive elements for basic and applied research in Magnonics [214,215]. On the other hand, appropriate integration of antiferromagnetic NiO clusters in ZnO core upsurged the desirable properties for specific applications like rechargeable lithium-ion batteries, solar cells and memory-devices [119,214–219]. Recently, Liu et al. demonstrated much higher photocatalytic performance of p-NiO/n-ZnO hetero-structures as compared to pure NiO and ZnO [59]. Woong et al. reported enhanced gas sensing characteristics with good stability and fast response kinetics for NiO-decorated ZnO nanowires [220]. The electrical properties in these two-phase composites are mainly dominated by the grain-boundary interface effect which is technologically important for solid state resistive-switching devices like varistors (voltage-dependent resistor) [214,215]. Recently, Zheng *et al.* reported excellent electrochemical performance of ZnO/NiO core-shell nanocomposites with a maximum specific real-capacitance of 4.1 F/cm^2 for the supercapacitor electrodes [220]. As compared to the hazardous leaded materials, the ZnO/NiO system is environment friendly, which makes it important material for the renewable energy source, especially in the field of supercapacitors and fuel cells having long-term cycling stability [220]. Moreover, the spinodal nanodecomposition and nanoprecipitation in semimagnetic-semiconductors (e.g. Mn-doped group-III Arsenides and antimonides, transition metal doped group-III nitrides and ZnO, and Cr-doped group-II chalcogenides) found

the cutting-edge application of computational and novel nanocharacterization methods [215]. Nevertheless, a detailed study related to the high temperature magnetic and structural properties of $Zn_{1-x}Ni_xO$ and $Ni_{1-x}Na_xO$ systems were not reported anywhere else when we initiated this work. Only very few reports are available in the literature on the high temperature magnetic and structural studies of bulk and nanosized NiO [137,205,221,222]. The first report dealing with the high-temperature (700 K) magnetic susceptibility of NiO single-crystals appeared in 1984 by Srinivasan and Seehra [205]. For the magnetization study these authors used both polycrystalline powders and strained (42 bars) NiO single-crystals elongated along <111> direction. According to this report the magnitude of exchange constants for NiO single crystals are: J_1 = 0.29 meV (34 K) and J_2 = 17.4 meV (202 K). These values are evaluated from the experimentally obtained magnetic susceptibility data χ(524 K) = 8.8×10^{-6} cm^3g^{-1} ($6.57\times10^{-4}cm^3mol^{-1}$) and random-phase approximation Green's function theory [205,222,223]. These results are consistent with the data obtained from experimental spin-wave dispersion curves (J_1 = 0.13 meV (-16 K) and J_2 = 1.90 meV (221 K)) and Raman scattering (J_2 = 1.98 meV (230 K)) [223,224]. Recent study on the crystallite size-dependent magnetization behavior of NiO nanoparticles revealed that the shifts of T_N towards low-temperature side with decrease in particle size (d) following the finite-size-scaling relation $\left(T_N(d) = T_N(\infty)\left[1-\left(\frac{\xi_0}{d}\right)^{\lambda}\right]\right)$ with the shift-exponent λ = 3.2 ± 0.2 and the correlation length ξ_o = 3.2 ± 0.2 nm [112]. The neutron diffraction studies and X-ray absorption fine structure measurements of NiO nanoparticles (4-9nm) reveal the exchange bias effect (H_{EB} ~ 6 kOe at 2 K measured under both zero-field-cooled and field-cooled conditions) driven by the 0.5 nm thick interface spins existing between core and shell structure of the NiO nanoparticle [225–227]. Earlier studies by Proenca et al. reported that the uncompensated spins (q) per NiO nanoparticles of size 12 to 70 nm are proportional to the 1/3 power of total number of spins ($q \propto (n_s)^{1/3}$) indicating the random distribution of q on the surface of antiferromagnetic nanoparticles [227]. Except these reports there is no other study available in the literature related to the high-temperature (300 K ≤ T ≤ 773 K) magnetic susceptibility of either bulk or nanocrystalline NiO [205,226]. The polarized neutron powder diffraction studies of bulk and nanoparticle antiferromagnetic NiO reveal that the spins are oriented with a 30º average angle to the primary (111) plane of the particles [228]. It is well known that oxygen vacancies are inherently linked with magnetic, electronic and charge transport properties of transition metal oxides and such vacancies play a major role in determining their multifunctionality [229,230]. It is also possible to tune the overall magnetic moment of the antiferromagnetic NiO nanoparticles by inducing the surface defects driven by the oxygen vacancies [229]. Strong coupling between such oxygen vacancies and nearest neighboring 'Ni' ions result in exchange bias (H_{EB}) as high as 5 kOe at low-temperature (<10 K) (majority of Ni^{2+} vacancies reside on the surface rather than in core, which leads to a large saturation magnetization M_S (~ 0.19 emu/g) and H_{EB}) [231]. Motivated by all the above literature an attempt has been made here to study the magnetic and ac-electrical transport properties of $Zn_{1-x}Ni_xO$/NiO and $Ni_{1-x}Na_xO$ bulk grain size polycrystals. In this chapter a special importance is given to evaluate the magnetic-exchange interaction (J_{ex}) and carrier-activation energy (ε_h) from different experimental methods and theoretical approaches. Finally, a

comparative analysis of the variation J_{ex}, particle moment (μ_p) and ε_h as function of doping concentration '*x*', oxygen stoichiometry (δ), and measuring temperature 'T' are presented for both the systems $Zn_{1-x}Ni_xO$/NiO and $Ni_{1-x}Na_xO$.

4.2 Experimental Details:

All the samples are prepared by standard solid-state-reaction technique as described in chapter 3. NiO samples are sintered at 1200°C under oxygen-rich conditions to get pale-apple-green colored $NiO_{1+\delta}$ samples. Whereas jet black color oxygen-deficient $NiO_{1-\delta}$ samples were prepared by sintering the pellets at very high temperatures between 1350 and 1450˚C. High-temperature (from 350K to 700K) magnetic measurements are performed using a vibrating sample magnetometer based physical property measurement system (PPMS) from Quantum Design Technology (with magnetic field capable of ±70 kOe). A high-precision impedance analyzer from Wayne–Kerr Electronics Pvt. Ltd (model 6530B) assembled with high-temperature accessories was used to study the dielectric properties between the frequencies 10^3 to 10^6 Hz with ac-peak-to-peak amplitude of 1 V.

4.3 High Temperature Magnetic-susceptibility Studies:

The temperature dependence of dc-magnetic susceptibility $\chi(T)$ measurements of $Zn_{1-x}Ni_xO$/NiO and $Ni_{1-x}Na_xO$ samples are performed in the presence of external magnetic field H =1000 Oe. Figures 4.1 shows the $\chi(T)$ plots and their derivatives of different compositions of $Zn_{1-x}Ni_xO$/NiO and $Ni_{1-x}Na_xO$. These samples are sintered at 1200°C under oxygen-rich condition yielding pale-apple-green colored $NiO_{1+\delta}$, as well as in oxygen-deficiency to give jet black $NiO_{1-\delta}$. Here $\chi(T)$ measurements are performed from T = 350 K to 700 K under both heating and cooling cycles in the presence of an external magnetic field H = 2kOe where the sample compartment was maintained under constant vacuum condition during the measurement. Two transitions are clearly observed in the $\chi(T)$ curve, as shown in figures 4.1a; the first transition across $T_1 \sim 534$ K and the second transition T_2 at 640 K, which are associated with T_N of NiO and Curie temperature T_C of 'Ni', respectively. Since the high temperature measurements were performed under vacuum, one can expect the formation of tiny Ni clusters through reduction process. The order parameters T_C and T_N are in good agreement with the previously reported literature values for stoichiometric NiO; T_N (T_1) = 523 K, and T_C (T_2) = 627 K for metallic Ni (inter diffusion of 'Ni' inside the NiO matrix) [183,232]. It is a well-known fact that the antiferro-to-paramagnetic transition in typical Mott insulators (like NiO, CoO or MnO) is linked with a definite crystal-structure change; for example, in case of stoichiometric NiO, a clear change from low-temperature rhombohedral phase (space-group R-3m) to high-temperature cubic phase occurs across T_N (space-group Fm-3m). It is also known that in antiferromagnetic systems, the peak temperature pertaining to the T_N occurs at a temperature slightly higher than actual anti-ferromagnetic ordering temperature [233–236]. The variation of the magnetic specific heat (C_P) of an antiferromagnetic system should closely resemble with the behavior of $\partial(\chi T)/\partial T$ [233–236]. Therefore, in order to accurately probe the magnetic transitions, we plotted the derivative of the product 'χT' with respect to temp-

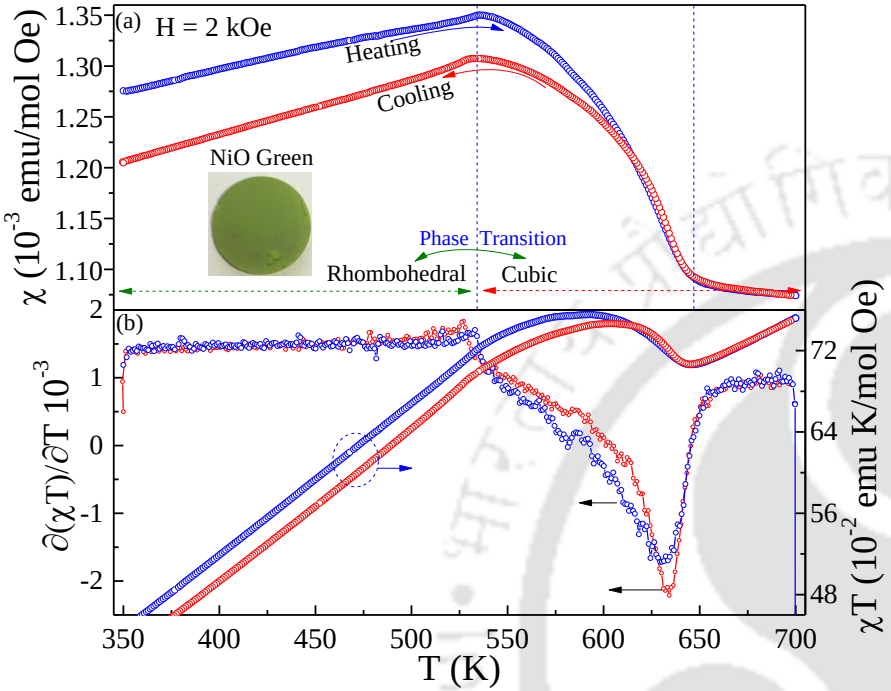

Figure 4.1: (a) Temperature dependence of dc magnetic susceptibility χ(T) and (b) the differential $\partial(\chi T)/\partial T$susceptibility(left-hand axis scale) and χT(right-hand axis scale) for an oxygen-rich NiO (x = 1) system measured under both heating and cooling cycles in the presence of external magnetic field H of 2 kOe. The inset shows the image of a NiO sample (pale apple green) sintered at 1200°C under an oxygen ambient.

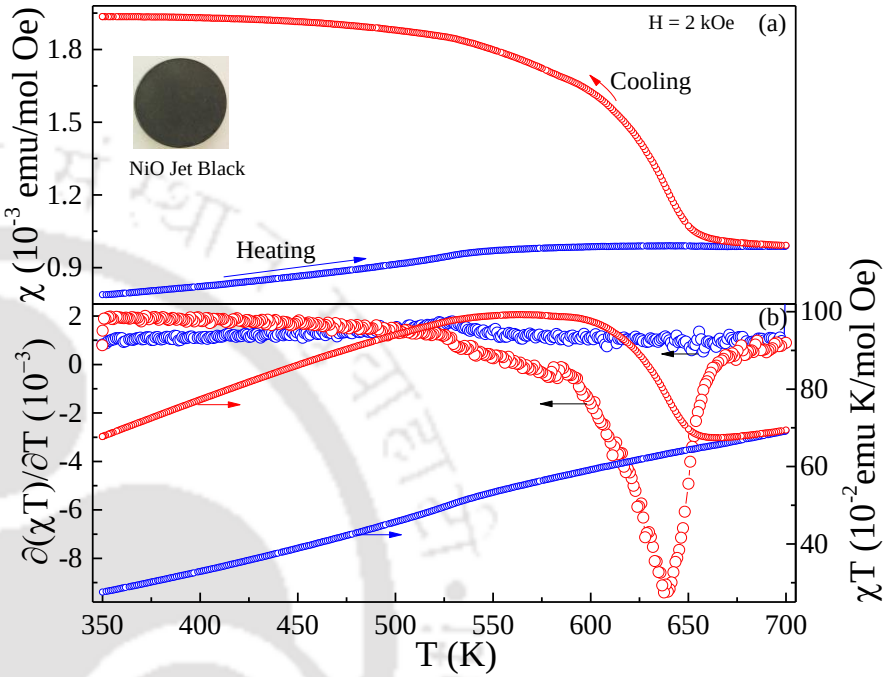

Figure 4.2: Temperature variation of (a) dc magnetic susceptibility χ(T) and (b) the differential $\partial(\chi T)/\partial T$susceptibility(left-hand axis scale) and χT(right-hand axis scale) recorded under both heating and cooling cycles in the presence of external magnetic field H of 2 kOe for oxygen-deficient NiO (x=1) sintered at high temperature ~1350°C in air. The inset depicts the jet-black sample color.

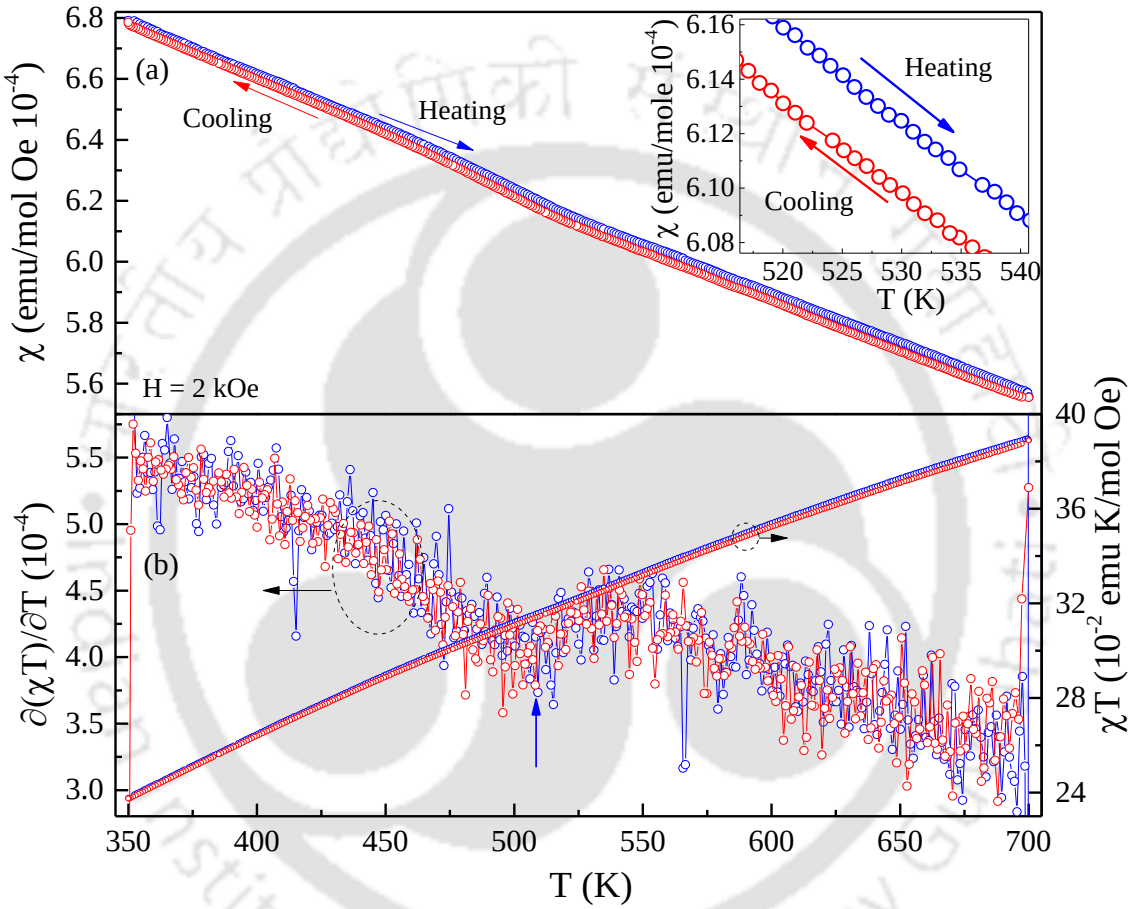

Figure 4.3: The Temperature dependence of (a) dc magnetic susceptibility χ(T) and (b) the differential $\partial(\chi T)/\partial T$ susceptibility(left-hand axis scale) and χT (right-hand axis scale) for the composition x=0.3 measured under both heating and cooling cycles in the presence of external magnetic field H=2 kOe.

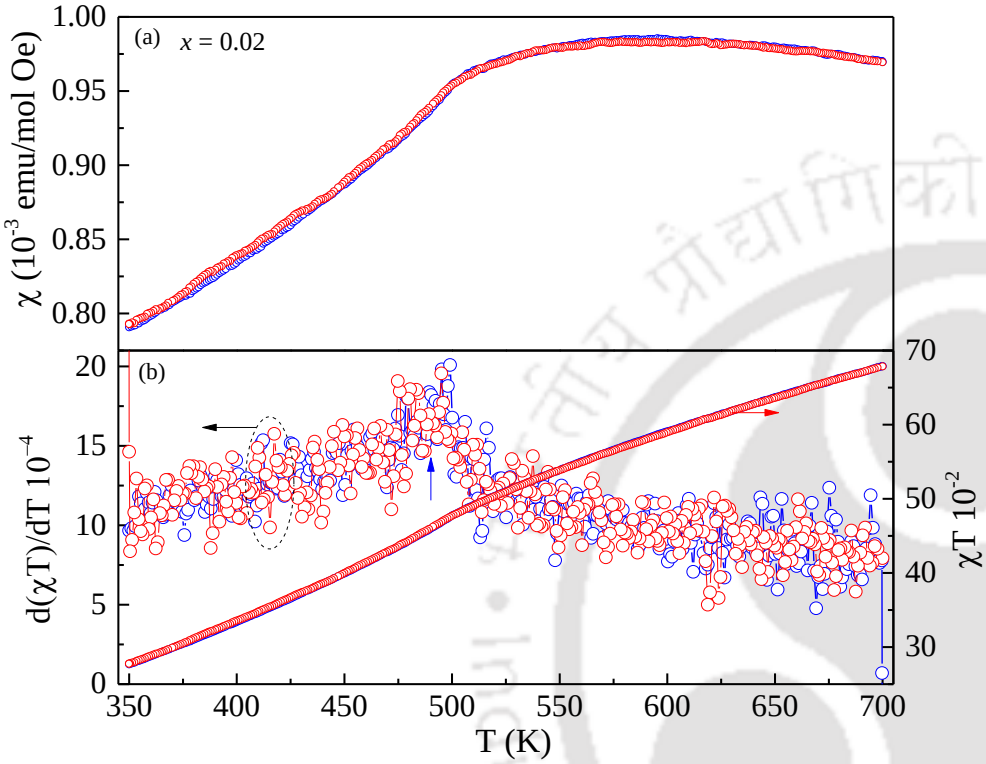

Figure 4.4: (a) Temperature dependence of dc magnetic susceptibility χ(T) and (b) the differential $\partial(\chi T)/\partial T$susceptibility(left-hand axis scale) and χT(right-hand axis scale) for $Ni_{1-x}Na_xO$(x = 0.02) system measured under both heating and cooling cycles in the presence of external magnetic field H of 2 kOe.

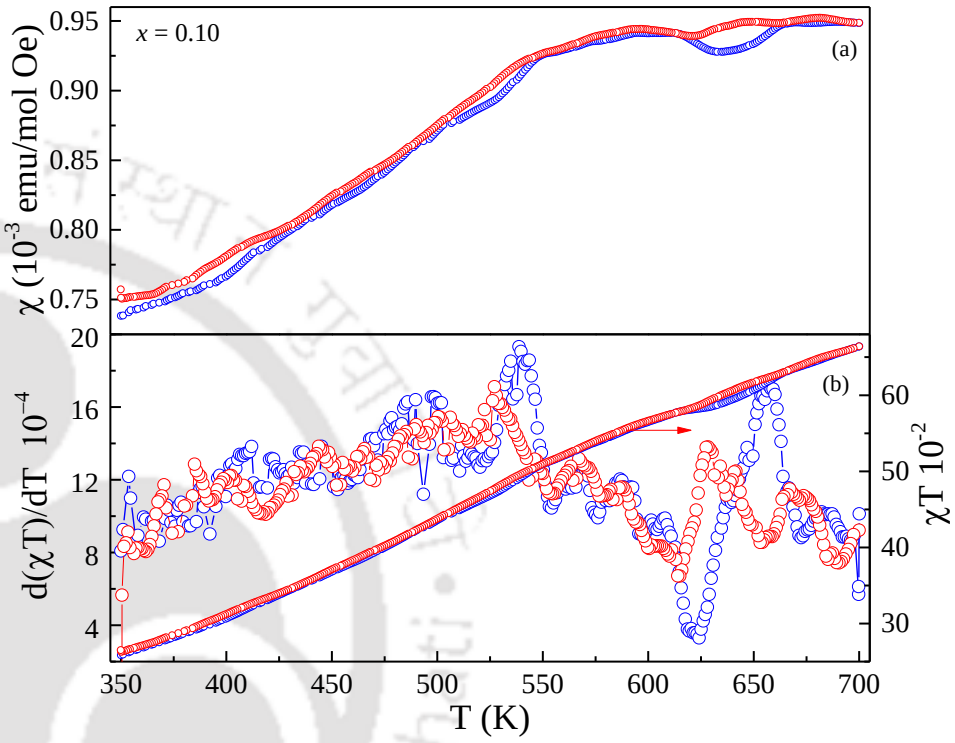

Figure 4.5: Temperature variation of (a) dc magnetic susceptibility χ(T) and (b) the differential $\partial(\chi T)/\partial T$susceptibility(left-hand axis scale) and χT(right-hand axis scale) recorded under both heating and cooling cycles in the presence of external magnetic field H of 2 kOe for $Ni_{1-x}Na_xO$(x = 0.10).

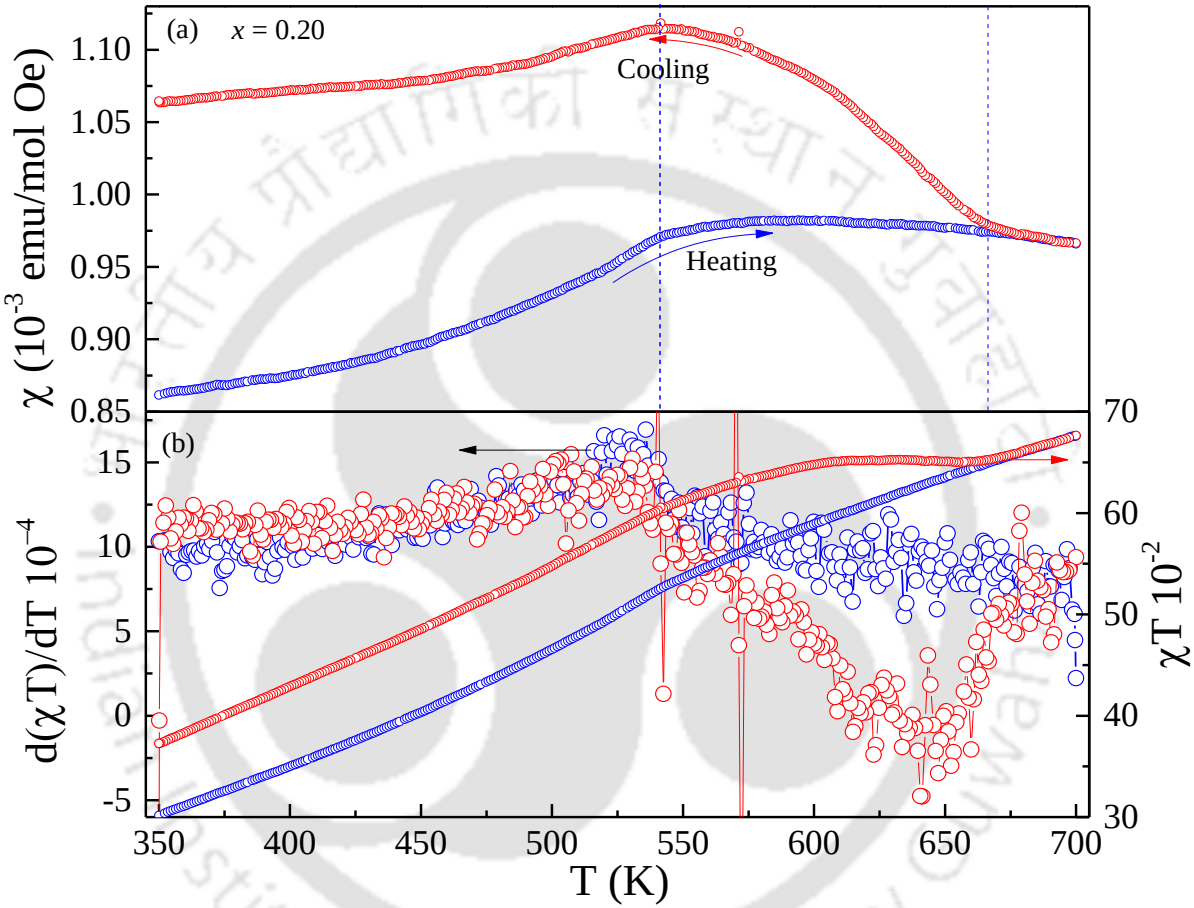

Figure 4.6: Temperature variation of (a) dc magnetic susceptibility χ(T) and (b) the differential $\partial(\chi T)/\partial T$ susceptibility(left-hand axis scale) and χT (right-hand axis scale) recorded under both heating and cooling cycles in the presence of external magnetic field *H* of 2 kOe for $Ni_{1-x}Na_xO$ (x = 0.20).

-erature 'T' on the L.H.S. and the variation of 'χT' with respect to 'T' on the R.H.S. in figures 4.1b. Consequently, a broad minimum (negative dip) was noticed across 634 K and a positive hump (peak) across 527 K was observed in the derivative plot of 'χT' (i.e. $\partial(\chi T)/\partial T$). Thus the antiferromagnetic transition obtained from the $\partial(\chi T)/\partial T$ versus T analysis is in line with the original reported values (i.e. $T_N \sim 523$ K). However, the T_C of 'Ni' appears 7 K above the standard value of T_C for Ni, which is 627 K because a small amount of metallic nickel forms at high temperatures when we subject NiO to vacuum condition. Thus the interface of NiO/Ni composite plays an important role and as a consequence, slight shift in T_C is expected. Similar analysis (Figure 4.2) leads to a weak anomaly across the T_N but a sharp peak at T_C for the oxygen deficient sample (jet-black colored NiO) which was sintered between 1350-1450°C. Figure 4.2a shows the 'χ' vs. T of the oxygen-deficient NiO sample measured under both cooling and heating cycles. The bifurcation of 'χ' vs. T data recorded under cooling and heating appears around 620 K and 670 K for oxygen rich and oxygen deficient samples respectively. Such large difference between the susceptibility curves are related with the inherent anisotropy effects present in the antiferromagnetic state of the sample [237,238]. Figure 4.2b represents the temperature variation of $\partial(\chi T)/\partial T$ and χT on the L.H.S and R.H.S, respectively. From this derivative analysis of 'χT' a weak hump across T_N and a strong dip across the T_C was observed. Such strong ferromagnetic character is appearing due to the dominance of metallic Ni character caused by the oxygen deficiency in the system. On the other hand, only straight-line behavior was observed in the χ vs. T data of $Zn_{0.70}Ni_{0.30}O$/NiO composite signifying the paramagnetic behavior of the system with very weak anomaly across the 510 K close to standard T_N value of NiO (Figure 4.3). Usually, as the Ni substitution increases at the tetrahedral zinc sites, one would expect a decrease in the average distance between two-successive nickel ions, consequently an increase in the coupling between Ni^{2+}-Ni^{2+} leading to a ferromagnetic interaction and diamagnetic contribution of $Zn^{2+}(3d^{10})$ gradually smears off. As the substitution level of Ni increases beyond x = 0.10, antiferromagnetic NiO emerges as secondary phase and this phase grows progressively with increasing 'x', accordingly the Ni-O-Ni superexchange interaction dominates over Ni^{2+}-Ni^{2+} direct interaction discussed above. Therefore, the Zn^{2+} ion virtually plays no role on the global magnetic behavior, however, one cannot rule out the possibility of interstitial Zn^{2+} ions and oxygen vacancies in the wideband-gap wurtzite matrix which may play a significant role in the dielectric and ac-transport properties of the two-phase composites [239,240]. Besides, Na doped NiO exhibits complete antiferromagnetic character without with any ferromagnetic component arising from Ni. Figure 4.4-4.6 shows the χ(T) and $\partial(\chi T)/\partial T$ plots for Na compositions x = 0.02, 0.1 and 0.2 in NiO matrix. These plots show the unaltered antiferromagnetic character of $Ni_{1-x}Na_xO$ except slight change in the T_N values (490 K, 532 K and 540 K for x = 0.02, 0.1 and 0.2, respectively) with increased χ values for higher Na doping concentration.

Moreover, using the Curie-Weiss $\left(\frac{1}{\chi} = \frac{T-\theta}{C}\right)$ analysis on the high temperature paramagnetic regime of χ(T) data, the effective magnetic moment μ_{eff} for both oxygen-rich and oxygen-deficient NiO samples are calculated. Figure 4.7 shows the temperature dependence of the inverse magnetic susceptibility (1/χ) of both the NiO samples

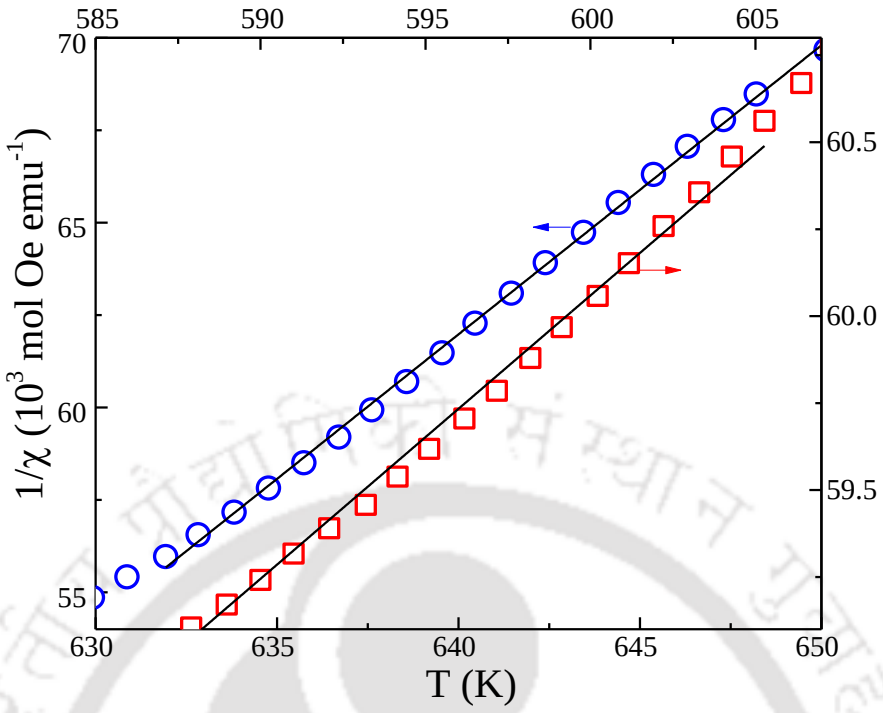

Figure 4.7: Inverse magnetic susceptibility $1/\chi$ plotted as a function of temperature for $NiO_{1+\delta}$ (right-hand axis scale) and $NiO_{1-\delta}$ (left-hand axis scale). The hollow symbols represent the experimental data and solid linear fits are the Curie–Weiss fits.

for $T > T_N$. In this figure, the solid lines are Curie-Weiss fits to the experimental data points depicted by hollow circles. Consequently, using the slope of these linearly fitted data the Curie constant 'C' = 1.47×10^{-2} emu-K/g-Oe and 1.27×10^{-3} emu-K/g-Oe, and $\mu_{eff} = 3.42\mu_B$ and $2.41\mu_B$ have been evaluated (μ_{eff} has been obtained using the following relation $(3k_BC/N_A)^{1/2}$) for Oxygen rich and deficient NiO systems, respectively. For oxygen rich NiO sample, the observed value of $\mu_{eff} = 3.42\ \mu_B$ is considerably higher than the previously reported values in pure NiO ($\mu_{eff} \sim 2.87\ \mu_B$) [241] and slightly higher ($0.46\ \mu_B$) than that for oxygen-deficient NiO. It is well known that NiO is a type-II antiferromagnetic system where the indirect exchange coupling is mediated by the oxygen ions [242]. Since the jet-black NiO system exhibits oxygen deficiency, it is possible that these deficiencies could lead to interruption of the indirect exchange coupling, providing a significant drop in the μ_{eff}.

4.3.1. Evaluation of Exchange constants: Theoretical background:

4.3.1.1 Magnetic ordering using Molecular Field Theory and Secular equations:

In this section, we establish the set of secular equations using molecular field theory (discussed in Chapter-I, section 1.4.1) and uses the results of our experimental data in consonance with the secular equations to evaluate the strength of exchange constants for the investigated system. In order to evaluate the exchange constants in these binary transition metal oxide systems we make use of the universal equation of the Heisenberg exchange Hamiltonian:

$$H = -2 \sum_{i \neq j} J_{ij} S_i \cdot S_j \qquad (4.1)$$

In the above equation J_{ij} is the exchange interaction between an *i* atom and one of it's *j* neighbors. Then the overall molecular-field acting on one atom of the i^{th} sublattice is

$$H_i = H_0 + \sum_{\substack{j=1 \\ i \neq j}}^{n} \gamma_{ij} M_j \qquad (4.2)$$

where γ_{ij} is the molecular field coefficient, M_j is the magnetization at j^{th} sublattice and '*n*' is the number of sublattices in the system. Succeeding the equation $\gamma = 2 J_{ab} z / N_a g^2 \mu_B^2$, we can write

$$\gamma_{ij} = 0 \qquad for\ i = j \qquad (4.3)$$

$$\gamma_{ij} = n\,(2 J_{ij} z_{ij}) / N g^2 \mu_B^2 \qquad for\ i \neq j \qquad (4.4)$$

where z_{ij} is the number of *j* neighbors of an *i* atom and N is the total number of atoms. The equations 4.3 and 4.4 state that the atoms interact with atoms on the other sublattices only. For example, in NiO, a given atom has 12 nearest neighbors at a distance of $a/\sqrt{2}$ on six different lattices and six next-nearest neighbors on the cubic edges at one lattice parameter '*a*' unit distance. Therefore, from the figure 1.16, we consider $\gamma_{12} = \gamma_{13} = \gamma_{14} = \gamma_{16} = \gamma_{17} = \gamma_{18}$ be γ_1 for the nearest neighbors (nm) and γ_{15} be γ_2 for the next-nearest neighbors (nnm). For each H,

$$\begin{aligned} H_1 &= H_0 + 8/6\ \gamma_1 M_2 + \ldots\ldots + 8\ \gamma_2 M_5 + \ldots..+ 8/6\ \gamma_1 M_8 \\ H_2 &= H_0 + 8/6\ \gamma_1 M_1 + \ldots\ldots + 8\ \gamma_2 M_6 + \ldots..+ 8/6\ \gamma_1 M_8 \\ &\ldots\ldots \\ &\ldots\ldots \\ H_8 &= H_0 + 8/6\ \gamma_1 M_1 + \ldots\ldots + 8\ \gamma_2 M_4 + \ldots..+ 8/6\ \gamma_1 M_7 \end{aligned} \qquad (4.5)$$

The expression for the magnetization (M) and magnetic field (H) can be represented by the Curie law,

$$\begin{aligned} M_i &= C / nT\ H_i \\ &= C / nT (H_0 + \textstyle\sum \gamma_{ij} M_j) \end{aligned} \qquad (4.6)$$

where the Curie constant, $C = N/8\ g^2\ \mu_B^2\ S(S+1)/3k_B$.

Subsequently, H_1, H_2, … , and H_8 in equation 4.5 can be replaced by 8T/C M_1, 8T/C M_2, … , and 8T/C M_8. Thus one can rewrite the equation 4.5 as

$$\begin{aligned} &8T/C\ M_1 - 8/6\ \gamma_1 M_2 - \ldots - 8\ \gamma_2 M_5 - \ldots - 8/6\ \gamma_1 M_8 = H_0 \\ &- 8/6\ \gamma_1 M_1 + 8T/C\ M_2 - \ldots - 8\ \gamma_2 M_6 - \ldots - 8/6\ \gamma_1 M_8 = H_0 \\ &\ldots\ldots\ldots.. \\ &- 8/6\ \gamma_1 M_1 - 8/6\ \gamma_1 M_2 - \ldots.- 8\ \gamma_2 M_4 - \ldots + 8T/C\ M_8 = H_0 \end{aligned} \qquad (4.7)$$

Thus, equation 4.7 can be represented in the form of matrix with the applied field $H_0 = 0$ and the determinant of the secular equation is (with $a_0 = 8T/C$, $a_1 = -4/3\ \gamma_1$, $a_2 = -8\gamma_2$),

$$\begin{vmatrix} a_0 & a_1 & \cdots & a_2 & \cdots & a_1 \\ a_1 & a_0 & \cdots & a_2 & \cdots & a_1 \\ \vdots & \vdots & \cdots & \vdots & \cdots & \vdots \\ a_2 & a_1 & \cdots & a_0 & \cdots & a_1 \\ \vdots & \vdots & \cdots & \vdots & \cdots & \vdots \\ a_1 & a_1 & \cdots & a_2 & \cdots & a_0 \end{vmatrix} = 0 \qquad (4.8)$$

The eight solutions of above equation 4.8 yield the transition temperatures. To solve this equation 4.8, the standard procedure of subtracting rows and columns is employed (without affecting the solutions), leading to only three independent solutions due to degeneracy. The first factor leads to quadruple degeneracy, $(a_0 - a_2)^4 = 0$ or $a_0 = a_2$. This yield:

$$T_{N2} = -C\,\gamma_2 \qquad (4.9)$$

In the remaining determinant, add row 1 to row 5. This changes the determinant 8 × 8 to 7 × 7. Repeat this step until the determinant becomes 4 × 4. Thus, we finally get a 3 × 3 matrix,

$$-A\begin{vmatrix} -A & -A & A+4a_1 \\ A & 0 & 2a_1 \\ 0 & A & 2a_1 \end{vmatrix} = 0 \qquad (4.10)$$

In the above equation $A \equiv (a_2 + a_0 - 2a_1)$

So, we have the results of equation 4.10 as

$$A^3 = 0, \text{ triple roots}$$

$$\text{and, } A = -8a_1, \text{ single root} \qquad (4.12)$$

From equations 4.11 and 4.12 respectively

$$T_N = C\,(-1/3\,\gamma_1 + \gamma_2) \qquad (4.13)$$

$$T_N = C\,(\gamma_1 + \gamma_2) \qquad (4.14)$$

The eigen vectors for each transition temperature can be obtained by substituting each solution of the matrix into original matrix. For the first case of $a_0 = a_2$, the result is

$$a_0\,(M_1 + M_5) + a_1(M_2 + M_3 + \ldots + M_8) = 0 \qquad (4.15)$$

This gives;

$$M_1 = -M_5, \text{ similarly } M_2 = -M_6,\ M_3 = -M_7,\ M_4 = -M_8 \qquad (4.16)$$

For the solution, $a_2 + a_0 - 2a_1 = 0$,

$$a_0\,(M_1 + M_2 + M_3 + M_4) - a_1\,(M_5 + M_6 + M_7 + M_8) + a_1\{3(M_1 + M_2 + M_3 + M_4) + 5(M_5 + M_6 + M_7 + M_8)\} = 0$$

The Eigen vectors of this equation are

$$M_1 = M_5,\ M_2 = M_6,\ M_3 = M_7,\ M_4 = M_8$$

$$\text{and } M_1 + M_2 + M_3 + M_4 = M_5 + M_6 + M_7 + M_8 = 0 \qquad (4.17)$$

And for the last case, $a_2 + a_0 + 6a_1 = 0$,

$$a_0\,(M_1 - M_5) + a_1(M_2 + M_3 + M_4 - 6M_5 + M_6 + M_7 + M_8) = 0$$

Thus, $$M_1 = M_2 = M_3 = M_4 = M_5 = M_6 = M_7 = M_8 \qquad (4.18a)$$

In summary, all the solutions are collectively written as;

For the first case, $T_{N2} = -C\,\gamma_2$, where $J_2 < 0$

$$M_1 = -M_5,\ M_2 = -M_6,\ M_3 = -M_7,\ \text{and } M_4 = -M_8 \qquad (4.18b)$$

This is what is observed in NiO and represents the antiferromagnetic ordering of Type II (say AF-2).

For the second case, $T_{N1} = C\,(-1/3\,\gamma_1 + \gamma_2)$, where $J_1 < 0$ and $J_2 > 0$

$$M_1 = M_5\,,\ M_2 = M_6\,,\ M_3 = M_7\,,\ M_4 = M_8$$

and $$M_1 + M_2 + M_3 + M_4 = M_5 + M_6 + M_7 + M_8 = 0 \qquad (4.19)$$

The above equation represents the antiferromagnetic ordering of Type I (AF-1).

And the last case, $T_C = C\,(\gamma_1 + \gamma_2)$, where $J_1 > 0$ and $J_2 > 0$

$$M_1 = M_2 = M_3 = M_4 = M_5 = M_6 = M_7 = M_8 \qquad (4.20)$$

This case represents the ferromagnetic state.

4.3.1.2 Equations for T_N and θ: Three types of ordering:

In this section we derive the definite expression for T_N and θ. For this we start with equation 4.19 which describes the antiferromagnetic ordering of magnetic atoms. Atoms are ordered ferromagnetically in *x–y* plane and the direction of spins is changed alternately as shown in figure 4.8 (a) choosing $M_1 = M_2 = -M_3 = -M_4$. This arrangement can also occur in *y–z* plane and *x–z* plane. The number of nearest neighbor pairs order antiparallel is the largest among the other orderings. Therefore, this feature of ordering represented in equation 4.19 is called the antiferromagnetic ordering of Type-I (AF-1). The atoms within planes perpendicular to a particular cube diagonal are ordered ferromagnetically and the directions of these atoms are antiparallel with adjacent planes as shown in figure 4.8 (b). Such kind of ordering is called antiferromagnetic ordering of Type-II (AF-2). There is another type of antiparallel-spin arrangement called antiferromagnetic ordering of Type-III (AF-3). This ordering is similar to Type-I (AF-1) with the only difference being the change in the direction of one spin at the cube edge followed by the same sublattice. This is shown in figure 4.8 (c). And in the last case shown in equation 4.20, M_1, M_2, …, and M_8, all have same magnitude and direction, leading to ferromagnetic state. The Curie-Weiss temperature θ and the Néel temperature T_N for the NiO system can be represented in terms of exchange constants J_1 and J_2. For this equation 4.7 can be rewritten as

$$\begin{aligned} M_1 &= C/8T\{H_0 + 4/3\,\gamma_1\,(M_2 + \ldots + M_8) + 8\,\gamma_2\,M_5\} \\ M_2 &= C/8T\{H_0 + 4/3\,\gamma_1\,(M_1 + \ldots + M_8) + 8\,\gamma_2\,M_6\} \\ &\ldots\ldots\ldots\ldots\ldots \\ M_8 &= C/8T\{H_0 + 4/3\,\gamma_1\,(M_1 + \ldots + M_7) + 8\,\gamma_2\,M_4\} \end{aligned} \qquad (4.21)$$

For $T > T_N$, in the paramagnetic region,

$$\begin{aligned} M &= \sum M_i \\ &= C/8T\{8H_0 + 4/3\,\gamma_1 6\,(M_1 + \ldots + M_8) + 8\,\gamma_2\,(M_1 + \ldots + M_8)\} \\ &= C/T\{H_0 + (\gamma_1 + \gamma_2)\,M\} \qquad (4.22) \end{aligned}$$

$$M = (C/T)(H_0/\{1 - C/T\,(\gamma_1 + \gamma_2)\}) \qquad (4.23)$$

and

$$\chi = \partial M/\partial H_0 = C/\{T - C\,(\gamma_1 + \gamma_2)\} = C/\{T + |\theta|\} \qquad (4.24)$$

Where the paramagnetic transition temperature, $\theta = |-C\,(\gamma_1 + \gamma_2)|$.

Since the FCC system possess 12 nearest neighbors and 6 next nearest neighbors. From equation 4.4, we can write

$$\gamma_1 = (2 \times 12)\, J_1 / (N/8\, g^2 \mu_B^2),$$

and $$\gamma_2 = (2 \times 6)\, J_2 / (N/8\, g^2 \mu_B^2) \quad (4.25)$$

Thus, the transition temperature θ has the form:

$$\theta = 2S(S+1)(12\, J_1 + 6J_2) / 3k_B \quad (4.26)$$

Similarly, the transition temperatures for each type of AFM ordering, determined for $H_0 = 0$, are also given by J_1 and J_2.

In equation 4.20,

$$T_C = C(\gamma_1 + \gamma_2)$$
$$= 2S(S+1)(12\, J_1 + 6J_2) / 3k_B \quad (4.27)$$

In equation 4.19,

$$T_{N1} = C(-1/3\, \gamma_1 + \gamma_2)$$
$$= 2S(S+1)(-4\, J_1 + 6J_2) / 3k_B \quad (4.28)$$

and in equation 4.18,

$$T_{N2} = -C\, \gamma_2$$
$$= -2S(S+1)(6J_2) / 3k_B \quad (4.29)$$

Since the FCC system possess 12 nearest neighbors and 6 next nearest neighbors. From equation 4.4, we can write

$$\gamma_1 = (2 \times 12)\, J_1 / (N/8\, g^2 \mu_B^2),$$
$$\gamma_2 = (2 \times 6)\, J_2 / (N/8\, g^2 \mu_B^2) \quad (4.25)$$

Thus, the transition temperature θ has the form: $\theta = 2S(S+1)(12\, J_1 + 6J_2) / 3k_B$ (4.26)

Similarly, the transition temperatures for each type of AFM ordering, determined for $H_0 = 0$, are also given by J_1 and J_2.

In equation 4.20,

$$T_C = C(\gamma_1 + \gamma_2)$$
$$= 2S(S+1)(12\, J_1 + 6J_2) / 3k_B \quad (4.27)$$

In equation 4.19,

$$T_{N1} = C(-1/3\, \gamma_1 + \gamma_2)$$
$$= 2S(S+1)(-4\, J_1 + 6J_2) / 3k_B \quad (4.28)$$

And in equation 4.18,

$$T_{N2} = -C\, \gamma_2$$
$$= -2S(S+1)(6J_2) / 3k_B \quad (4.29)$$

$$= -2S(S+1)(6J_2) / 3k_B \quad (4.30)$$

The results for the transition temperatures show that, in ferromagnetic ordering, the real transition temperature, T_C, and the paramagnetic transition temperature, θ, are the same in equations 4.27 and 4.28. Nonetheless, the transition temperature, T_N, for the antiferromagnetic ordering are different depending on the magnetic ordering. Based on the above mathematical treatment, we have determined the magnitudes of exchange constants J_1 and J_2 (Type-II antiferromagnetic NiO) for both oxygen rich and deficient samples using $\chi(T)$ data across the T_N. For this, we first adopted molecular-field approximation method to evaluate these constants using the following relations:

$$T_N = 2J_2 S(S+1), \quad (4.31)$$

$$\chi(T_N) = Ng^2\mu_B^2 / 12(J_1 + J_2), \quad (4.32)$$

Using $\chi(T_N) = 0.01362$ emu/mole from figure 4.1, S = 1, and g=2.23, we obtained $|J_2|$ ~133.5 K (1.15 meV)

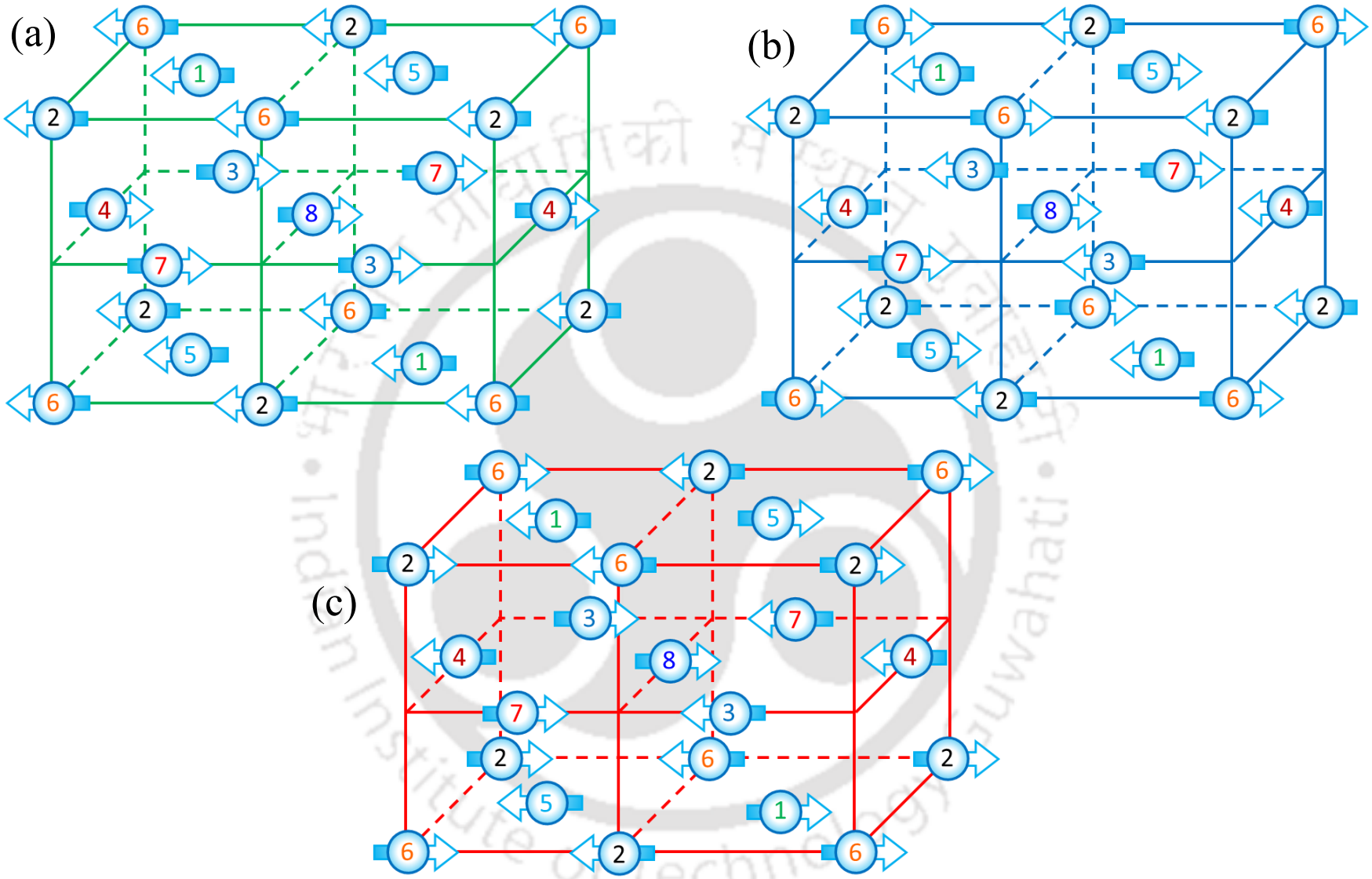

Figure 4.8: Schematic representation of different types of antiparallel spin arrangements in FCC lattice [100].

and $|J_1|$ ~18.3 K (0.15 meV) for oxygen rich NiO sample. Near T_N, it is reasonable to use S=1 since zero-point spin reduction is applicable only well below T_N. Similar analysis leads to $|J_2|$ ~ 131.5 K (1.13 meV) and $|J_1|$~ 47.87 K (0.41 meV) for oxygen deficient NiO. For Type-II (AF-2) antiferromagnetic systems, particularly NiO, the magnitude of exchange constant $|J_2|$ should be much higher as compared to the $|J_1|$ ($|J_2|>>|J_1|$) [222]. Although the calculated exchange constants follow the trend $|J_2|>>|J_1|$, these values are not in-line with the previously obtained exchange constants using Raman scattering and Neutron diffraction data [202,243]. Since, the molecular field theory neglects the higher order terms, it usually does not give accurate values of exchange constants [205]. Therefore, an attempt has been made here to estimate $|J_1|$ and $|J_2|$ using the random-phase approximation Green's-function theory in which the expression for $\chi(T_N)$ is same as in equation-2 whereas the quantity "kT_N/J_2" is a function of 'S' and the ratio $\left|J_1/J_2\right|$. Previous studies by Bartel et al. described the exchange-striction effects in both the ordered antiferromagnetic state as well as in disordered paramagnetic states of NiO using the random-phase Green's function approximation [244]. Using the similar analysis for S=1, we extracted the relation between k_BT_N/J_2 versus $\left|J_1/J_2\right|$ which is shown in figure 4.9 [244]. To obtain $|J_1|$ and $|J_2|$, we followed the successive iteration method by assuming $|J_1|$= 0 initially. Consequently, k_BT_N/J_2 = 2.67 and $|J_2|$=200 K for T_N = 534 K was obtained. Substituting the value of $|J_2|$ in equation-2 (i.e. $|J_1|+|J_2|$ = 115.2 K for $NiO_{1+\delta}$), $|J_1|$=84.8 K has been extracted. Consequently, the ratio $\left|J_1/J_2\right|$ becomes 0.424 and its corresponding value of kT_N/J_2 is 2.589. The above procedure is repeated until the convergence of both values of $|J_1|$ and $|J_2|$ are reached, the procedure finally yielding $|J_1|$ = 91 K (0.7 meV) and $|J_2|$ = 207 K (1.78 meV) for $NiO_{1+\delta}$ system. Similarly, for $NiO_{1-\delta}$ and $Zn_{0.70}Ni_{0.30}O$/NiO the exchange constants $|J_1|$ and $|J_2|$ are 32.6 K (0.28 meV) and 197 K (1.69 meV), and 56 K

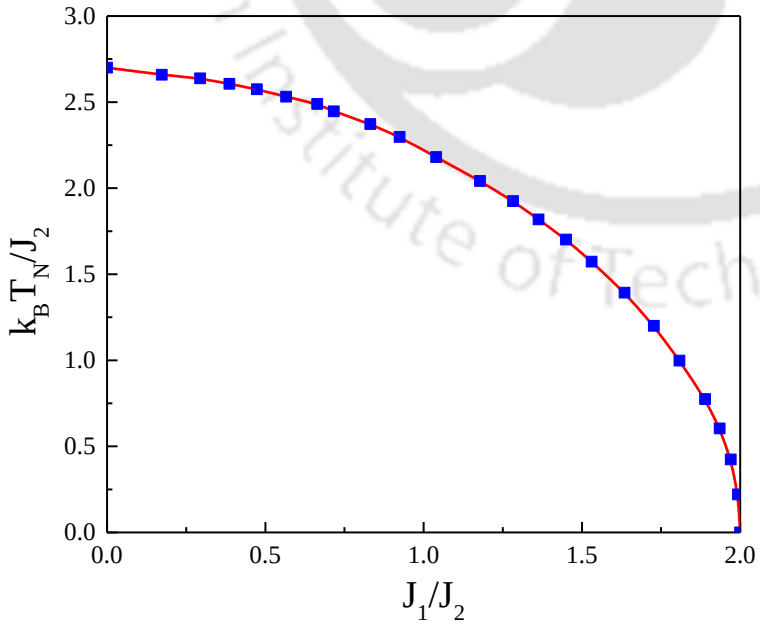

Figure 4.9: The ratio of calculated values of k_BT_N/J_2 plotted against J_1/J_2 obtained by Green's function theory for the type-II antiferromagnetic systems of f.c.c lattice with S=1 (here J_1 and J_2 are nearest neighbor and next-nearest neighbor exchange constants, respectively) [244].

(0.48 meV) and 195 K (1.68 meV) respectively. A systematic comparison of obtained exchange parameters ($|J_1|$ and $|J_2|$) with the previously available studies for various antiferromagnetic (AF) systems calculated from various experimental and theoretical methods such as Inelastic Neutron diffraction, Raman Scattering, Molecular field theory and Green's-function analysis are listed in Table-4.1. From this data one can observe that the magnitudes of $|J_1|$ and $|J_2|$ determined from the Green's-function analysis are consistent with the values obtained from the spin-wave dispersion curves (J_1 ~ 16 K (0.13 meV) and J_2 ~ 221 K (1.90 meV)) and Raman scattering (J_2 ~230 K (1.98 meV)) data, but significantly different from the values obtained from molecular-field approximation [205]. Figure 4.10 shows the phase diagram for the exchange constants J_1 and J_2 obtained from various experimental data of magnetic ions occupying the face centered cubic lattice where J_1 is less than J_2 for typical Mott-Insulators like NiO, CoO and MnO [222,245]. The bold solid lines represent the phase-boundaries between different antiferromagnetic (AF) regions; for example, systems like (*i*) NdP, NdAs, NdBi and NdSb should lie between AF1 and ferromagnetic (F) regions with $J_1 \sim 0$, (*ii*) EuO, EuS and EuSe should lie between F and AF2 with $J_1 \sim -J_2$, (*iii*) NiO, CoO, α-MnS and MnO lies between AF2 and AF3 with $J_1 \sim 2J_2$, and (*iv*) β-MnS and $Cd_{1-x}Mn_xTe$ lies between AF3 (Type-3) and AF1 (Type-1) regions with $J_2 \sim 0$. The J_1 and J_2 values obtained from the Green's function analysis are lying in the first quadrant of the phase diagram, as shown in figure 4.10, and located close to the phase boundaries between AF2 (Type-2) and AF3 (Type-3).

The temperature variation of saturation magnetization M_0 has been used to determine the magnitude of T_N for the composite system $Zn_{1-x}Ni_xO$-NiO where there is no definite transition in χ(T) curves. Thus, in order to evaluate M_0 we measured a series of magnetization isotherms (M –H) at several temperatures from H = 0 Oe up to 50 kOe and fitted the data with the modified Langevin function [112]:

$$M = M_0 L\left(\frac{\mu_P H}{k_B T}\right) + \chi_a H \qquad (4.33)$$

In the above equation, M_0 is the saturation magnetization, μ_P is the magnetic moment per particle, χ_a is the AFM component of the magnetic susceptibility and the Langevin function *L(x)* is defined as *L(x) = Coth x -1/x*. The AFM component of the magnetic susceptibility 'χ' is obtained from the slope of the linear part in high-field M-H isotherms and M_0 from the saturation point of *L(x)* in high field M-H curves. The temperature dependent behavior of M_0 for $NiO_{1+\delta}$ and $NiO_{1-\delta}$ is shown in figure 4.11. Similarly, the temperature dependence of M_0 for $x = 0.02$ and 0.2 of $Ni_{1-x}Na_xO$ bulk samples are shown in figure 4.12. An almost linear decrease in $M_0(T)$ has been observed as predicted by Makhlouf et al. and Seehra et al. [221,250]. These authors suggested that M_0 originates from the surface moments and these surface moments should vary linearly near T_N. As the temperature approaches to 'T_N' the surface moments decrease and $M_0 \rightarrow 0$. By linear extrapolation of $M_0(T)$ up to $M_0 \rightarrow 0$; we have evaluated the magnitude of 'T_N' ~ 541 K and 470 K for the oxygen rich NiO and oxygen deficient NiO samples, respectively. Similar analysis yields 'T_N' ~ 395.5 K and 486 K for $Zn_{0.77}Ni_{0.23}O$ and $Zn_{0.70}Ni_{0.30}O$ bulk samples sintered at1200°C for 12 hours in oxygen-rich ambience (Figure 4.13).

Table 4.1: The summary of the values of J_1 and J_2 calculated by the various methods for different antiferromagnetic materials.

System	Neutron Diffraction		Raman Scattering		Molecular Field Theory		Green's Function Theory	
	$-J_1/k_B$	$-J_2/k_B$	$-J_1/k_B$	$-J_2/k_B$	$-J_1/k_B$	$-J_2/k_B$	$-J_1/k_B$	$-J_2/k_B$
NiO	8.0 [206]	111 [206]	~0 [243]	107 [243]	82 [205]	65 [205]	17 [205]	101 [205]
$NiO_{1-\delta}$	–	–	–	–	47.87	131.5	32.6	197
$NiO_{1+\delta}$	–	–	–	–	18.3	133.5	91	207
$Zn_{0.7}Ni_{0.3}O$	–	–	–	–	128.5	122.5	56	195
MnO	10 [246]	11 [246]	–	–	7.1 [245]	3.3 [245]	5 [245]	5.5 [245]
FeO	12.06 [247]	21.35 [247]	–	–	7.8 [245]	8.3 [245]	-0.9 [245]	8.0 [245]
CoO	8.12 [248]	1.24 [248]	–	–	1.3 [245]	19.5 [245]	2.8 [245]	13.7 [245]
$MnTe_2$	–	–	–	–	6.7 [249]	1.6 [249]	–	–
MnS_2	–	–	–	–	5.5 [249]	5.9 [249]	–	–

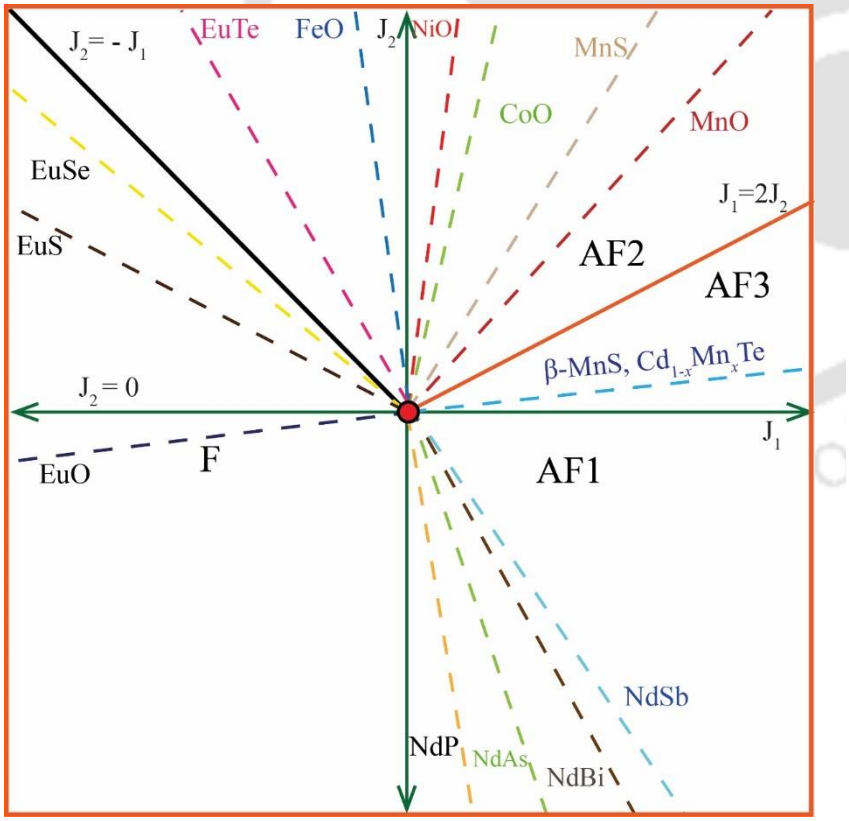

Figure 4.10: Phase diagram of type-II antiferromagnetic systems with f.c.c lattice represented in terms of the nearest neighbor and next-nearest neighbor exchange constants J_1 and J_2, respectively [222, 245].

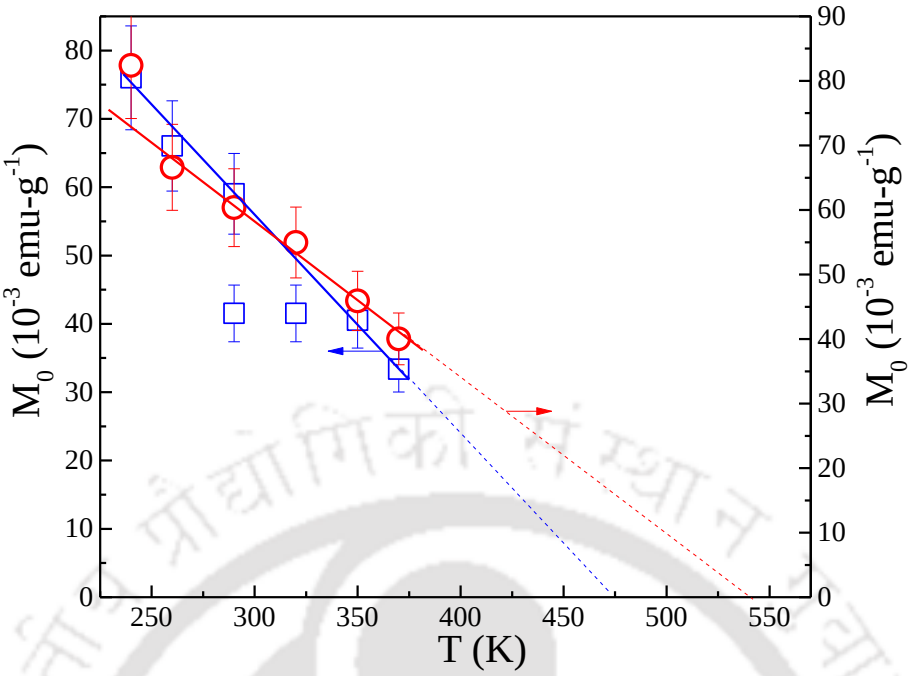

Figure 4.11: Temperature dependence of saturation magnetization 'M_0' obtained from the modified Langevin's function for $NiO_{1+\delta}$ (R.H.S scale) and $NiO_{1-\delta}$ (L.H.S scale). The solid lines connecting the data points represent linear fits whereas the dotted lines are extrapolations to $M_0 \rightarrow 0$ providing the rough estimation of the Néel temperature T_N.

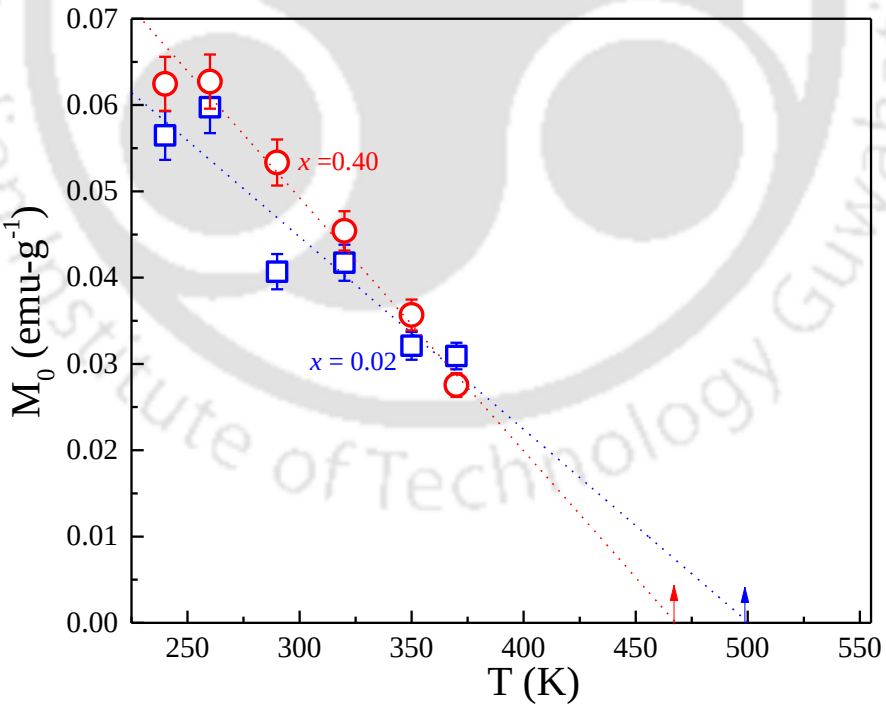

Figure 4.12: Temperature dependence of saturation magnetization 'M_0' obtained from the modified Langevin's function for $Ni_{1-x}Na_xO$ (x=0.02 and 0.40). The dotted lines connecting the data points represent linear fits whereas the dotted lines are extrapolations to $M_0 \rightarrow 0$ providing the rough estimation of the Néel temperature T_N.

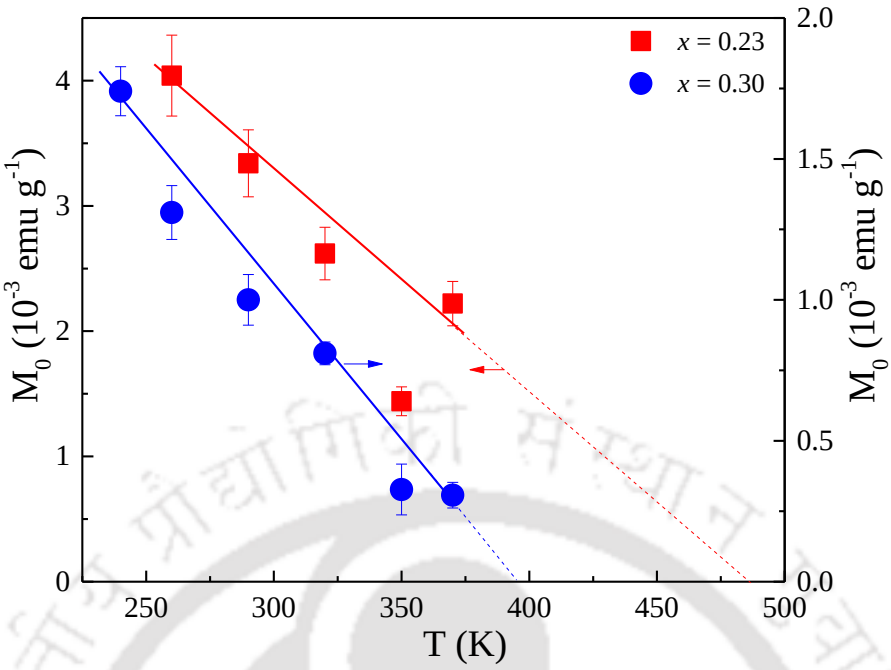

Figure 4.13: Temperature variation of saturation magnetization 'M_0' obtained from the modified Langevin's function for $Zn_{1-x}Ni_xO$/NiO (x = 0.23 and 0.30) two-phase composite system. The solid lines connecting the data points represent linear fits whereas the dotted lines are extrapolations to $M_0 \rightarrow 0$ providing the rough estimation of the Néel temperature T_N.

4.3.2 Correlating the Magnetic Ordering with Temperature Dependence of Dielectric Properties:

Figure 4.14 shows the temperature dependence of the relative dielectric permittivity ϵ_R(T) (left-hand axis) and loss-tangent Tan(δ) (right-hand axis) of the composites $Zn_{1-x}Ni_xO$/NiO with compositions x = 0.30 and 1.0 measured at ac-driving frequency $f = 10^6$ Hz. Both ϵ_R(T) and Tan(δ) exhibit similar behavior and show a hump across 539 K and a giant peak across 641 K associated with T_N (= 523 K) of NiO and T_C (631 K) of 'Ni' clusters present in the $Zn_{1-x}Ni_xO$ systems. These two dielectric anomalies are consistent with the magnetic measurements discussed above for the $Zn_{1-x}Ni_xO$/NiO system. These transitions are highly susceptible to the frequency of the applied electric field, the 'Ni' concentration in ZnO, and heat treatment conditions. [251,252] On the other hand, the charge transport mechanism in the present system follows the Mott's variable-range-hopping (VRH) of charge carriers, confirmed from the slope values obtained (-0.250) from ln(ln[ρ/ρ_0]) versus ln[T] plots. [175,176] Moreover, using the values of characteristic parameters 'ρ_0' and 'T_0' obtained from the Mott VRH analysis, we have estimated the density of states of the charge carriers across the Fermi level 'N(ϵ_F)', given by the relation $N(\epsilon_F) = 16\alpha^3/k_BT_0$, by considering the decay length 'α' ~ $10^8 cm^{-1}$. The obtained value of N(ϵ_F) is 1.642×10^{23} $eV^{-1}cm^{-3}$ and 5.06×10^{20} $eV^{-1}cm^{-3}$ for x = 0.30 and 1.0, respectively. According to the Mott VRH theory the average hopping length 'R_H' and hopping energy 'W_H' between the localized sites are related to the N(ϵ_F) by the following equations [237,238,253,254]:

$$R_H = \left[\frac{3}{2\pi\alpha N(\varepsilon_F)k_BT}\right]^{\frac{1}{4}} \qquad (4.34)$$

$$W_H = \left[\frac{3}{4\pi N(\varepsilon_F)R^3}\right] \qquad (4.35)$$

Substituting the value of decay length 'α' and density of states N(ϵ_F) to the equations (4) and (5), we obtained 'R_H' ~ 2.19 nm (0.85 nm) and 'W_H' ~ 188 meV (77 meV) for x = 0.30 (1.0). Additionally, the average hopping activation energy 'ϵ_h' has been estimated by fitting the temperature dependent ac-resistivity ρ_{ac}(T) data to the following equation: [176,186,237,252,255]:

$$\rho(T) = \frac{\hbar kT}{\Delta N_C e^2 a^2 \sqrt{\pi}} \left\{\frac{(4\varepsilon_b k_B T)^{\frac{1}{2}}}{\varphi^2}\right\} \exp\left[\frac{\varepsilon_d + \varepsilon_h(T)}{k_B T}\right] \qquad (4.36)$$

where 'ϵ_b' is the small polaron binding energy which is related to the electron-lattice coupling constant 'A', the effective ionic mass 'M', and lattice vibrational frequency ω(T) by the relation $A^2/2M\omega^2$(T). The parameter 'a' signifies the approximate distance between nearest-neighbor 'Ni' ions; 'ΔN_C' is vacancy concentration of 'Ni^{++}' ions corrected for compensating centers, 'φ' is the transfer integral corresponding to Ni^{2+}-O-Ni^{3+}, and 'k_B' is the Boltzmann constant. Substituting the value of Seebeck coefficient α in units of 2.303 k_B/e, we estimated the value of dissociation energy ϵ_d ~ 0.2 eV. Using the obtained ϵ_d value in equation (4.36) one can roughly estimate the behavior of 'ϵ_h(T)'. [181] Figure 4.15 shows the temperature variation of the hole activation energy 'ϵ_h(T)' for x = 0.3 and 1 (both oxygen rich and deficient NiO systems). These ϵ_h versus T curves exhibit clear anomalies across T_N where NiO exhibits a crystallographic transition from rhombohedral (R-3m) to cubic (Fm-3m) phase associated

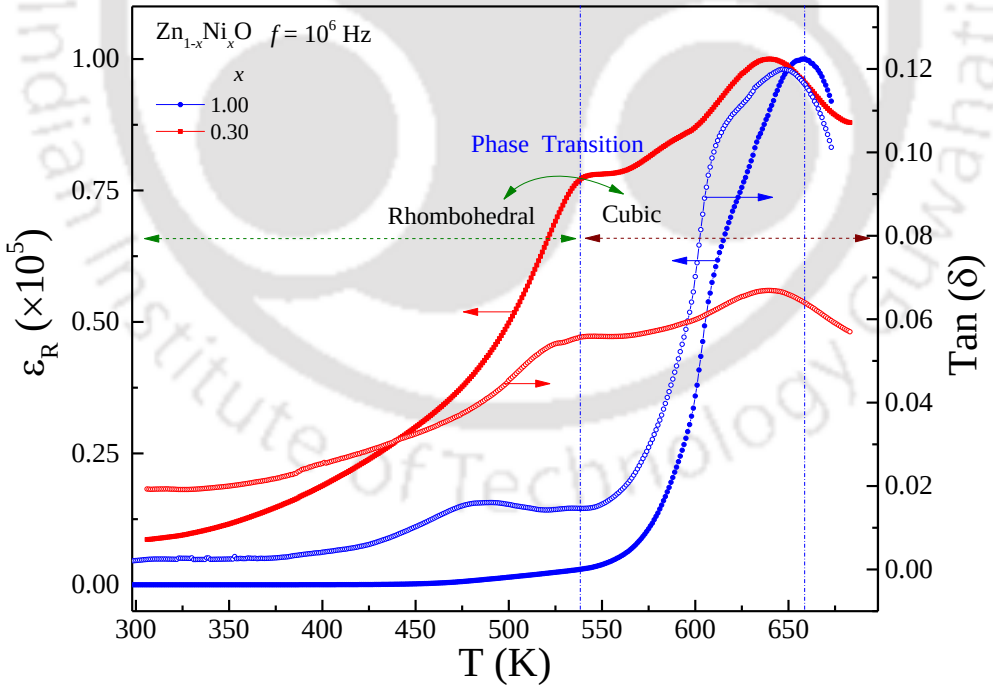

Figure 4.14: The temperature dependence of relative dielectric permittivity 'ε_R' of $Zn_{1-x}Ni_xO$/NiO for x = 0.30 and 1 measured at constant ac-driving frequency $f = 10^6$ Hz. The R.H.S scale shows the corresponding dissipation factor (Tan δ). The horizontal arrow lines indicate a crystal structure change from rhombohedral to cubic across T_N (= 539 K) of pure NiO.

with the AF to paramagnetic transition across 523 K. [246,247,256] Following the theoretical analysis reported by Keem et al. [204], the localized charge carrier hopping energy at a particular site can be determined by considering the energies of both lattice (ϵ_L) and magnetic (ϵ_m) contributions distinctly at a given temperature using the following equation:

$$\varepsilon_h(T) = \frac{\varepsilon_b}{2} + \varepsilon_m(0) - \varepsilon_m(T) = \frac{\varepsilon_b}{2} + \sum_j{}' J_{ij}\left\{\langle S_i.S_j\rangle_0 - \langle S_i.S_j\rangle_T\right\} = \frac{\varepsilon_b}{2} - 6J_{12}\langle S\rangle_0^{\,2}\{1-\xi(T)\}, \qquad (4.37)$$

In the above equation the parameter ϵ_m(T) stands for the magnetic energy of the nickel ion at temperature 'T', 'S_i' is the spin moment on i^{th} site, 'J_{ij}' is the exchange coupling parameter summed over nearest neighbors, and 'ξ(T)' is the fraction specifying the ratio of sublattice magnetization. Considering, the spin S = [S(S+1)]$^{0.5}$ $\hbar$, for divalent nickel ion, the hole activation energy is estimated as ϵ_h(T) = ϵ_b/2-12J[1-ξ(T)]. In order to evaluate the temperature variation of 'J' we extracted the magnitude of 'ξ(T)' from high-temperature dc-magnetic susceptibility data, the average hopping energy from equation (6) and 'ϵ_b' = 0.01 eV chosen from [68] and [69]. The inset of figure 10 shows 'J' versus 'T' for both the compositions (x = 0.3 and 1) which clearly shows the anomalous change in the values of 'J' between 400 K and 550 K. We obtained |J_{max}| = 0.87 meV (f = 10^6Hz) and 11 meV (f = 10^6Hz) for x = 0.3 and 1, respectively synthesized under oxygen rich conditions where we expect a stoichiometric oxide.

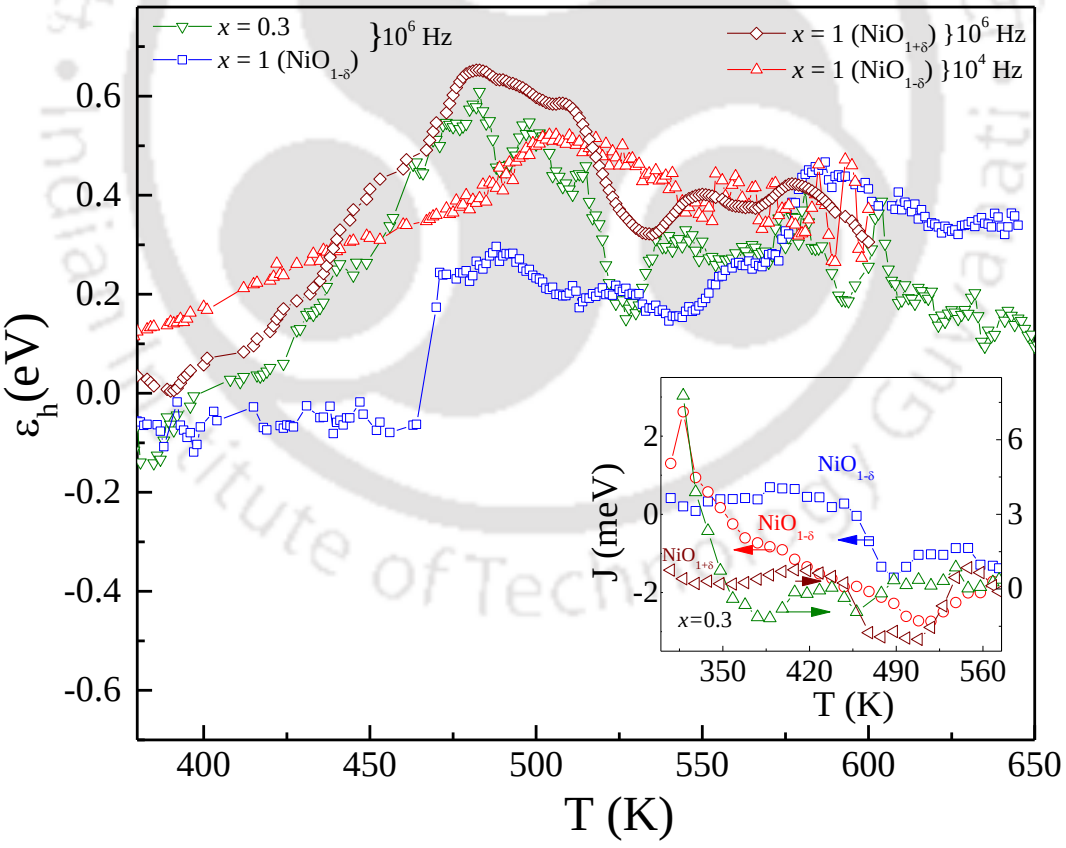

Figure 4.15: Temperature dependence of hole activation energy ε_h(T) for $NiO_{1+\delta}$, oxygen deficient $NiO_{1-\delta}$ and $Zn_{0.70}Ni_{0.30}O$/NiO evaluated for two different ac-frequencies ν = 10^6 Hz and 10^4 Hz. Inset depicts the temperature variation of the nearest neighbor exchange-coupling parameter J(T).

However, for samples prepared under oxygen deficient condition $|J_{max}|$ = 0.92 meV and 1.61 meV (for $f = 10^6$Hz). These calculated values of 'J' at different temperatures are of the same order as those 'J' values estimated in the previous section using the magnetization data and random-phase Green's function approximation.

4.4 Conclusions:

In this chapter the nature of high-temperature magnetic ordering in $Zn_{1-x}Ni_xO$/NiO and $Ni_{1-x}Na_xO$ is investigated by means of temperature dependence of magnetic-susceptibility χ(T). A systematic correlation of the magnetic exchange interaction with the ac-resistivity data has been presented. The magnitudes of exchange constants J_1 and J_2 calculated from high temperature magnetic susceptibility data for different values of 'x' are compared with the molecular-field approximation ($J_1 \sim 0.15$ meV and $J_2 \sim 1.15$ meV for $x = 1$) and Green's-function theory ($J_1 \sim 0.7$ meV and $J_2 \sim 1.78$ meV). For $Ni_{1-x}Na_xO$ system we obtained $J_1 \sim 0.20$ meV and $J_2 \sim 1.61$ meV for $x = 0.02$. The data obtained from the magnetization isotherms are fitted to the modified Langevin function $M = Mo\,L\left(\frac{\mu_P H}{k_B T}\right) + \chi_a H$ to extract the T_N of NiO clusters present in the $Zn_{1-x}Ni_xO$ matrix. Similar analysis (M_0(T)) gives T_N = 500 K for $x = 0.02$ of $Ni_{1-x}Na_xO$ system. The analysis of temperature dependence of ac-resistivity, ρ_{ac}(T), reveals the existence of VRH of charge carriers between the localized states through a mechanism involving spin-dependent activation energies. The average distance between the two successive hops, and the associated hopping energy for $x = 0.30$ was of the order of 2.19 nm, and 188 meV, respectively. The nearest-neighbor exchange-coupling parameters J_{ij} evaluated from the small-polaron model applied to the experimentally obtained ρ_{ac} (T) data for both oxygen rich and deficient composites of $Zn_{1-x}Ni_xO$/NiO shows clear anomalies across T_N. The maximum value of J_{ij} (*i.e.* J_{max} = 1.61 meV) determined from the above analysis is in agreement with the magnitude of J_2 obtained from the high-temperature magnetic susceptibility data using Green's-function analysis. The average of J_{ij} evaluated from both ac-resistivity and dc-magnetization data are close to the Exciton binding energy (~ 60 meV) of undoped wurtzite ZnO.

Chapter-V

Vibrational Excitations, Electron Spin-Resonance and Magnetic-Interactions in the Nanocomposites of $Zn_{1-x}Ni_xO$ /NiO

In this chapter, we present the formation mechanism of $Zn_{1-x}Ni_xO$/NiO nanocomposites and explore the role of surface and finite-size effects on various physical properties of the nanocomposites. This chapter also focus the vibrational excitations in these nanostructures using Raman spectroscopy, and low-temperature ($5\ K \leq T \leq 320\ K$) magnetic ordering using both electron spin-resonance and SQUID magnetometry. This chapter highlights the changes occurring in the magnetic ordering of $Zn_{1-x}Ni_xO$/NiO nanocomposites in comparison with their bulk counterparts. The introductory section presents a detailed literature review dealing with the industrial applications of low-dimensional nanostructures of ZnO/NiO and their composites together with gaps in the literature. In the later sections, we present the details of formation mechanism and the particulars of various characterization techniques employed, experimental results and their discussion followed by a brief summary of results.

5.1 Background, Motivation and Gaps in the Research Work:

The low-dimensional nanostructures of ZnO and NiO based composites have opened their prospective applications in drug-delivery, heterogeneous catalysts, supercapacitors, thermo-power generators and photo-catalysts [219, 257–259]. The fast reversible Faradaic reactions of Ni^{2+}/Ni^{3+} surface ions in NiO nano-flakes result in higher discharge capacities (70-100 %) which makes NiO/Ni a potential candidate for anode-electrodes in electrochemical supercapacitors [260]. Efficient catalytic activity, good biocompatibility, high carrier mobility, chemical stability and excellent electrochemical characteristics of these oxides make them potential candidates for novel biosensor applications as well [260–262]. Few experimental studies reveal that, nanostructures of TMO's can be used as signal enhancing platforms for highly sensitive DNA sensors [260,262]. Some recent reports revealed that the nano-composites of xanthine oxidase (XO_x) and nickel oxide based bio-electrodes exhibit superior bio-sensing response as compared to the other transition metal oxide composites [262]. Excellent thermoelectric properties and environment-friendly adsorbent characteristics of ZnO-NiO nanocomposites have drawn immense scientific attention recently [19-21]. Consequently, several authors investigated the thermoelectric properties of 'Ni' doped ZnO, and reported highest power factor (0.6 mW m^{-1} K^{-2}) and figure of merit ZT (0.09) [263,264]. Maarouf *et al*. reported a crossover from *p*- to *n*- type electrical conductivity in $ZnO–P_2O_5$/Ni composites above the percolation threshold (28 vol. %) across 400 K. These authors also reported a giant Seebeck coefficient of ~ −5000 μV/K and huge power factor of ~2×10^{-4} Wm^{-1} K^{-2} [264]. Also, the adsorbent properties of ZnO-NiO nanocomposites can be used to remove Pb(II) and Cd(II) from the aqueous solutions with larger adsorption capacity (1519.7 mgg^{-1}) [265]. Such nanocomposites can be successfully recycled for three consecutive adsorption-desorption cycles with only a marginal loss in its efficiency indicating the high reusability of the nanocomposites. These studies suggest that ZnO/NiO nanocomposite can act as environment-friendly

recyclable adsorbents for the removal of heavy metal ions from aqueous systems [265]. Such vast applications of the ZnO/NiO system motivated us to investigate its physical properties under reduced dimensions aiming to probe its fundamental behavior and explore the extent of scientific potential. Another very important aspect that has not yet been explored in these composites is the magnetic ordering with semiconducting/metallic behavior (popularly known as Semi-Magnetic-Semiconductors or Diluted-Magnetic-Semiconductors) which may find potential applications in magneto-electronic devices [123,266–269]. The magnetic, optical and transport properties of Ni doped ZnO system has been widely investigated in the literature to realize intrinsic magnetic ordering [123,266–271]. Nonetheless, a detailed investigation of the vibrational excitation, electron-spin-resonance (ESR) studies in $Zn_{1-x}Ni_xO$/NiO two-phase nanocomposites was not investigated when we started working on this problem. Focusing on the above issues, an attempt has been made to investigate the temperature dependent ESR and vibrational spectra of $Zn_{1-x}Ni_xO$/NiO nanorods of length 789 ~ nm and diameter ~ 90 nm.

5.2 Details of Synthesis and Characterization:

Different compositions ($0.002 \leq x \leq 1$) of the nanoparticles and bulk grain sized samples of $Zn_{1-x}Ni_xO$/ NiO of were synthesized by using sol-gel process as described in Chapter II. The metal-acetates of $C_4H_{10}O_6Zn$ and $C_4H_{14}NiO_8$ were first taken as precursors with oxalic acid ($C_2H_2O_4$) and ethanol (C_2H_6O) as solvents to dissolve the acetates [112]. Stoichiometric amounts of the above mentioned precursors were first dissolved in ethanolic solution under constant stirring at 70-80°C for 3 hours in air using a spiral-cooled-condenser (figure 2.2a) to obtain a green color sol. A solution containing six grams of oxalic acid was dissolved in 200 ml of ethanol and added drop-wise to the above prepared warm-transparent sol to obtain a light green color gel. This gel product was allowed to grow for 6 hours in air and then dried at 80-110˚C for 24 hours to obtain a dehydrated xerogel network (figure 2.2b). This dried mixed-oxalate product was crushed in an agate mortar and sieved through 240 Mesh to obtain fine uniform distribution of the particles. Similar procedure is implemented for the synthesis of various compositions (x) of Ni doped Zn-oxalate hydrate. For the thermal stability of the oven-dried oxalate-product and to optimize the calcination temperature we have performed the thermo-gravimetric analysis (TGA), differential thermal analysis (DTA), and differential scanning calorimetry (DSC) using a Netzsch TGA-DSC setup (Model: STA 449F3y). For this, two compositions are chosen namely $Zn_{0.99}Ni_{0.01}C_2O_4.2H_2O$ and $Zn_{0.70}Ni_{0.30}C_2O_4.2H_2O$. For this measurement a small quantity of sample in the form of fine powder was heated at a constant rate of 10˚C/min from 40˚C to 900˚C in nitrogen ambience and the weight of the sample was monitored simultaneously. Figure 5.1 shows the weight loss (%) with increase in temperature of mixed oxalate products $Zn_{1-x}Ni_xC_2O_4.2H_2O$ for x = 0.01 and 0.30. The right hand side scale of this graph represents the first derivative of weight loss DTA (-[dW/dT] vs. T). Both the curves show identical behavior except at higher temperatures, the decomposition starts much faster for x = 0.30. The first stage of thermal decomposition occurs in two different temperature regimes 124-196°C and 143-226 °C, with a weight loss of ~ 17.4 % and 17.3 % for $Zn_{0.99}Ni_{0.01}C_2O_4.2H_2O$ and $Zn_{0.70}Ni_{0.30}C_2O_4.2H_2O$, respectively. This weight loss is ascribed to the removal of crystallizing water comprising

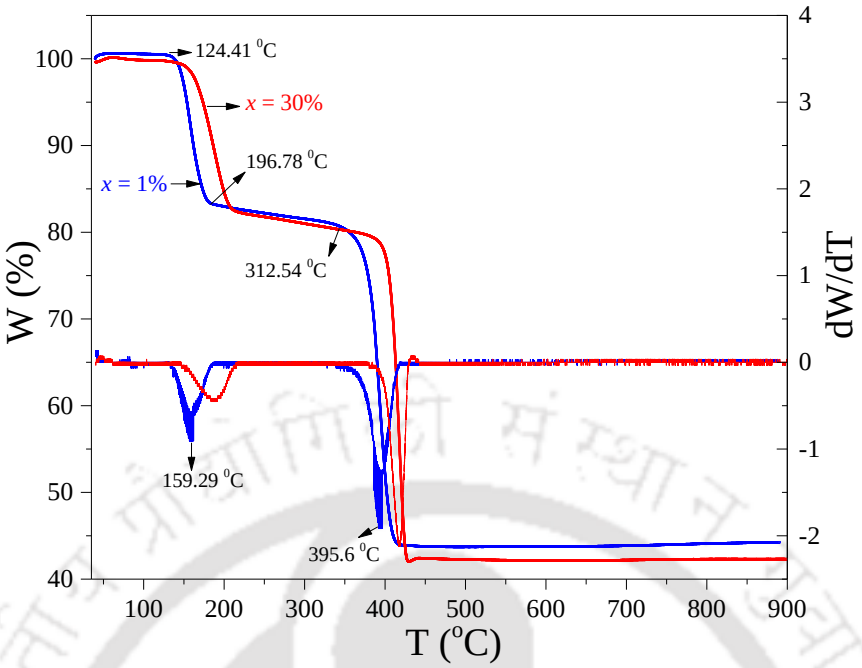

Figure 5.1: Weight percent (W(%)) versus temperature (T), *i.e.*, thermogravimetric analysis (L.H.S. scale) and differential thermal analysis dW/dT vs. T plots (R.H.S. scale) of mixed oxalate dihydrates α-$C_2O_4Zn_{0.99}Ni_{0.01}\cdot 2H_2O$, and α-$C_2O_4Zn_{0.70}Ni_{0.30}\cdot 2H_2O$ measured in nitrogen environment.

both physisorbed and chemisorbed water [112]. The maximum change in the weight loss occurs at 159.3°C and 187°C for $Zn_{0.99}Ni_{0.01}C_2O_4.2H_2O$ and $Zn_{0.70}Ni_{0.30}C_2O_4.2H_2O$ respectively, as shown by the minimum in DTA curves. The second stage of decomposition occurs quite rapidly with a maximum weight loss of ~ 37.64 % and 37.3 % in the temperature range 322-462°C and 376-443°C for $Zn_{0.99}Ni_{0.01}C_2O_4.2H_2O$ and $Zn_{0.70}Ni_{0.30}C_2O_4.2H_2O$, respectively. This rapid loss of weight can be attributed due to the decomposition of the oxalate into carbon monoxide CO and carbon dioxide CO_2 finally yielding the stable oxide-compounds $Zn_{0.99}Ni_{0.01}O$ and $Zn_{0.70}Ni_{0.30}O$ [112]. Since no significant weight-loss was noticed above 440°C, we optimized the calcination temperature (T_{cal}) to be ≥ 500ºC. Subsequently, all the synthesized samples are calcined at or above 500˚C for 2-8 hours in air for proper decomposition, yielding the desired compound $Zn_{1-x}Ni_xO$/NiO with fine ash color powder. For low nickel compositions the color of the sample looks like ash-dust color and black color powder for higher nickel compositions [112]. For large grain-sized samples, the calcined product was heated at 600˚C for 8 hours and then pressed into thin pellets using a hydraulic press followed by sintering at 1200-1350°C for 12 hours in air. Similar procedure was employed to synthesize pure NiO bulk grain size samples [112,272]. The crystal structure and chemical purity of the above synthesized samples were studied using a Panalytical-XPert Pro diffractometer and Rigaku X-ray diffractometer (model TTRAX III) with Cu-K_α radiation as source. For the electron spin resonance spectroscopic measurements, a Bruker EMX EPR spectrometer (Model 1444) working in the X-band frequency (9.451 GHz) was employed. This setup was assembled with low-temperature liquid nitrogen cryostat capable of reaching 120 K. For room temperature Raman scattering measurements two different Raman

spectrometers were used, (*i*) Horiba Jobin Yvon (LabRam HR) micro-laser Raman system operating at 514 nm wavelength excitation laser for nanocomposite system and (*ii*) Renishaw Ramascope system operating at 532 nm excitation line of an Ar^+ laser with an accuracy of ±1.5 cm^{-1} was used to investigate the vibrational spectra of bulk system. A scanning electron microscope (SEM) (LEO-1430vp) has been employed to study the morphology and microstructure of the samples.

5.3 Experimental Results and Discussion:

5.3.1 Formation Mechanism and Phase Evaluation:

Figure 5.2 depicts the X-ray diffraction pattern of both calcined product and sintered pellets at 1200°C for 12 hours in the air. This comparative representation displays significant broadening of the diffraction pattern of the nanoparticles of $Zn_{1-x}Ni_xO$ as compared to the large grain size bulk-system. Up to moderate compositions ($x \leq 0.05$) all the diffraction pattern closely resembles with the hexagonal wurtzite crystal structure of pure ZnO with space group P63mc and lattice parameters a = 3.24 Å, and c = 5.17 Å [112,122]. However, face centered cubic

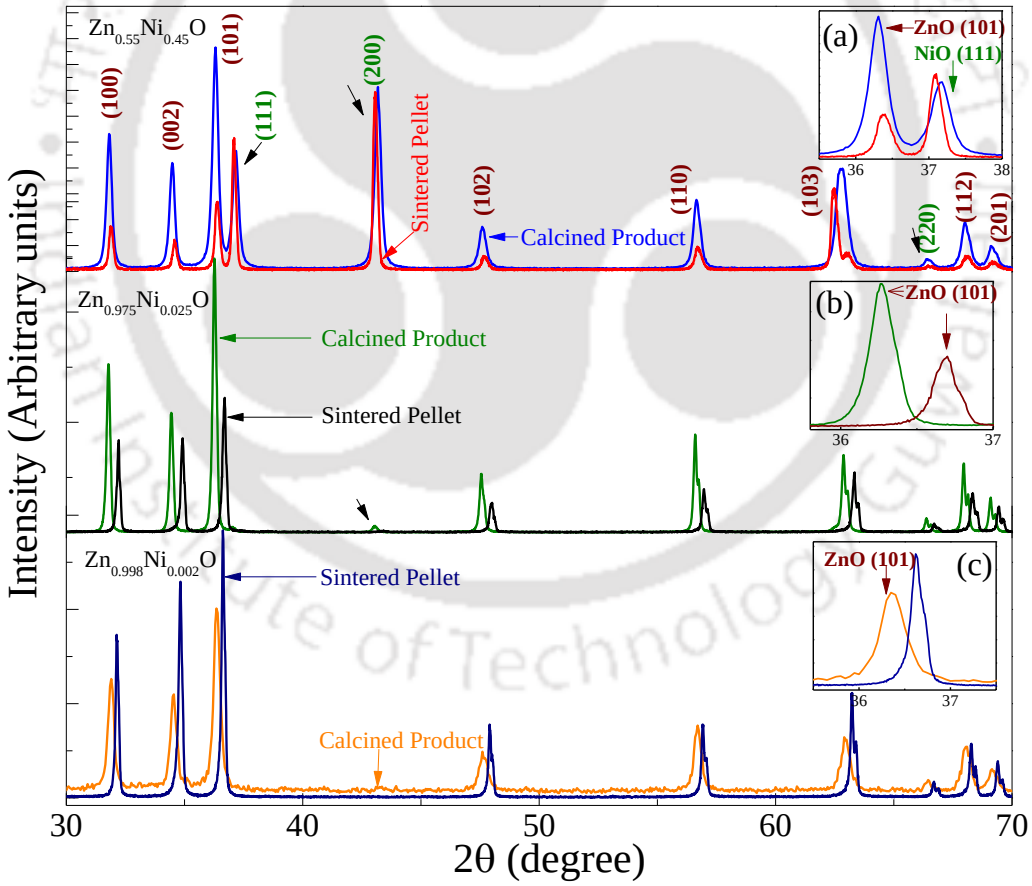

Figure 5.2: X-ray diffraction pattern of the oven dried oxalate product after calcination at 600 °C for 8 h in air and sintered pellets at 1200 °C for 12 h in air (shown by the arrows). The shift of the diffraction peak positions is clearly shown in the insets (a)–(c).

NiO emerges out as a secondary phase for higher compositions ($0.05 \leq x \leq 0.45$) (shown by the arrow marks in figure 5.2). Also, both the lattice constants '*a*' and '*c*' of the nanosize particles of primary phase increases slightly as compared to the bulk samples. The zoomed view of the diffraction intensity versus Bragg angle for the (101) plane of $Zn_{1-x}Ni_xO$ and (111) plane of NiO system is shown in the inset of figure 5.2 which clearly depicts the peak shift.

Detailed information on the composition dependence of unit-cell volume 'V_C' for primary-compound ($Zn_{1-x}Ni_xO$) and secondary-phase (NiO) under both reduced dimensions and bulk grain sizes are provided in figure 5.3. Accordingly, for lower nickel doping concentration, the hexagonal unit cell decrease which is associated with the lower ionic size of $d_{Ni} \sim 1.38$ Å of Ni^{2+} as compared with the size $d_{Zn} \sim 1.48$ Å of Zn^{2+} sites [112,183,266,272,273]. At very high doping levels the hexagonal unit cell is elongated along the *a*-axis and shrinks in the direction of c-axis for bulk $Zn_{1-x}Ni_xO$ samples. While, both the axis '*a*' and '*c*' of h.c.p $Zn_{1-x}Ni_xO$ shrinks in case of nanometer size particles leading to an overall decrease of the unit-cell volume V_c (~ 47.40 $Å^3$) as shown in figure 5.3. Nonetheless, the change in the magnitude of V_c for f.c.c. NiO clusters is very less as compared to that of $Zn_{1-x}Ni_xO$ system. In order to estimate the average grain size 'P' of the particles, we employed the Williamson-Hall (W-H) equation. The W-H analysis is governed by the below relation in which one can estimate the contribution of micro-strain 'η' on x-ray line broadening [123,239,267–269,274]:

$$\beta \cos\theta = \frac{K\lambda}{P} + \eta \sin\theta \qquad (5.1)$$

where 'β' is the full width at half maximum of diffraction peak intensity, K (~0.89) is the shape factor and λ is wavelength of Cu K_α X-ray radiation. Figure 5.4 shows the W-H plot corresponding to the '$\beta\ Cos\ \theta$' versus '$Sin\ \theta$' of both the systems nanosize particles and bulk samples of $Zn_{1-x}Ni_xO$ ($0.002 \leq x \leq 0.45$). From the slope and intercept of these plots we calculated the values of $P \sim 353.4$ Å and 225.8 Å, and 'η' ~ 1.43×10^{-3} and 5.37×10^{-4}

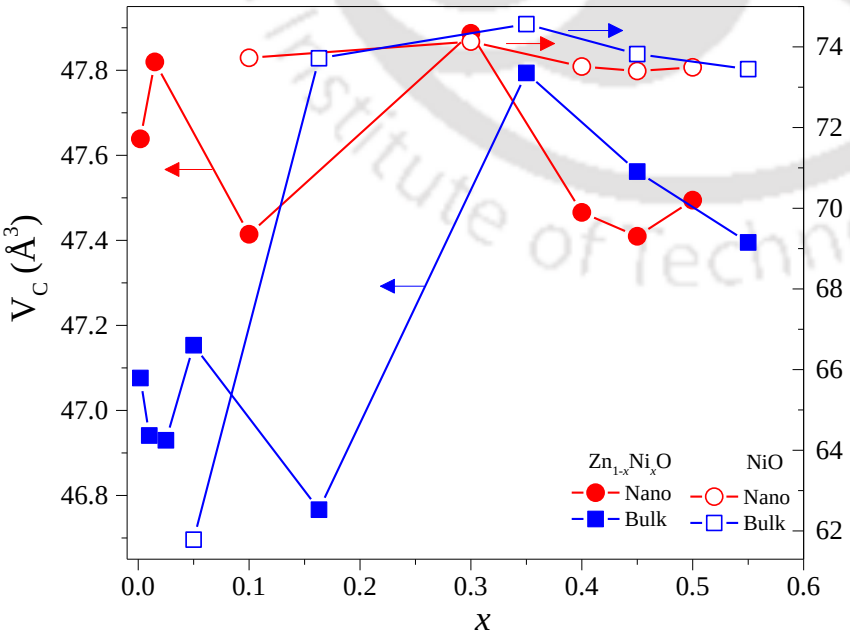

Figure 5.3: Unit-cell volume V_c as a function of composition "*x*" for both hexagonal $Zn_{1-x}Ni_xO$ major phase and f.c.c. NiO present in $Zn_{1-x}Ni_xO$ core-matrix as a secondary phase under both low-dimensional nanostructures and bulk grain sized samples.

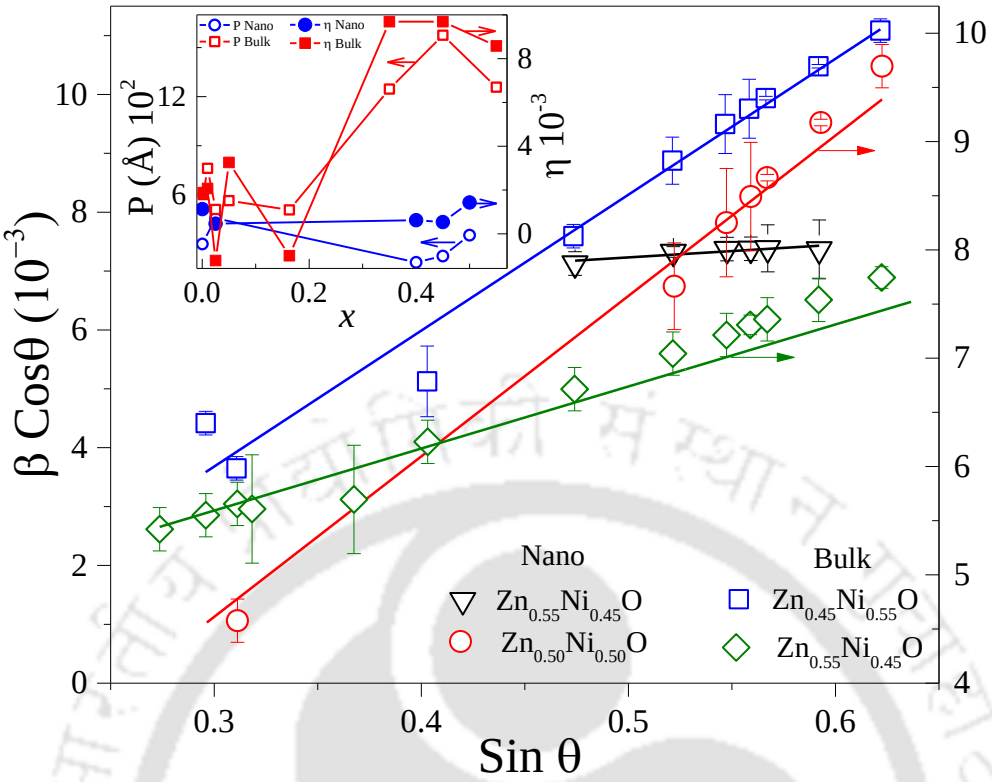

Figure 5.4: Williamson-Hall plots (β cosθ versus sinθ) of both bulk grain size pellets of $Zn_{0.45}Ni_{0.55}O$ and $Zn_{0.55}Ni_{0.45}O$ polycrystals and nanosize samples of $Zn_{0.55}Ni_{0.45}O$ and $Zn_{0.50}Ni_{0.50}O$. The inset shows variation of crystallite size "P" and micro-strain "η" as a function of composition "x."

for x = 0.50 and 0.45 of $Zn_{1-x}Ni_xO$ nanoparticles, respectively. Similarly, for bulk samples P ~ 1257.921 Å and 1575.453 Å, and 'η' ~ 9.69×10^{-3} and 8.58×10^{-3} for x = 0.55 and 0.45, respectively. The inset of figure 5.4 depicts the variation of 'P' and 'η' as a function of 'x' where both 'P' and 'η' shows a decreasing trend at low compositions and increases beyond 'x_c'. Such a dependence of average grain size and micro-strain on the doping concentration is associated with the anisotropy of the system. For $x<x_c$, the magnitude of 'η' is practically insignificant, thus, the broadening of x-ray diffraction lines is mostly due to the crystallite size effects. While, for $x > x_c$ a sudden shootout of the micro-strain occurs due to the rapid formation of the secondary phase NiO (which may distort the $Zn_{1-x}Ni_xO$ grains). Figure 5.5 shows the High-Resolution SEM micrographs recorded under secondary electron mode of the pre-sintered product of $Zn_{0.70}Ni_{0.30}O$/NiO in the form of nanocomposite. This micrograph shows randomly arranged nanorods of diameter ~ 90 nm along with the NiO nanoparticles of size 10-20 nm deposited along the length of nanorods.

5.3.2 Probing the Local Environment by Electron-Spin-Resonance Spectroscopy:

In order to understand the local atomic environment, clustering of cations and their interactions we have performed the electron-spin-resonance (ESR) measurements between 120 K and 320 K. Here two batches of nanocrystalline samples were investigated separately: First batch is nanocomposites of $Zn_{1-x}Ni_xO$/NiO system of

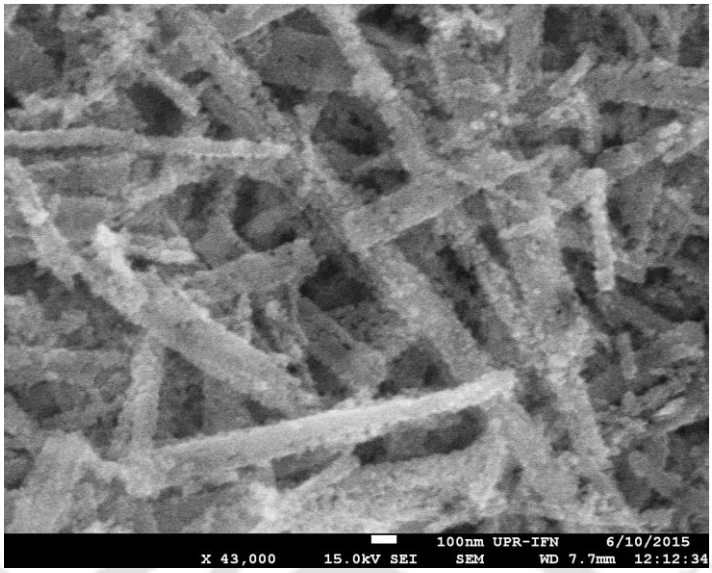

Figure 5.5: High-resolution scanning electron micrograph of $Zn_{0.70}Ni_{0.30}O$/NiO nanocomposite.

various compositions ($0.01 \leq x \leq 0.3$), and (*ii*) the second batch is consisting of pure NiO nanoparticles of average size 15 nm. Figure 5.6a,b shows the first derivative absorption spectra of ESR signal recorded at different temperatures for both batches of the samples described above. For higher compositions ($x \geq 0.30$) of $Zn_{1-x}Ni_xO$/NiO system all the spectra exhibit broad Lorentzian-type signal, however, for lower and intermediate compositions three main resonance lines are detected together with a composite asymmetric line at lower fields (Figure 5.6a). These absorption signals (from left to right) are arising due to the superparamagnetic NiO and ZnO defects [183,221,239,266,275,276]. It is evident that the intensity of first two absorption signals increases progressively with increasing the '*x*' and as the composition approaches unity the first two signals merges and an intense broad signal starts appearing. Such behavior can be attributed to increase in the strength of magnetic interaction between two adjacent Ni ions as the average distance between them is expected to decrease with increasing the composition. For higher compositions ($x = 0.30$) spectrum shows a typical shift of ~ 566 Oe from the free electron resonance field position 3373 Oe for T = 300 K. The corresponding *g*-factor is 2.4. Usually, the ground state term symbol for the Ni^{2+} ($3d^8$) $3F^4$ configuration in the octahedral crystal field is the orbital singlet $^3A_2$ (t^6_{2g} e^2_g) and the corresponding spin Hamiltonian can be written as $H = g\beta\, H{\cdot}S$ where $S = 1$ [277]. The deviation of the g-value from the free electron g = 2.0023 might be due to the admixture of terms $^3T_2$ (t^5_{2g} e^3_g) via spin-orbit coupling [278,279].

On the other hand, the ESR spectra of NiO nanoparticles of average size 15 nm recorded at various temperatures between 120 K and 308 K exhibits single broad signal without any hyperfine splitting. In the case of $Zn_{1-x}Ni_xO$/NiO system a systematic shift of resonance field H_R towards the lower fields is evident with increase of *x* in the ZnO matrix. Usually, H_R is expected to decrease with decreasing temperatures for the cubic crystal structured compounds when the magnitude of first-order anisotropy constant K_1 becomes less than zero, and H_R

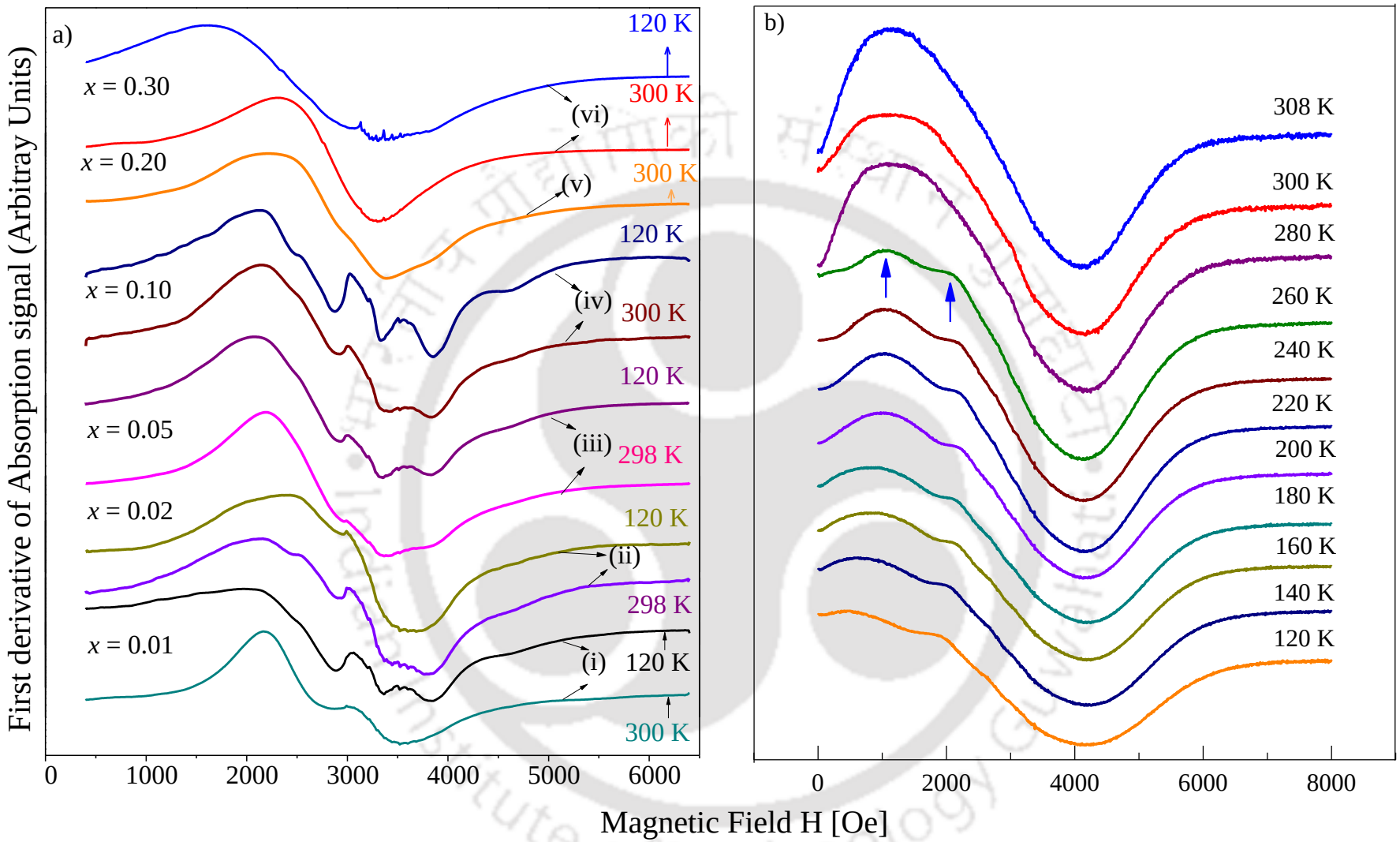

Figure 5.6: (a) First-derivative absorption signal of X-band electron-spin-resonance spectrum recorded at two different temperatures 120 K and 300 K for various compositions of $Zn_{1-x}Ni_xO$/NiO nanocomposite. (b) The first-derivative absorption signal of X-band electron-spin-resonance spectrum of pure NiO nanoparticles of size ~15 nm recorded at various temperatures dependence between 120 K and 310 K.

shows an opposite trend for systems with $K_1 > 0$ [275]. For polycrystalline samples the resonance field can be theoretically fitted with the expression $H_R = \omega/\gamma - H_I$, where $\omega = 2\pi f_m$, H_I = effective internal magnetic field and $\gamma = 2\pi g\mu_B/h$. For ferromagnetic systems with significant magnetocrystalline anisotropy the following relation holds good $H_A = -(2K_1/M_S)$, where H_A is the anisotropy field. If the first-order anisotropy constant K_1 takes negative sign then the anisotropy field becomes positive and resulting the ESR spectra to shift towards lower magnetic fields. On the contrary, if the applied magnetic field is less than anisotropy field two lines often appear in the spectra. In such kind of spectra the line with lower magnetic field corresponds to magnetic domains whose magnetization direction align parallel to the easy axis whereas the line corresponding to higher magnetic field aligns along the applied field direction [178,275,280]. Here for NiO nanoparticles the ESR spectra (figure 5.6b) exhibits significant peak broadening and the H_R shifts towards lower fields with decrease in the temperature which is a expected for ensemble of randomly oriented antiferromagnetic nanoparticles [221].

The temperature variation of H_R and peak-to-peak linewidth ΔH_{PP} of the ESR signal for both systems $Zn_{0.7}Ni_{0.3}O$/NiO and NiO nanoparticles are shown in figure 5.7. For $x \sim 0.3$ the two-phase composite exhibits $\Delta H_{PP} \sim 2076$ Oe and $H_R \sim 2310$ Oe at T = 140 K. The larger values of ΔH_{PP} are usually observed in any nanoparticle system which can be qualitatively explained by the presence of enhanced anisotropy of the magnetic nanoparticles [281]. From figure 5.7, a broad transition across 140 K has been noticed in H_R(T) while a dip in the ΔH_{PP}(T) is noticed at the same temperature for $Zn_{0.7}Ni_{0.3}O$/NiO. Such transition may be due to the blocking or fr-

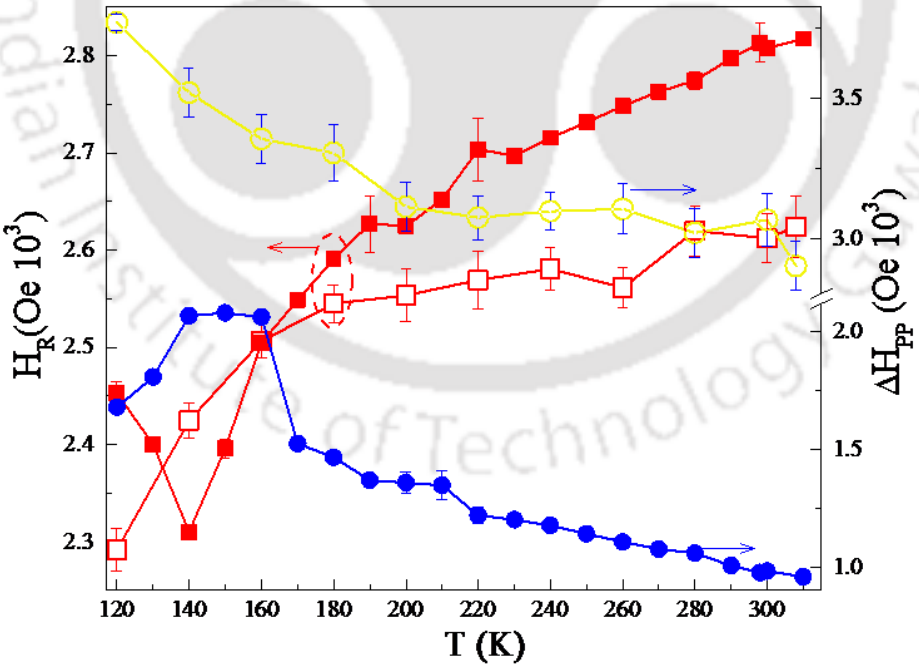

Figure 5.7: Temperature variation of the resonance field H_R (L.H.S. scale) and peak-to-peak line-width ΔH_{PP} (R.H.S. scale) of electron-spin-resonance spectra of $Zn_{0.70}Ni_{0.30}O$/NiO nanocomposite and pure NiO nanocrystallites.

-ezing effects of tiny superparamagnetic NiO nanoparticles or amorphous nickel clusters (Ni^{3+}) within the $Zn_{1-x}Ni_xO$ matrix. Such small amorphous Ni clusters within the nonmagnetic system are very difficult to trace experimentally using either the diffraction or high-resolution transmission electron-microscopic techniques. The above results indicate that for heavy doping-level the overall composite exhibits a long-range magnetic ordered system. In order to explain these results, we made a comparative analysis between the Ni doped ZnO system and pure NiO. It is well known that bulk NiO exhibits antiferromagnetic ordering with Néel temperature T_N ~ 523 K, [183] therefore, at higher temperatures (T >140 K) the long-range magnetic ordering is not expected either from NiO or amorphous Ni^{3+} because the blocking temperatures of such superparamagnetic particles generally appear at low temperature [221]. Furthermore, it is challenging to observe ESR signal in stoichiometric NiO because of extremely large linewidth (Figure 5.7). Previous studies on the single crystals of ZnO-Ni system by Holtan et al. reported a very high intensity anisotropic ESR signal corresponding to the nickel ions existing in the 3^+ valence state with spin S = 3/2 occupying the tetrahedral Zn^{2+} sites [43]. If some of the Ni clusters are presented with the oxidation states 2^+, 3^+ and 1^+ individually at the interstitial sites of the nanocomposite, one should expect a strong symmetric Lorentzian line corresponding to Ni^{3+} and Ni^{2+} species in $Zn_{1-x}Ni_xO$/NiO [282]. In the present case the observed ESR signal in composite system across the room temperature is expected due to the $Zn_{0.7}Ni_{0.3}O$ only which confirms the incorporation of Ni^{2+} ions at Zn^{2+} sites. Therefore, the conclusions gathered in the previous report using the XPS spectra are further supported by the ESR studies [283].

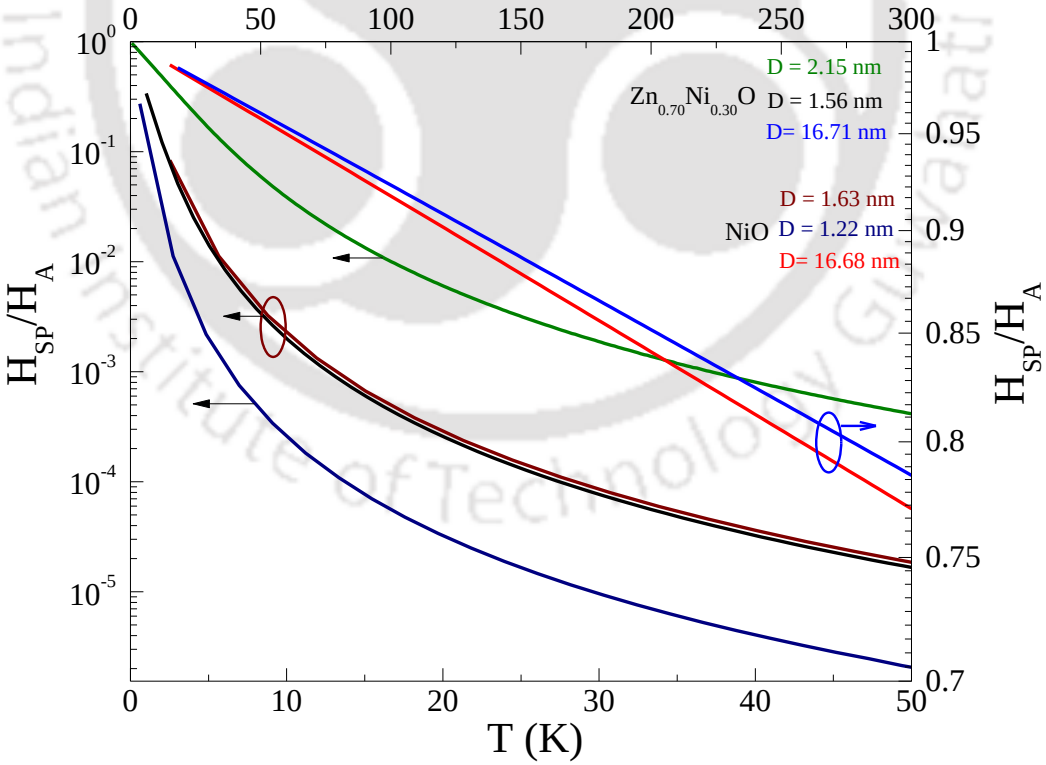

Figure 5.8: Simulated curves of ratio of anisotropy energies of nanosize particles and bulk crystals (H_{SP}/H_A) versus temperature (T) for different sizes of amorphous Ni^{3+} crystals possibly present in both $Zn_{0.70}Ni_{0.30}O$ and NiO system.

Usually, the anisotropic spin interactions are responsible for the broadening of the ESR linewidth ΔH_{PP}, however, the exchange interaction causes narrowing of ΔH_{PP}, such that, $\Delta H_{PP} \sim H_A^2/H_{ex}$, where H_A and H_{ex} are the equivalent anisotropy and exchange fields, respectively [239]. Besides, the effective anisotropy (K_{eff}) also has substantial influence on the H_R because the peak-to-peak broadening is controlled by the anisotropic spin and exchange interaction [221,284]. Quantitatively, one can relate the crystallite size (P), exchange field (H_{ex}), peak-to-peak line width (ΔH_{PP}), saturation magnetization (M_o) and, bulk and surface anisotropy constants (K_b, K_s) are linked according to the following relation [111].

$$\Delta H_{PP} \sim \frac{4\,(K_b+\frac{6}{P}K_s)^2}{H_{ex}{M_o}^2} \qquad (5.2)$$

For a spherical nanoparticle the effective anisotropy constant (K_{eff}) is related with the bulk and surface anisotropy constants, K_b and K_S, respectively as $K_{eff} = K_b + (6/P)K_S$. Due to the dominance of uncompensated surface spins, the surface anisotropic constant (K_S) increases with the reduction of 'P' which in-turn results in the enhancement of the K_{eff}. In the case of a perfect antiferromagnetic system the absorption derivative should decreases gradually and become invisible on approaching the antiferro- to paramagnetic Néel temperature T_N [284]. Majority of the previous reports shown that the existence of broad ESR line at temperatures close to 10 K suggesting the presence of dipole-dipole interaction and exchange interactions [284].

5.3.2.1 Implementation of Raikher and Stepanov model:

At room temperature NiO nanoparticles exhibits isotropic line of Lorentzian shape with H_R = 2724 Oe (figure 5.6b). Close examination of the spectra recorded for T< 260 K exhibits a shoulder across H=2064 Oe due to the superposition of two isotropic signals with different absorption intensity as shown by arrow mark in figure 5.6b. The extent of splitting becomes more prominent at low temperatures which give the signatures of very tiny amount of amorphous Ni^{3+} species with strong relaxation mechanism [285]. Appearance of such new signal in the ESR spectra of NiO nanoparticles at low temperatures has also been observed in various other binary antiferromagnetic systems with triangular lattice (Yafet-Kittle type) [286]. Between the temperatures 308 K and 280 K the spectra were symmetric but for T ≤ 260 K the symmetry breaks down and the degree of asymmetry increases with decreasing the temperature. It is clearly evident from the right-hand-side scale of figure 5.7 that upon cooling, ΔH_{pp} of pure NiO nanoparticles increases progressively and reaches its maximum value at 120 K. Up to 180 K the resonance field H_R decreases slowly but below 180 K, H_R drops rapidly to its lower values (~ 2.25 kOe) and ΔH_{pp} increases abruptly for T < 180 K. This behavior may be attributed to the blocking or freezing of the spins below 180 K as evident from the previously reported magnetization data [112,284,286–288]. For a rough estimation of the size of Ni^{3+} amorphous clusters we used the Raikher and Stepanov model of dispersed ferromagnetic nanoparticles for cubic symmetries [275,289,290]. For this study we used the analysis done by de-Biasi and Devezas [53], accordingly, a mathematical relation is formulated by focusing the ratio of the surface anisotropy field (H_{SP}) to the bulk cubic anisotropy (H_A~103 Oe) with the function $\xi = M_S VH/k_B T$. The quantities in the above function 'ξ' are (*i*) 'V' is the volume of the nanoparticle, (*ii*) M_S (~ 27 emu g^{-1}) is the intrinsic

magnetic moment and (*iii*) k_B being the Boltzmann constant. After averaging over the angle 'θ' between the magnetic moment and the magnetic field, the exact relation between the above mentioned parameters turns out to be [275]

$$\frac{H_{SP}}{H_A} = \frac{1 - 10\xi^{-1}\,Coth(\xi) + 45\xi^{-2} - 105\xi^{-3}\,Coth(\xi) + 105\xi^{-4}}{Coth(\xi) - \xi^{-1}} \qquad (5.3)$$

We first plotted the variation of H_{SP}/H_A as a function of 'V' for two different set of 'H_R' and 'T' obtained from our ESR measurements (2.817×10^3 Oe, 120 K and 2.452×10^3 Oe, 300 K). The intersect of these two curves provides the magnitude of 'V' and is the solution for above equation for the two sets of 'H_R' and 'T' mentioned above. We then back substituted the value of 'V' in $\xi = M_S VH/k_B T$ and in equation (5.3), and generated the temperature variation of H_{SP}/H_A for both the systems $Zn_{0.7}Ni_{0.3}O$/NiO nanocomposite as well as NiO nanoparticles separately (shown in figure 5.8). From the known values of M_S, 'H_R' and 'V' we have evaluated the size ($2r = [6V/\pi]^{1/3}$) of the amorphous Ni^{3+} clusters in $Zn_{0.7}Ni_{0.3}O$ matrix. At temperatures close to 120 K and for resonance field $H_R = 2.817\times10^3$ Oe, the size of the amorphous Ni^{3+} clusters turn out to be 2.15 nm. For $H_R = 2.452\times10^3$ Oe and T = 300 K their size becomes 1.56 nm. Similar analysis for the case of pure NiO nanoparticles yields the size of the Ni^{3+} clusters to be 1.63 nm and 1.22 nm for $H_R = 2.817\times10^3$ Oe (T=120K), and 2.452×10^3 Oe (T=300K), respectively. Over-all, a ferromagnetic material with high uniaxial anisotropy H_A, the resonance field is expressed as $H_R = (h_o f/2\mu_B) - H_A$; where '$h_o$' is the peak to peak height of the ESR signal and 'f' is the frequency of the microwave radiation. According to the above relation, the resonance field should shift towards the low field side by H_A and the effective 'g' value will increase. In the present case, we observed a significant decrease of H_R with decreasing the temperature. This scenario is associated with the increase of anisotropy of the overall composite system. So, we expect that anisotropy field plays a major role on the observed ESR spectra. Such signatures can be easily traced by means of large coercive fields (H_C) at low temperatures. Since the system under investigation is a polycrystalline material with randomly oriented nanometer size spherical particles, the demagnetizing fields associated with the anisotropy may also cause the resonance field to shift to lower values.

Figure 5.9a,b shows the absorption intensity ($I_0 = (\Delta H_{PP})^2 h$) and the peak-to-peak height (h_o) of the ESR spectra as a function of temperature for both the systems $Zn_{1-x}Ni_xO$/NiO nanocomposite and NiO nanoparticles. Figure 5.9a provides more extensive confirmation for the existence of blocking/freezing effects below 140 K where the temperature variation of intensity of the ESR signal 'I_o(T)' and h_o(T) displays a clear anomaly across 140 K suggesting the blocking effects of the magnetic nanoparticles. Nonetheless, for NiO nanoparticles the quantities I_o and h_o rapidly increase with lowering the temperature and reach a maximum value across 200 K and decreases rapidly below 180 K. Such reduction in I_0 and h_o for T < 180 K also strongly corroborates the blocking/ freezing of the spins associated with the reduction of the magnetic-moment as observed in the previously reported magnetization data [221,284,286–288].

5.3.2.2 Statistical Analysis using Nagata and Ishihara Model:

For a complete understanding of the variations in H_R and ΔH_{PP} in an ensemble of magnetic nanoparticles we implement the statistical analysis proposed by Nagata and Ishihara [291]. According to this model the demagnetization field associated with the shape anisotropy of the ellipsoidal magnetic nanoparticle in which the major-axis aligned along the applied magnetic-field direction results significant changes in the H_R and ΔH_{PP} [291]. Randomly oriented polycrystalline ellipsoidal-shape nanoparticles with the major axis aligned along the applied field direction can cause considerable variations in the H_R and ΔH_{PP} values. Consequently, all the nanoparticles which are oriented partially should exhibit the square power-law variation of the ΔH_{PP} which will be proportional to the shift of mean resonance field $\delta H_R \propto (\Delta H_{PP})^{n=2}$. However, for randomly oriented nanoparticles δH_R should be proportional to $(\Delta H_{PP})^3$. In order to understand the effective orientation of the nanoparticles the above statistical analysis has been carried out. Considering the typical values of g ~ 2.23 and H_R ~ 2970 Oe for the case of perfect NiO without any defects or secondary phases (for T > 310 K) and by making use of the equation $\delta H_R = 2970 - H_R(T)$, we have plotted the log-log plots *i.e.* ln [δH_R] as a function of ln [ΔH_{PP}] (Figure 5.9). Accordingly, we have estimated the value of '*n*' from the ln-ln graph between δH_R and ΔH_{PP} as shown in the inset of figure 5.9b. The slope of ln δH_R versus lnΔH_{PP} graph gives n = 2.13 for $Zn_{1-x}Ni_xO$/NiO composite and 2.85 for NiO nanoparticles. Thus, we conclude that n = 2.13 is close to the value predicted theoretically for partially oriented nanocrystallites present in the composites, however, n = 2.85 (~3) suggesting the random orientation of the NiO nanoparticles.

5.3.3 Vibrational Excitations using Raman Spectroscopy:

In order to probe the role of NiO on the vibrational properties and molecular bond structure of $Zn_{1-x}Ni_xO$, Raman spectroscopic measurements was performed for both the nanostructures and bulk grain sized samples. Figure 5.10a shows the Raman spectra recorded at Room temperature for various compositions of $Zn_{1-x}Ni_xO$/NiO ($0.30 \leq x \leq 1$) under the backscattering configuration. All these nanocomposites exhibit first order Raman scattering modes at 439 and 573 cm^{-1} similar to pure ZnO which are assigned with high frequency E_2(h) mode and longitudinal optical E_1(LO) mode, respectively [292–294]. The sharp and intense nature of E_2(h) peak confirms the presence of wurtzite h.c.p. crystal structure of ZnO [58, 59]. Nevertheless, this peak becomes more diffusive and broad as the 'Ni' concentration increased inside ZnO matrix, suggests the increased degree of disorderness as the 'Ni' doping concentration increases [243]. These results are consistent with our X-ray diffraction patterns discussed earlier in section 4.4.1. These spectra did not show the presence of low frequency non-polar E_2(l) mode (usually appears across 101 cm^{-1}) since this wavenumber lies outside the lower limit of our experimental setup. Furthermore, broadness of E_1(LO) mode was ascribed to the relaxation of Raman selection rule caused by lattice defects and significant amount of distortion present in the system. Further, we observed the signatures of second order Raman scattering in these two-phase nanocomposites due to the disordered nature of crystal structure which enables the two-phonon scattering process outside the first Brillouin zone.

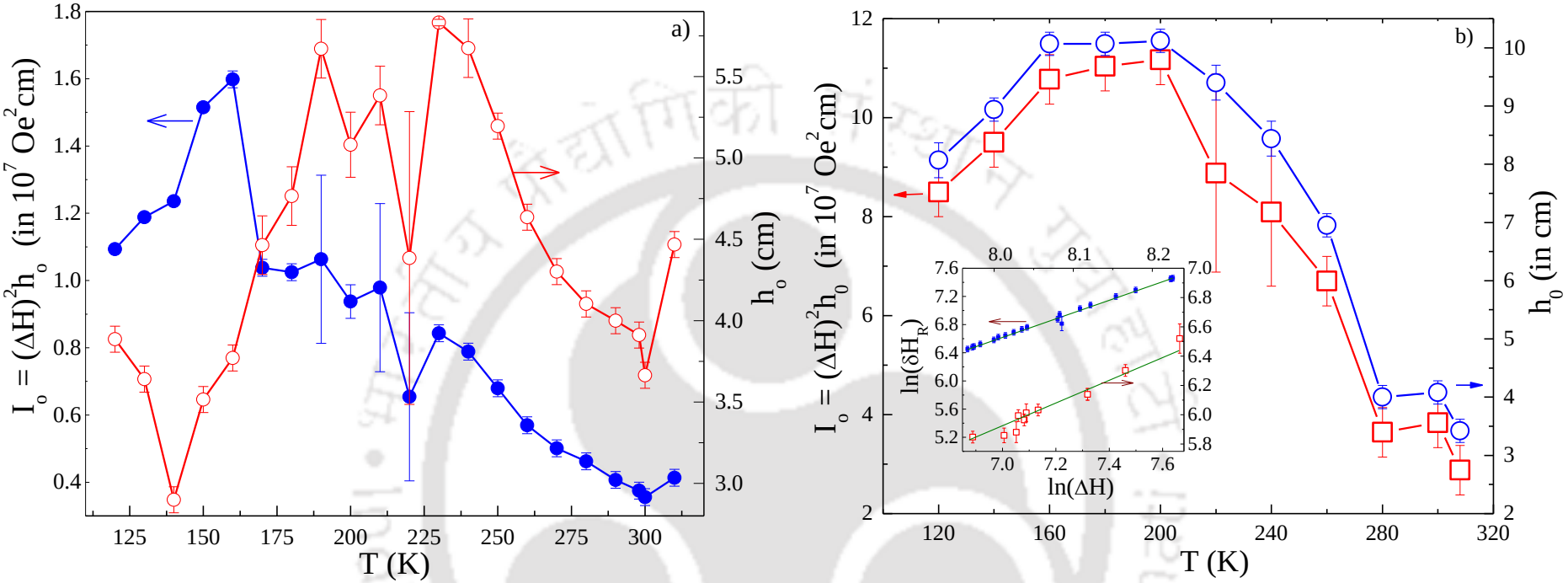

Figure 5.9: (a) Intensity [$I_0 = (\Delta H)^2 h_0$] of the electron-spin-resonance signal versus temperature (T) (L.H.S. scale) and peak-to-peak height (h_0) versus temperature (T) (R.H.S. scale) of $Zn_{0.70}Ni_{0.30}O$/NiO composite system. (b) The temperature dependence of electron-spin-resonance signal Intensity [$I_0 = (\Delta H)^2 h_0$] (L.H.S. scale) and peak-to-peak height h_0(T) (R.H.S. scale) of pure NiO nanocrystallites. The inset shows ln[δH_R] versus ln[ΔH_{PP}] of both $Zn_{0.70}Ni_{0.30}O$/NiO nanocomposite and pure NiO nanoparticles.

Theoretically, the hexagonal wurtzite ZnO with C_{6v} point group symmetry exhibits twelve phonon modes, among which nine modes will be optical and three modes will be acoustical phonon modes [292]. Usually, only eight optical modes appear in the Raman spectra of pure ZnO which are mathematically expressed by the relation $A_1 + 2E_2 + E_1$, where A_1 and E_1 branches further split into longitudinal optical (LO) and transverse optical (TO) modes due to the presence of Columbic force [292,294,295]. The 'E_2' mode is associated with the nonpolar characteristics of ZnO and further splits into high frequency $E_2(h)$ mode and low frequency $E_2(l)$ mode related with the motion of 'O' and 'Zn' sub-lattice, respectively [292]. Instead, pure NiO exhibit one-magnon mode, five vibrational modes and a two-magnon mode in its Raman spectra [296–298]. The magnon modes are temperature dependent and completely disappear across the Nèel temperature T_N (~ 523 K) of NiO. Further, the second order Raman modes are observed at 330.06, 677, 987 and 1141 cm^{-1}, corresponding to $[E_2(h) - E_2(l)]$, $[E_1(TA) + E_1(LO)]$, $2E_1(TO)$ and $2E_1(LO)$, respectively [291,293,294]. These second order Raman modes do not show any specific variation by increasing the 'Ni' content. Additionally, we have observed few extra Raman modes at 558, 900 and 1584 cm^{-1} associated with the presence of secondary phase NiO which is the only antiferromagnetic constituents in the nanocomposite [296,299,300]. In the paramagnetic regime ($T > T_N$) where NiO exhibits perfect cubic crystal structure the zero wave-vector phonons transform as Γ_4^-, hence no first order phonon scattering is expected for NiO [296]. Nevertheless, for the pure NiO we observed two first order vibrational phonon modes; (*i*) transverse optical phonon mode (TO) at 402 cm^{-1} (a broad hump in the Raman spectra), and (*ii*) longitudinal optical phonon mode (LO) at 551 cm^{-1} for the pure NiO nanocomposites [296]. The main origin of these first order Raman modes is due to the parity-breaking-via-imperfections caused by nickel vacancies [296]. Such first order phonon modes shift towards lower frequency side as compared to standard reported values for NiO [296,298–300]. Earlier work by Dietz *et al*. reveals that the oxygen content in NiO plays a major role on the Raman scattering which ultimately decides the global shift of this spectra towards low wavenumbers (440 cm^{-1} to 400 cm^{-1}) [296]. Their results suggest significant decrease in the strength of first order vibrational modes for oxygen rich NiO as compared to the perfect stoichiometric NiO. On the other hand, the vibrational modes appeared at 740, 880 and 1094 cm^{-1} for NiO nanoparticles are assigned as combinational modes of 2TO, TO+LO and 2TO, respectively [299,300]. Nevertheless, the weak peak depicted by the dotted-line at 1550 cm^{-1} (2M) in all samples is associated with scattering from two-magnon process driven by large inter-sub-lattice exchange interaction.

On the contrary, the bulk samples exhibit slightly different Raman spectra. Figure 5.10b shows the Raman shift of various compositions for the two-phase bulk-composite system $Zn_{1-x}Ni_xO$/NiO. These spectra depict an intense mode at 437.8 cm^{-1} assigned as non-polar $E_2(h)$ mode which is a specific characteristic of h.c.p. ZnO [292–294]. The other first order vibrational modes are observed at 97.9, 378.4, 407.7 and 583.6 cm^{-1}, corresponding to $E_2(l)$, $A_1(TO)$, $E_1(TO)$ and $A_1(LO)$ modes, respectively [292–294]. All these first-order modes are consistent with the previously reported values of single crystalline ZnO [292–294,300–304]. The $E_2(h)$ and $E_2(l)$ are non-polar modes associated with the vibrations of 'O' and 'Zn' atoms, respectively [292–294]. We also observed the signature of second-order Raman scattering at 201.8, 330.8, 537.3 and 1149 cm^{-1} corresponding to $2E_2(l)$,

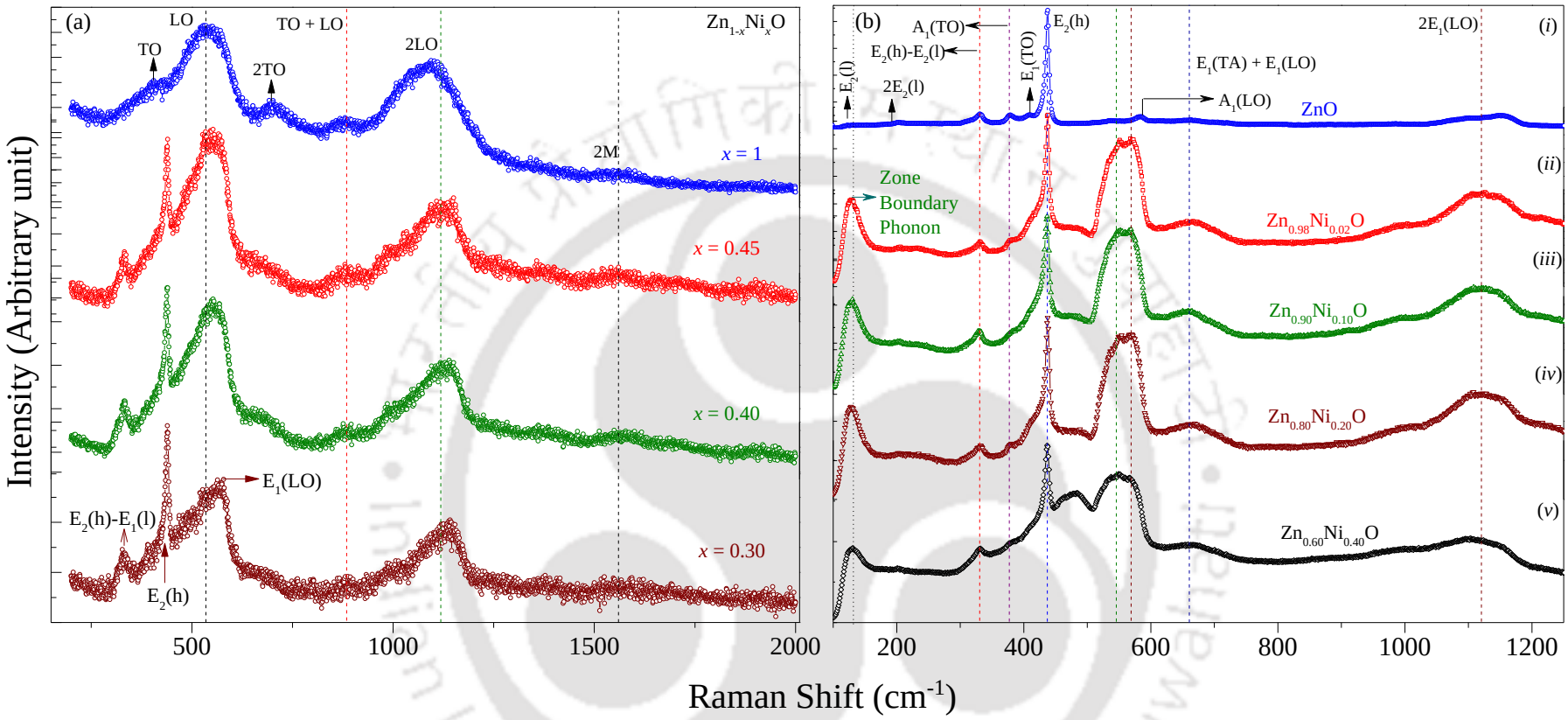

Figure 5.10: Raman shift of $Zn_{1-x}Ni_xO$/NiO two-phase (a) nanocomposite and (b) bulk system.

[E_2(h)-E_2(l)], [E_2(*h*)+E_2(*l*)] and 2E_1(LO), respectively [292–294]. Such second order Raman modes appear due to the disordered nature of crystal structure whose wavenumbers are determined by the selection rules of two-phonon scattering processes [292–294]. Moreover, the intensity of E_2(*h*) mode diminishes and the peak width increases for $x > 0.05$ (figure 5.10 b ii-v). Such weakened behavior of E_2(*h*) mode is the indication of the onset of destabilization of wurtzite h.c.p. nature of $Zn_{1-x}Ni_xO$ and dominance of F.C.C NiO of the composites [305]. The rapid change in the unit-cell volume 'V_C' of wurtzite h.c.p. $Zn_{1-x}Ni_xO$ and F.C.C. NiO can be clearly seen from figure 5.3. Also, the incorporation of 'Ni' leads to decrease in symmetry of the first order Raman modes which indicate increase in the distortion of the h.c.p. lattice within the $Zn_{1-x}Ni_xO$/NiO [293]. These results are further supported by our crystal-structure analysis where a sudden increase of the micro-strain 'η' was observed due to the rapid formation of the secondary phase NiO which may influence the microstructure of $Zn_{1-x}Ni_xO$ (inset of Figure 5.4).

Moreover, a broad and intense band across 560 cm^{-1} was observed which becomes wider and splits by increasing the doping level. Usually, the appearance of such additional modes is ascribed to the localized vibrational modes (LVM) of impurities or defects [306,307]. The highest frequency of these LVM can be estimated using a simple mass-defect approximation given by the relation [308]:

$$\omega_{LVM} \approx \omega_{ZnO}\sqrt{\frac{\mu_{ZnO}}{\mu_{NiO}}} \qquad (5.4)$$

where μ is the reduced mass of ZnO and NiO. However, using this approximation the estimated highest LVM frequency (~ 442 cm^{-1}) is considerably lower than the frequency of the observed mode (~ 560 cm^{-1}). Therefore, this additional mode could be one of the silent Raman modes of wurtzite ZnO, as proposed by Serrano et al. using the density of phonon states (DOPS) calculations for wurtzite-ZnO [309]. Previous studies by Bundesmann *et al*. reported that the anomalous Raman mode appeared between wavenumbers 500 cm^{-1} and 600 cm^{-1} is due to the intrinsic host-lattice defects related to the Ga doping inside wurtzite ZnO [310]. Hung et al. explained that such behavior originates due to the dominance of DOPS of the high-energy phonon branch [305]. A large peak-width is a typical characteristic of such high-energy phonon modes, which is clearly noticed in the present case (figure 10-b) [311]. Usually, the DOPS emerge in highly degenerated crystals where the translational invariance of the crystal lattice is weak, which finally leads to the relaxation of Raman modes and allows the scattering events from the whole Brillouin zone [305]. Another additional mode at 129 cm^{-1} is noticed in all the samples of $Zn_{1-x}Ni_xO$/NiO system (as shown in figure 5.10b indicated with a black color dotted line). This additional feature was mainly associated with the antiferromagnetic NiO present in the $Zn_{1-x}Ni_xO$ matrix [305]. This mode appears much above the low-frequency 1M magnon mode (~ 37 cm^{-1}) of NiO, thus the possibility of 1M magnon mode is ruled out [292]. Earlier studies showed the strong temperature dependence of this Raman mode which disappear above 300 K and reappears during cooling, but did not show any peak-shift [292]. Such behavior may be associated with the Zone boundary phonon effects, which are usually forbidden in the Raman spectroscopy but can be

allowed in the presence of strong magnetic interaction between two successive 'Ni' atoms present in ZnO matrix [292].

5.3.4 Magnetic Properties of Nanocomposites of $Zn_{1-x}Ni_xO$/NiO:

Figure 5.11 shows the temperature dependence of dc-magnetic susceptibility, ($\chi(T)=M(T)/ H_{dc}$) measured under zero-field-cooled (ZFC) and field-cooled (FC) conditions at an external applied magnetic field H_{dc} = 500 Oe for different crystallite sizes (4.1 nm ≤ d ≤ 22 nm) of $Zn_{1-x}Ni_xO$ (for x=1). The main feature of these curves is bifurcation between the χ_{ZFC} and χ_{FC} curves below the Blocking temperature ($T_B = T_1 \sim 105$ K) indicating the superparamagnetic behavior of the fine-particles. We also observed a systematic in T_B (from 290 K to 115 K) with increase in particle size d from 4.1nm to 22.0 nm. The effect of external magnetic field and particle size on the nature of blocking temperature T_B are discussed below. In order to understand the nature of magnetic interactions, we have determined the magnitudes of exchange constants J_1 and J_2 associated with the nearest and next-nearest-neighbor exchange parameters, respectively. We used the molecular-field approximation method for Type-II anti-

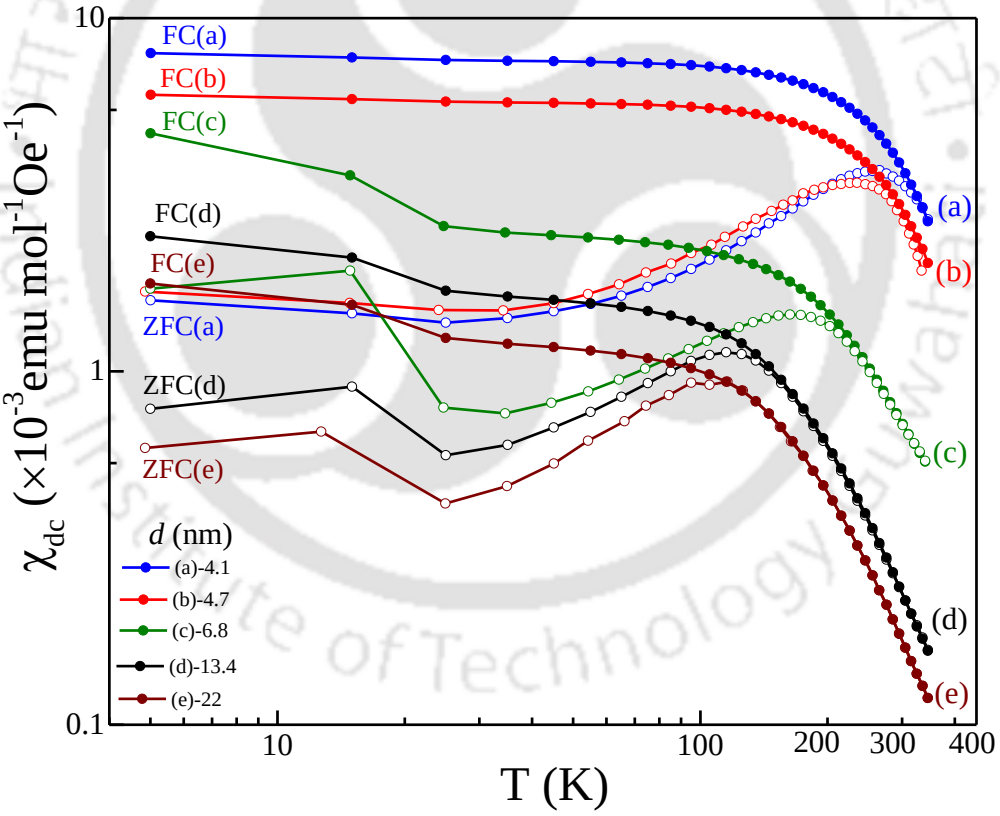

Figure 5.11: Temperature dependence of dc-magnetic susceptibility χ(T)=M/H measured under zero field cooled (ZFC) and field cooled (FC) conditions at an external applied magnetic field H_{dc} = 500 Oe for $Zn_{1-x}Ni_xO$ (x=1) nanoparticles with different crystallite sizes (4.1 nm ≤ d ≤ 22 nm).

-ferromagnetic system (AF-2) and calculated the magnitudes of exchange constants J_1 and J_2 by using the following relations [205]:

$$T_N = 2J_2S(S+1), \quad (5.5)$$

$$3\theta = S(S+1)(J_1Z_1 + J_2Z_2), \quad (5.6)$$

in the above equations, Z_1 and Z_2 are the number of nearest neighbor and next nearest neighbors, respectively. Here T_N is the Nèel Temperature, for antiferromagnetic NiO T_N ~ 523 K and S equal to 1 since the zero-point spin reduction is applicable only well below T_N. Substituting the value of T_N and θ in the above equations, we obtained $|J_2|$ ~130.7 K (11.26 meV) and $|J_1|$ ~ 68.8 K (5.92 meV) for x = 0.01. For AF-2 systems, particularly NiO, the magnitude of exchange constant $|J_2|$ should be much higher as compared to $|J_1|$ ($|J_2|>>|J_1|$) which is evident in the present system. [222,312] Depending upon the site-location of the magnetic ions inside the face-centered cubic lattice the strength of exchange constants J_1 and J_2 vary [222]. Based on the magnitudes of these exchange constants, the long-range ordered system can be divided into three antiferromagnetic categories (AF-I, AF-II and AF-III), and a ferromagnetic order FM (as discussed in section 4.3.1 of Chapter-IV). [222,313] For example, the exchange constants for the systems like NdP, NdAs, NdBi and NdSb lie between AF-I and FM regions with $J_1 \sim 0$, and the series EuO, EuS and EuSe lie between FM and AF-II with $J_1 \sim -J_2$ (Figure 4.10 of Chapter-IV). For the binary transition-metal oxides such as MnO, FeO, CoO and NiO systems, second AF-II is apparently quite stable which lies between AF-II and AF-III phase boundaries with $J_1 \sim -2J_2$ [222,313]. On the other hand, the system β-MnS and $Cd_{1-x}Mn_xTe$ lie between AF-III and AF-I regions with $J_2 \sim 0$. For the present case the magnitude of exchange constant J_2 is much higher as compared to the J_1 indicating the AF-II type ordering for x = 1. Here we also used random phase Green's function approximation to evaluate the exchange constants for x = 1; this analysis yields $|J_2|$ ~197 K (1.69 meV) and $|J_1|$ ~ 32.6 K (0.28 meV) for oxygen deficient system and $|J_2|$ ~207 K (1.7meV) and $|J_1|$ ~91 K (0.78 meV) for oxygen rich [313].

We have also evaluated the role of 'd' and 'H_{dc}' separately on magnitudes of J_1 and J_2 for x =1 using the values of 'C' and 'θ' (extracted from the slope and intercept of the inverse magnetic susceptibility data shown in figure 5.12(a-c)). Consequently, the variation of $\left|\frac{J_2}{J_1}\right|$ with respect to 'x', 'd' and 'H_{dc}' are shown in figure 5.13(a-c). For the x = 1, the ratio of exchange constants, $\left|\frac{J_2}{J_1}\right|$ increases progressively with increasing the particle-size upto a certain critical value d_c (~ 6.8 nm), beyond which the ratio $\left|\frac{J_2}{J_1}\right|$ starts to decrease continuously indicating that the system is approaching AF-III phase boundary and permanently departures from AF-II magnetic phase boundary. Figure 5.12(a-c) show the temperature dependence of the inverse magnetic susceptibility (χ^{-1}(T)) above T_1 for different values of d, H_{dc}, x. The high temperature linear regime was fitted to the Curie-Weiss law $\left(\frac{1}{\chi} = \frac{T-\theta}{C}\right)$ to obtain the Curie and Weiss constants 'C' and 'θ', respectively. Using the magnitude of 'C' we estimated the effective magnetic moment μ_{eff} from the relation $\mu_{eff} = (3k_BC/N_A)^{1/2}$. For x = 1, the calculated magnitude of μ_{eff} is

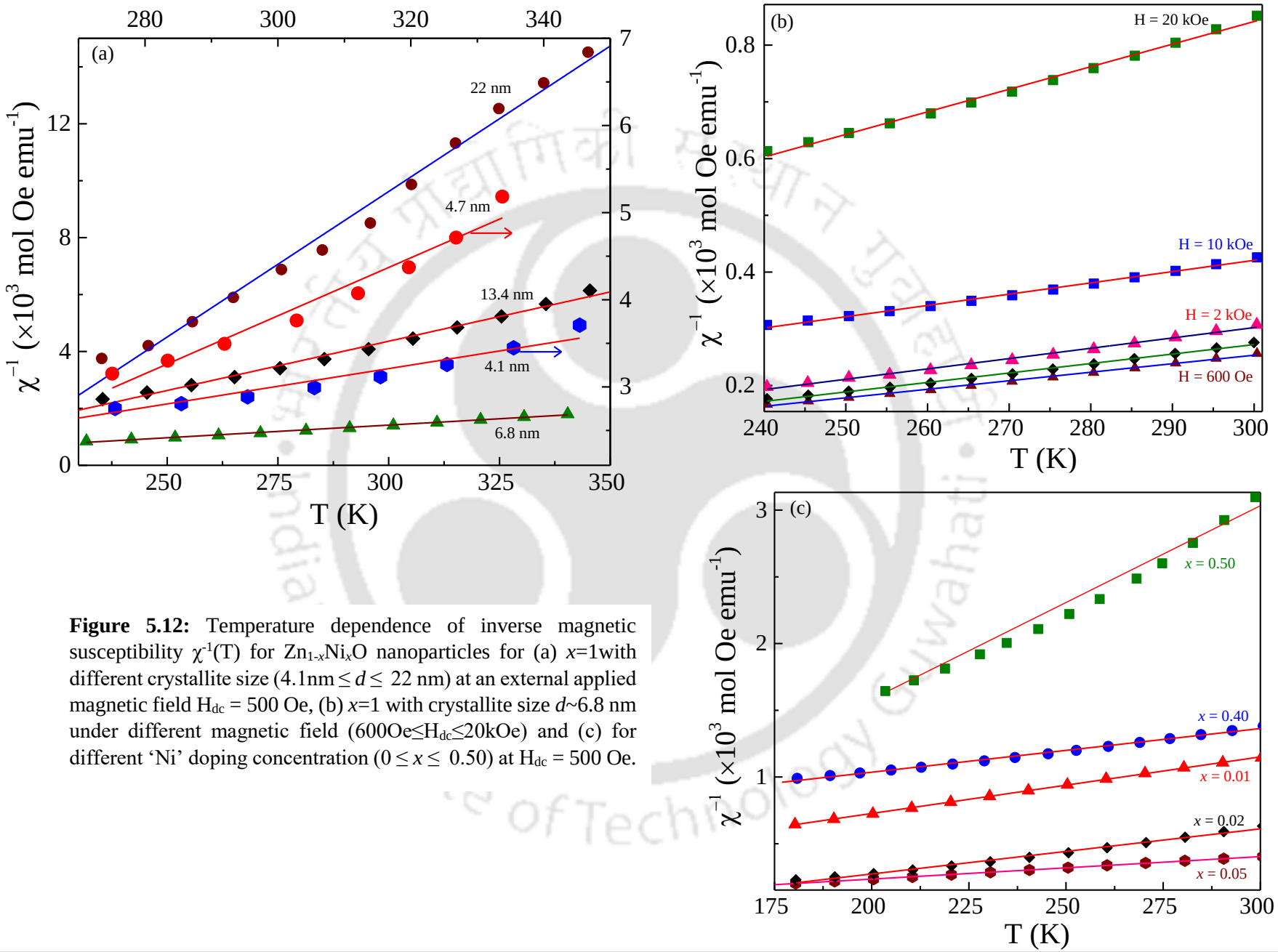

Figure 5.12: Temperature dependence of inverse magnetic susceptibility $\chi^{-1}(T)$ for $Zn_{1-x}Ni_xO$ nanoparticles for (a) x=1with different crystallite size ($4.1nm \leq d \leq 22$ nm) at an external applied magnetic field H_{dc} = 500 Oe, (b) x=1 with crystallite size d~6.8 nm under different magnetic field ($600Oe \leq H_{dc} \leq 20kOe$) and (c) for different 'Ni' doping concentration ($0 \leq x \leq 0.50$) at H_{dc} = 500 Oe.

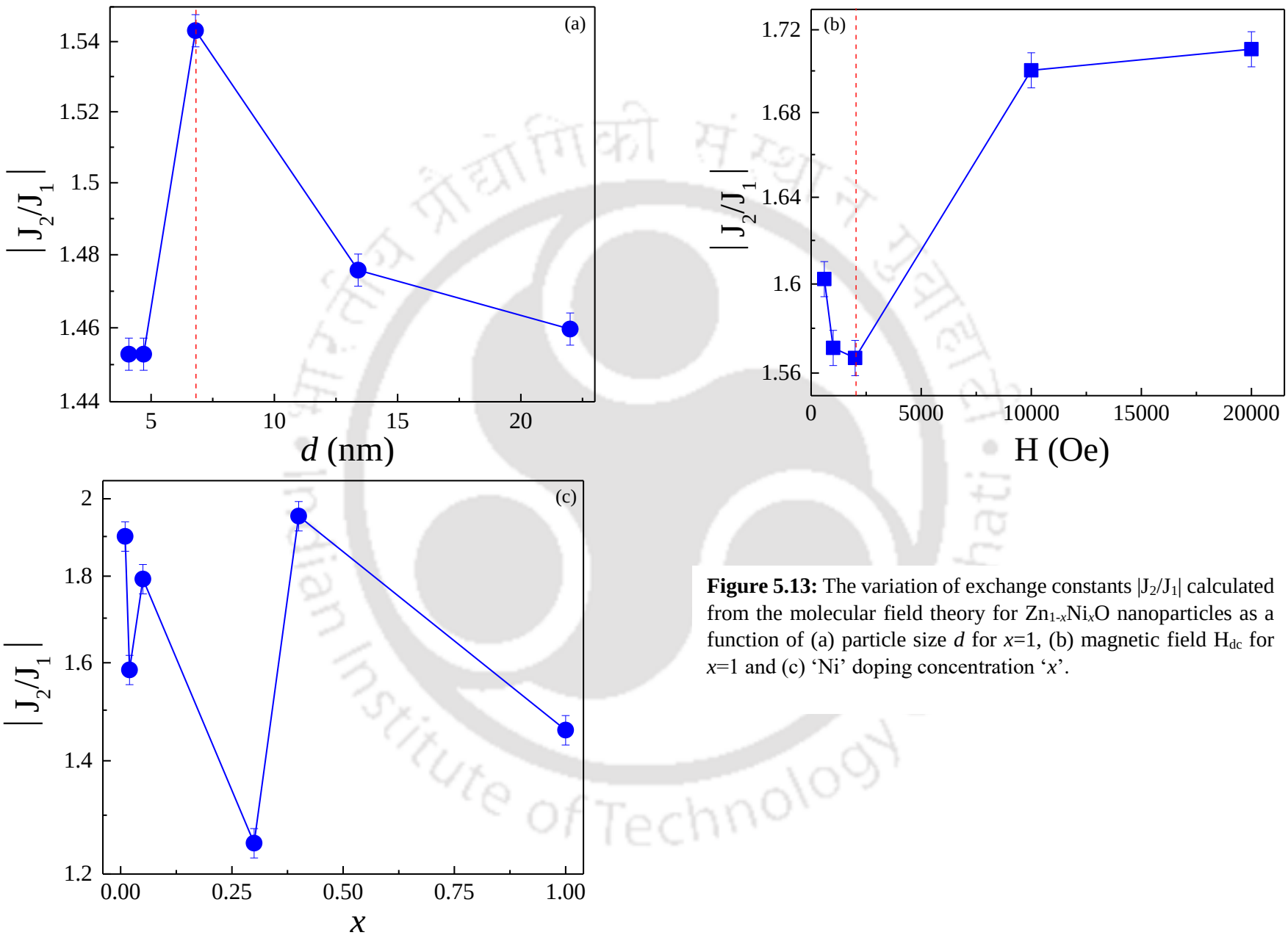

Figure 5.13: The variation of exchange constants $|J_2/J_1|$ calculated from the molecular field theory for $Zn_{1-x}Ni_xO$ nanoparticles as a function of (a) particle size *d* for *x*=1, (b) magnetic field H_{dc} for *x*=1 and (c) 'Ni' doping concentration '*x*'.

~ 2.25 μ_B, which is significantly smaller (~3.42 μ_B) as compared to its bulk counterpart. [313] As the doping concentration of 'Ni' increase, the value of μ_{eff} increase from 1.38 μ_B (x = 0.01), to 2.70 μ_B (x = 0.3) (figure 5.12b). Whereas, μ_{eff} decreases from 2.25 μ_B to 1.42 μ_B as H_{dc} increases from 600 Oe to 20 kOe, respectively for x = 1 (figure 5.12c).

In order to understand the role of surface effects on the magnetic properties of these composites we have estimated the anisotropy constant K_{eff} for various compositions of the investigated system using the expression

$$K_{eff} = K_b + \frac{6K_s}{d} \qquad (5.7)$$

In the above equation, K_b is the bulk anisotropy constant and the second term 'K_S' is the contribution from surface anisotropy. Usually, the applicability of above equation is valid for nanoparticles having d > 4 nm. [314–316] Recently, Pisane *et al*., studied the effect of decreasing particle size on the magnetic anisotropy and proposed a core-shell-surface layer model to explain the behavior of magnetic anisotropy for nanoparticles with very smaller particle size [314]. These authors extended the equation (5.7) by including the effect of shell thickness 'd_{sh}' and suggested the following relation:

$$K_{eff} = K_b + \frac{6K_s}{d} + K_{sh}\left\{\left[1 - \left(\frac{2d_{sh}}{d}\right)\right]^{-3}\right\} \qquad (5.8)$$

The factor $\{[1 - (2d_{sh}/d)]^{-3}\}$ in the last term of equation (5.8) represents the ratio of shell-volume to core-volume and it contains the contribution of the spins in the shell with effective anisotropy K_{sh} which is different from K_S and K_b [314]. In order to check the validity of the equations (5.7) and (5.8) for the present system, we have plotted

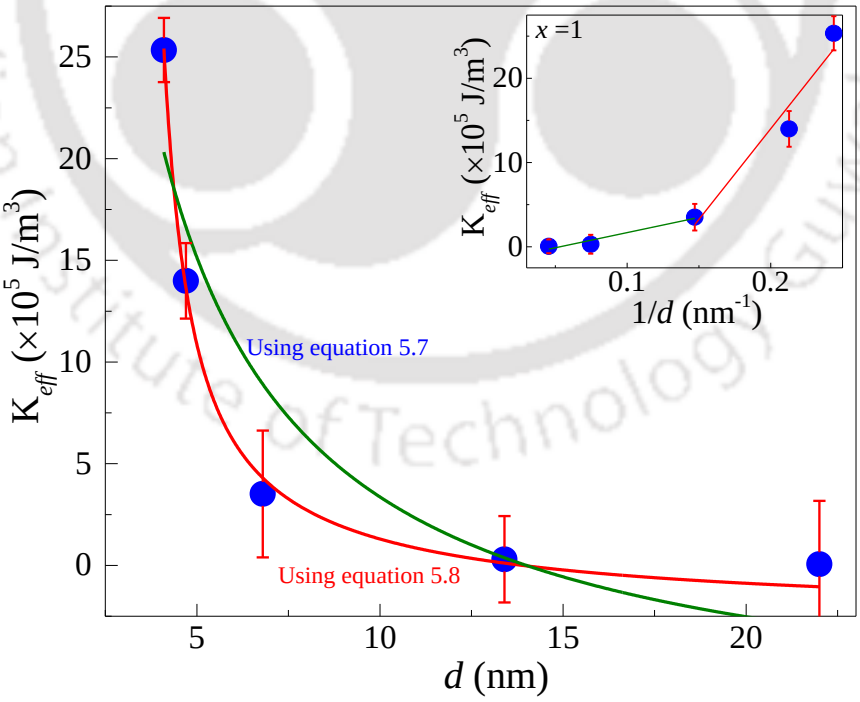

Figure 5.14: The variation of effective anisotropy constant K_{eff} with crystallite-size d for x=1. The solid-continuous lines are fits to equations 5.7 and 5.8 as mentioned in the text. The inset shows the K_{eff} versus 1/d plot.

the particle size '*d*' dependence of K_{eff} (as shown in figure 5.14 for x = 1) and fitted the data with equations (5.7) and 5.8, respectively. For x= 1, the data is well fitted with the equation (5.8), yielding the following parameters K_s = 2.42 erg/cm^2 and K_b = 2.61×10^6 erg/cm^3, K_{sh} = 9.56×10^5 erg/cm^3 and d_{sh} = 1.34 nm. On the contrary, for x = 1, the K_{eff} versus 1/d variation (inset of figure 5.14) exhibits two linear regions with different slopes, which clearly suggests that the experimental data is deviating from equation (5.7). In order to understand the effect of external magnetic field on the magnetic behavior of the composites we measured χ(T) under both ZFC and FC conditions with different magnitudes of H_{dc} between 50 Oe and 10k Oe for a constant d = 6.8 nm for x = 1 (Figure 5.15). In all these curves a broad hump (T_1) between the temperatures 220 K and 211 K and a sharp peak at low temperatures (T_2 ~ 12 K - 9.5 K) are clearly evident which are associated with the blocking and glassy behavior, respectively. The inset of figure 5.15 shows the magnified view of both χ_{ZFC}(T) and χ_{FC}(T) curves in the low-temperature range 4 K – 28 K; from this figure one can clearly notice the shift of T_2 towards lower temperatures with increasing the external magnetic field. This two peak-behavior in χ(T) usually signifies a certain distribution of blocking temperature in the nanosized system having different particle sizes [136]. In order to understand such distribution of blocking temperatures, we plotted the temperature variation of difference in the magnetization between FC and ZFC per unit field [$\Delta h = (M_{FC} - M_{ZFC})/H$] measured at different values of H_{dc} for x = 1 (figure 5.16). Usually, the

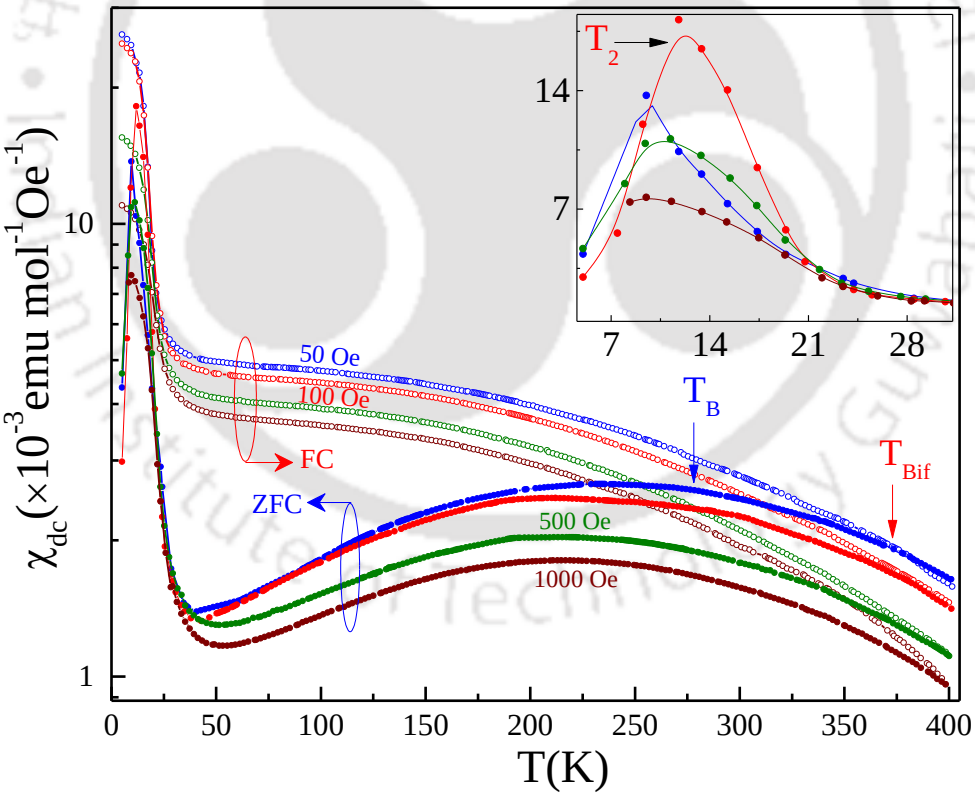

Figure 5.15: The dc-magnetic susceptibility χ_{dc}(T) measured under ZFC and FC conditions for $Zn_{1-x}Ni_xO$ (x=1) nanoparticles with external magnetic field H_{dc} between 50 Oe and 1 kOe for a constant d = 6.8 nm. The inset shows the zoomed view of χ_{ZFC}(T) curves in the low-temperature range between 4 K and 28 K.

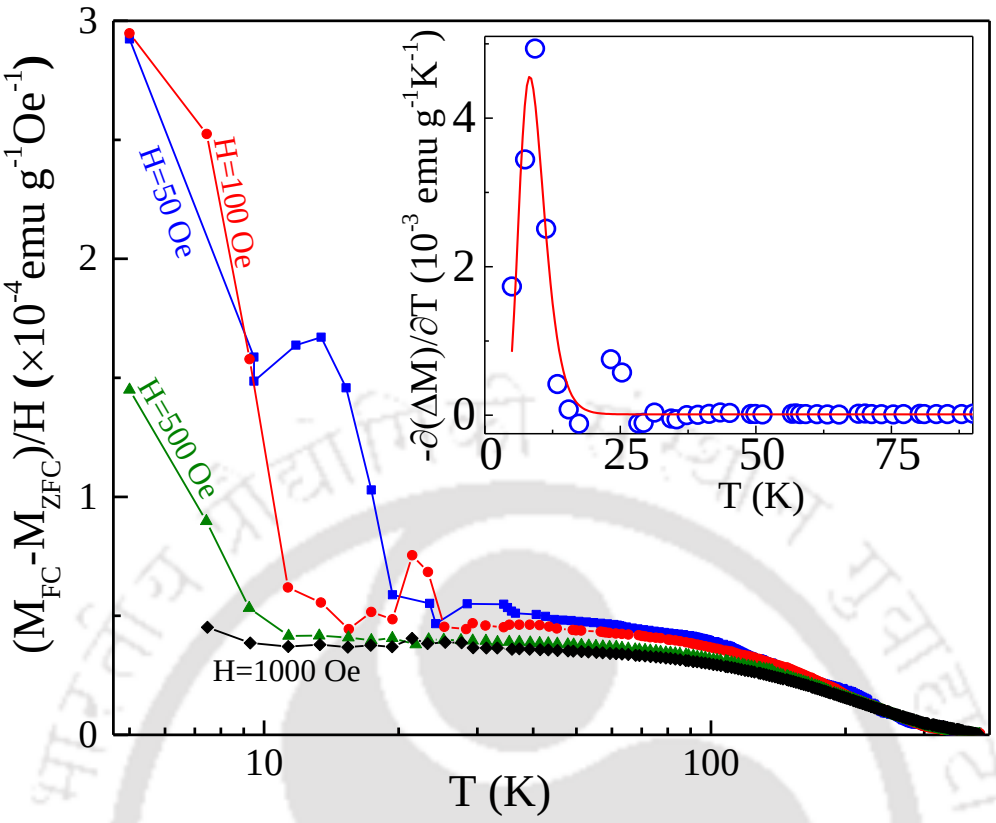

Figure 5.16: Difference between M_{FC} and M_{ZFC}, *i.e.* (M_{FC}-M_{ZFC})/H as a function of temperature. The inset shows the temperature derivative of the difference between M_{FC} and M_{ZFC} ($\partial(M_{FC} - M_{ZFC})/\partial T$) for H_{dc}=100 Oe. Solid line is a fit of the experimental data to the log-normal distribution function.

derivative of magnetization difference (i.e. $\partial(M_{FC} - M_{ZFC})/\partial T$) follows log-normal distribution function given by the below relation:

$$f(T_B) = \frac{1}{\sqrt{2\pi}\sigma T_B} exp\left\{\frac{-\left[ln\left(T_B/T_{BM}\right)\right]^2}{2\sigma^2}\right\} \quad (5.9)$$

In the above equation, σ is the standard deviation and T_{BM} is the mean blocking temperature. Using this log-normal distribution we have calculated the mean 'σ' and 'T_{BM} (=T_1)' by fitting the derivative of $\Delta M = M_{FC} - M_{ZFC}$ at two different temperature regimes: regime-(*i*) 5 K < T < 50K and regime-(*ii*) 50 K < T < 400 K, where we observed a sharp peak and a broad maximum, respectively. From this fitting analysis we obtained 'σ' = 0.25 and 0.89, and T_{BM} = 8 K and 310 K for regime-(*i*) and regime-(*ii*), respectively. The smaller value of 'σ' (~ 0.25) for the first temperature regime signify the narrow particle size distribution. Whereas, a broad distribution (σ ~ 0.89) is observed for regime-(*ii*). Previous report by Biasi *et al*. interpreted the presence of two such maxima (T_1 and T_2) in χ_{ZFC} by using a simple core-shell model with a uniaxial anisotropy acting on the core, and a surface anisotropy acting on the shell for ferromagnetic amorphous nanoparticles [317]. These authors reproduced their experimental data qualitatively by applying Monte Carlo simulations based on this core-shell model [317]. Moreover, the application of external magnetic field usually breaks the energy barrier symmetry and induces spin reorientation

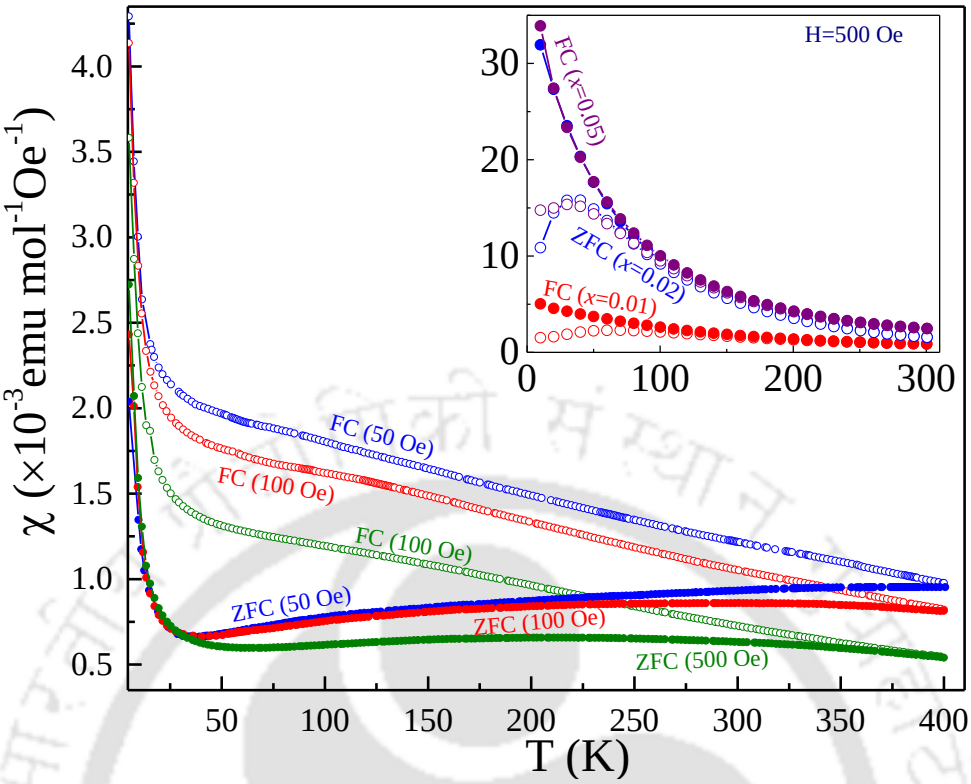

Figure 5.17: Temperature dependence dc-magnetic susceptibility χ(T) $Zn_{1-x}Ni_xO$ (x=0.40) nanoparticles with 50 Oe ≤ H_{dc} ≤ 500 Oe. The inset shows the χ_{ZFC} (T) and χ_{FC}(T) curves for x=0.01,0.02 and 0.05 at constant H_{dc} = 500 Oe.

away from the anisotropic axis and align along the direction of external magnetic field which results the conventional χ_{FC} curves [315]. Figure 5.17 shows the χ_{FC}(T) and χ_{ZFC}(T) curves for the sample with x = 0.40 (d = 18.7 nm) measured for different values of H_{dc} = 50, 100 and 500 Oe. The inset shows same measurement repeated for three different compositions 'x'= 0.01, 0.02 and 0.05 measured in the presence of H_{dc} = 500 Oe. The bifurcation temperature between the χ_{FC}(T) and χ_{ZFC}(T) curves (T_{Bif}) and the blocking temperature for this nanocomposite (with x= 0.40) occurs at relatively higher temperatures (T_{Bif} = 400 K and T_B = 348.15 K) as compared to the case of x = 1 (T_{Bif} = 356.64 K and T_B = 234.36 K). Such increase in 'T_{Bif}' and 'T_B' towards higher temperature as compared to x = 1 system is attributed to the smaller d values (~6.8 nm) for x = 1 than d = 18.7 nm for x = 0.4 which in turn effects the magnetic interaction between the nanocrystallites [318]. The compositional dependence of T_{Bif} and T_B are shown in figure 5.18, wherein both T_{Bif} and T_B shift towards higher temperature until a critical composition x_c ~ 0.5 which is consistent with the decrease in d values from 45.7 nm to 35.33 nm for x = 0.02 and 0.5, respectively, and decreases beyond x_c. For x_c ~ 0.5 the large difference (~94 K) between the 'T_{Bif}' and 'T_B' is observed (at H = 50 Oe) due to the increased interparticle interaction between the nanocrystallites [284]. In general, for the systems that exhibit significant interparticle interaction the following relation holds good: $T_{Bif} = \beta T_B$, where β lies between 1.0 to 2.0 and depends upon the log-normal particle size distribution (β ~ 1.30 for x =0.40). Usually, when the standard deviation of the lognormal distribution (obtained from equation 5.9) increases

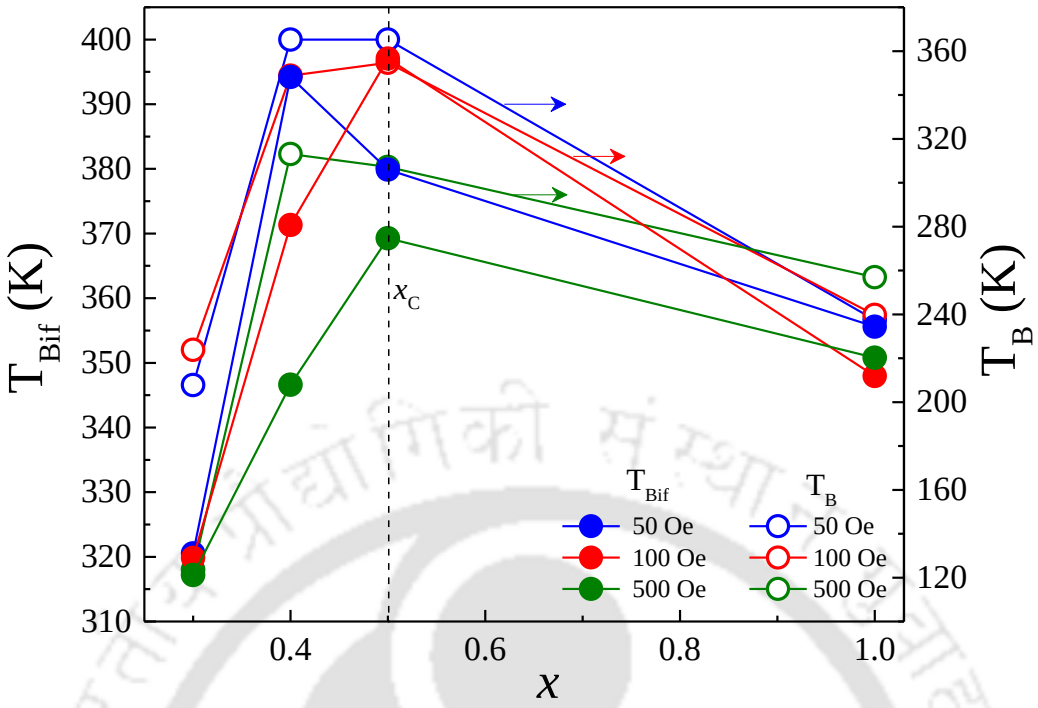

Figure 5.18: Compositional dependence of T_{Bif} (L.H.S) and T_B (R.H.S) for $Zn_{1-x}Ni_xO$ ($0 \leq x \leq 0.50$) nanoparticles at three different magnetic fields H_{dc}= 50 Oe, 100 Oe and 500 Oe.

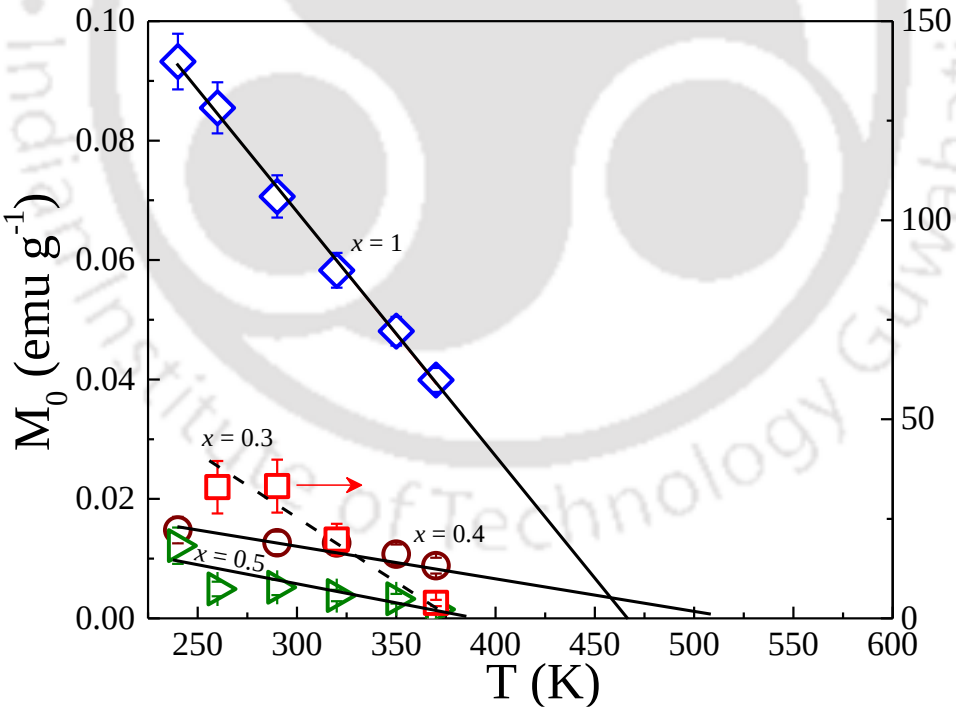

Figure 5.19: Temperature variation of saturation magnetization $M_0(T)$ obtained from the modified Langevin function for the composition x = 0.30, 0.40, 0.50 and 1.0. The solid lines connecting the data points represent linear fits whereas the dotted lines are extrapolations to $M_0 \rightarrow 0$ providing a rough estimation of the Néel temperature T_N.

from 0.0 to 1.5 the value of β increases from 1.0 to around 2.0. [112,284,319] In order to determine the magnetic moment per particle (μ_P) and T_N of the investigated system a series of isothermal magnetization curves (M-H) were measured from H_{dc} = 0 to 50 kOe at several temperatures above T_B. Before measuring each M-H isotherm at specific temperature we increased the system temperature above T_B to bring the virgin state (paramagnetic state) of the system. These isotherms are fitted to the modified Langevin function given by the following relation and estimated the saturation magnetization M_0:

$$M = M_0 L\left(\frac{\mu_P H}{k_B T}\right) + \chi_a H \qquad (5.10)$$

In the above equation, M_0 is the saturation magnetization, μ_P is the magnetic moment per particle, and χ_a is the antiferromagnetic component of the magnetic susceptibility. Figure 5.19 shows the temperature dependence of M_0 obtained by performing the modified Langevin fitting analysis for the compositions x = 0.30, 0.40, 0.50 and 1. For all the compositions a linear decrease in M_0(T) is observed. Generally, such linear decrease in M_0(T) is associated with the uncompensated surface moments which vary linearly near to the ordering temperature T_N [221,319,320]. As the temperature approaches to 'T_N' the surface moments decrease and $M_0 \rightarrow 0$. By linear extrapolation of M_0(T) up to $M_0 \rightarrow 0$ (as shown by the solid lines in figure 5.19), we have evaluated the magnitude of 'T_N' ~ 463 K and 551 K for x = 1 and x = 0.40, respectively. The observed value of T_N (~ 463 K) for the nanocomposites with x = 1 is shifted by 60 K towards lower temperature as compared to its bulk counterpart [321,322]. These observations are in-line with the previous studies on the crystallite size-dependent magnetization of NiO nanoparticles. These results provide the evidence for shifting of T_N towards low-temperature side with decrease in crystallite size, *d*. Such variation in T_N usually follows the finite-size-scaling relation $\left(T_N(d) = T_N(\infty)\left[1 - \left(\frac{\xi_0}{d}\right)^{\lambda}\right]\right)$, in this equation the parameter λ is the shift-exponent and ξ_o is the correlation length. Typical values of λ and ξ_o for AF-II Type systems are 3.2±0.5 and 3.2±0.2 nm, respectively [112]. We have also evaluated the magnitude of magnetic moment per particle (μ_P) by fitting the experimental curves (M-χ_aH)/M_0 versus H/T curves given by the modified Langevin equation (5.10) (as shown in figure 5.20 for x = 1 and in figure 5.21 for x = 0.05, 0.30 and 0.40). The obtained values of μ_P (~1619.7 μ_B for x = 1) are in well agreement with the previously reported values [323]. Such large values of μ_P signify the presence of strong dipolar interaction between the nanocrystallites. Presence of such dipolar interaction is also supported by the significant difference observed between T_B and T_{Bif} as discussed earlier. Previous reports by Tiwari *et al*. performed a detailed study of the magnetic properties of pure NiO nanoparticles of different sizes and reported that the average uncompensated moment for 5.1nm NiO nanoparticles is of the order of ~100 μ_B [324]. These authors also reported that the origin of T_B due to the spin-glass freezing and not to the interparticle dipole-dipole interaction since the obtained μ_p ~100 μ_B is comparatively smaller as compared to the dipolar interaction [324]. Usually, the dipolar interactions effectively increase with increase in particle volume [325]. The inset of figure 5.20 shows temperature dependence of μ_P (for x = 1), which increases linearly with increasing the temperature. Previous studies by Shim *et al*. reported

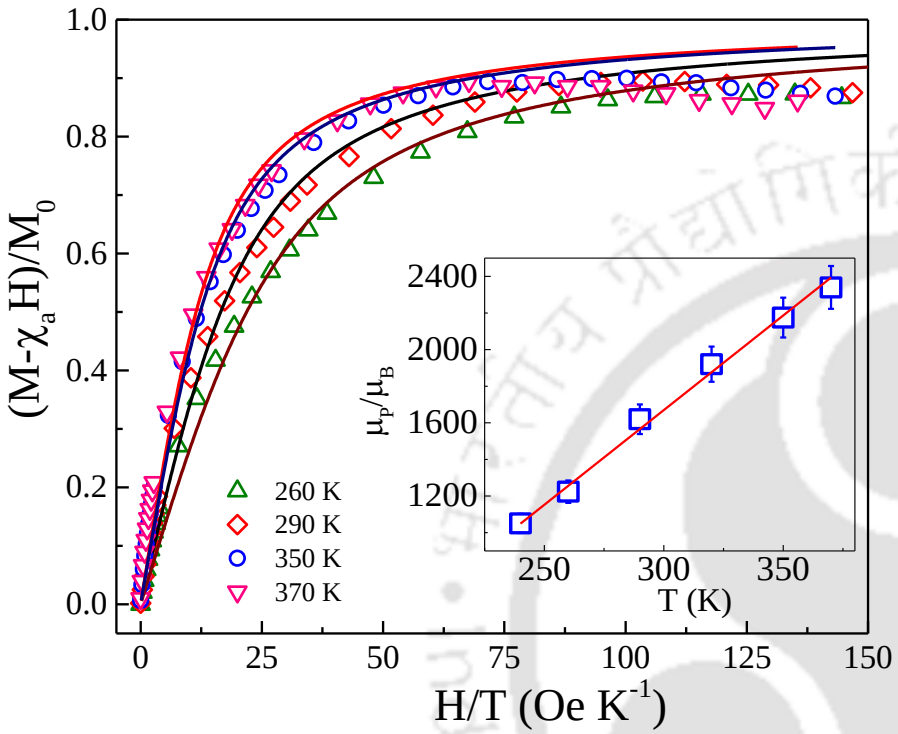

Figure 5.20: H/T dependence of $(M-\chi_a H)/M_0$ for x=1 nanoparticles. The hollow symbols represent the experimental data and solid lines are fits to the modified Langevin function. The inset shows the temperature dependence of magnetic moment per particle (μ_P) obtained from the modified Langevin fit.

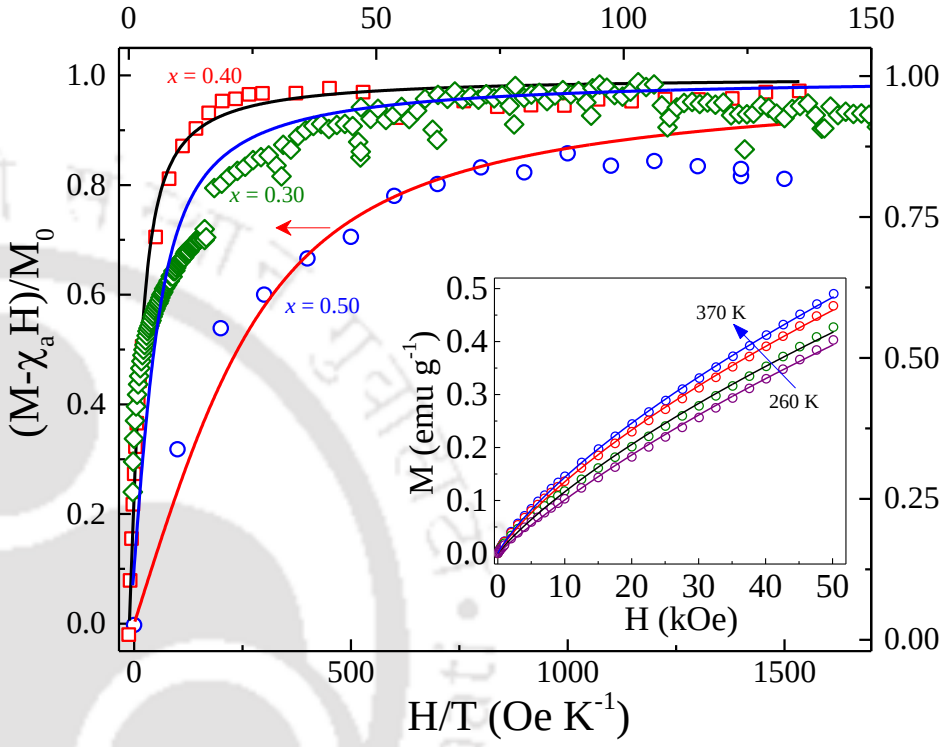

Figure 5.21: H/T dependence of $(M-\chi_a H)/M_0$ for x=0.05, 0.30 and 0.40 nanoparticles. The hollow symbols represent the experimental data and solid lines are fits to the modified Langevin function. The inset shows the M-H isotherms measured at different temperatures. The solid continuous lines are the simulated M-H isotherms using the log-normal moment distribution function.

that the μ_P of NiO nanoparticles of size ~ 5 nm shows temperature independent behavior , however, with increasing particle size ($d \geq 12$ nm) μ_P exhibit linear response signifying the presence of dipolar interaction [323]. We have performed similar analysis (see figure 5.21) wherein the quantity $(M-\chi_a H)/M_0$ was plotted as a function of H/T for the x = 0.05, 0.30 and 0.40. In this figure the solid continuous lines are the Langevin fits to the experimental data and this analysis yields μ_P = 112 μ_B, 3002 μ_B and 3543 μ_B for x = 0.05, 0.30 and 0.40, respectively which are comparable with μ_P = 1637.6 μ_B obtained from the moment distribution of spin clusters given by the following relation [326]:

$$M = M_s \int_0^\infty f(\mu)\ L\left(\frac{\mu H}{k_B T}\right) d\mu \qquad (5.11)$$

where, $f(\mu)$ is the moment distribution function defined by the relation $f(\mu) = \frac{1}{\sqrt{2\pi}\sigma\mu} \exp\left\{\frac{-\left[\ln\left(\mu/T_{BM}\right)\right]^2}{2\sigma^2}\right\}$, M_S is the saturation magnetization, and $L(x)$ is the Langevin function (for σ = 0.89, obtained from our lognormal distribution function). The simulated isotherms for x = 1 are represented by solid continuous lines in the inset of figure 5.21. It is interesting to note that the simulated patterns are in good agreement with the experiment data shown by the hollow symbols in the inset of figure 5.21.

5.4 Conclusions:

On the basis of the evidences gathered from TGA-DSC, XRD, ESR, Raman, and magnetic measurements, the following conclusions are drawn. (*i*) The calcination temperature of the oven dried mixed oxalate product was optimized above 500˚C for 2-8 hours in air, such heat treatment conditions cause proper decomposition of the precursors and yield the desired compound $Zn_{1-x}Ni_xO$/NiO. (*ii*) For dilute and intermediate compositions ($0.02 \leq x \leq 0.05$) wurtzite *h.c.p* $Zn_{1-x}Ni_xO$ structure is stable, however above $x \geq 0.10$ NiO phase emerges as secondary phase. (*iii*) The temperature dependence of X-band ESR parameters, $H_R(T)$ and $\Delta H_{PP}(T)$ follow the power-law variation ($\delta H_R = (\Delta H_{PP})^n$) of Nagata and Ishihara model with n ≃ 2.13 signifying the presence of partially oriented nanocrystallites of $Zn_{0.7}Ni_{0.3}O$. However, the power-law variation gives n ≃ 2.85 for NiO suggesting a random orientation of nanocrystallites. (*iv*) The numerical calculations based on Raikher and Stepanov model yield the size of amorphous Ni^{3+} clusters present in the $Zn_{1-x}Ni_xO$/NiO nanocompsites. (*v*) Raman analysis shows the signature of Zone boundary phonon effects associated with the strong magnetic interaction between two successive 'Ni' atoms in ZnO matrix. (*vi*) The magnitudes of exchange constants $|J_1|$ and $|J_2|$ were evaluated for the nanocomposites of $Zn_{1-x}Ni_xO$/NiO ($0 \leq x \leq 1$) using the molecular field approximation for Type-II AFM system. Accordingly, we obtained $|J_2|$ = 130.7 K (11.26 meV) and $|J_1|$ = 68.8 K (5.92 meV) for x = 0.01, and 11.26 meV and 7.17 meV for x = 1, respectively, which lie in between AF-II and AF-III phase boundaries. (*vii*) A core-shell surface layer model was demonstrated for the first time to explain the behavior of magnetic anisotropy in the present nanocomposite system. (*viii*) The statistical distribution of blocking temperatures were analyzed by means of log-normal distribution function associated with the temperature dependence of $\partial(M_{FC} - M_{ZFC})/\partial T$.

Chapter-VI

Conclusions and Scope for Future Research

6.1 Conclusions:

This chapter contains all the important findings of the present research work together with a brief summary of future scope arising from these studies. As discussed in the previous chapters, we mainly focused on the structural, dielectric and magnetic properties of wide-bandgap transition-metal-oxides and Mott insulator composites; the similarities and differences of their properties are recapitulated here. Dielectric and magnetic properties in these polycrystalline composites have shown several interesting features including the thermally driven structural phase transition leading to a dielectric anomaly across 540 K which can be exploited to develop spin-valve and memristive devices. Succeeding a brief summary of the key results, we concluded this chapter by identifying few possible frontiers of future research work related to the tailoring of the exchange interactions and dielectric transitions.

In Chapter 3 we have demonstrated that the composite system consisting of wurtzite h.c.p structure of ZnO and rhombohedrally distorted NiO exhibits a clear dielectric anomaly with relaxor behavior across the transition temperature T^* ~ 541 K due to compositional heterogeneity. Evidence for such compositional heterogeneity and the possibility of formation of tiny polar clusters in the ZnO-NiO composites are presented. Furthermore, a giant dielectric peak across 410˚C in pure NiO was noticed together with the anomaly across the antiferro- to paramagnetic Néel temperature T_N of NiO. For $T > T^*$ the relative dielectric permittivity ($\varepsilon_r(T)$) cusp follows the empirical scaling law based on the equation ($\varepsilon_A/\varepsilon_r = 1+0.5(T-T_A)^2/\delta^2$) with the shape parameter value 'δ' ~ 88 and 39.73 ˚C for $x = 0.30$ and 0.16, respectively. Such dynamic variation of dispersive $\varepsilon_r(T^*)$ obeys the Vogel–Fulcher law with Debye frequency $\nu_0 \sim 1.33 \times 10^9$ Hz and 1.33×10^6 Hz, freezing temperature T_g ~ 181˚C and 240˚C, and activation energy E_A = 0.11eV and 0.023 eV for x ~ 0.30 and 0.16, respectively. The magnitudes of diffuseness exponent 'γ' = 1.91 and 1.77 estimated from the experimental data for the compositions x = 0.30 and 0.16, respectively are close to the ideal relaxor ferroelectric system ('γ' = 2). These results confirm the relaxor behavior (mixed ferroelectric–glass phase) for heavily doped $Zn_{1-x}Ni_xO$/NiO system which is further supported from C-V butterfly shape hysteresis loops recorded at room-temperature. Similar results are observed in Na doped NiO system without any relaxor characteristics. The temperature dependence of ac-resistivity provided strong evidence for variable-range-hopping of charge carriers between the localized states for all the samples. The effect of non-ohmic sample-electrode contact impedance and negative-capacitance on the global dielectric behavior of these composites are also discussed in Chapter 3. The observed dielectric anomaly can be tuned using frequency of the ac-signal and the cation deficiency 'Δ' of $Ni_{1-\Delta}O$ within the core ZnO matrix. This way of tuning the T^* may open a constructive approach for the development of the spin-valve devices and varistor components together with piezoelectric devices functioning at just above the room temperature. The temperature variation of carrier hopping energy $\varepsilon_h(T)$ and nearest-neighbor exchange-coupling parameter $J_{ij}(T)$ evaluated from the small-polaron model

exhibits a well-defined anomaly across T_N. For all the composite systems, the average exchange-coupling parameter $(J_{ij})_{AVG}$ nearly equals to 70 meV which is slightly greater than the Exciton binding energy 60 meV of pure zinc-oxide. The magnitudes of ε_h (~0.17 eV) and J_{ij} (~11 meV) of pure NiO synthesized under oxygen rich conditions are consistent with the previously reported theoretical estimations based on the Green's function analysis.

The electronic structure of the bulk sample probed by the X-ray photoelectron spectroscopy (XPS) reveals that both Ni-2*p* and Zn-2*p* exhibit doublet corresponding to $2p_{3/2}$ and $2p_{1/2}$ with spin-orbit splitting $\Delta \sim 17.9$ eV and 23.2 eV, respectively, confirming the divalent oxidation state of Zn and Ni. However, in the case of pure NiO the difference in the binding energy of Ni $2p_{3/2}$ and Ni $2p_{1/2}$ is ~ 18.75 eV (> 18 eV) signifying the excess oxygen in the system. Minute change in the Ni-2*p* satellite peaks with increasing the composition '*x*' is associated with the attenuation in nonlocal screening because of reduced site occupancy of two adjacent Zn ions. On the other hand, the XPS spectra of $Ni_{1-x}Na_xO$ bulk samples reveals that the O-1*s* spectra can be deconvoluted into three Gaussian-Lorentzian peaks centered at 528.9 eV and 530.76 eV corresponding to the surface and chemically bonded oxygen ions, respectively. While, the Na-1*s* core level photoelectron spectra exhibit single major peak at ~1076.12 eV signifying the presence of monovalent oxidation state of sodium. The temperature dependent X-ray diffraction measurements reveal that the axial-rhombohedral angle 'α'(T)' of oxygen-rich NiO system exhibits an abrupt drop from 60º8′ to 60º at 300ºC associated with the crystal structure relaxation from rhombohedral to cubic phase which is accompanied by the change in the magnetic ordering from antiferromagnetic to paramagnetic state. We have studied the nature of high-temperature magnetic properties and the exchange interactions in both $Zn_{1-x}Ni_xO$/NiO composite system as well as in $Ni_{1-x}Na_xO$. The magnitudes of exchange constants J_1 and J_2 calculated from temperature magnetic susceptibility data for different values of '*x*' are compared with the molecular-field approximation ($J_1 \sim 0.15$ meV and $J_2 \sim 1.15$ meV for $x = 1$) and Green's-function theory ($J_1 \sim 0.7$ meV and $J_2 \sim 1.78$ meV). The data obtained from the magnetization isotherms are fitted to the modified Langevin function $M = Mo\ L\left(\frac{\mu_P H}{k_B T}\right) + \chi_a H$ to extract the T_N of NiO clusters present in the $Zn_{1-x}Ni_xO$ matrix. We have correlated the magnitudes of J_1 and J_2 estimated from the magnetization data with the theoretical analysis involving the spin-dependent activation energies yielding an average superexchange interaction energy J_{AVG}. For $x > 0.30$, the maximum value of J_{AVG} (~ 1.61 meV) determined from the above analysis is consistent with the magnitude of J_2 obtained from the high-temperature magnetic susceptibility data using Green's-function analysis.

Next, we extended the study to the low-dimensional nanostructures of $Zn_{1-x}Ni_xO$ and NiO synthesized by sol-gel process and carried out their characterization. On the basis of thermal analysis, we optimized the calcination temperature of the ovendried mixed oxalate product at 500˚C or above for 2-8 hours in air to yield the desired compound $Zn_{1-x}Ni_xO$/NiO. The crystal structure studies carried out by X-ray diffraction reveals the formation of wurtzite h.c.p structure of $Zn_{1-x}Ni_xO$ for dilute and intermediate compositions ($0.02 \leq x \leq 0.05$), nevertheless, for $x \geq 0.10$ NiO emerges as secondary phase. The following noteworthy results are obtained from temperature dependence of X-band electron spin resonance studies: (*i*) The resonance field H_R(T) and peak-to-peak width

$\Delta H_{PP}(T)$ follows power-law variation ($\delta H_R = (\Delta H_{PP})^n$) of Nagata and Ishihara model with exponent value $n \simeq 2.13$ signifying the presence of partially oriented nanocrystallites of $Zn_{1-x}Ni_xO$, but, the power-law variation gives $n \simeq 2.85$ for $x = 1$ (NiO) suggesting a random orientation of nanocrystallites. (*ii*) The numerical calculations based on Raikher and Stepanov model yield the size of amorphous Ni^{3+} clusters present in the $Zn_{1-x}Ni_xO$/NiO nanocompsites. Raman analysis shows the signatures of zone-boundary-phonon effects associated with the strong magnetic interaction between two successive 'Ni' atoms in ZnO matrix. In addition to the 2M Magnon mode, two extra modes appear at 558 and 900 cm^{-1} due to the increased volume fraction of NiO within the $Zn_{1-x}Ni_xO$ matrix.

The last section of Chapter 5 deals with the results of temperature dependence of magnetic susceptibility of the two-phase nanocomposite of $Zn_{1-x}Ni_xO$/NiO. The irreversible behavior of susceptibility curves $\chi_{ZFC}(T)$ and $\chi_{FC}(T)$ provides strong evidence of the superparamagnetic behavior of these composites. The magnitudes of exchange constants $|J_1|$ (= 11.26 meV) and $|J_2|$ ((5.92 meV)) were determined from the molecular field approximation for dilute compositions $x \leq 0.01$. For heavily doped composites ($x \geq 0.7$) these magnitudes turnout to be 11.26 meV and 7.17 meV which lie in between AF-II and AF-III phase boundaries. A new core-shell surface layer model ($K_{eff} = K_b + \frac{6K_s}{d} + K_{sh}\left\{\left[1 - \left(\frac{2d_{sh}}{d}\right)\right]^{-3}\right\}$) was demonstrated for the first time to explain the behavior of magnetic anisotropy in these nanocomposites. This model yields the anisotropy constants $K_{surface} = 2.42$ erg/cm^2, $K_{bulk} = 2.61\times10^6$ erg/cm^3 and $K_{shell} = 9.56\times10^5$ erg/cm^3 for shell thickness $d_{sh} \sim 1.34$ nm ($x = 1$). The statistical distribution of blocking temperatures were analyzed by means of log-normal distribution function ($f(\mu) = \frac{1}{\sqrt{2\pi}\sigma\mu}\exp\left\{\frac{-\left[\ln\left(\mu/T_{BM}\right)\right]^2}{2\sigma^2}\right\}$) associated with the temperature dependence of $\partial(M_{FC} - M_{ZFC})/\partial T$. Such statistical analysis yields standard deviation 'σ' = 0.89 for $x = 1$ indicating the presence of strong inter-particle interaction in the nanocomposites. The isothermal magnetization curves (M-H) are successfully fitted to the modified Langevin function $M = Mo\,L\left(\frac{\mu_P H}{k_B T}\right) + \chi_a H$ and the ordering temperature of the nanocomposite $Zn_{1-x}Ni_xO$/NiO was successfully extracted.

6.2 Future Scope:

In the current thesis we explored only electronic, structural, magnetic and dielectric properties of $Zn_{1-x}Ni_xO$/NiO and $Ni_{1-x}Na_xO$ oxides. Below we enumerate some possible extensions of the current work.

- One can study the Neutron diffraction across the long-range ordering temperatures which can provide additional information about the magnetic structure. Such studies also verify the conclusions drawn from the magnetization studies.
- To perform the electronic band-structure calculations using density function theory and make a comparative study with the experimental results obtained from the Raman, ESR, and XPS measurements. These results can also be correlated with the diffusive reflectance spectroscopy in the UV-Vis-NIR range.

- To synthesize the low-dimensional nanostructures of Na, Mg, or Li doped NiO/ZnO and perform a systematic comparative study of their structural, optical, dielectric and magnetic properties with their bulk counterparts. Such nanostructures play a major role in fuel-cells, Li-ion batteries and catalysts.
- This study can be extended to various other doping elements, either non-magnetic or magnetic (e.g. Mg, Al, Ti, Ru, Co, V and Cr at Ni or Zn sites in NiO or ZnO matrix) and probe the differences occurring in the electronic structure, optical and magnetic properties as compared to the pristine compounds.

Bibliography:

[1] G. D. Wilk, R. M. Wallace, and J. M. Anthony, J. Appl. Phys. **89**, 5243 (2001).
[2] W. J. Zhu, T.-P. Ma, T. Tamagawa, J. Kim, and Y. Di, IEEE Electron Device Lett. **23**, 97 (2002).
[3] W.-J. Qi, R. Nieh, B. H. Lee, L. Kang, Y. Jeon, and J. C. Lee, Appl. Phys. Lett. **77**, 3269 (2000).
[4] S. Hall, O. Buiu, I. Z. Mitrovic, Y. Lu, and W. M. Davey, J. Telecommun. Inf. Technol. 33 (2007).
[5] M. Lanza, Materials (Basel). **7**, 2155 (2014).
[6] A. Sawa, Mater. Today **11**, 28 (2008).
[7] G. Ribes, J. Mitard, M. Denais, S. Bruyere, F. Monsieur, C. Parthasarathy, E. Vincent, and G. Ghibaudo, IEEE Trans. Device Mater. Reliab. **5**, 5 (2005).
[8] C. Zhao, C. Z. Zhao, S. Taylor, and P. R. Chalker, Materials (Basel). **7**, 5117 (2014).
[9] J. S. Meena, S. M. Sze, U. Chand, and T.-Y. Y. Tseng, Nanoscale Res. Lett. **9**, 526 (2014).
[10] S. Krishnan, S. Bhansali, E. Stefanakos, and Y. Goswami, Procedia Chem. **1**, 409 (2009).
[11] S. Grover, O. Dmitriyeva, M. J. Estes, and G. Moddel, IEEE Trans. Nanotechnol. **9**, 716 (2010).
[12] F. Aydinoglu, M. Alhazmi, B. Cui, O. M. Ramahi, M. Irannejad, A. Brzezinski, and M. Yavuz, Austin J. Nanomed. Nanotechnol **1**, (2013).
[13] S. Dueñas, H. Castan, H. Garcia, and L. Bailon, in *Dielectr. Mater.* (InTech, 2012).
[14] P. Bain, Ashim Kumar and Chand, *Ferroelectricity* (Wiley Online Library, 1968).
[15] B. C. Stuart, M. D. Feit, A. M. Rubenchik, B. W. Shore, and M. D. Perry, Phys. Rev. Lett. **74**, 2248 (1995).
[16] P. Barber, S. Balasubramanian, Y. Anguchamy, S. Gong, A. Wibowo, H. Gao, H. J. Ploehn, and H. C. Zur Loye, Materials (Basel). **2**, 1697 (2009).
[17] R. J. Cava, J. Mater. Chem. **11**, 54 (2001).
[18] J. McPherson, J. Y. Kim, A. Shanware, and H. Mogul, Appl. Phys. Lett. **82**, 2121 (2003).
[19] D. J. Griffiths, *Introduction To Electrodynamics* (Prentice-Hall of India, 1989).
[20] C. Kittel, *Introduction to Solid State Physics* (Wiley, 2005).
[21] L. M. Wang and R. Richert, J. Phys. Chem. B **109**, 11091 (2005).
[22] S. Altieri, M. Finazzi, H. H. Hsieh, H.-J. Lin, C. T. Chen, T. Hibma, S. Valeri, and G. a Sawatzky, Phys. Rev. Lett. **91**, 137201 (2003).
[23] M. Filippi, B. Kundys, R. Ranjith, A. K. Kundu, and W. Prellier, Appl. Phys. Lett. **92**, (2008).
[24] T. Tunç, İ. Uslu, İ. Dökme, Ş. Alt, Ş. Altındal, and H. Uslu, Int. J. Polym. Mater. **59**, 739 (2010).
[25] J. H. Hannay, Eur. J. Phys. **4**, 141 (1983).
[26] P. Van Rysselberghe, J. Phys. Chem. **36**, 1152 (1931).
[27] V. A.P., Phys. A Stat. Mech. Its Appl. **241**, 216 (1997).
[28] K. Urano and M. Inoue, J. Chem. Phys. **71**, 791 (1976).
[29] C. Kittel, *Introduction to Solid State Physics* (Publication, New York, NY : Wiley, 1953).
[30] M. Barsoum and M. W. Barsoum, *Fundamentals of Ceramics* (CRC press, 2002).
[31] K. S. Cole and R. H. Cole, J. Chem. Phys. **9**, 341 (1941).
[32] R. H. Cole, J. Chem. Phys. **23**, 493 (1955).
[33] S. Havriliak and S. Negami, J. Polym. Sci. Part C **14**, 99 (1966).
[34] C. Zhao, C. Z. Zhao, M. Werner, S. Taylor, and P. Chalker, Nanoscale Res. Lett. **8**, 1 (2013).
[35] S. S. Fouad, G. B. Sakr, I. S. Yahia, D. M. Abdel-Basset, and F. Yakuphanoglu, Phys. B Condens. Matter **415**, 82 (2013).
[36] V. V. Laguta, M. D. Glinchuk, and I. V. Kondakova, Phys. Solid State **46**, 1262 (2004).
[37] R. Pirc and R. Blinc, Phys. Rev. B **76**, 1 (2007).
[38] A. P.-T. Millán, José Philippe Godignon, Autom. Časopis Za Autom. Mjer. Elektron. Računarstvo I Komun. **53**, 107 (2012).
[39] D. Huang, Z. Liu, Y. Li, and Y. Liu, J. Alloys Compd. **698**, 276 (2017).
[40] P. Lunkenheimer, S. Krohns, S. Riegg, S. G. Ebbinghaus, A. Reller, and A. Loidl, Eur. Phys. J. Spec. Top. **180**, 61 (2009).
[41] Y. Tokura, J. Appl. Phys. **79**, 5 (1996).
[42] S. Maensiri, P. Thongbai, and T. Yamwong, Acta Mater. **55**, 2851 (2007).
[43] Y. Li, L. Fang, L. Liu, Y. Huang, and C. Hu, Mater. Sci. Eng. B Solid-State Mater. Adv. Technol. **177**, 673 (2012).
[44] S. Manna and S. K. De, Solid State Commun. **150**, 399 (2010).
[45] A. A. Dakhel, J. Alloys Compd. **488**, 31 (2009).

[46] J. Wu, C.-W. Nan, Y. Lin, and Y. Deng, Phys. Rev. Lett. **89**, 217601 (2002).
[47] G. A. Slack, J. Appl. Phys. **31**, 1571 (1960).
[48] B. G. Kim, S. M. Cho, T. Y. Kim, and H. M. Jang, Phys. Rev. Lett. **86**, 3404 (2001).
[49] S. Nakamura, S. Soeya, N. Ikeda, and M. Tanaka, J. Appl. Phys. **74**, 5652 (1993).
[50] J. M. McKay and V. E. Henrich, Phys. Rev. Lett. **53**, 2343 (1984).
[51] P. Wu, V. Ligatchev, Z. G. Yu, J. Zheng, M. B. Sullivan, and Y. Zeng, Phys. Rev. B - Condens. Matter Mater. Phys. **79**, 3 (2009).
[52] J. Y. Kim, M. Perez, J. A. Chem, J. A. Rodriguez, J. C. Hanson, and A. I. Frenkel, J. Am. Chem. Soc. **124**, 15 (2002).
[53] G. Liu, X. Q. Liu, and X. M. Chen, Appl. Phys. A Mater. Sci. Process. **116**, 1421 (2014).
[54] C. Noguera, J. Phys. Condens. Matter **12**, (2000).
[55] J. Yang, J. Wang, X. Li, J. Lang, F. Liu, L. Yang, H. Zhai, M. Gao, and X. Zhao, J. Alloys Compd. **528**, 28 (2012).
[56] G. Heiland and P. Kunstmann, Surf. Sci. **13**, 72 (1969).
[57] T. Yamashita, R. Hansson, and P. C. Hayes, J. Mater. Sci. **41**, 5559 (2006).
[58] Q. Li, T. T. Shen, Y. L. Cao, K. Zhang, S. S. Yan, Y. F. Tian, S. S. Kang, M. W. Zhao, Y. Y. Dai, Y. X. Chen, G. L. Liu, L. M. Mei, X. L. Wang, and P. Grünberg, Sci. Rep. **4**, (2014).
[59] S. C. Pillai, J. M. Kelly, R. Ramesh, and D. E. McCormack, J. Mater. Chem. C **1**, 3268 (2013).
[60] S. T. Tan, B. J. Chen, X. W. Sun, W. J. Fan, H. S. Kwok, X. H. Zhang, S. J. Chua, S. T. Tan, B. J. Chen, X. W. Sun, and W. J. Fan, J. Appl. Phys. **13505**, 13505 (2011).
[61] C. Wang, L. Liu, Q. Li, S. Huang, J. Zhang, J. Zheng, and C. Cheng, J. Appl. Phys. **116**, 124101 (2014).
[62] Z. Wang, XS and Wu, ZC and Webb, JF and Liu, Appl. Phys. A Mater. Sci. \& Process. **77**, 561 (2003).
[63] D. Y. Li, Y. J. Zeng, D. Batuk, L. M. C. Pereira, Z. Z. Ye, C. Fleischmann, M. Menghini, S. Nikitenko, J. Hadermann, K. Temst, A. Vantomme, M. J. Van Bael, J. P. Locquet, and C. Van Haesendonck, ACS Appl. Mater. Interfaces **6**, 4737 (2014).
[64] J. C. Slater, Phys. Rev. **49**, 931 (1936).
[65] J. C. Slater, Phys. Rev. **82**, 538 (1951).
[66] M. S. Seehra and J. M. Honig, *Basic Properties of Binary Oxides* (University of Seville Press, 1984).
[67] P. P. Edwards, C. N. R. Rao, and N. F. Mott, *The Metallic and Nonmetallic States of Matter* (Taylor & Francis London, UK, 1985).
[68] G. Kotliar and J. Liu, Phys. Rev. B **38**, 5142 (1988).
[69] X. G. Wen and P. A. Lee, Phys. Rev. Lett. **76**, 503 (1996).
[70] C. M. Varma, Phys. Rev. Lett. **83**, 3538 (1999).
[71] S. Chakravarty, R. B. Laughlin, D. K. Morr, and C. Nayak, Phys. Rev. B - Condens. Matter Mater. Phys. **63**, (2001).
[72] Y. Muraoka and Z. Hiroi, Appl. Phys. Lett. **80**, 583 (2002).
[73] P. Karen, P. M. Woodward, J. Lindén, T. Vogt, A. Studer, and P. Fischer, Phys. Rev. B **64**, (2001).
[74] F. Walz, J. Phys. Condens. Matter **14**, (2002).
[75] M. Avinor, C. B. Bargeron, and H. G. Drickamer, Inorg. Chem. **10**, 1338 (1971).
[76] J. S. Smart, *Effective Field Theories of Magnetism* (Saunders, 1966).
[77] Z. M. Dang, J. B. Wu, L. Z. Fan, and C. W. Nan, Chem. Phys. Lett. **376**, 389 (2003).
[78] S. Tadigadapa and K. Mateti, Meas. Sci. Technol. **20**, 92001 (2009).
[79] M. D. Mccluskey and S. J. Jokela, J. Appl. Phys. **106**, 0 (2009).
[80] M. Ozgür, D. Hofstetter, and H. Morkoç, Proc. IEEE **98**, 1255 (2010).
[81] P. Gopal and N. A. Spaldin, Phys. Rev. B **74**, 94418 (2006).
[82] M. Pinarbasi, S. Metin, H. Gill, M. Parker, B. Gurney, M. Carey, C. Tsang, M. Pinarbasi, S. Metin, H. Gill, and M. Parker, J. Appl. Phys. **87**, 5714 (2000).
[83] C.-C. Hsu, H.-W. Su, C.-H. Hou, J.-J. Shyue, and F.-Y. Tsai, Nanotechnology **26**, 385201 (2015).
[84] G. E. L. Processing, J. Am. Chem. Soc. **127**, 6135 (2005).
[85] D. Levy and M. Zayat, *The Sol-Gel Handbook* (2015).
[86] L. L. Hench and J. K. West, Chem. Rev. **90**, 33 (1990).
[87] R. Corriu and N. Trong Anh, *Molecular Chemistry of Sol-Gel Derived Nanomaterials* (2009).
[88] V. G. Kessler, in *Sol-Gel Handb.* (2015), pp. 195–224.
[89] C. Brinker and G. Scherer, Adv. Mater. **3**, 912 (1990).
[90] S. Thota, T. Dutta, and J. Kumar, J. Phys. Condens. Matter **18**, 2473 (2006).
[91] D. C. Joshi, S. Nayak, A. Kumar, A. Mohanta, D. Pamu, and S. Thota, J. Appl. Phys. **119**, 74303 (2016).
[92] J. Rodríguez-Carvajal, Lab. Léon Brillouin (CEA-CNRS), CEA/Saclay, 91191 Gif Sur Yvette Cedex,FRANCE. (2015).
[93] W. Kraus and G. Nolze, J. Appl. Crystallogr. **29**, 301 (1996).

[94] J. F. Moulder, *Handbook of X-Ray Photoelectron Spectroscopy: A Reference Book of Standard Spectra for Identification and Interpretation of XPS Data* (1992).
[95] J. J. Shea, IEEE Electr. Insul. Mag. **19**, 73 (2003).
[96] P. S. Bagus, E. S. Ilton, and C. J. Nelin, Surf. Sci. Rep. **68**, 273 (2013).
[97] N. J. Kidner, B. J. Ingram, Z. J. Homrighaus, T. O. Mason, and E. J. Garboczi, MRS Online Proc. Libr. Arch. **756**, (2003).
[98] B. Fe and O. Nb, Phys. B Phys. Condens. Matter **406**, 3470 (2011).
[99] O. S. Doroshkevych, A. V Shylo, O. V Saprukina, I. A. Danilenko, T. E. Konstantinova, and L. A. Ahkozov, World J. Condens. Matter Phys. **2**, 1 (2012).
[100] P. Electrochemistry, C. Elements, C. Equivalent, and C. Models, Appl. Note AC **286**, R491 (2010).
[101] J. R. Macdonald and W. B. Johnson, in *Impedance Spectrosc. Theory, Exp. Appl. Second Ed.* (2005), pp. 1–26.
[102] G. Maes, Spectrochim. Acta Part A Mol. Biomol. Spectrosc. **59**, 211 (2003).
[103] D. S. Moore, in *Handb. Spectrosc. Second. Enlarg. Ed.* (2014), pp. 1813–1830.
[104] Philip H. Rieger, *Electron Spin Resonance* (The Royal Society of Chemistry, Thomas Graham House, Science Park, Milton Road, Cambridge CB4 0WF, UK, 2007).
[105] H. H. Woodbury and G. W. Ludwig, Phys. Rev. **117**, 102 (1960).
[106] J. Clarke and A. I. Braginski, *The SQUID Handbook* (2005).
[107] S. Shapiro, Phys. Rev. Lett. **11**, 80 (1963).
[108] O. Bierwagen and S. F. Fischer, Phys. Status Solidi **211**, 19 (2014).
[109] C. Rödl and A. Schleife, Phys. Status Solidi **211**, 74 (2014).
[110] C. Q. Zhang, J. P. Tu, Y. F. Yuan, X. H. Huang, X. T. Chen, and F. Mao, J. Electrochem. Soc. **154**, A65 (2007).
[111] M. Xu, Q. Li, Y. Ma, and H. Fan, Sensors Actuators B Chem. **199**, 403 (2014).
[112] S. Thota, J. H. Shim, and M. S. Seehra, J. Appl. Phys. **114**, 214307 (2013).
[113] D. C. Joshi, S. Thota, S. Nayak, D. D. Harish, P. Mahesh, A. Kumar, D. Pamu, and M. Qureshi, J. Phys. D. Appl. Phys. **47**, 435305 (2014).
[114] K. Y. Lee, H. Hwang, and W. Choi, ACS Appl. Mater. Interfaces **6**, 15575 (2014).
[115] T. J. Athauda, U. Butt, and R. R. Ozer, RSC Adv. **3**, 21431 (2013).
[116] M. F. Al-Kuhaili, S. M. A. Durrani, and I. A. Bakhtiari, Appl. Surf. Sci. **255**, 3033 (2008).
[117] Q. Xu, D.-M. Xu, M. Guan, Y. Guo, Q. Qi, and G.-D. Li, Sens. Actuat B-Chem **177**, 1134 (2013).
[118] V. Manthina, J. P. Correa Baena, G. Liu, and A. G. Agrios, J Phys Chem C **116**, 23864 (2012).
[119] L. Yan, F. Wu, L. Peng, L.-J. Zhang, P. Li, S. Dou, and T. Li, Int. J. Photoenergy **2012**, 1 (2012).
[120] S. H. Hwang, J. Song, Y. Jung, O. Y. Kweon, H. Song, and J. Jang, Chem. Commun. **47**, 9164 (2011).
[121] H. Pang, Y. Ma, G. Li, J. Chen, J. Zhang, H. Zheng, and W. Du, Dalt. Trans. **41**, 13284 (2012).
[122] S. Thota and J. Kumar, J. Nanosci. Nanotechnol. **8**, 4073 (2008).
[123] R. Elilarassi and G. Chandrasekaran, Am. J. Mater. Sci. **2**, 46 (2012).
[124] H. B. Wang, Y. Chen, H. B. Wang, C. Zhang, F. J. Yang, J. X. Duan, C. P. Yang, Y. M. Xu, M. J. Zhou, and Q. Li, Appl. Phys. Lett. **90**, 52505 (2007).
[125] D. Lisjak, I. Zajc, M. Drofenik, and J. Jamnik, Solid State Ionics **99**, 125 (1997).
[126] D. Lisjak, M. Drofenik, G. Dražič, and D. Kolar, J. Mater. Sci. **33**, 4201 (1998).
[127] G. Dražič and D. Lisjak, Mikrochim. Acta **132**, 289 (2000).
[128] G. Srinet, R. Kumar, and V. Sajal, Ceram. Int. **39**, 7557 (2013).
[129] A. Mhamdi, B. Ouni, A. Amlouk, K. Boubaker, and M. Amlouk, J. Alloys Compd. **582**, 810 (2014).
[130] C. K. Ghosh, S. Malkhandi, M. K. Mitra, and K. K. Chattopadhyay, J. Phys. D. Appl. Phys. **41**, 245113 (2008).
[131] S. Hagino, K. Yoshio, and T. Yamazaki, Ferroelectrics **264**, 37 (2001).
[132] Y.-H. H. Lin, M. Li, C.-W. W. Nan, J. Li, J. Wu, and J. He, Appl. Phys. Lett. **89**, 32907 (2006).
[133] S. Maensiri, P. Thongbai, and T. Yamwong, Appl. Phys. Lett. **90**, 21 (2007).
[134] S. Thota, T. Dutta, and J. Kumar, J. Phys. Condens. Matter **18**, 2473 (2006).
[135] R. H. Kodama and A. E. Berkowitz, Phys. Rev. B **59**, 6321 (1999).
[136] S. Thota and J. Kumar, J. Phys. Chem. Solids **68**, 1951 (2007).
[137] H. P. Rooksby, Acta Crystallogr. **1**, 226 (1948).
[138] Y. Shimomura and I. Tsubokawa, J. Phys. Soc. Jpn. **9**, 19 (1954).
[139] A. Schrön, C. Rödl, and F. Bechstedt, Phys. Rev. B **86**, 1 (2012).
[140] J. Mohapatra, D. K. Mishra, S. K. Kamilla, V. R. R. Medicherla, D. M. Phase, V. Berma, and S. K. Singh, Phys. Status Solidi **248**, 1352 (2011).
[141] H. K. Yadav, K. Sreenivas, V. Gupta, J. F. Scott, and R. S. Katiyar, Appl. Phys. Lett. **92**, 2908 (2008).
[142] A. P. Rambu, L. Ursu, N. Iftimie, V. Nica, M. Dobromir, and F. Iacomi, Appl. Surf. Sci. **280**, 598 (2013).
[143] F. Hai-Bo, Y. Shao-Yan, Z. Pan-Feng, W. Hong-Yuan, L. Xiang-Lin, J. Chun-Mei, Z. Qin-Sheng, C. Yong-Hai, and W. Zhan-Guo, Chinese Phys. Lett. **24**, 2108 (2007).

[144] K. C. Barick, M. Aslam, V. P. Dravid, and D. Bahadur, J. Colloid Interface Sci. **349**, 19 (2010).
[145] K. J. Gaskell, A. Starace, and M. A. Langell, J Phys Chem C **111**, 13912 (2007).
[146] M. A. Peck and M. A. Langell, Chem. Mater. **24**, 4483 (2012).
[147] W. Shin and N. Murayama, Int. Conf. Thermoelectr. ICT, Proc. 356 (1999).
[148] A. J. Sievers and J. B. Page, Infrared Phys. **32**, 425 (1991).
[149] I. F. Chang, Phys. Rev. B **14**, 4318 (1976).
[150] R. H. Lyddane, R. G. Sachs, and E. Teller, Phys. Rev. **59**, 673 (1941).
[151] W. Cochran, Ferroelectrics **35**, 3 (1981).
[152] J. Hlinka, T. Ostapchuk, D. Nuzhnyy, J. Petzelt, P. Kuzel, C. Kadlec, P. Vanek, I. Ponomareva, and L. Bellaiche, Phys. Rev. Lett. **101**, 1 (2008).
[153] Barker Jr, Phys. Rev. B **12**, 4071 (1975).
[154] Dhananjay, J. Nagaraju, and S. B. Krupanidhi, J. Appl. Phys. **99**, 2 (2006).
[155] M. D. Glinchuk, E. V. Kirichenko, V. A. Stephanovich, and B. Y. Zaulychny, J. Appl. Phys. **105**, 2 (2009).
[156] M. K. Gupta, N. Sinha, and B. Kumar, J. Appl. Phys. **112**, 2010 (2012).
[157] Z. M. Dang, H. P. Xu, D. Xie, and L. Li, Mater. Lett. **61**, 511 (2007).
[158] P. J. Gielisse, J. N. Plendl, L. C. Mansur, R. Marshall, S. S. Mitra, R. Mykolajewycz, and A. Smakula, J. Appl. Phys. **36**, 2446 (1965).
[159] D. Viehland, S. J. Jang, L. E. Cross, and M. Wuttig, J. Appl. Phys. **68**, 2916 (1990).
[160] C. C. Homes, Science (80-.). **293**, 673 (2001).
[161] Z.-G. Ye, *Handbook of Advanced Dielectric, Piezoelectric and Ferroelectric Materials: Synthesis, Properties and Applications* (2008).
[162] B. G. Kim, S. M. Cho, T. Y. Kim, and H. M. Jang, Phys. Rev. Lett. **86**, 3404 (2001).
[163] I. Grinberg, Y.-H. Shin, and A. M. Rappe, Phys. Rev. Lett. **103**, 197601 (2009).
[164] J. A. Mydosh, *Spin Glasses: An Experimental Introduction* (1993).
[165] G. Smolensky, Ferroelectrics **53**, 129 (1984).
[166] A. P. Ramirez, M. A. Subramanian, M. Gardel, G. Blumberg, D. Li, T. Vogt, and S. M. Shapiro, Solid State Commun. **115**, 217 (2000).
[167] G. Shirane, R. Newnham, and R. Pepinsky, Phys. Rev. **96**, 581 (1954).
[168] E. Buixaderas, V. Bovtun, M. Kempa, M. Savinov, and D. Nuzhnyy, **14111**, 0 (2010).
[169] K. Uchino and S. Nomura, Ferroelectrics **44**, 55 (1982).
[170] G. Burns, Phys. Rev. B **13**, 215 (1976).
[171] H. Yu and Z. Ye, J. Appl. Phys. **103**, 34114 (2008).
[172] A. A. Bokov, Y.-H. Bing, W. Chen, Z.-G. Ye, S. a. Bogatina, I. P. Raevski, S. I. Raevskaya, and E. V. Sahkar, Phys. Rev. B **68**, 52102 (2003).
[173] M. Yu, H. Qiu, X. Chen, H. Li, and W. Gong, Mater. Chem. Phys. **126**, 797 (2011).
[174] N. Kilinç, S. Öztürk, L. Arda, A. Altindal, and Z. Z. Öztürk, J. Alloys Compd. **536**, 138 (2012).
[175] D. Yu, C. Wang, B. L. Wehrenberg, and P. Guyot-Sionnest, Phys. Rev. Lett. **92**, 216802 (2004).
[176] N. Mott, *Conduction in Non-Crystalline Materials* (1993).
[177] R. M. Hill, Phys. Status Solidi **34**, 601 (1976).
[178] A. H. Morrish, Phys. Princ. Magn. by Allan H. Morrish, Pp. 696. ISBN 0-7803-6029-X. Wiley-VCH, January 2001. **1**, (2001).
[179] H. Sato, T. Minami, S. Takata, and T. Yamada, Thin Solid Films **236**, 27 (1993).
[180] J. G. Aiken and A. G. Jordan, J. Phys. Chem. Solids **29**, 2153 (1968).
[181] M. A. Wittenauer and L. L. Van Zandt, PHILOS MAG B **46**, 659 (1982).
[182] J. R. Drabble and A. W. Palmer, J. Appl. Phys. **37**, 1778 (1966).
[183] S. Thota and J. Kumar, J. Phys. Chem. Solids **68**, 1951 (2007).
[184] W. J. Moore, *Seven Solid States: An Introduction to the Chemistry and Physics of Solids* (WA Benjamin, 1967).
[185] M. A. Kolber and R. K. MacCrone, Phys. Rev. Lett. **29**, 1457 (1972).
[186] I. G. Austin and N. F. Mott, Adv. Phys. **18**, 41 (1969).
[187] J. Singh, J. Lumin. **60**–**61**, 772 (1994).
[188] X. Q. Liu, Y. J. Wu, and X. M. Chen, Solid State Commun. **150**, 1794 (2010).
[189] D. Adler and J. Feinleib, Phys. Rev. B **2**, 3112 (1970).
[190] M. K. Gupta, N. Sinha, B. Kumar, M. K. Gupta, N. Sinha, and B. Kumar, J. Appl. Phys. **112**, 14303 (2012).
[191] C. M. Osburn and R. W. Vest, J. Phys. Chem. Solids **32**, 1343 (1971).
[192] F. Friedman, F. L. Weichman, and D. S. Tannhauser, Phys. Status Solidi **27**, 273 (1975).
[193] M. L. Volpe and J. Reddy, J. Chem. Phys. **53**, 1117 (1970).
[194] M. R. Notis, R. M. Spriggs, and W. C. Hahn Jr, J. Appl. Phys. **44**, 4165 (1973).
[195] S. P. Mitoff, J. Chem. Phys. **727**, 882 (1961).

[196] P. Lunkenheimer, A. Loidl, C. R. Ottermann, and K. Bange, Phys. Rev. B **44**, 5927 (1991).
[197] K. Jung, H. Seo, Y. Kim, H. Im, J. Hong, J.-W. W. Park, and J.-K. K. Lee, Appl. Phys. Lett. **90**, 52104 (2007).
[198] S. H. Lee, C. E. Tracy, and J. R. Pitts, Electrochem. Solid-State Lett. **7**, A299 (2004).
[199] J. E. Keem and J. M. Honig, *Selected Electrical and Thermal Properties of Undoped Nickel Oxide* (1978).
[200] T. Holstein, ANN PHYS-NEW YORK **8**, 343 (1959).
[201] D. Emin, Adv. Phys. **24**, 305 (1975).
[202] L. C. Bartel and B. Morosin, Phys. Rev. B **3**, 1039 (1971).
[203] S. Thota, J. H. Shim, and M. S. Seehra, J. Appl. Phys. **214307**, 4 (2013).
[204] J. E. Keem, J. M. Honig, and L. L. Van Zandt, Philos. Mag. Part B **37**, 537 (1978).
[205] G. Srinivasan and M. S. Seehra, Phys. Rev. B **29**, 6295 (1984).
[206] M. T. Hutchings and E. J. Samuelsen, Phys. Rev. B **6**, 3447 (1972).
[207] Z. L. Wang, J. Phys. Condens. Matter **16**, R829 (2004).
[208] D.-K. Hwang, M.-S. Oh, J.-H. Lim, and S.-J. Park, J. Phys. D. Appl. Phys. **40**, R387 (2007).
[209] T. Zhang, J. Yu, Y. Deng, N. Tian, and P. Gao, Sci. China Technol. Sci. **58**, 1328 (2015).
[210] Y. Hong, C. Tian, B. Jiang, A. Wu, Q. Zhang, G. Tian, and H. Fu, J. Mater. Chem. A **1**, 5700 (2013).
[211] G. Applerot, A. Lipovsky, R. Dror, N. Perkas, Y. Nitzan, R. Lubart, and A. Gedanken, Adv. Funct. Mater. **19**, 842 (2009).
[212] X. Lu, G. Wang, S. Xie, J. Shi, W. Li, Y. Tong, and Y. Li, Chem. Commun. **48**, 7717 (2012).
[213] X. Li, B. Wei, J. Wang, X. Li, H. Zhai, and J. Yang, J. Alloy. Compd. **689**, 287 (2016).
[214] T. Jungwirth, X. Marti, P. Wadley, and J. Wunderlich, Nat. Nanotechnol. **11**, 231 (2016).
[215] T. Dietl, K. Sato, T. Fukushima, A. Bonanni, M. Jamet, A. Barski, S. Kuroda, M. Tanaka, P. N. Hai, and H. Katayama-Yoshida, Rev. Mod. Phys **87**, 1311 (2015).
[216] S. C. Pillai, J. M. Kelly, R. Ramesh, and D. E. McCormack, J MATER CHEM C **1**, 3268 (2013).
[217] A. Sedky and E. El-Suheel, in *World Acad. Sci. Eng. Technol. Int. J. Math. Comput. Phys. Electr. Comput. Eng.* (2012), pp. 496–502.
[218] F. Kharchouche, S. Belkhiat, and D. E. C. Belkhiat, Sci. Meas. Technol. IET **7**, 326 (2013).
[219] S. C. Pillai, J. M. Kelly, D. E. McCormack, and R. Ramesh, J. Mater. Chem. **18**, 3926 (2008).
[220] R. Zhang, J. Miao, F. Shao, W. T. Huang, C. Dong, X. G. Xu, and Y. Jiang, J. Non. Cryst. Solids **406**, 102 (2014).
[221] M. S. Seehra, P. Dutta, H. Shim, and A. Manivannan, Solid State Commun. **129**, 721 (2004).
[222] M. S. Seehra and T. M. Giebultowicz, Phys. Rev. B **38**, 11898 (1988).
[223] R. E. Dietz, G. I. Parisot, and A. E. Meixner, Phys. Rev. B **4**, 2302 (1971).
[224] M. T. Hutchings and E. J. Samuelsen, Phys. Rev. B **6**, 3447 (1972).
[225] N. Rinaldi-Montes, P. Gorria, D. Martinez-Blanco, A. B. Fuertes, L. F. Barquin, I. Puente-Orench, and J. A. Blanco, Nanotechnology **26**, 305705 (2015).
[226] M. Jagodič, Z. Jagličić, A. Jelen, J. B. Lee, Y.-M. Kim, H. J. Kim, and J. Dolinšek, J. Phys. Condens. Matter **21**, 215302 (2009).
[227] M. P. Proenca, C. T. Sousa, A. M. Pereira, P. B. Tavares, J. Ventura, M. Vazquez, and J. P. Araujo, Phys. Chem. Chem. Phys. **13**, 9561 (2011).
[228] E. Brok, K. Lefmann, P. P. Deen, B. Lebech, H. Jacobsen, G. J. Nilsen, L. Keller, and C. Frandsen, Phys. Rev. B **91**, 14431 (2015).
[229] S. Mandal, K. S. R. Menon, S. K. Mahatha, and S. Banerjee, Appl. Phys. Lett. **99**, 232507 (2011).
[230] W.-L. L. Jang, Y.-M. M. Lu, W.-S. S. Hwang, T.-L. L. Hsiung, and H. P. Wang, Appl. Phys. Lett. **94**, 62103 (2009).
[231] S. Mandal, S. Banerjee, and K. S. R. Menon, Phys. Rev. B **80**, 214420 (2009).
[232] L. Xia, W. Li, C.-X. Wang, Y. Zhang, J.-Z. Jiang, and S.-L. Zhang, J. Raman Spectrosc. **45**, 822 (2014).
[233] A. Punnoose, H. Magnone, and M. S. Seehra, IEEE Trans. Magn. **37**, 2150 (2001).
[234] M. E. Fisher, Philos. Mag. **7**, 1731 (1962).
[235] E. E. Bragg and M. S. Seehra, Phys. Rev. B **7**, 4197 (1973).
[236] Y. A. Kumzerov, N. F. Kartenko, L. S. Parfeneva, I. A. Smirnov, A. A. Sysoeva, H. Misiorek, and A. Jezowski, Phys. Solid State **54**, 1066 (2012).
[237] I. Rawal and A. Kaur, J. Appl. Phys. **115**, 43717 (2014).
[238] S. Upadhyay, O. Parkash, and D. Kumar, J. Alloys Compd. **432**, 258 (2007).
[239] S. Thota, T. Dutta, and J. Kumar, J. Phys. Condens. Matter **18**, 2473 (2006).
[240] P. V Radovanovic and D. R. Gamelin, Phys. Rev. Lett. **91**, 157202 (2003).
[241] M. Tadic, D. Nikolic, M. Panjan, and G. R. Blake, J. Alloy. Compd. **647**, 1061 (2015).
[242] G. Fischer, M. Däne, A. Ernst, P. Bruno, M. Lüders, Z. Szotek, W. Temmerman, and W. Hergert, Phys. Rev. B **80**, 14408 (2009).
[243] R. E. Dietz, G. I. Parisot, and A. E. Meixner, Phys. Rev. B **4**, 2302 (1971).

[244] L. C. Bartel and B. Morosin, Phys. Rev. B **3**, 1039 (1971).
[245] H. J. Shim, Magnetic and Structural Properties of Nanoparticles of Nickel Oxide, 2006.
[246] S. A. Makhlouf, H. Al-Attar, and R. H. Kodama, Solid State Commun. **145**, 1 (2008).
[247] M. S. Jagadeesh and M. S. Seehra, Phys. Rev. B **23**, 1185 (1981).
[248] G. E. Kugel, B. Hennion, and C. Carabatos, Phys. Rev. B **18**, 1317 (1978).
[249] K. Tomiyasu and S. Itoh, J. Phys. Soc. Japan **75**, 84708 (2006).
[250] M. S. Lin and H. Hacker, Solid State Commun. **6**, 687 (1968).
[251] D. C. Joshi, S. Nayak, A. Kumar, A. Mohanta, D. Pamu, and S. Thota, J. Appl. Phys. **119**, 74303 (2016).
[252] D. C. Joshi, K. Dasari, S. Nayak, R. Palai, P. Suresh, and S. Thota, J. Electron. Mater. **45**, 2059 (2016).
[253] P. Mahesh, S. Thota, and D. Pamu, IEEE Trans. Dielectr. Electr. Insul. **22**, 3668 (2015).
[254] V. Ambegaokar, B. I. Halperin, and J. S. Langer, Phys. Rev. B **4**, 2612 (1971).
[255] M. Pollak, J. Non. Cryst. Solids **11**, 1 (1972).
[256] M. C. Biesinger, L. W. M. Lau, A. R. Gerson, and R. S. C. Smart, Appl. Surf. Sci. **257**, 887 (2010).
[257] R. Zhang, J. Miao, F. Shao, W. T. Huang, C. Dong, X. G. Xu, and Y. Jiang, J. Non-Cryst. Solids **406**, 102 (2014).
[258] J. Gangwar, K. K. Dey, S. K. Tripathi, M. Wan, R. R. Yadav, R. K. Singh, A. K. Srivastava, and others, Nanotechnology **24**, 415705 (2013).
[259] Y. V Panasiuk, O. E. Raevskaya, O. L. Stroyuk, S. Y. Kuchmiy, V. M. Dzhagan, M. Hietschold, and D. R. T. Zahn, Nanotechnology **25**, 75601 (2014).
[260] N. Kumar, A. Dorfman, and J. Hahm, Nanotechnology **17**, 2875 (2006).
[261] M. Ahmadi, R. Younesi, T. Vegge, and M. J. F. Guinel, Mater. Res. Express **1**, 25501 (2014).
[262] S. K. Yadav, J. Singh, V. V. Agrawal, and B. D. Malhotra, Appl. Phys. Lett. **101**, 23703 (2012).
[263] H. Colder, E. Guilmeau, C. Harnois, S. Marinel, R. Retoux, and E. Savary, J. Eur. Ceram. Soc. **31**, 2957 (2011).
[264] A. Maaroufi, O. Oabi, B. Lucas, A. El Amrani, and S. Degot, J. Non-Cryst. Solids **358**, 3312 (2012).
[265] K. Y. Kumar, H. B. Muralidhara, Y. Arthoba Nayaka, H. Hanumanthappa, M. S. Veena, and S. R. K. Kumar, in *Adv. Nanomater. Emerg. Eng. Technol. (ICANMEET), 2013 Int. Conf.* (2013), pp. 95–101.
[266] S. Thota and J. Kumar, J. Nanosci. Nanotechnol. **8**, 4073 (2008).
[267] X. Liu, F. Lin, L. Sun, W. Cheng, X. Ma, and W. Shi, Appl. Phys. Lett. **88**, 62508 (2006).
[268] D. More, C. Phadnis, S. Basu, A. Pathak, I. Dubenko, N. Ali, S. N. Jha, D. Bhattachryya, and S. Mahamuni, J. Phys. D Appl. Phys. **47**, 45308 (2014).
[269] M. Yilmaz, Phys. Scr. **89**, 95802 (2014).
[270] J. Zhu, J. Wang, Y. Zhou, and F. Wang, J. Mater. Sci. Mater. Electron. **25**, 791 (2014).
[271] Y. Chen, S. Gong, B. Zhang, W. Cao, D. Yu, Z. Liu, and W. Wang, Microelectron. Eng. **103**, 106 (2013).
[272] D. C. Joshi, S. Thota, S. Nayak, D. D. Harish, P. Mahesh, A. Kumar, D. Pamu, and M. Qureshi, J. Phys. D Appl. Phys. **47**, 435305 (2014).
[273] D. C. Joshi, D. D. Harish, S. Nayak, D. Roy, M. Qureshi, R. L. N. Saiprasad, T. Shiyani, D. Pamu, and S. Thota, in *Emerg. Electron. (ICEE), 2014 IEEE 2nd Int. Conf.* (2014), pp. 1–4.
[274] M. Snure, D. Kumar, and A. Tiwari, Appl. Phys. Lett. **94**, 12510 (2009).
[275] V. Singh and M. S. Seehra, J. Phys. Condens. Matter **21**, 456001 (2009).
[276] K. Hoffmann and D. Hahn, Phys. Status Solidi A **24**, (1974).
[277] R. P. S. Chakradhar, B. M. Nagabhushana, G. T. Chandrappa, J. L. Rao, and K. P. Ramesh, Appl. Magn. Reson **33**, 137 (2008).
[278] J. S. Thorp and M. D. Hossain, J. Magn. Magn. Mater. **22**, 311 (1981).
[279] S. R. P. Smith, F. Dravnieks, and J. E. Wertz, Phys. Rev. **178**, 471 (1969).
[280] A. E. Clark and E. P. Wohlfarth, Vol. 1North-Holland, Amsterdam 531 (1980).
[281] S. Blundell and D. Thouless, *Magnetism in Condensed Matter* (Oxford university press Oxford, 2001).
[282] J. W. Orton, P. Auzins, and J. E. Wertz, Phys. Rev. **119**, 1691 (1960).
[283] D. C. Joshi, S. Nayak, P. Suresh, K. S. Suresh, B. V Kumar, and S. Thota, Phys. Status Solidi **252**, 2323 (2015).
[284] H. Shim, A. Manivannan, M. S. Seehra, K. M. Reddy, and A. Punnoose, J. Appl. Phys. **99**, 210 (2006).
[285] R. Stoyanova, E. Zhecheva, and S. Angelov, Solid State Ionics **59**, 17 (1993).
[286] W. Xing, F. Li, Z. Yan, and G. Q. Lu, J. Power Sources **134**, 324 (2004).
[287] M. S. Seehra, *Basic Properties of Binary Oxides* (University of Seville Press, Seville, Spain, 1984).
[288] K.-C. Liu and M. A. Anderson, J. Electrochem. Soc. **143**, 124 (1996).
[289] Y. L. Raikher and V. I. Stepanov, Zh. Eksp. Teor. Fiz **102**, 1409 (1992).
[290] E. De Biasi, C. A. Ramos, R. D. Zysler, and H. Romero, Phys. Rev. B **65**, 144416 (2002).
[291] K. Nagata and A. Ishihara, J. Magn. Magn. Mater. **104**, 1571 (1992).
[292] H. K. Yadav, K. Sreenivas, V. Gupta, and R. S. Katiyar, J. Raman Spectrosc. **40**, 381 (2009).
[293] K. Samanta, P. Bhattacharya, R. S. Katiyar, W. Iwamoto, P. G. Pagliuso, and C. Rettori, Phys. Rev. B **73**, 245213 (2006).

[294] C. A. Arguello, D. L. Rousseau, and S. P. da S. Porto, Phys. Rev. **181**, 1351 (1969).
[295] K. Samanta, P. Bhattacharya, R. S. Katiyar, W. Iwamoto, P. G. Pagliuso, and C. Rettori, Phys. Rev. B **73**, 1 (2006).
[296] R. E. Dietz, W. F. Brinkman, A. E. Meixner, and H. J. Guggenheim, Phys. Rev. Lett. **27**, 814 (1971).
[297] D. Preston and E. Dietz, *The Art of Experimental Physics* (Wiley, New York, 1991).
[298] E. Cazzanelli, A. Kuzmin, G. Mariotto, and N. Mironova-Ulmane, J. Phys. Condens. Matter **15**, 2045 (2003).
[299] E. Cazzanelli, A. Kuzmin, N. Mironova-Ulmane, and G. Mariotto, Phys. Rev. B **71**, 134415 (2005).
[300] B. Zhang, X.-T. Zhang, H.-C. Gong, Z.-S. Wu, S.-M. Zhou, and Z.-L. Du, Phys. Lett. A **372**, 2300 (2008).
[301] Q. J. Ren, S. Filippov, S. L. Chen, M. Devika, N. K. Reddy, C. W. Tu, W. M. Chen, and I. A. Buyanova, Nanotechnology **23**, 425201 (2012).
[302] A. G. Milekhin, N. A. Yeryukov, L. L. Sveshnikova, T. A. Duda, E. I. Zenkevich, S. S. Kosolobov, A. V Latyshev, C. Himcinski, N. V Surovtsev, S. V Adichtchev, and others, J. Exp. Theor. Phys. **113**, 983 (2011).
[303] H. H. Brodsky, Phys. Rev. B **16**, 8 (1977).
[304] N. Mironova-Ulmane, a Kuzmin, I. Steins, J. Grabis, I. Sildos, and M. Pärs, J. Phys. Conf. Ser. **93**, 12039 (2007).
[305] G. J. Huang, J. B. Wang, X. L. Zhong, G. C. Zhou, and H. L. Yan, J. Mater. Sci. **42**, 6464 (2007).
[306] E. Chikoidze, Y. Dumont, H. J. Von Bardeleben, J. Gleize, F. Jomard, E. Rzepka, G. Berrerar, D. Ferrand, O. Gorochov, and A. Physics, Appl. Phys. A **88**, 167 (2007).
[307] M. Schumm, M. Koerdel, S. Müller, H. Zutz, C. Ronning, J. Stehr, D. M. Hofmann, and J. Geurts, N J. Phys. **10**, 43004 (2008).
[308] A. Hoffmann, A. Kaschner, and C. Thomsen, Phys. Status Solidi **6**, 1783 (2003).
[309] R. Lauck, M. Cardona, A. Rubio, J. Serrano, A. H. Romero, F. J. Manjon, R. Lauck, M. Cardona, and A. Rubio, Phys. Rev. B **69**, 94306 (2004).
[310] F. J. Manjón, B. Mari, J. Serrano, A. H. Romero, and B. Marí, J. Appl. Phys. **97**, 53516 (2005).
[311] C. Bundesmann, N. Ashkenov, M. Schubert, D. Spemann, T. Butz, E. M. Kaidashev, M. Lorenz, and M. Grundmann, Appl. Phys. Lett. **83**, 1974 (2003).
[312] G. Srinivasan and M. S. Seehra, Phys. Rev. B **28**, 6542 (1983).
[313] D. C. Joshi, P. Pramanik, S. Nayak, K. Dasari, R. J. Choudhary, and S. Thota, J. Phys. D. Appl. Phys. **50**, 325002 (2017).
[314] K. L. Pisane, S. Singh, and M. S. Seehra, Appl. Phys. Lett. **222409**, 1 (2017).
[315] G. C. Papaefthymiou, Nano Today **4**, 438 (2009).
[316] S. L. F. Bodker, S Morup, Phys. Rev. Lett. **72**, 8 (1994).
[317] E. De Biasi, C. A. Ramos, R. D. Zysler, E. De Biasi, C. A. Ramos, R. D. Zysler, and H. Romero, Phys. Rev. B **65**, 144416 (2002).
[318] H. Shim, P. Dutta, M. S. Seehra, and J. Bonevich, Solid State Commun. **145**, 192 (2008).
[319] M. S. Seehra, H. Shim, P. Dutta, A. Manivannan, and J. Bonevich, J. Appl. Phys. **97**, 1 (2005).
[320] S. A. Makhlouf, F. T. Parker, and A. E. Berkowitz, Phys. Rev. B **55**, R14717 (1997).
[321] W. L. Roth, J. Appl. Phys. **303**, 30 (1959).
[322] D. C. Joshi, S. Nayak, P. Suresh, K. S. Suresh, B. V. M. Kumar, and S. Thota, Phys. Status Solidi Basic Res. **252**, (2015).
[323] B. Hyunja, J. Shim, M. E. Bachlechner, D. Ph, W. Virginia, and H. J. Shim, Magn. Struct. Prop. Nanoparticles Nickel Oxide (2006).
[324] S. D. Tiwari and K. P. Rajeev, Phys. Rev. B - Condens. Matter Mater. Phys. **72**, 1 (2005).
[325] R. W. Chantrell, N. Walmsley, J. Gore, and M. Maylin, Phys. Rev. B **63**, 1 (2000).
[326] P. Padhan, N. K. Pandey, S. Srivastava, R. K. Rakshit, V. N. Kulkarni, and R. C. Budhani, Solid State Commun. **117**, 27 (2001).